Experimental Research on Particulate Matter Emissions from Gasoline Direct Injection Engines

Submitted by

Fan Xu

St Cross College

A thesis submitted in partial fulfilment of the requirements

for the degree of Doctor of Philosophy

Department of Engineering Science

University of Oxford

Trinity Term 2012

Experimental Research on Particulate Matter Emissions from Gasoline Direct Injection Engines

Fan Xu Doctor of Philosophy
St Cross College, Oxford Department of Engineering Science

A thesis submitted in partial fulfilment of the requirements for the degree of Doctor of Philosophy at the University of Oxford, Trinity Term 2012

ABSTRACT

As the legislation on vehicle emissions is becoming more and more stringent, increasing attention has been paid to the fine particles emitted by diesel and gasoline vehicles. The high number emission of fine particles has been shown to have a large impact on the atmospheric environment and human health. Researchers have shown that gasoline engines, especially Gasoline Direct Injection (GDI) engines, tend to emit large amounts of small size particles compared to Port Fuel Injection (PFI) gasoline engines and diesel engines fitted with Diesel Particulate Filters (DPFs). As a result, the particle number emissions of GDI engines will be restricted by the EU6 legislation. The particulate emission level of GDI engines means that they would face some challenges in meeting the EU6 requirement.

This thesis undertakes research in the following area. Firstly, the filtration efficiencies of glass fibre filters were quantified using a Cambustion Differential Mobility Spectrometer 500 (DMS500) to see if all of the particles from the sampled gas can be collected by the filters. Secondly, various valve timings and different injection modes such as double injection with a second injection after compression, single early injection and split early injection were implemented to measure the Particulate Matter (PM) emissions and combustion characteristics of a GDI engine under warm-up operating conditions. Thirdly, the techniques for removing volatile particles were investigated using a catalytic Volatile Particle Remover (VPR) and an Evaporation Tube (ET) with hot air dilution under various test conditions.

The results show that for the glass fibre filters tested here, the transmission efficiencies of the particles are very low, indicating that PM sampling using fibre filters is an effective method of studying the particulate emissions from the engine.

Particle number emissions using double injection with injection after compression were much higher than those with single injection during the intake stroke. Under 1200 rpm, 110 Nm cold engine operation, no reduction effect on PM emissions was shown by using split intake injection to further facilitate homogeneous mixture formation compared with single intake injection. Valve timings showed moderate effects on particulate emissions. Properly adjusted timing for exhaust valve closure led to reduced particulate emissions by a factor of about 2 and the combustion characteristics were not adversely affected much.

The VPR temperature and exhaust residence time did not show much effect on the catalytic VPR performance once the mass flow rate of exhaust was above 0.09 g/s. Generally, the transmission efficiencies of the VPR follow the trends of the scaled PMP counting efficiency specification. Hot air dilution is effective in reducing the small size particles. At 23 nm, the transmission efficiencies are within the error range of the PMP specification. The catalytic VPR and the Evaporation Tube were all found to be effective in reducing the particle number of small size (nucleation mode) particles. Both systems have some particle loss mainly due to the physical effects of diffusion and thermophoresis.

Until now, GDI engines have not been optimised for reducing particulate emissions as the focus has been on gaseous emissions and fuel economy. With careful re-optimisation of the catalyst light-off and engine calibration (especially for transients) then there is scope for GDI engines to meet forthcoming emissions legislation.

CONTENTS

ACKNOWLEDGMENTS

I would like to express my sincere gratitude to my supervisor Professor Richard Stone for offering me the DPhil studying opportunity, without the guidance and help from whom my research would not have been possible. I wish to thank Professor Stone for his professional advice, technical assistance, strategic direction. His kindness and generous support has always strengthened my confidence to overcome difficulties, which is also crucial to the completion of my project.

I want to send my special appreciation to China Scholarship Council (CSC) and Education Section of the Chinese Embassy in the UK for their help and financial support to my DPhil study and Jaguar Land Rover for contributing to laboratory expenses. Thanks also to Roger Cracknell from Shell for the provision of the test fuels.

During the course of my doctorate study I have made lots of friends, in particular in the Internal Combustion Engines Group (Longfei Chen, Ben Twiney, Mike Braisher, Huayong Zhao, Mengchen Hu, Felix Leach, Nathan Hinton, Kun Liang, Paul Bailey and Mike Dadd). It is their help and friendship that makes my life exciting. I would also like to thank all the staff in the Electronic and Mechanical Workshops who have ever facilitated me in building up testing equipment.

Last but not least I would like to express my earnest gratitude to my parents and my former supervisors Professor Jianxin Wang, Professor Shijin Shuai and Professor Zhi Wang at Tsinghua University for their consistent support and advice towards my research. Had it not been their encouragement, I would not have made progress this far.

Nomenclature

S.I. units and standard notations for chemical elements, formulae, and abbreviations are used in this thesis. Other abbreviations are listed below.

Acronyms

ABDC	After Bottom Dead Centre
Acc	Accumulation Mode
AFR	Air Fuel Ratio
ATDC	After Top Dead Centre
BMEP	Brake Mean Effective Pressure
BSFC	Break Specific Fuel Consumption
BSP	British Standard Pipe
BTDC	Before Top Dead Centre
°CA	Crank Angle Degree
CI	Compression Ignition
CMD	Count (number) Mean Diameter
CO	Carbon Monoxide
CO_2	Carbon Dioxide
CPC	Condensation Particle Counter
CPMA	Centrifugal Particle Mass Analyser
CPS	Cam Profile Switching
CRDI	Common Rail Direct Injection
CS	Catalytic Stripper
CVI	Closed Valve Injection
CVS	Constant Volume Sampling
DAM	Diameter of Average Mass
DAQ	Data Acquisition
DDC	Dekati Diffusion Charger
DFV	Diesel Fuelled Vehicle
DI	Direct Injection
DISC	Direct Injection Stratified Charge
DISI	Direct Injection Spark Ignition
DMA	Differential Mobility Analyser
DMS	Differential Mobility Spectrometer
Dp	Particle Diameter
DPF	Diesel Particle Filter
DR	Dilution Ratio
ECU	Engine Control Unit
EGR	Exhaust Gas Recirculation
ELPI	Electrical Low Pressure Impactor
EOI	End of Injection
ET	Evaporation Tube
EVC	Exhaust Valve Closing

EVO	Exhaust Valve Opening
FID	Flame Ionization Detector
FTP	Federal Test Procedure
GCMS	Gas Chromatography and Mass Spectrometry
GDI	Gasoline Direct Injection
GF/A	Whatman® Glass Microfiber filter Grade GF/A
GFV	Gasoline Fuelled Vehicle
GMEP	Gross Mean Effective Pressure
GRPE	The Working Party on Pollution and Energy
GSD	Geometric Standard Deviation
HC	Hydrocarbon
HDAQ	High Speed Data Acquisition
HEPA	High Efficiency Particulate Air (filter)
HWFET	Highway Fuel Economy Test
IMEP	Indicated Mean Effective Pressure
IMEPn	Net Indicated Mean Effective Pressure
IUFC15	Inrets 15 × Urbain Fluide Court
IVC	Intake Valve Closing
IVO	Intake Valve Opening
kph	Kilometre per Hour
LabVIEW	Laboratory Virtual Instrument Engineering Workbench
Lambda	Relative Air Fuel Ratio
LAT	Laboratory of Applied Thermodynamics
LDAQ	Low Speed Data Acquisition
LEPA	Low Efficiency Particulate Air (filter)
LII	Laser-Induced Incandescence
LPM	Litre per Minute
LS	Lab's Own Systems
MAP	Manifold Absolute Pressure
MATLAB	Matrix Laboratory
MFB	Mass Fraction Burned
MFM	Mass Flow Meter
N_2	Nitrogen
NA	Naturally Aspirated
NaCl	Sodium Chloride
NEDC	New European Drive Cycle
NI	National Instruments™
NMHC	Non-Methane Hydrocarbons
normpdf	Normal Probability Density Function
NO_x	Mixture of Nitric Oxide and Nitrogen Dioxide
Nucl	Nucleation Mode
O_2	Oxygen
OVI	Open Valve Injection
PAH	Polycyclic Aromatic Hydrocarbon
PAS	Power-Assisted Steering
PFI	Port Fuel Injection
PI	Positive Injection
PID	Proportional-Integral-Derivative
PISI	Port-Injection Spark-Ignition
PM	Particulate Matter

PMEP	Pumping Mean Effective Pressure
PMP	Particle Measurement Program
Pn	Particle number
PNC	Particle Number Counter
PND1	Primary Hot Diluter
PND2	Secondary Cold Diluter
ppm	Part per Million
PURA	Shell PURA (gasoline)
rpm	Revolutions Per Minute
RS	Reference System
SGDI	Spray-Guided Direct Injection
SI	Spark Ignition
SMPS	Scanning Mobility Particle Sizer
SOF	Soluble Organic Fraction
SOI	Start of (fuel) Injection
SPCS	Solid Particle Counting System
SPSS	Solid Particle Sampling System
Std	Standard Deviation
TD	Thermo-Denuder
TDC	Top Dead Centre
TGA	Thermo-Gravimetric Analysis
THC	Total Hydrocarbon
TTL	Transistor-Transistor Logic
TWC	Three Way Catalyst
UDC	Urban Driving Cycle
ULEV	Ultra-Low Emission Vehicle
UN-ECE	United Nations Economic Commission for Europe
VCT	Variable Cam Timing
VPR	Volatile Particle Remover
VPR-DF	VPR Dilution Factor
VVE	Exhaust Valve Retard Angle
VVI	Intake Valve Advance Angle
VVT	Variable Valve Timing
VVTH	Variable Valve Timing with High Lift
VVTL	Variable Valve Timing with Low Lift
WGDI	Wall-Guided Direct Injection
WOT	Wide Open Throttle

Symbols

a	Particle Radius
C_c	Cunningham Slip Correction Factor
C_m	Velocity Jump Coefficient
C_s	Thermal Creep Coefficient
C_t	Temperature Jump Coefficient
D	Particle Diffusion Coefficient
d_f	Fibre Diameter
d_p	Particle Diameter
E	Total Efficiency of a Filter
E_D	Single-Fibre Efficiency for Diffusion

E_{DR}	Interaction Term for Interception and Diffusion
E_{I}	Single-Fibre Efficiency for Impaction
E_{R}	Single-Fibre Efficiency for Interception
E_{Σ}	Single-Fibre Efficiency
k	Boltzmann Constant
K	Thermophoretic Coefficient
k_{g}	Thermal Conductivity of the Gas
k_{p}	Thermal Conductivity of the Particle
Ku	Kuwabara Hydrodynamic Factor
$\dot{m}$	Mass Flow Rate Through the VPR
$\mathrm{MFM}_{\mathrm{add\ gas}}$	Mass Flow Rate of the Additional Gas
$\mathrm{MFM}_{\mathrm{air}}$	Mass Flow Rate of Dilution Air
$\mathrm{MFM}_{\mathrm{bypass}}$	Bypass Mass Flow Rate
$\mathrm{MFM}_{\mathrm{DMS}}$	Sampling Mass Flow Rate of the DMS
$\mathrm{MFM}_{\mathrm{DMS+FID}}$	Sampling Mass Flow Rate of the DMS and FID
$\mathrm{MFM}_{\mathrm{exhaust}}$	Mass Flow Rate of Exhaust
$\mathrm{MFM}_{\mathrm{filter}}$	Mass Flow Rate through the Filter
$\mathrm{MFM}_{\mathrm{pump}}$	Mass Flow Rate through the Vacuum Pump
$n_{d\mathrm{p}}$	Number Concentration of the Particle with Diameter d_{p}
P	Penetration Efficiency
P_{diff}	Particle Penetration of Diffusion
Pe	Peclet Number
$\mathrm{P_m}$	Particle Mass
$\mathrm{P_n}$	Particle Number
Pr	Prandtl number
P_{th}	Particle Penetration of Thermophoresis
R_s	Specific Gas Constant of Exhaust
Stk	Stokes Number
t_{r}	Residence Time
U_0	Face Velocity
V_{TS}	Terminal Settling Velocity
$\dot{V}$	Volume Flow Rate through the VPR

Greek letters

α	Volume Fraction of Fibres (solidity)
λ	Gas Mean Free Path
η	Dynamic Viscosity
$\eta_{d\mathrm{p}}$	Transmission Efficiency of the Particle with Diameter d_{p}
μ	Count (number) Mean Diameter
σ_g	Geometric standard deviation
ρ_{p}	Density of Particle

LIST OF FIGURES

LIST OF TABLES

Chapter 1. Overview on Particulate Matter (PM) Emissions from Motor Vehicle

This chapter starts with a literature review, and at the end of this chapter there is an overview of the thesis structure and the contributions from the current work.

1.1 Introduction

As the regulation for CO_2 emissions of cars is becoming more and more stringent, vehicle manufacturers are increasing their efforts to lower the fuel consumption of cars, and high efficiency combustion engines are needed to achieve that. Gasoline direct injection (GDI) engines have shown benefits in fuel consumption over port fuel injection (PFI) engines [1]. So many companies have been devoting themselves to developing GDI engines over the past few years. Moreover, downsized gasoline engines - combining turbocharging and direct injection - have shown significant improvement in the fuel economy over naturally aspirated PFI engines with the same performance [2,3].

Kirwan et al. [4] show that the 3-cylinder turbocharged GDI engine is a cost effective powertrain for the compact car segment. Fig. 1.1 shows that downsizing results in a load increase to higher BMEP at constant speed and downspeeding results in higher load and lower engine speed. Both downsizing and downspeeding would lead to higher overall efficiency and thus reduced fuel consumption. Turbocharged GDI engines offer higher low end torque compared to turbocharged PFI engines due to their improved intake scavenging efficiency and intake charge cooling to reduce engine knock tendency, which is essential to maintain good driveability with downsizing and downspeeding in turbocharged engines.

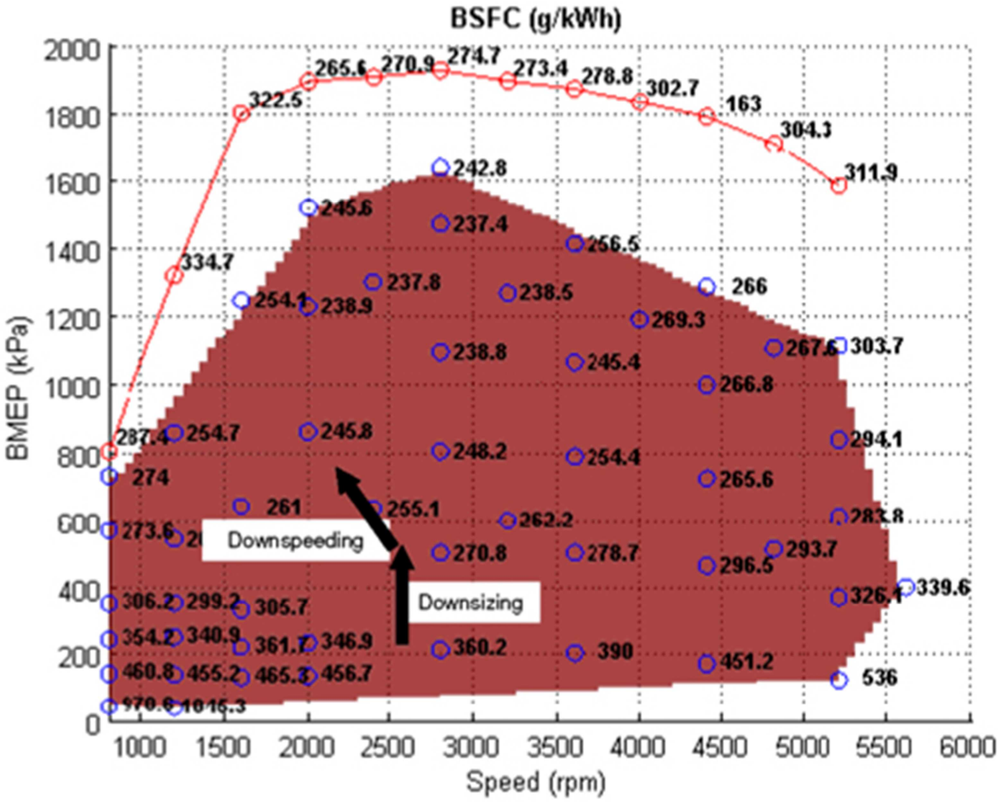

Fig. 1.1 Schematic representation of engine downsizing and downspeeding on an engine map [4].

On the other hand, the limits on vehicle pollutant emissions are becoming lower and lower, increasing attention has been paid to the fine particles emitted by diesel and gasoline vehicles. Researchers have shown that Gasoline Direct Injection (GDI) engines tend to emit large amounts of small size particles compared to Port Fuel Injection (PFI) gasoline engines and diesel engines fitted with Diesel Particulate Filters (DPFs). These contribute to a small portion of the particle mass emission but they contribute to a large portion of the particle number emission. Since there is a growing awareness that the particle number has more impact on the environment, a particle number measurement will be required by EU6 emissions legislation. Thus, collaborative particle measurement programmes have been executed by EU governments, and particle measurements have been carried out at different research institutions for both diesel and gasoline vehicles. The particulate emission level of GDI engines means that they would face some challenges in meeting the EU6 requirement. So it is important to further investigate the characteristics of GDI particle emissions, including their chemical composition, physical characteristics, formation mechanisms and elimination methods.

This chapter gives an overview of the legislation on particle emissions from vehicles and recent research on particle measurement techniques.

1.2 Overview of Legislation on Vehicle Emissions

Table 2.1 and Table 2.2 show the EU5 and EU6 emission standards, respectively [5]. It can be seen that the particle mass limit for passenger cars with Gasoline Direct Injection (GDI) engines will be implemented in the EU5 emission standard. Further, in EU6, a particle number limit will be determined and implemented on all spark ignition engines, for which the value would be defined before September 2014. The number limit for diesel engined passenger cars has been set to 6×10^{11} #/km. Thus, not only diesel engines are facing a challenge in meeting a further particle emissions limit, but also gasoline engines, especially direct injection engines, which will have to employ some additional methods or strategies to fulfill the legislative requirements.

Preliminary results have shown that, the direct injection gasoline engines emit more particles than either port fuel injection (PFI) gasoline engines or diesel engines with a diesel particulate filter (DPF). The characteristics of particles emitted by gasoline direct injection engines have to be further investigated.

Table 1.1 EU5 emission limit [5]

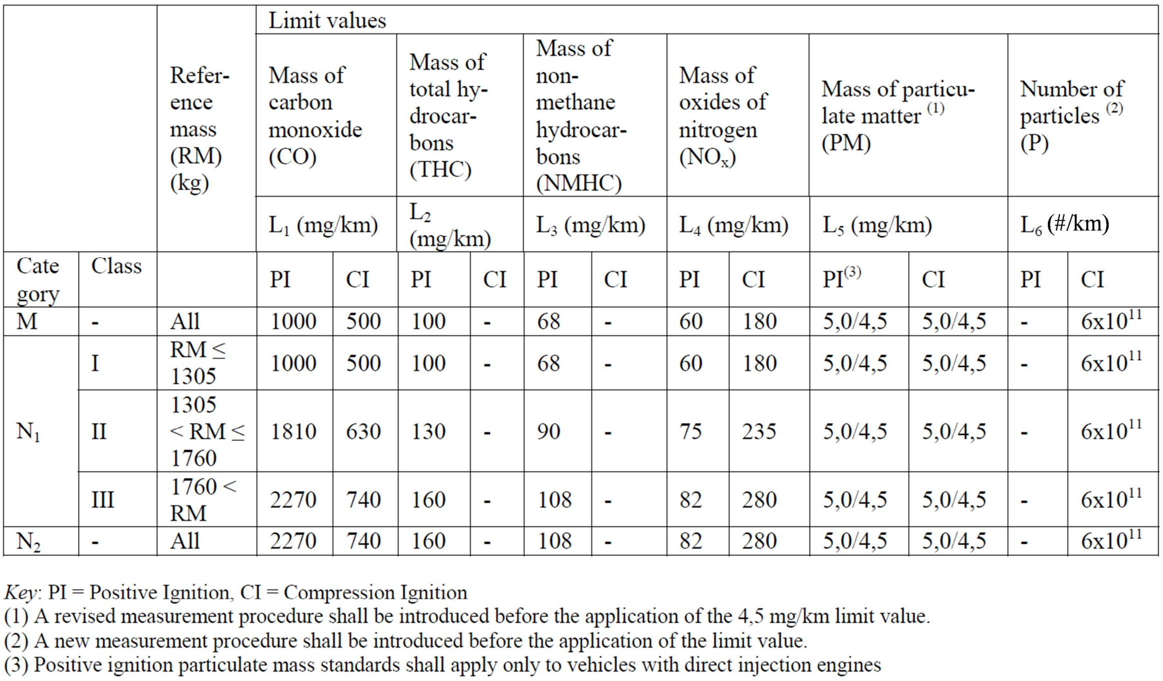

		Reference mass (RM) (kg)	Limit values											
			Mass of carbon monoxide (CO)		Mass of total hydrocarbons (THC)		Mass of non-methane hydrocarbons (NMHC)		Mass of oxides of nitrogen (NO_x)		Mass of particulate matter [(1)] (PM)		Number of particles [(2)] (P)	
			L_1 (mg/km)		L_2 (mg/km)		L_3 (mg/km)		L_4 (mg/km)		L_5 (mg/km)		L_6 (#/km)	
Category	Class		PI	CI	PI	CI	PI	CI	PI	CI	PI(3)	CI	PI	CI
M	-	All	1000	500	100	-	68	-	60	180	5,0/4,5	5,0/4,5	-	$6x10^{11}$
N_1	I	RM ≤ 1305	1000	500	100	-	68	-	60	180	5,0/4,5	5,0/4,5	-	$6x10^{11}$
	II	1305 < RM ≤ 1760	1810	630	130	-	90	-	75	235	5,0/4,5	5,0/4,5	-	$6x10^{11}$
	III	1760 < RM	2270	740	160	-	108	-	82	280	5,0/4,5	5,0/4,5	-	$6x10^{11}$
N_2	-	All	2270	740	160	-	108	-	82	280	5,0/4,5	5,0/4,5	-	$6x10^{11}$

Key: PI = Positive Ignition, CI = Compression Ignition
(1) A revised measurement procedure shall be introduced before the application of the 4,5 mg/km limit value.
(2) A new measurement procedure shall be introduced before the application of the limit value.
(3) Positive ignition particulate mass standards shall apply only to vehicles with direct injection engines

Table 1.2 EU6 emission limit [5]

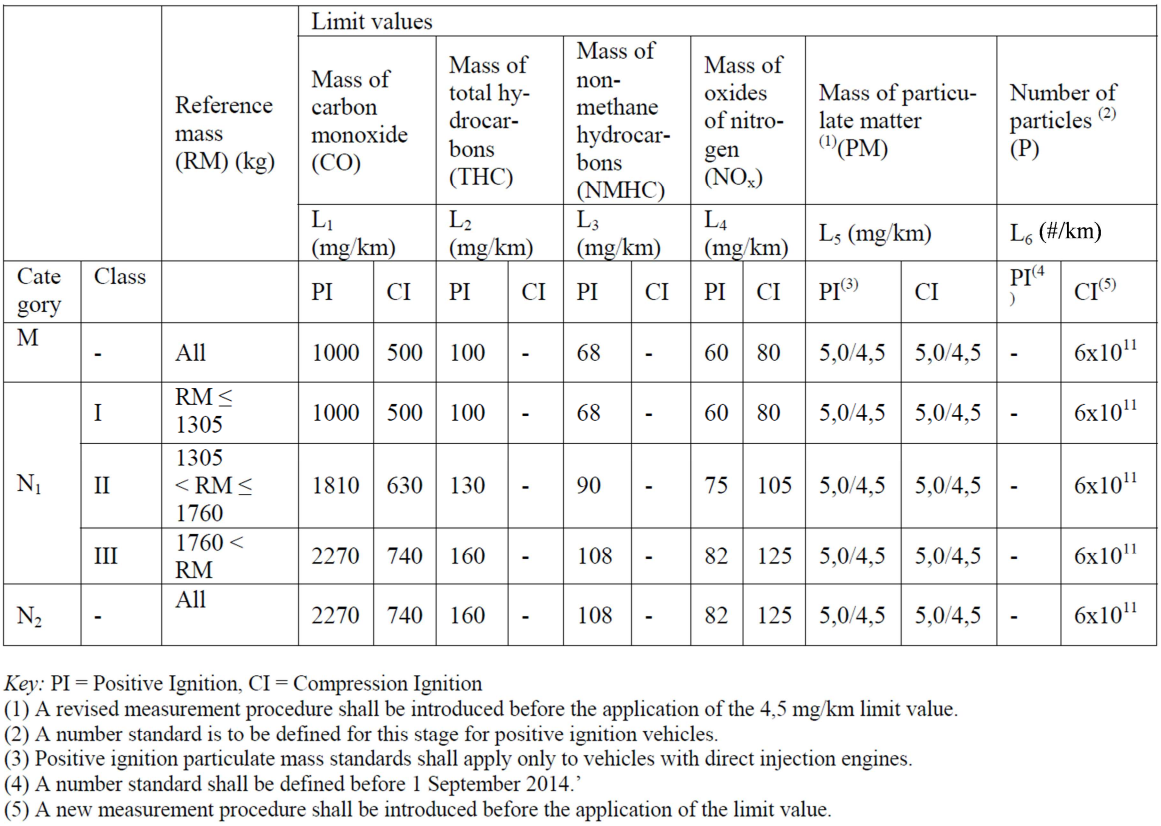

		Reference mass (RM) (kg)	Limit values											
			Mass of carbon monoxide (CO)		Mass of total hydrocarbons (THC)		Mass of non-methane hydrocarbons (NMHC)		Mass of oxides of nitrogen (NO_x)		Mass of particulate matter (1)(PM)		Number of particles (2) (P)	
			L_1 (mg/km)		L_2 (mg/km)		L_3 (mg/km)		L_4 (mg/km)		L_5 (mg/km)		L_6 (#/km)	
Category	Class		PI	CI	PI	CI	PI	CI	PI	CI	PI(3)	CI	PI(4)	CI(5)
M	-	All	1000	500	100	-	68	-	60	80	5,0/4,5	5,0/4,5	-	$6x10^{11}$
N_1	I	RM ≤ 1305	1000	500	100	-	68	-	60	80	5,0/4,5	5,0/4,5	-	$6x10^{11}$
	II	1305 < RM ≤ 1760	1810	630	130	-	90	-	75	105	5,0/4,5	5,0/4,5	-	$6x10^{11}$
	III	1760 < RM	2270	740	160	-	108	-	82	125	5,0/4,5	5,0/4,5	-	$6x10^{11}$
N_2	-	All	2270	740	160	-	108	-	82	125	5,0/4,5	5,0/4,5	-	$6x10^{11}$

Key: PI = Positive Ignition, CI = Compression Ignition
(1) A revised measurement procedure shall be introduced before the application of the 4,5 mg/km limit value.
(2) A number standard is to be defined for this stage for positive ignition vehicles.
(3) Positive ignition particulate mass standards shall apply only to vehicles with direct injection engines.
(4) A number standard shall be defined before 1 September 2014.'
(5) A new measurement procedure shall be introduced before the application of the limit value.

1.3 Overview on Recent Research of Particle Measurement

A brief summary of the particulate matter (PM) formation is given by Stone [6]. PM is formed in both spark ignition and diesel engines, but because the emissions from spark ignition engines are not visible (being sub-micron) they have been ignored in the past. The particulate matter legislation for diesel engines has become increasingly stringent, and for automotive applications a diesel particulate filter (DPF) is invariably needed. The particulate matter emissions from a compression ignition engine with a diesel particulate filter can now be lower than from direct injection gasoline engines (see Section 1.3.1), so it is not surprising that legislation for gasoline engines now includes particulate matter. Eastwood [7] provides a very comprehensive review of the formation, composition, characterisation, toxicology, and after treatment of particulate matter.

The origins of the particles and their ensuing contribution to the particle composition are summarized in Fig. 1.2.

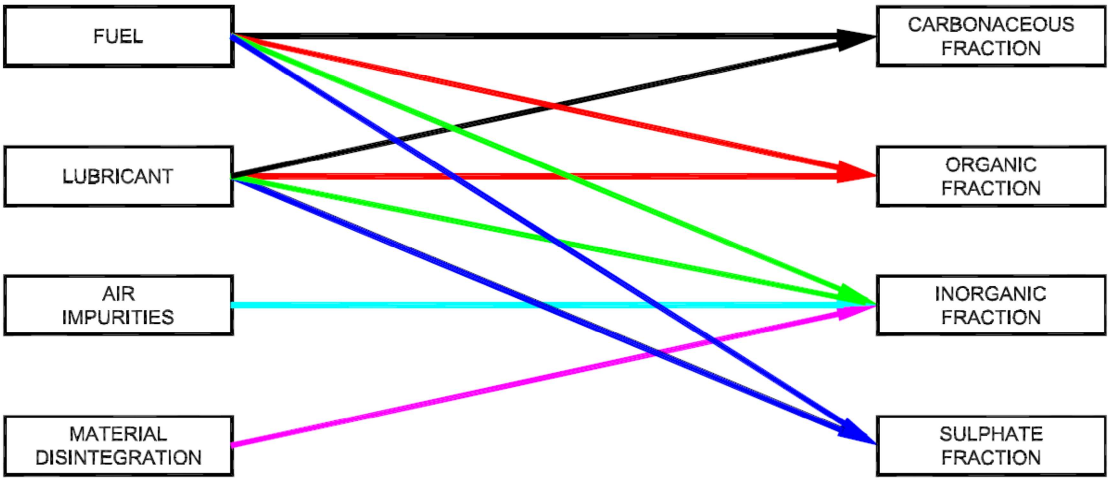

Fig. 1.2 Routes for the formation of particulate matter, adapted from Eastwood [7].

In Fig. 1.2 the carbonaceous fraction comes from pyrolysis of the fuel and oil, while the organic fraction is from the partial combustion of the fuel and oil. Wear products will normally be metallic and this leads to the inorganic fraction, along with any metals that have been present in the fuel or oil (possibly as additives). Any sulphur in the fuel or oil is oxidized and combines with water, leading to the production of sulphuric acid and sulphates;

it is of course inorganic but of sufficient quantity to justify separate identification.

The mechanisms for the production of the primary particles are complex and their modelling is especially challenging, and Eastwood [7] provides a comprehensive review. The primary particles are partly graphitic in structure, which has a planar structure with a hexagonal arrangement of carbon atoms – like a ‘matrix’ of benzene rings with the hydrogen removed and then fitted together.

When there are aromatic components present in the fuel, it is easy to imagine how the combustion process leads to a benzene ring (C_6H_6, which is intrinsically stable), but primary particles are also formed from fuel with no aromatic content, and this can be formed by the polymerization of acetylene (C_2H_2). Acetylene is a common intermediate species in combustion, especially with rich mixtures. Even if the overall air fuel ratio is weak of stoichiometric, inhomogeneities in the mixture will lead to locally rich regions. Other species can also lead to the formation of aromatic compounds. The precursors of graphite are the polycylic aromatic hydrocarbon (PAH) compounds, of which some examples are shown in Table 1.3.

Table 1.3 shows how the same number of carbon rings can form different shapes, and that 5 atom carbon rings are possible, in which case the molecule will not be planar. The level of aromaticity also varies (shown by the circle that represents molecular orbitals above and below the plane of the carbon atoms, but each containing 3 electrons). The position of the benzene ring can vary within some PAHs, and for a given number of rings both the number of hydrogen atoms and the number of carbon atoms can vary. The PAH molecules are mostly planar, and when they stack together a graphitic structure is formed, while if they are orientated randomly this results in an amorphous structure.

Table 1.3 Polycylic aromatic hydrocarbon (PAH) compounds

Phenathrene $C_{14}H_{10}$	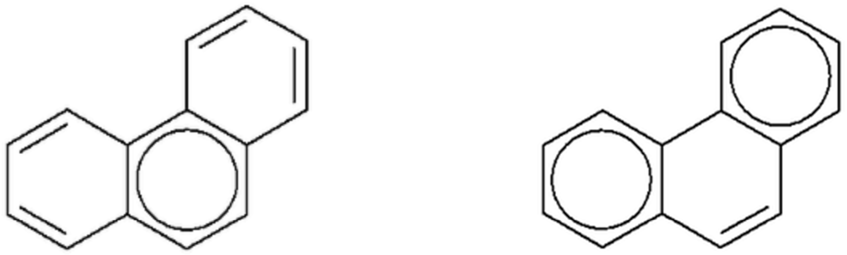		
Anthracene $C_{14}H_{10}$			
Chrysene $C_{18}H_{12}$	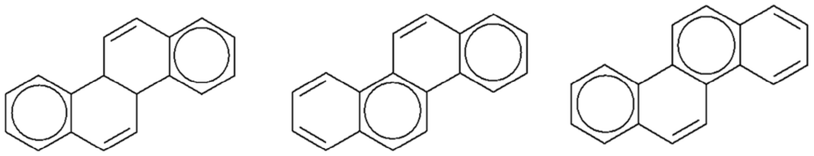		
Napthacene (Tetracene) $C_{18}H_{12}$			
Pyrene $C_{16}H_{10}$	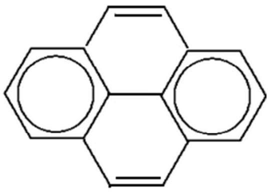	Corannulene $C_{20}H_{10}$	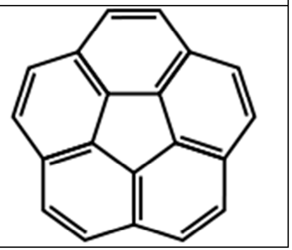

Modelling the growth of PAH molecules is computationally very demanding, Raj et al [8], and requires identification of the different types of site on a PAH molecule, as shown in Fig 1.3. PAH molecules can grow by the hydrogen-abstraction–carbon-addition (HACA) mechanism involving the addition of acetylene (C_2H_2) or other species at aromatic radical sites. The model reported by Raj et al [8] describes the structure and growth of planar PAH molecules and is based on reactions at radical sites available in the literature, and additional reactions obtained from quantum chemistry calculations. This provides a detailed model of soot particle composition and the associated surface growth and oxidation reactions using quantum chemistry and Kinetic Monte Carlo (KMC) simulations. It is necessary to use a statistical representation of the PAH molecules and their functional sites because tracking every single molecule is computationally prohibitive. It is also necessary to model when the molecules are held together in a particle through physical forces (rather than chemical bonds) to form aggregates, and to include the condensation/adsorption of hydrocarbons onto the surface of the aggregates.

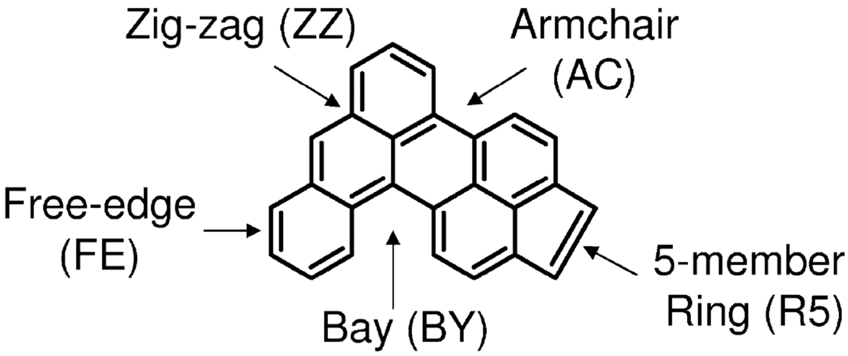

Fig. 1.3 Different types of site on a PAH molecule, with acknowledgement to Markus Kraft, University of Cambridge.

1.3.1 Particle Measurements from Gasoline Engines

With the tightening of emissions legislation, more research institutions are concerning themselves with particle emissions from gasoline engines, especially those with direct injection.

Recently, much attention has been given to the influence of fine particulate matter (PM) in the atmosphere on human health. Concerns about possible adverse health effects of particles from engines, led to a re-examination of PM standards and measurement protocols by Kittleson [9]. Fig. 1.4 shows idealized diesel exhaust particle number and mass weighted size distributions. The particle emissions can be divided into three modes, namely nucleation mode, accumulation mode and coarse mode. Most of the particle mass exists in the so-called accumulation mode in the 0.1-0.3 μm diameter range. This is where the carbonaceous agglomerates and associated adsorbed materials reside. The nucleation mode typically consists of particles in the 0.005-0.05 μm diameter range. This mode usually consists of volatile organic and sulphur compounds that form during exhaust dilution and cooling, and may also contain solid carbon and metal compounds. The nucleation mode typically contains 1-20% of the particle mass and more than 90% of the particle number. The coarse mode contains 5-20% of the particle mass. It consists of accumulation mode particles that have been deposited on the cylinder and exhaust system surfaces and later re-entrained. By number, most of the particles emitted by a diesel engine (the same is true for a spark-ignition engine) are nanoparticles. Kittleson [9] proposed that if nanoparticles would be a problem from diesel engines, then spark-ignition engines may be important sources too. And if nanoparticles are primarily composed of volatile materials, as was the case in engines they tested, then they are formed as the exhaust dilutes and cools. The number and size of nanoparticles would depend upon the details of the dilution process. Thus, atmospheric dilution should be simulated in order to make representative measurements.

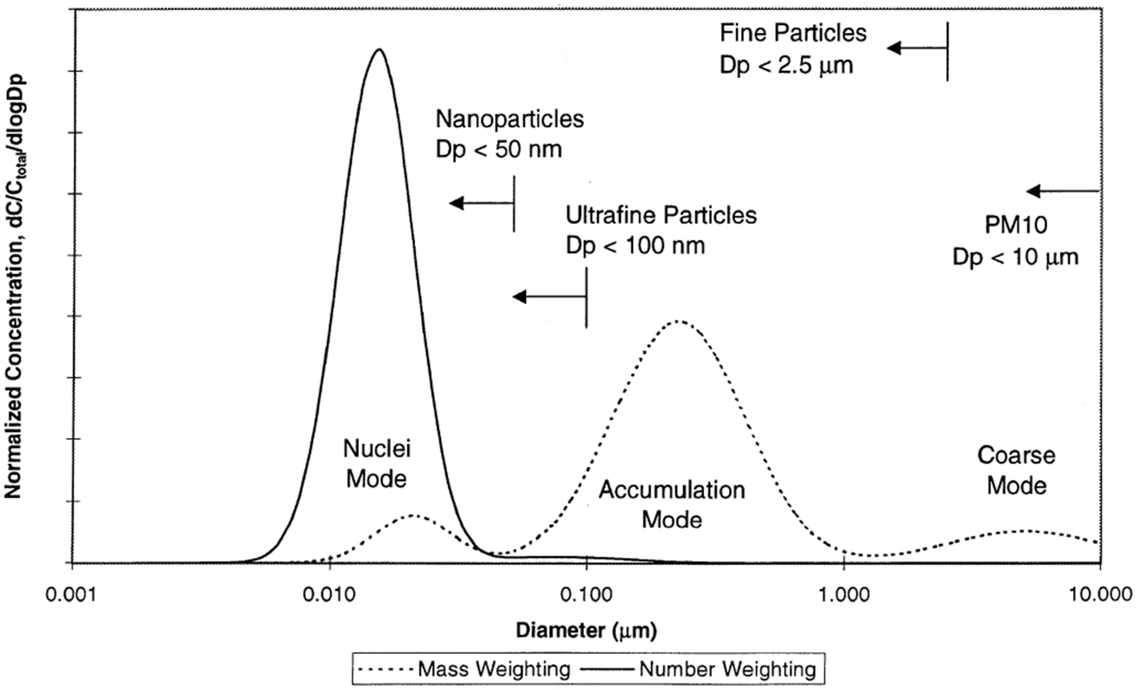

Fig. 1.4 Typical engine exhaust size distributions for mass and number weightings [9].

A number of vehicles with port fuel injection (PFI) were tested by Maricq et al. [10] from Ford. They concluded that particles were generated during acceleration and cold start in the

FTP cycle. After catalyst light-off, particle emissions diminished to near negligible levels at moderate cruise speeds and during deceleration. Particle emissions from diesel and gasoline vehicles were tested by Geller et al. [11]. And the physical and chemical characteristics of PM were studied. A Scanning Mobility Particle Sizer (SMPS), a Condensation Particle Counter (CPC), an Electrical Low Pressure Impactor (ELPI) and a Dekati Diffusion Charger (DDC) were used to measure the particle number concentration, particle size distribution and the active surface area of airborne particles.

A Scanning Mobility Particle Sizer (SMPS) can be used to measure particle size distributions and concentrations [11]. It consists of a neutralizer/charger, a mobility section, a particle detection instrument, and a computerized control and data acquisition system. Particles coming from a diluted exhaust sample pass first through a radioactive source bipolar ion neutralizer. This brings the particle charge distribution level to a minimum Boltzmann's distribution of charge. The aerosol then enters the mobility section close to its inner surface. Clean sheath air flows close to the central rod. When a voltage scan is applied to the rod, charged particles move in the radial direction inward or outward, depending on their polarity. Particles with the right polarity and electrical mobility exit through holes at the bottom of the central rod. A Condensation Particle Counter (CPC) monitors the number concentration of the total particle population [11]. It consists of a saturator, condenser, particle sensor, flow meter, and pump. The aerosol entering the instrument is first saturated with alcohol and then cooled in the condenser tube. During the cooling process, the alcohol condenses on the particles, and droplets of approximately 5-10μm in diameter are formed. The droplets flow from the condenser tube into a particle-sensing region. A laser light source is focused on a narrow volume in this region. The CPC operates in a single particle count mode for particle number concentrations lower than the threshold value. It counts pulses generated by individual particles passing through the view volume. An Electrical Low Pressure Impactor

(ELPI) monitored the number weighted size distribution in real time [11]. It consists of three main components: a cascade impactor, a unipolar diode charger and a multichannel electrometer. The charger is used to charge sampled particles to a well defined charge level. The charged particles are then introduced into the cascade impactor that classifies the aerosols into 12 size fractions according to their inertia and consequently their aerodynamic diameter. A Dekati Diffusion Charger (DDC), a prototype diffusion charger calibrated by the Laboratory of Applied Thermodynamics (LAT) at Aristotle University in Thessaloniki, measured the active surface area of airborne particles in real time [11]. Ions were used to label the aerosol and the output signal corresponded to the electrical current generated by the ion accumulated onto the particles.

Fig. 1.5 shows that the particle number emitted by the gasoline engine was an order of magnitude lower than the conventional diesel, while the diesel engine with a DPF exhibited the lowest particle number emission.

PM emissions from four PFI vehicles were tested on a chassis dynamometer by Kasper et al. [12]. The particle number concentrations were low at low speed cruise conditions, but were significantly higher during hard acceleration or highly transient phases of the test cycles. Also on-road size distributions of five SI vehicles were compared with a diesel vehicle by Kittelson et al. [13]. Under steady highway cruise conditions, they were unable to measure a significant particle signature above background for any of the cars. However, during full throttle accelerations from 80 to 113 km/h, the automotive test fleet produced size distributions similar to modern, heavy-duty diesel vehicles (Fig. 1.6). The gasoline vehicles emitted lower particle number concentrations in the upper end (60 – 300nm) of the accumulation mode where most of the particle mass is found. However, older, high mileage vehicles emitted a greater number of nucleation mode particles compared to the lower mileage vehicles.

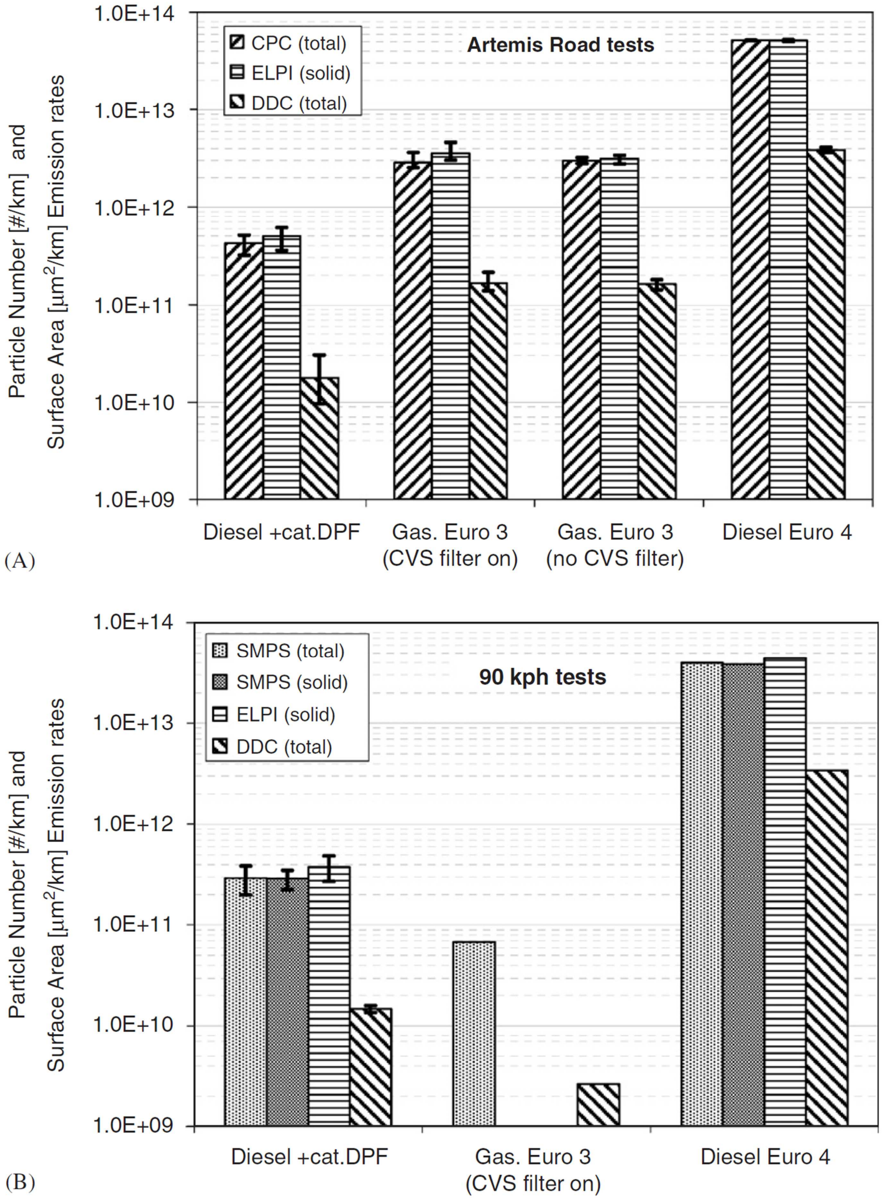

Fig. 1.5 (A) Cycle average particle emissions of the various vehicles tested. (B) Particle emissions of the various vehicles tested over the 90 kph tests [11].

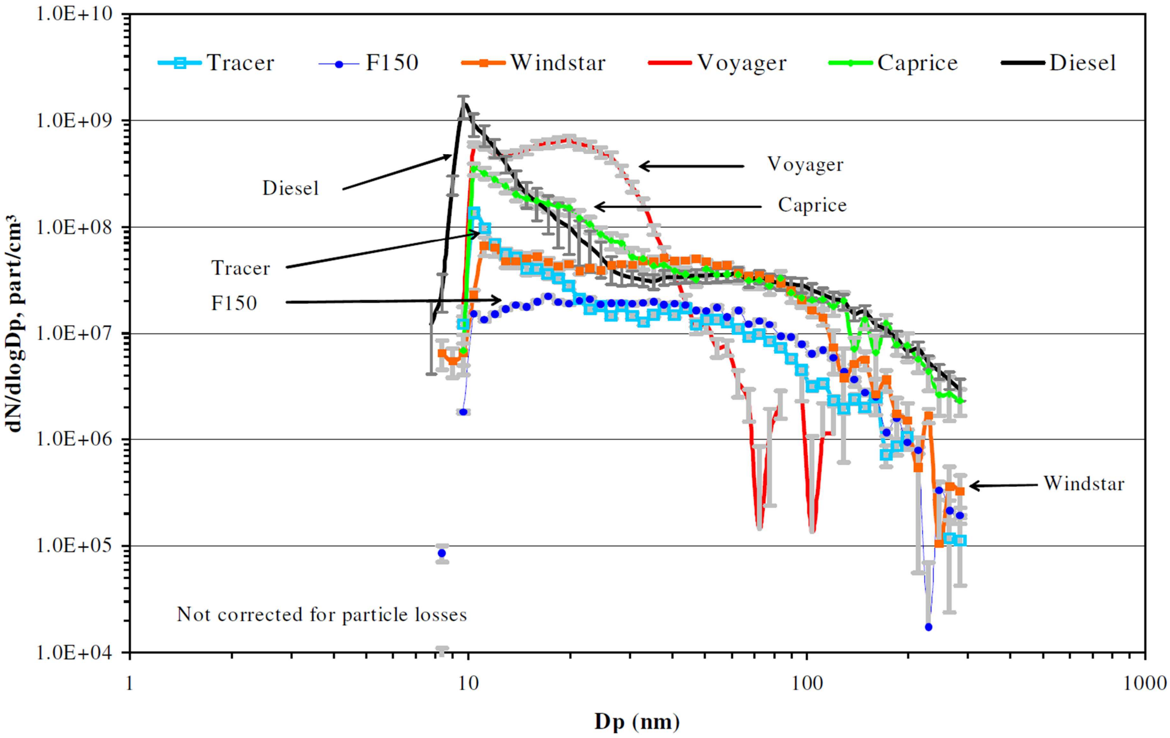

Fig. 1.6 Average on-road acceleration size distributions for five PFI and one diesel engined vehicles [13].

Four laboratories in France (IFP, PSA, Renault and UTAC) conducted an interlaboratory test on the determination of the exhaust particle number using CPC and ELPI analyzers [14]. Fig. 1.7 shows the total particle number of the four vehicles tested. The EU3 diesel with DPF (Diesel 3) showed the lowest particle number emission, and EU3 (Diesel 1) and EU4 diesel (Diesel 2) without DPF showed the highest particle number, while the EU4 PFI gasoline engine (Gasoline) with stoichiometric operation was in the middle. Also, the CPC and ELPI analysers gave quite similar spectra for the particle number versus time on the NEDC.

A PFI gasoline and a CRDI diesel light duty vehicles which were compliant with ULEV and EURO 4 regulations were evaluated by Lee et al. [15], where the particle number and size distribution characteristics were tested under different engine operation conditions and vehicle certification modes, such as NEDC, FTP-75, and HWFET [16]. The particle size distribution was analysed by a DMS500 and the time-resolved particle number concentration level was measured through the procedure recommended by the PMP [17]. It was concluded that the PM size distributions measured in the gasoline and diesel engines were bi-modal (with nucleation and accumulation modes). Gasoline engines mainly emitted PM in nucleation mode (d_p < 50 nm), while diesel engines mainly generated accumulation mode (d_p > 50 nm) particles. The aftertreatment of the gasoline engine had a slight effect on PM reduction at various part load conditions, while particle number concentration levels were reduced by a maximum of 3 orders of magnitude by the DPF fitted to the diesel engine. Gasoline and diesel fuelled vehicles both emit PM during transient operation. The total particle concentrations with various test modes for gasoline and diesel showed similar levels (Fig. 1.8).

In 1999, a Mitsubishi car with 1.8L gasoline direct injection (GDI) engine was tested by Graskow et al. [18], where particle size distribution was measured using SMPS and CPC from engine-out exhaust before the TWC. The average particle number concentration increased from 1.1×10^8 particles/cm^3 at 13 km/hr to 2.8×10^8 particles/cm^3 at 70 km/hr, where the engine was working under stratified operation. At 90 km/hr, the particle number concentration reduced to 9.3×10^7 particles/cm^3 where the engine was running with a stoichiometric mixture. Fig. 1.9 shows the particle size distributions reported by them. From 32 km/hr to 90 km/hr, the majority of the particles emitted were in the accumulation mode (i.e. 30 nm < d_p < 1 μm).

Laser-induced incandescence (LII) and ELPI have been utilized by Smallwood et al. [19] to investigate the soot concentration of a gasoline direct injection vehicle during the FTP and HWFET driving cycles. Both LII and ELPI demonstrated that the maximum emission rates occurred during acceleration transients. From the LII results, there was a clear correlation between acceleration and soot emission rates. They suggested that the wide measurement range and low detection limit of LII make it a preferred standard instrument for soot measurements.

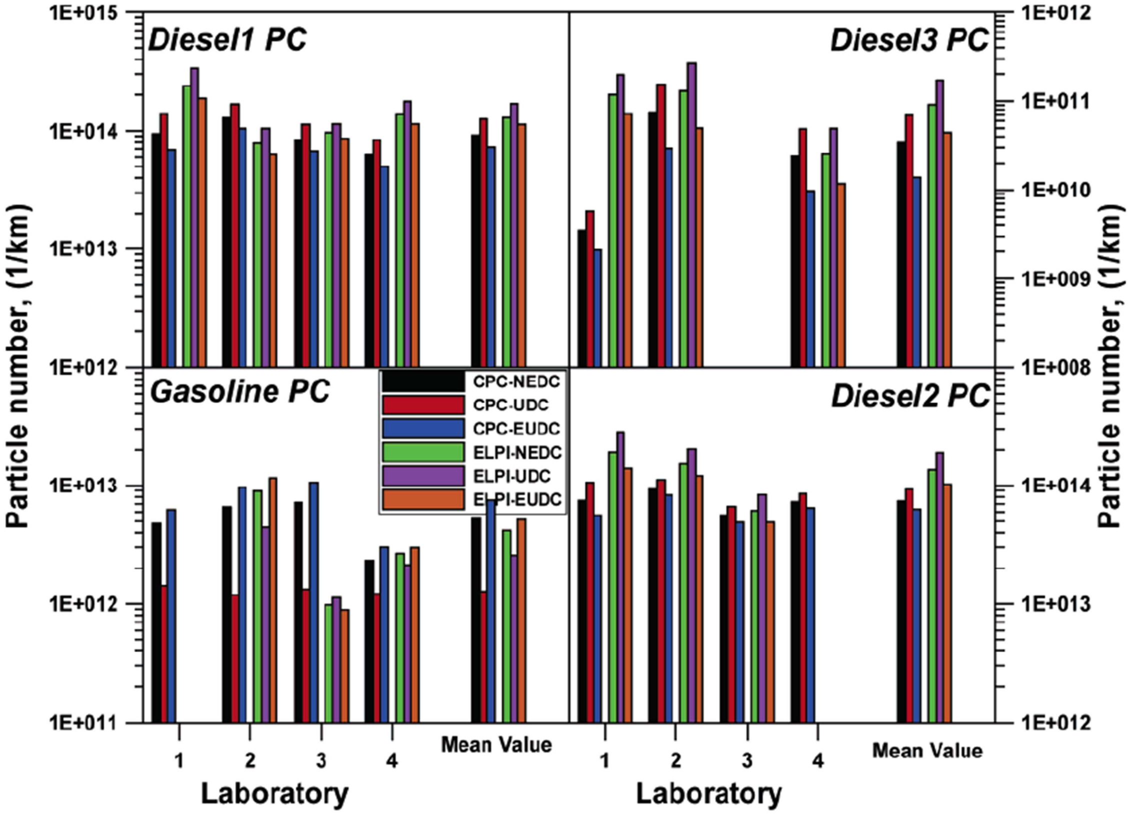

Fig. 1.7 Particle number measured by CPC and ELPI of four Passenger Cars (PC) [14].

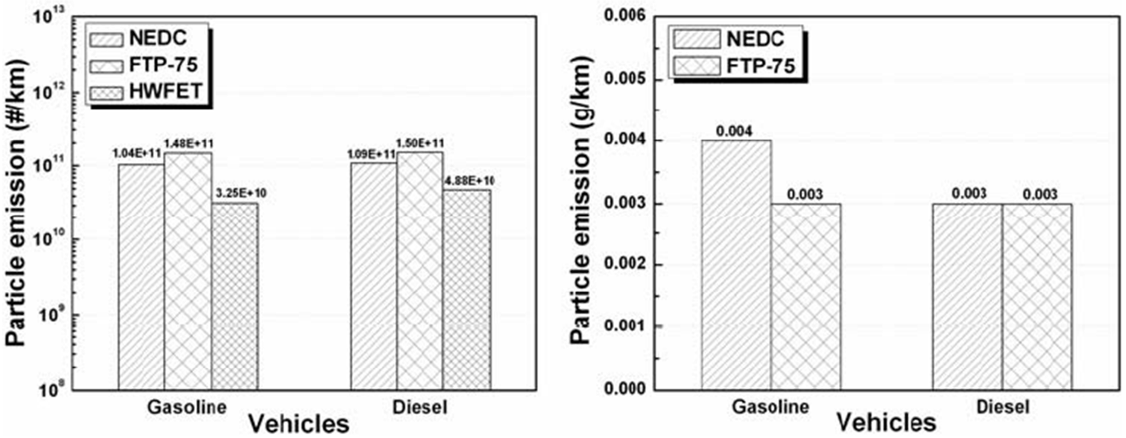

Fig. 1.8 Comparison of total particle number and total particle mass concentrations for different driving modes [15].

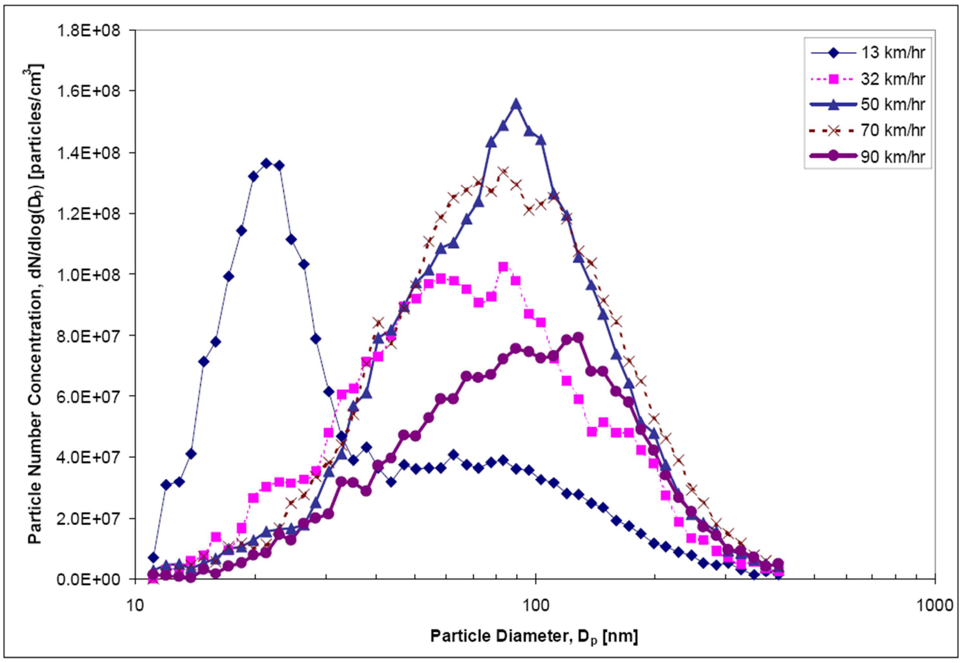

Fig. 1.9 Number-Weighted Exhaust Particle Size Distributions [18].

The particle size distributions for gasoline and diesel engines were examined by Harris and Maricq [20] using a SMPS, for engine dynamometer tests that were performed without catalyst aftertreatment. The number weighted size distributions of GDI engine particulate emissions during stratified operation are shown in Fig. 1.10. Also, Harris and Maricq [20] reported that when the GDI engine was running homogeneously with early injection, the shape of the particle size distributions were similar, but the overall particle emissions were about 100 times lower than those during stratified operation. They concluded that the soot formation in both diesel and GDI gasoline engines evolved to universal asymptotic size distributions that represent distinct signatures for the two engine types, and these characteristic distributions were lognormal (or close to) and not the self-preserving distributions predicted from coagulation dynamics.

A tandem DMA-ELPI measurement of exhaust particle effective densities from two light-duty diesel vehicles and a GDI vehicle were performed by Maricq and Xu [21]. They concluded that there was a characteristic steep decrease in effective density as the particle mobility diameter increased, regardless of whether soot was generated by a rich ethylene flame or emitted by diesel or GDI engines. At 50nm the effective density was about 1.2g/cm^3, varying weakly with soot source, whereas by 300nm it had fallen fourfold to about 0.3g/cm^3. The level of accuracy, the possibility of transient PM mass measurement, and freedom from hydrocarbon artifacts make the calculation of PM mass from particle size distribution measurements an attractive alternative to filter based measurement.

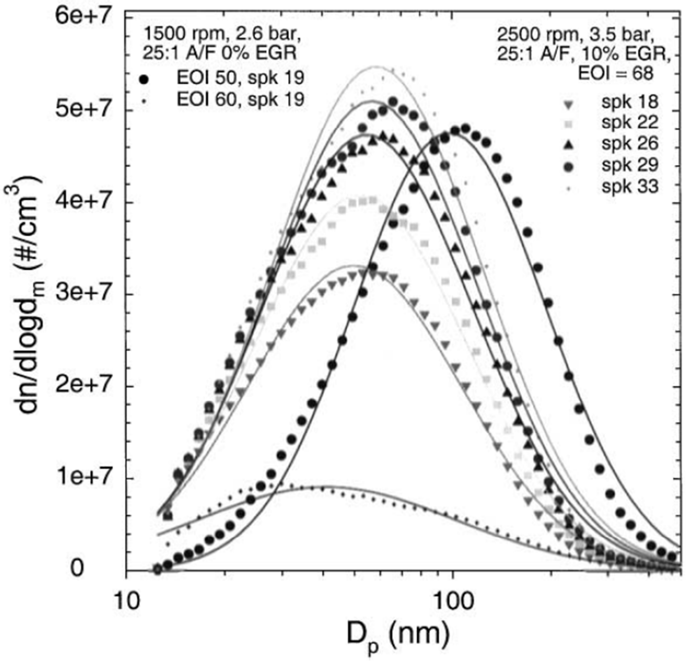

Fig. 1.10 Number Weighted mobility diameter distributions of GDI engine particulate matter emissions under various spark timing and injection timing [20].

Particle measurements were performed in the exhaust of five light-duty vehicles at +23, -7, and -20 °C ambient temperatures by Mathis et al. [22]. The PFI and CI-DPF vehicles showed the lowest particle emissions, while particle emissions for CI vehicle were the highest. And the level of particle emissions from GDI vehicle was between that of PFI and CI vehicles (Fig. 1.11).

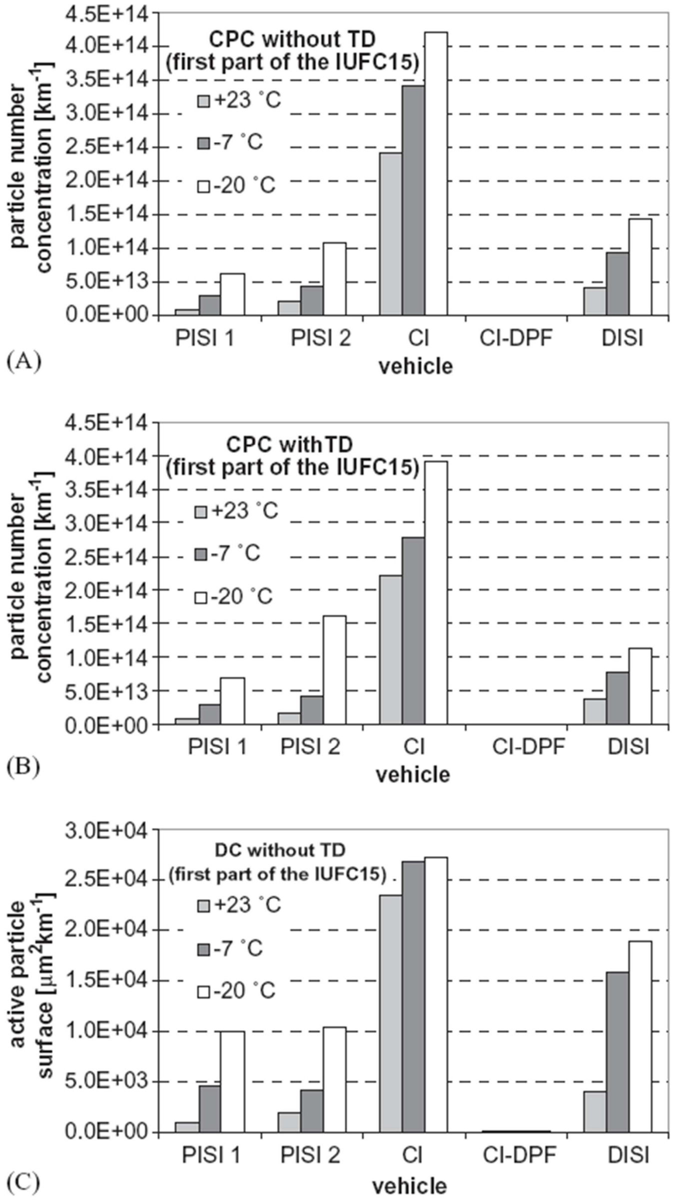

Fig. 1.11 Cold start emissions of particles during the IUFC15 driving cycle at +23, -7, and -20 °C ambient temperatures (PISI: port-injection spark-ignition, CI: compressed ignition, DPF: diesel particle filter, GDI: direct-injection spark-ignition) [22].

An overview of the results on light duty vehicles collected in the "PARTICULATES" project was presented by Ntziachristos et al. [23], which aimed at the characterization of exhaust particle emissions from road vehicles. The main idea of the sampling system was to provide sampling conditions which favour nucleation mode formation and this was achieved by using a moderate primary dilution ratio (12.5:1) and cooling of the exhaust with conditioned air at 32 °C. They argued that the diesel vehicle without a DPF showed the highest PM emissions, and the trap equipped diesel could reduce the PM number by 2 to 4 orders of magnitude. PFI gasoline vehicles were found to be emitting at or below the levels of DPF equipped diesel vehicles. However, GDI engined vehicles may have difficulty meeting the EU5 legislation, though their emissions are well below the diesel EU 4 limit (Fig. 1.12).

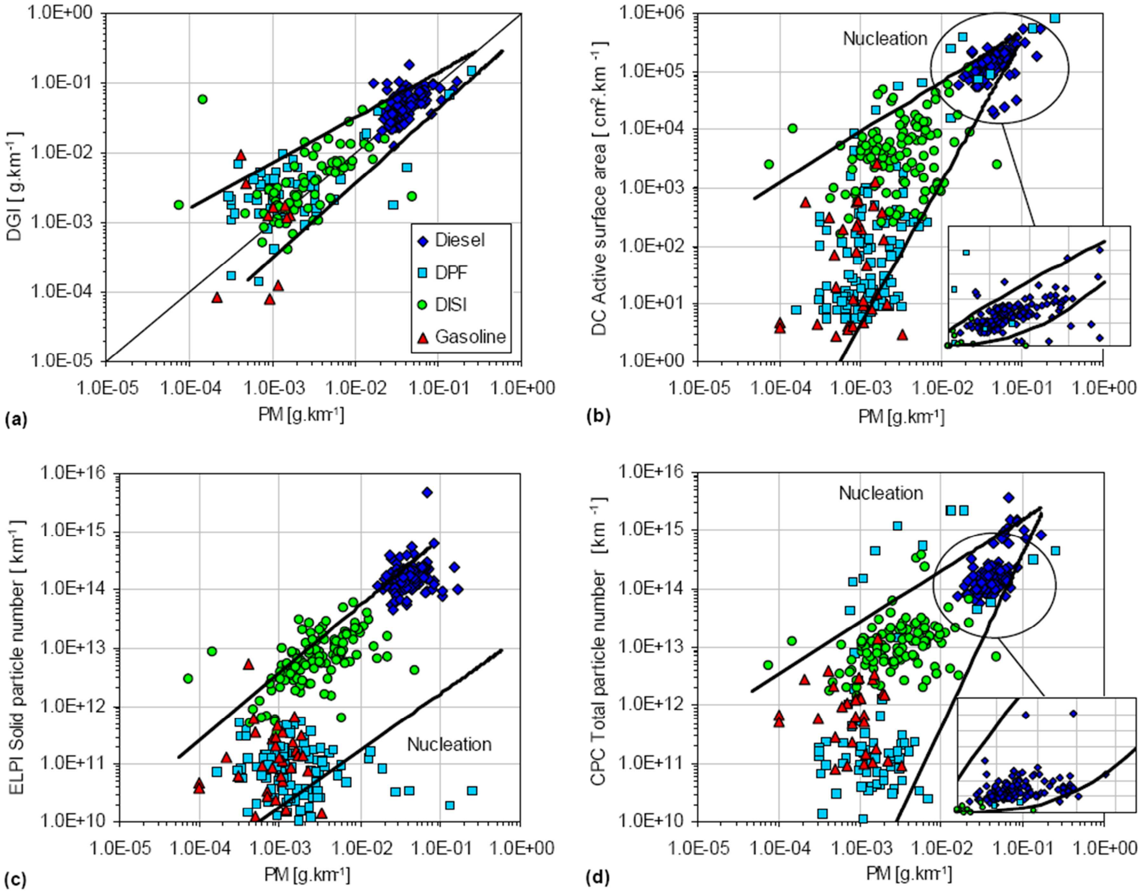

Fig. 1.12 Correlation of different particle properties with the regulated PM procedure. Emissions collected over the NEDC cycles (cold and hot start) and the three Artemis Cycles. (a) Total mass in gravimetric impactor, (b) Active surface from the diffusion charger, (c) Total solid particle number from the ELPI, (d) Total particle number from the CPC. "Nucleation" designates the side of the correlation where nucleation mode should become visible [23].

The particle emissions from a number of EU4 vehicles operating with different fuels were tested by Ericsson et al. [24] using CPC and ELPI instruments. The CPC was arranged according to the most recent version of the Particle Measurement Programme (PMP) protocol for the NEDC. In Fig. 1.13, higher particle number and mass emissions are observed for the DI vehicles (E and F). The particle numbers for these vehicles are similar, around 10^{13} /km, while the spray-guided direct injection (SGDI) vehicle (F) shows remarkably lower PM emissions by mass compared to the wall-guided direct injection (WGDI) vehicle (E), indicating significantly smaller particles in the case of the SGDI vehicle. For the SGDI vehicle, it was found that the vehicle switched to lean mode after the first UDC cycle, and stayed at high lambda values throughout the cycle with a few exceptions, which were likely to be due to regeneration of the lean NO_x trap. In the search for a correlation between particulate number and the lambda trace, they concluded that the continuous contribution of particle emissions originated from the stratified mode, as the particulate number decreases dramatically at low values (lambda < 1.1). The difference in particulate number between homogeneous and stratified mode was approximately 40 times (calculated at the 70 km/h steady state lambda shifts at t ~ 900 s and 1000 s).

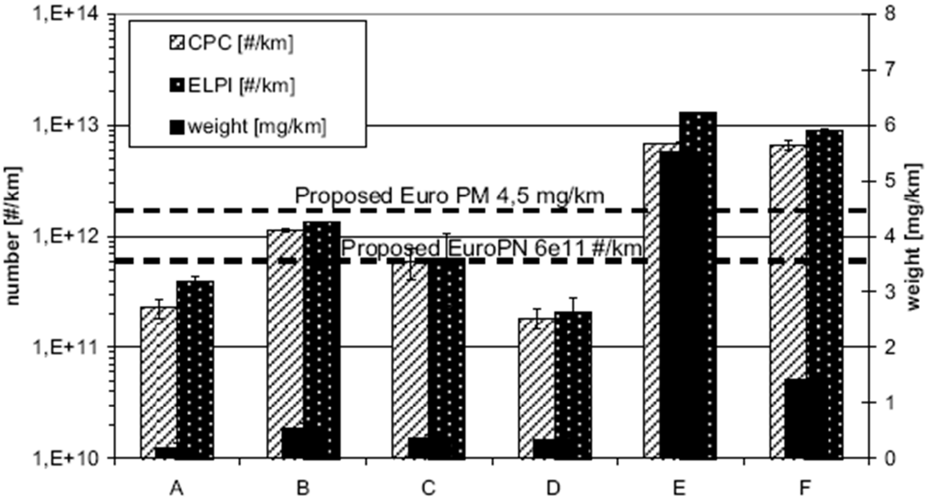

Fig. 1.13 Particulate numbers measured with ELPI and CPC and particulate mass measured gravimetrically, over the NEDC for different vehicles (A-F). The proposed post-Euro IV legal limits are indicated for comparison. A: E5 PFI, B: E5 PFI, C: E85 PFI, D: Diesel CRDI with DPF, E: E5 WGDI, F: E5 SGDI [24].

In recent years, the Particle Measurement Programme (PMP) has been set-up as a working group of the UN-ECE GRPE, focusing on the development of new particle measurement techniques to complement or replace the existing particulate mass measurement technique, with special consideration to measuring particle emissions at very low levels [17, 25].

Fig. 1.14 shows that the particle measurement system (reference system (RS)) consists of a cyclone, a primary hot diluter (PND1), an evaporation tube (ET), a secondary cold diluter (PND2) and particle number counters (PNCs). Fig. 1.15 shows the particle number results from their tests. Mean emissions from the DPF-equipped Diesels were lower than 10^{11} /km except for DPF#3 which can be considered a special case. Emissions from the PFI were statistically similar to the Golden Vehicle (a diesel reference vehicle equipped with a DPF), while GDI emissions levels were 40 to 140 times higher. Conventional diesel particle number emissions were larger than 2×10^{13} /km.

They concluded that the particulate mass emissions followed the following general trend: Conventional Diesel > GDI > porous DPF ~ PFI ~ DPF. While the particle number emissions are in the following order: Conventional Diesel > GDI > porous DPF > PFI = DPF.

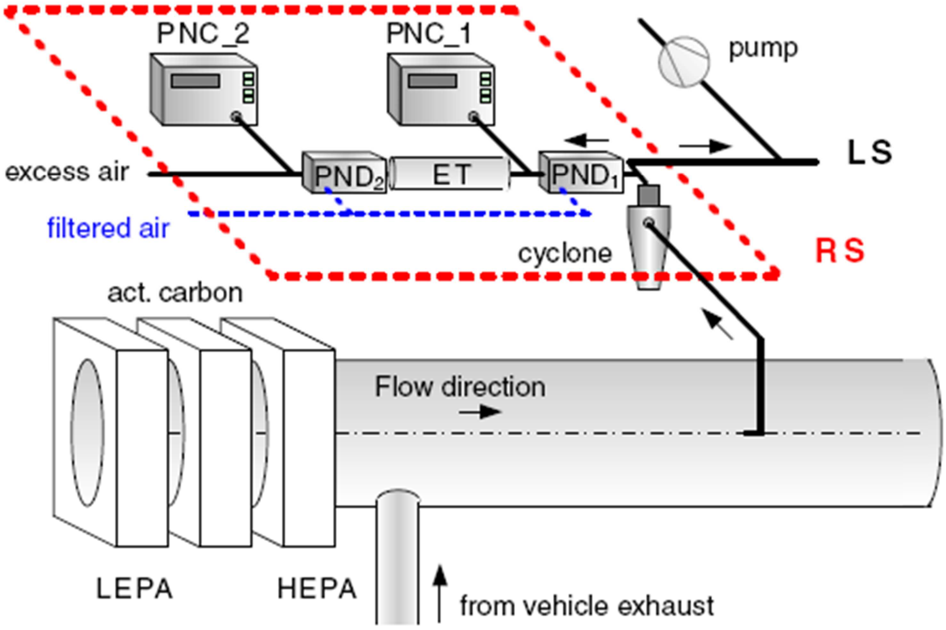

Fig. 1.14 Schematic reference system (RS). PND1: primary diluter, PND2: secondary diluter, ET: evaporation tube, LEPA: low efficiency particle filter, HEPA: high efficiency particle filter, PNC: particle number counter, LS: lab's own systems [25].

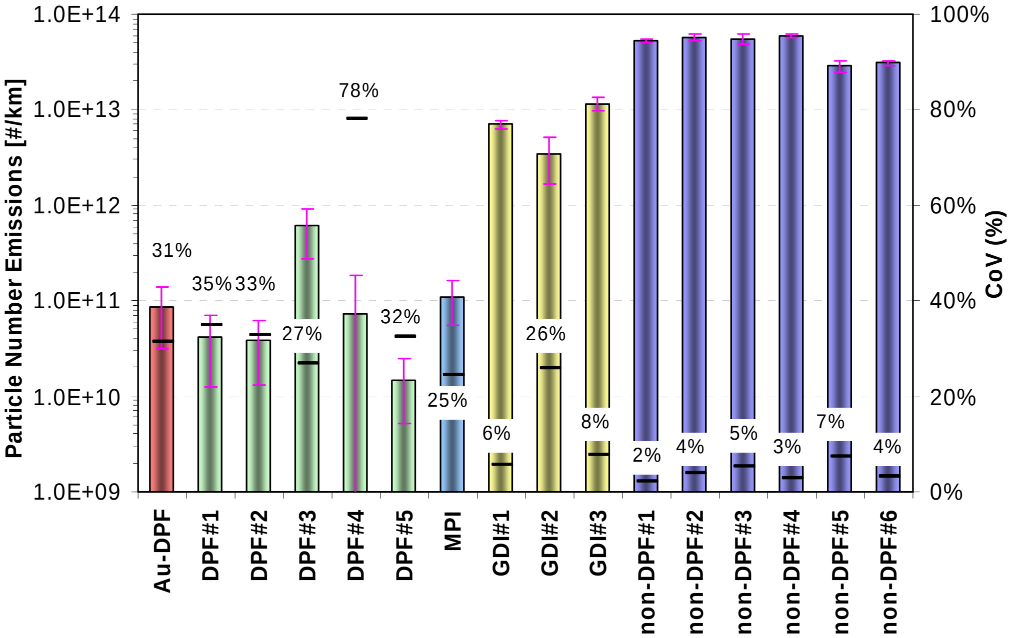

Fig. 1.15 Particle Number Emissions and Repeatability Data – All Vehicles [17]

The particle emissions from a number of EU4 or EU5 compliant vehicles have been measured by Braisher et al. [26]. It was shown that the particle number emissions from a spray guided GDI engine were much higher than those from a PFI or a DPF equipped diesel engine, especially under engine cold start and acceleration operations in the NEDC. A latest generation turbocharged GDI vehicle has been tested by Peckham et al. [27] using a PMP solid particle counting system and a DMS500 (Fig. 1.16). The DMS500 lognormal fitting was used to give the accumulation mode particle number. They reported that the particle number from the vehicle over the NEDC was 2×10^{12} /km, where a large portion of the particles was emitted within the first 200 s in the driving cycle. Even small lambda fluctuation between 0.97 and 1.03 during steady-state cruise after catalyst light-off would increase particle number emissions. A high level of particle number emissions was seen under acceleration and high load operations with rich lambda transients under these conditions.

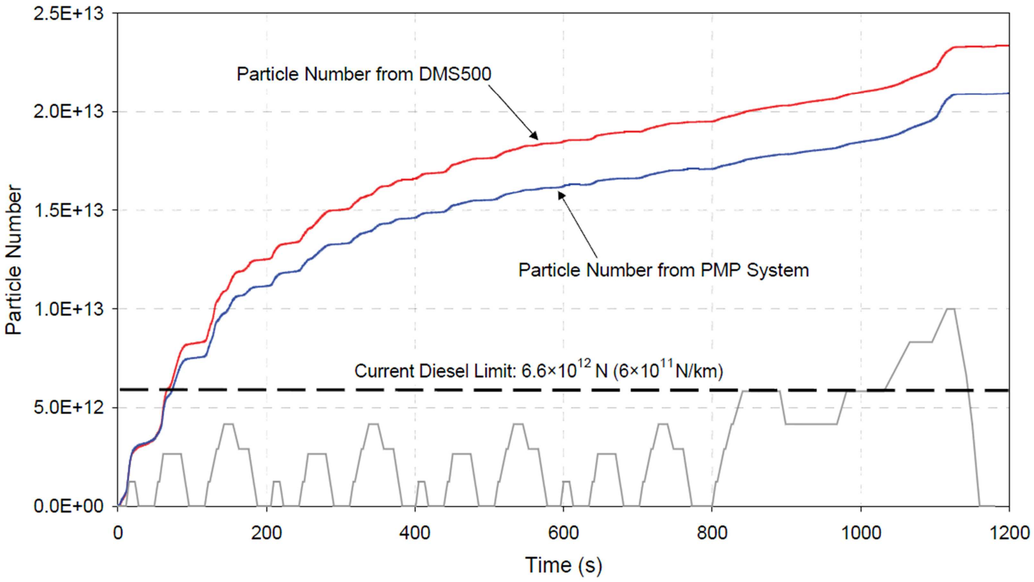

Fig. 1.16 NEDC particle number results for PMP and DMS500 systems [27].

CONCAWE has undertaken some research on the measurement of particle emissions from light-duty vehicles [28]. Two diesel vehicles and two GDI vehicles were tested for particulate mass and particle number emissions under regulated NEDC driving cycle. Particle number emissions were compared using procedures that had been developed in two different studies: the procedure previously used in the DG TREN “Particulates” Consortium Study (2001) and a second that has been adopted for Euro 5b certification of new light-duty diesel vehicles based on results from the Particle Measurement Programme (PMP).

It was concluded that the measurement techniques for particle number emissions used in the DG TREN programme (using an ELPI) and this PMP follow-up study (using a CPC) gave comparable results on similar vehicles and fuels, despite different exhaust dilution and sampling protocols. The particle number (P_n) emissions from GDI cars were about the same order of magnitude as from the DPF-equipped diesel vehicles (Fig. 1.17 and Fig. 1.18).

Although most research has found that particle number emissions from GDI engines were higher than those of DPF-diesel or PFI gasoline engines by an order of magnitude [17, 22-25], the research from CONCAWE [28] showed that P_n emissions from the GDI vehicles were of the same order as those from the DPF diesel vehicles over the NEDC cycle. So it is of interest to further investigate the particle emissions from the most recent GDI vehicles. It is well known that when a GDI engine operates in stratified overall lean conditions, it will emit a high concentration of particle numbers. But during stoichiometric operation, if using a piezoelectric injector with a GDI engine, and using multiple injections to further support homogenization and low spray penetration, the P_n emissions may be lowered. By combining turbocharging for downsizing, stoichiometric GDI engines would show advantages on fuel economy over turbocharged PFI engines [1-4] and lowered P_n emission compared with lean GDI engines.

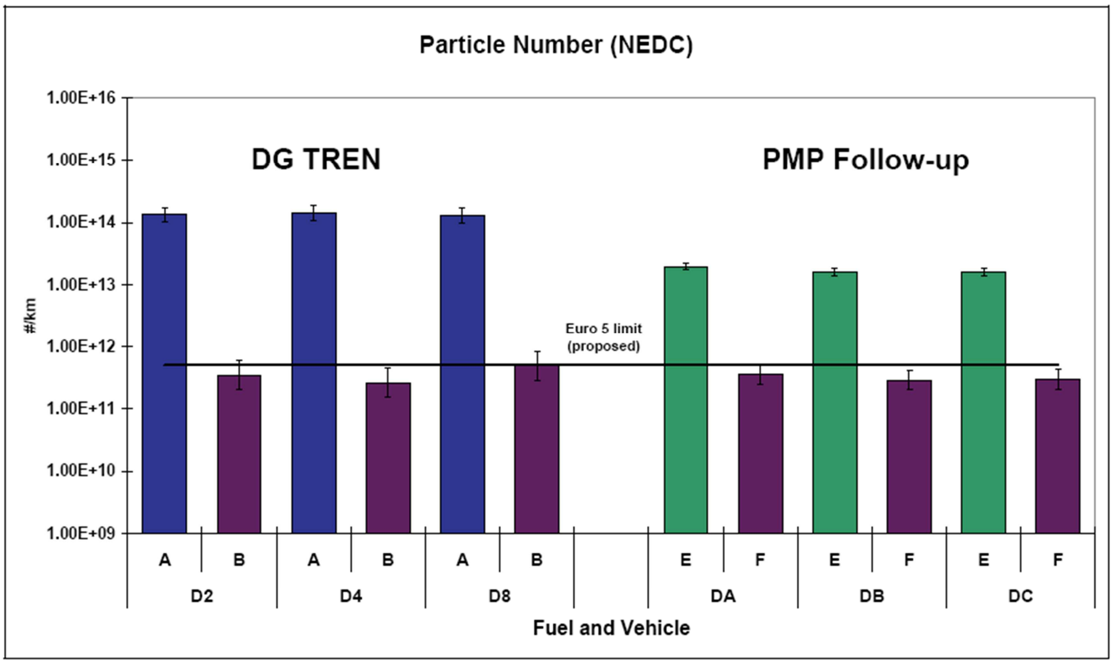

Fig. 1.17 P_n Emissions from diesel Vehicles over the NEDC from the DG TREN Study and from the Current PMP Follow-up Study. DA, DB and represent different diesel fuels, and A, B, E and F represent different diesel vehicles (B and F equipped with DPF) [28].

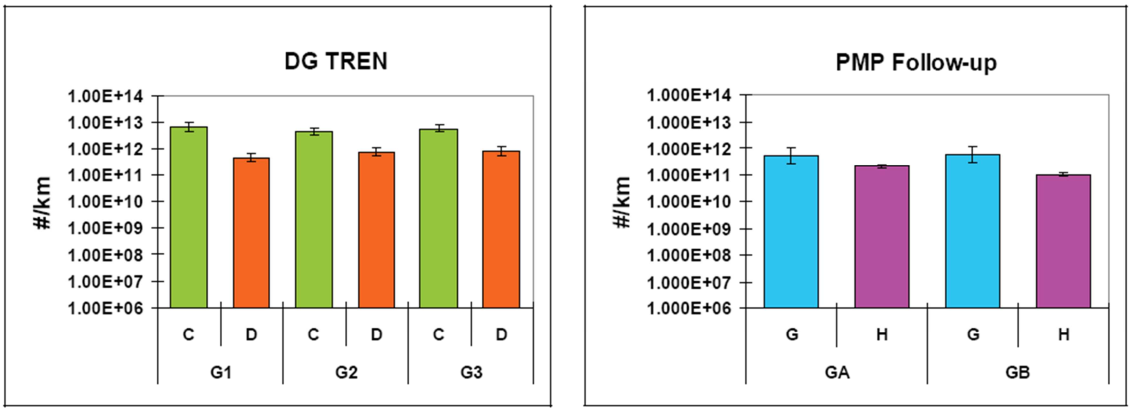

Fig. 1.18 P_n Emissions from GDI Vehicles over the NEDC from the DG TREN Study and from the Current PMP Follow-up Study. GA and GB represent different gasoline fuels, and C, D, G and H represent different GDI vehicles [28].

1.3.2 Formation Mechanisms for Particle Emissions from Gasoline Engines

As the mixture preparation and combustion processes in gasoline engines are quite different from those in diesel engines, there is a great difference between the PM emission characteristics of gasoline and diesel engines. Also, for the gasoline engines, there seems to be some relationship between PM emissions and HC emissions [15,19,29]. In recent years, some research has been carried out to investigate the mechanism of PM formation in gasoline engines.

The mechanism of particle formation in PFI engines was investigated by Kayes and Hochgreb [29-31]. The effects of engine operating conditions, fuel, oil and catalyst on PM formation were experimentally investigated. A physically-based model was formulated to characterize mechanisms leading to measured PM emission. Their conclusions are as follows.

1. When **equivalence ratio** varied over the range of 0.7 to 1.3, HC emissions varied by less than an order of magnitude, while PM number and mass concentrations varied by 1 and 2 orders of magnitude, respectively. The combination of the effects of nucleation, oxidation and growth all contribute to the behaviour of PM with respect to equivalence ratio.

2. **Fuel injection timing** would affect PM emissions. Open valve injections (OVI) showed higher PM emissions than closed valve injection (CVI).

3. Decreased **coolant and oil temperatures** resulted in a lowered rate of fuel evaporation in the intake port for PFI engines, thus raising the concentration of in-cylinder liquid fuel and this led to higher HC emissions. Also the increased liquid fuel in the cylinder produced higher PM emissions, because the liquid fuel can burn and generate soot as well as increased HC emissions which can then adsorb onto the particles.

4. The variation of PM concentration with respect to **spark timing** reflects the competing effects of both flame and post-flame temperatures on nucleation and oxidation, as well as the effect of HC concentrations on adsorption. Advanced spark timing resulted in increased peak temperature and thus raised the rate of PM nucleation as well as enhancing the post-flame oxidation. As spark timing advanced, exhaust temperatures decreased, leading to slower post-flame HC oxidation.

5. As **EGR** was increased, the inlet manifold temperature increased, resulting in a higher evaporation rate. At fixed manifold pressure, the amount of air supply to the engine was decreased with increased EGR. The reduced concentration of gas and liquid phase fuel combined with decreased in-cylinder temperatures resulted in a sharp decrease in the amount of PM nucleated as the EGR rate increased.

6. As **engine load** increased, the PM concentrations increase. At increased engine load, the mass of fresh charge taken into the cylinder increased, and the residual gas fraction was reduced, leading to a decreased intake temperature. This has an adverse effect on the liquid fuel evaporation, and as a result, the increased liquid fuel concentration and the increased in-cylinder temperature led to an increase in the PM nucleated. Also, as the oxygen

concentration increased, the PM nucleated through liquid fuel burning would increase, since the probability of liquid fuel ignition and subsequent soot production is strongly dependent on the oxygen concentration. In contrast, the in-cylinder and exhaust temperature increased as the load increased, and this favours PM oxidation. Also, the reduced HC emissions at the increased load resulted in reduced HC adsorption. So the increase in PM with increased load indicates that the effects of increased nucleation are stronger than the increased oxidation and decreased growth.

7. The effect of **engine speed** on PM emissions was not clear. The lack of monotonic trends may reflect competing formation, growth, and oxidation mechanisms.

8. **Fuel characteristics** showed a marked effect on PM emissions. For volatility and/or molecular weight iso-octane increased the PM emissions compared with Propane, and for chemical composition toluene increased the PM emissions compared with iso-octane. The very low PM emissions using propane relative to those using iso-octane suggests that either PM nucleation from burning liquid fuel or nucleation from high molecular weight partial oxidation products would lead to greater rates of PM formation. Although toluene and iso-octane have similar boiling point, the partial oxidation products of toluene are much more likely to be soot precursors than those of iso-octane, which would grow into PAHs that facilitate PM nucleation.

9. **Oil composition and viscosity** had a moderate influence on PM emissions. There was little difference in PM emission between viscosity-30 mineral oil and viscosity-40 mineral oil. But when viscosity-30 synthetic oil was used, the PM emissions were 70 % higher compared with those of viscosity-30 mineral oil, suggesting that synthetic oil was more inclined to generate PM.

10. It was found that the **efficiency of a catalyst on PM emissions** was less than that on HC, CO and NO_x emissions. And the particle size was not significantly reduced as exhaust passed through the catalyst, which had been expected to reduce due to the elimination of HCs adsorbed on particles.

HC emissions and soot emissions from a direct injection stratified charge (DISC) spark ignition engine was discussed by Sandquist et al. [32]. The experiments were conducted at engine part-load, stratified operation. The injection timing was varied to alter the mixture preparation time. The measurements indicated that overmixing (quenching) at the boundaries of the mixture cloud, and undermixing both in the spray centre and the surface of the piston bowl are the dominating mechanisms for HC emission formation in the engine. Also, when the injection timing is retarded, blowdown HC increased, indicating a higher level of undermixing which led to increased soot formation.

In-cylinder combustion process and soot formation was investigated by Wyszynski et al. [33] on a single cylinder GDI optical engine. Measurements were performed with early injection and late injection. For early injection, soot incandescence was seen in two distinct areas, with a peak corresponding to peak pressure, and a secondary peak at lower temperatures and at later image timings. The first soot peak was indicative of a pool fire, which was caused from liquid fuel wetting the piston crown. The later soot peak corresponded to late oxidation of soot, probably formed during combustion of liquid fuel. For late injection, soot incandescence occurred when the MFB was ~50 % for all cases.

PM emissions from spray-guided GDI (SGDI), wall-guided GDI (WGDI) and PFI engines were compared by Price et al. [34] in a single cylinder engine using different fuels. The spray guided GDI showed significantly lower PM emissions than an engine with a wall guided combustion system (Fig. 1.19). The PM emissions from the spray-guided GDI engine was similar to that from the PFI engine, where significant accumulation mode PM was not detected. The number concentration of the spray-guided GDI engine was also similar to that of the PFI engine and less than an order of magnitude more. So the elevated injection pressure and reduced fuel impingement on the combustion chamber contributed to the reduced PM emissions. The main influencing factors for PM emissions were in the following order: fuel type > air-fuel ratio > injection timing > ignition timing.

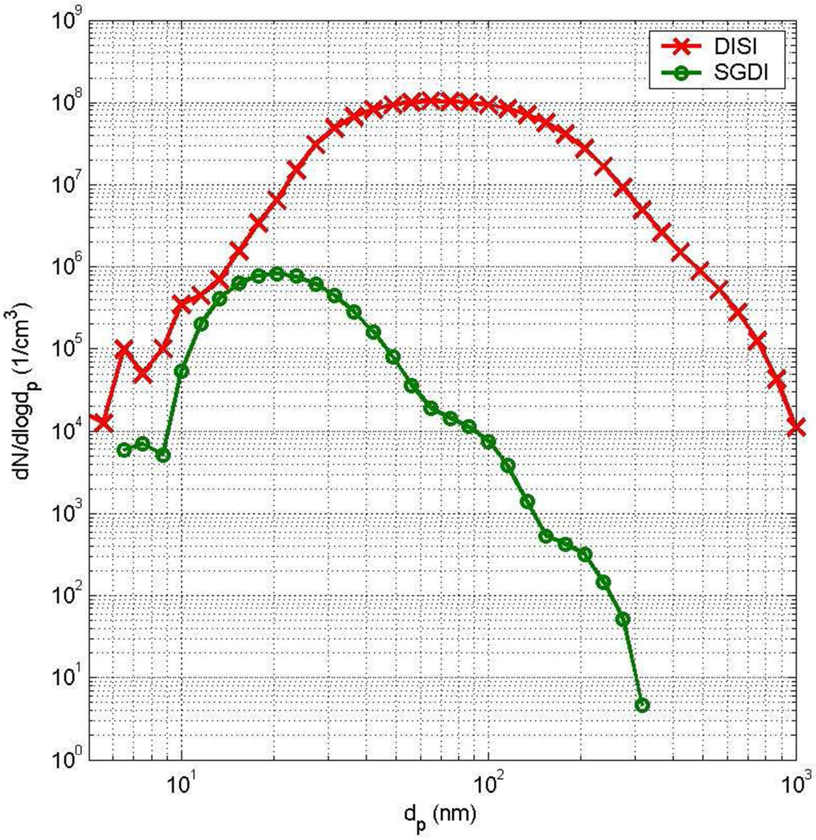

Fig. 1.19 Representative PM size distribution for the GDI engine and the SGDI engine [34].

In-cylinder soot formation and oxidation in a stratified-charge gasoline direct injection (GDI) engine was studied in an optical engine [35-37]. The principal soot sources for stratified operation were measured. It can be argued that first, soot was formed as a partially premixed flame propagated through the locally rich zones, but this soot oxidized rapidly due to its high temperature and rapid mixing with surrounding hot lean regions. Second, soot was formed in a pool fire caused by thin films of liquid fuel on the piston surface. This kind of soot can exist until late in the engine cycle, when further oxidation was unlikely, which was indicated by the lower temperature and disappearing OH* chemiluminescence. Third, using a multihole injector can reduce the maximum wall film mass by an order of magnitude compared with using a hollow-cone swirl injector.

In some research, the soot formation process has been modelled. A phenomenological engine model has been developed to study direct injection of liquid fuels in diesel and gasoline engines by Siewert [38], where emissions sub-models for NO_x, soot and unburned fuel were added. A detailed model for the formation of soot in internal combustion engines was presented by Mosbach et al. [39], in which a detailed chemical kinetic mechanism describing the combustion of primary reference fuels was extended to include small polycyclic aromatic hydrocarbons as soot precursor species.

1.3.3 Volatile Nucleation Particles

It is difficult to measure the number of volatile nucleation particles, because they experience physical changes during the sampling process and are highly sensitive to the dilution conditions, i.e. the configuration of the dilution system and dilution ratio [40, 41]. Nucleation and coagulation are likely to change particle number concentrations as dilution is varied; nucleation is favoured by lower dilution ratios and is likely to increase the number concentration of the nucleation mode under those conditions [40]. Other research shows that the results from particle mass measurement (including volatile particles) showed poor repeatability (~55 % variability), while the results from particle number measurement (measuring non-volatile particles) showed relatively good repeatability (~40 % variability) [42].

Nucleation particles are more likely to be formed in engines with high soluble organic fraction (SOF) emissions. Also, GDI vehicles were found to have the same level of total particle number as solid particle number emissions [23]. While diesel engines equipped with a DPF were found to tend to generate high levels of volatile nucleation particles during the DPF regeneration process. During regeneration, the particles emitted from a loaded DPF were measured to be 200 times that of a similar regeneration but from an empty DPF [43]. PMP measurements also showed a large portion of volatile particles during the regeneration process. During non-regeneration cycles, there was not much difference between the emissions of semi-volatiles + solids and the emissions of solids. On the other hand, the emissions of semi-volatiles + solids from a regeneration NEDC cycle can be 6500 times that of a non-regeneration cycle and the regeneration was found to take place at intervals of about every 1100 km or once every 98 NEDC cycles for the test vehicle [17]. If semi-volatile particles and regeneration effects are included in the emissions regulations, the particle number emissions of diesel engines with DPF would be much higher than the case when only considering solid particles. This would be sufficient to increase NEDC cycle emissions by a factor of ~60. While for GDI vehicles, the semi-volatiles + solids emissions are approximately the same as the solid particle emissions. So the effects of nucleation particles from diesel and gasoline engines on the environment and human health, as well as their measurement method, need to be further investigated.

Large PAHs with 6-8 aromatic rings were detected in the fine particulate matter emitted from gasoline vehicles [44]. The PAH emissions and the potential carcinogenicity for the measured PAHs per km driving distance were found to increase with increasing average speed for the gasoline fuelled vehicles (GFVs), while the diesel fuelled vehicles (DFVs) displayed the opposite trend [45]. Furthermore, the DFVs tended to emit higher amounts of PAHs and displayed a higher potential carcinogenicity of the measured PAHs than the GFVs in the urban driving cycle, while the opposite was found in the rural road and motorway driving cycles [45].

1.3.4 Effects of Fuel Characteristics on Particulate Emissions

It was found that the sulphur content did not show a clear influence on particle emissions from GDI vehicles [46]. Both nucleation and accumulation particles did not seem to be affected by the sulphur content of gasoline. The effects of oxygenate fuel blends on PM emissions from a spray guided gasoline engine was investigated by Price et al. [47]. The lowest PM number concentrations were measured for E85. Using gasoline, E30 and M30 generally emitted similar particle emissions but the highest PM number concentrations were consistently found when using M85. M85 seemed to generate a higher level of nucleation particles than gasoline. For late injection, fuel volatility determined whether the time for evaporation or piston and wall wetting was the dominant source of PM emissions. Ericsson et al. [24] also found that E85 showed lower PM emissions both on a mass and number basis over the NEDC cycle. Alternative fuels such as bio-ethanol (E85), bio-diesel, and natural gas displayed the potential to reduce particulate number emission due to their oxygen content or low carbon fuel characteristics [48]. Using PFI engines, the particle number emission of E85 was 37% lower than that of gasoline. As the ethanol content in gasoline increased, an increase in both particle number and mass was found by Chen [49] under both cold and warm engine operating conditions. This is because both the spray break-up and evaporation efficiency was affected by ethanol addition as a result of its high vaporization enthalpy and low energy density.

It was shown by Khalek et al. [50] on a GDI engine that the solid particle number emissions using a fuel with high vapour pressure was much lower than that using a fuel with low vapour pressure. A PM index has been given by Aikawa et al. [51], which showed that fuel components with low vapour pressure and high double bond equivalent would increase PM emission.

The effects of organometallic fuel additives on nanoparticle emissions from gasoline passenger cars were examined by Gidney et al. [52]. They indicated that Mn and Fe additives resulted in the formation of a distinct nucleation mode, where the particles in this mode were nearly all solid (like metal oxides) and all below the current lower size limit of the EU number regulations.

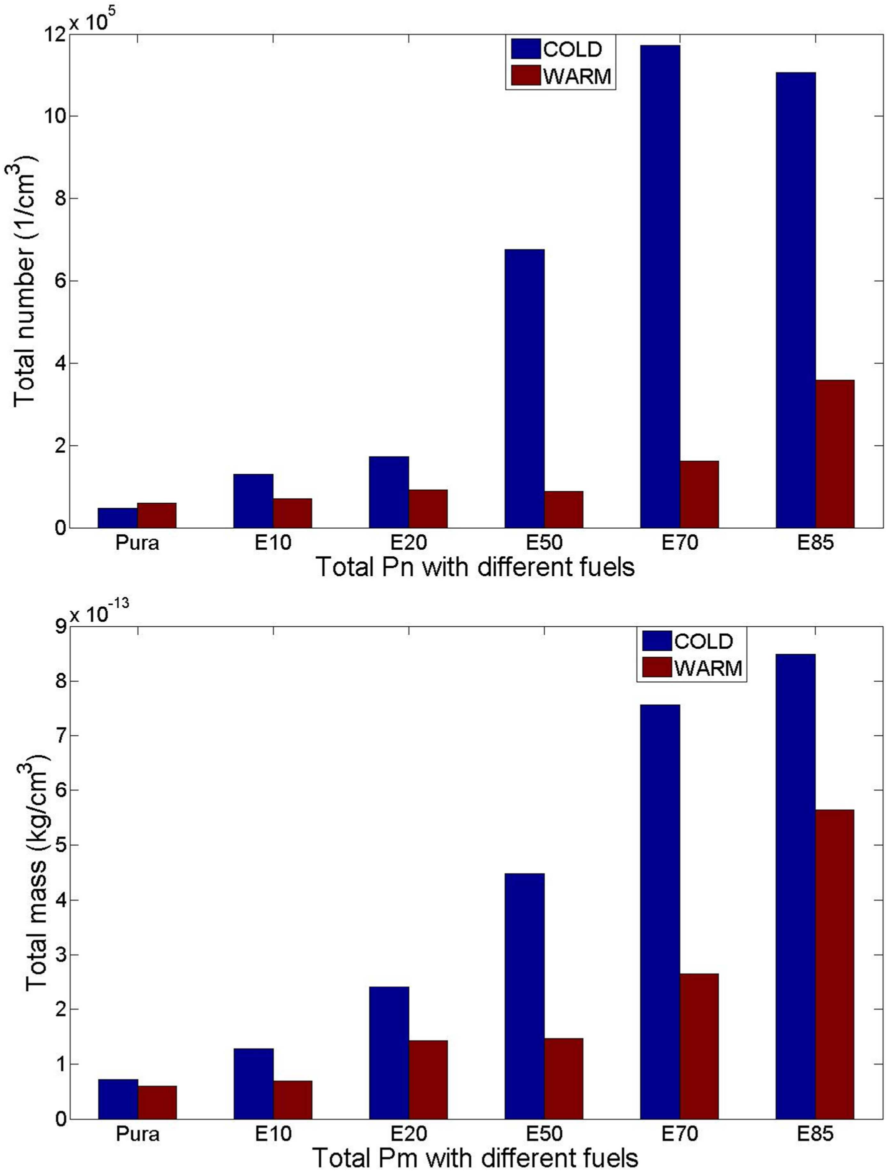

Fig. 1.20 Total particulate number (top) and total particulate mass (bottom) emissions for different PURA/ethanol blends in a cold (20ºC) and a warm (80ºC) engine [49].

1.3.5 Reduction of Particle Emissions from GDI Engines

As shown in recent research, the particle emissions from PFI engines were about 1-2 orders of magnitude lower than that of GDI engines, and GDI engines will have to meet stringent regulation on particle number emissions from EU6. If the limit for particle number emission of GDI engines is the same as that of diesel engines, current GDI engines would face a challenge in meeting the limit. So it is important to reduce the particle emissions from GDI engines.

If particle aftertreatment is not to be added, stratified operation may have to be abandoned, because stratified combustion showed higher particle emissions even with a spray-guided combustion system [24]. Spray-guided combustion systems have to be utilized, and finer atomization has to be achieved to reduce the fraction of liquid fuel at the start of combustion. In order to achieve further fuel economy gains over PFI engines, turbocharging systems have to be used.

Possible methods for reducing particulate emissions from GDI engines are listed as follows.

- Avoiding rich mixture excursions.
- Use fuels with a low final boiling point and a lower aromatic content.
- Use a higher injection pressure to increase charge homogeneity.
- Use hot EGR to improve charge homogeneity.
- Combine PFI and GDI injection systems; additional benefit of PFI is better efficiency at part load operation since the charge is cooled less, so that pumping work is reduced since the manifold absolute pressure is higher for a given trapped mass.

Particle traps have been proposed for the aftertreatment system of GDI engines [53-55]. An open flow filter and a wall flow filter were compared by Andersson et al. [54]. The result showed that the open flow filter was not able to meet the efficiency requirement, while the wall flow filter showed a satisfactory reduction efficiency. In addition, an electrostatic particle trap for GDI engine was preliminarily tested by Rubino et al. [55]. The engine testing result shows that, at moderate speeds and loads, the capture efficiency was 60-85% for homogeneous combustion and 50-60% for stratified lean combustion.

The choice of a method for reducing particle emissions from gasoline engine will have to be made on the basis of a compromise between cost and PM reduction efficiency. If the cost is high and the benefit on fuel economy due to direct injection is relatively small, GDI engines would not be that attractive compared with PFI and diesel engines.

1.4 Summary

Gasoline Direct Injection Engines have been developed by automotive manufacturers in the past 15 years because of their potential for reducing fuel consumption. Combined with forced induction, gasoline direction injection is a key enabler to facilitate engine downsizing. However, the literature showed that GDI engines can emit one order of magnitude more particulate matter number emissions than conventional PFI engines. Particle number and particle mass emissions from gasoline engines will be limited in the upcoming European legislation. So it is essential to characterize the PM emissions from GDI engines to see if their further development would be restricted by the legislation.

The literature on the PM emissions from GDI engines has been reviewed in this chapter. The particle number emissions from GDI engines must be improved to meet further legislation. First of all, the mixture preparation should be optimized to form a more homogeneous fuel-air mixture. Thus, higher injection pressure such as 200 bar rail pressure can be utilized to achieve better fuel spray atomization and break-up. Secondly, in-cylinder air flow motion should be designed to be synergistic with the fuel spray pattern, reducing fuel spray impingement on the cylinder wall or the piston top. Thirdly, the injection strategy during cold start should be optimized to achieve both fast catalyst light-off and lowered particle and gaseous emissions. Also, the air to fuel ratio should be kept as close as possible to stoichiometric during engine acceleration and any change of load, decreasing the rich mixture excursions under these engine conditions, as the particle number emissions from GDI engines were found to be more sensitive to the rich deviations during transient operations compared to PFI engines.

The outline of the thesis is listed as follows.

- In Chapter 2, the experimental equipment is described in details. The data processing methods for interpreting the data from the Cambustion Differential Mobility Spectrometer (DMS500) is discussed. A data integration program was developed to assemble data from the data acquisition systems, engine control and management system and the DMS500.

- In Chapter 3, the filtration efficiencies of glass fibre filters were quantified using the DMS500 to see if all of the particles from the sampled gas can be collected by the filters. A theoretical calculation based on single fibre filtration mechanisms was performed to make a semi-quantitative comparison with the experimental results.

- In Chapter 4, various valve timings and different injection modes such as double injection with a second injection after compression, single intake injection and split intake injection were implemented to measure the Particulate Matter (PM) emissions and combustion characteristics of a GDI engine under cold operating conditions.

- In Chapter 5 and 6, the techniques for removing volatile particles were investigated using a catalytic Volatile Particle Remover (VPR) and an Evaporation Tube (ET) with hot air dilution under various test conditions.

Chapter 2. Experimental Equipment and Data Processing Methods

2.1 Introduction

Most of the experimental work described in the following chapters was conducted using a V8 AJ133 GDI engine and a differential mobility spectrometer DMS500. This chapter provides details of the test engine, the test facilities and data processing methods.

The DMS500 has been extensively used in this study to obtain PM size distributions and total particle number concentrations. Therefore the DMS500 data processing is discussed in this chapter on calculating the lognormal parameters from the raw size distribution. Different calculation methods are compared, which are the lognormal fitting output by the DMS500 and a fitting program using a MATLAB optimization function.

In order to integrate data from different sources, a data integration program was developed using MATLAB software. The data files recorded by the high speed and low speed engine data acquisition (DAQ) system, engine control and management system and DMS500 are analysed by the program and then the derived results are output to separate Excel files and a single summary Excel file for all the test points.

2.2 V8 Engine Test Bench and Data Acquisition System

The engine test apparatus and data acquisition system are described in this section. The test engine used here is a V8 5L naturally aspirated GDI engine from Jaguar. A data acquisition system consists of sensors on the test bench, amplifiers, analogue to digital convertors and data acquisition cards installed on a PC. The National Instruments^{TM} LabVIEW (Laboratory Virtual Instrument Engineering Workbench) software is used to control and communicate with the data acquisition card.

2.2.1 V8 AJ133 GDI

The test engine is a naturally aspirated, V8 gasoline direct injection (GDI) engine. The main parameters of the engine are listed in Table 2.1. The Jaguar V8 Engine has a single spark plug in each cylinder and each spark plug is controlled by an individual coil. The valve timing, spark timing, injection timing, fuel pressure and relative air fuel ratio (Lambda) etc. can be controlled using ETAS software installed on a PC, which is connected to the engine control unit (ECU) through an interface module. The V8 engine employs a spray guided direct injection combustion system. Fig. 2.1 illustrates the layout of the injection and combustion system. The six-hole solenoid injector is vertically mounted in the centre of the cylinder whilst a 12mm spark plug is packaged beside the injector and is installed at an angle of 18 degrees to the vertical axis of the cylinder [56]. The multi-hole injector produces six spray plumes which direct fuel to various regions in the cylinder with 2 plumes along both sides of the spark plug. The V8 engine is fitted with four variable cam timing (VCT) actuators and intake cam profile switching (CPS). The inlet and exhaust camshaft VCT phasers are designed to provide 62 and 50 degrees of variable valve timings, respectively.

Table 2.1 Main Parameter of the Test Engine

Type	NA V8 GDI, 4 Stroke	
Bore × Stroke / mm	92.5 × 93	
Displacement / cm^3	4999	
Compression Ratio	11.5	
Nominal Power	283 kW	
- at Speed	6500 rpm	
Max Torque	515 Nm	
- at Speed	3500 rpm	
Injector	High pressure 6 hole nozzle	
Injection Pressure / MPa	15 max	
Valves per Cylinder	2 intake, 2 exhaust	
Inlet Valve Lift:	Low 5.5 mm	High 10.53 mm
IVO/IVC	34° ATDC/244° ATDC	24° ATDC/274° ATDC
EVO/EVC	244° BTDC/6° ATDC	244° BTDC/6° ATDC

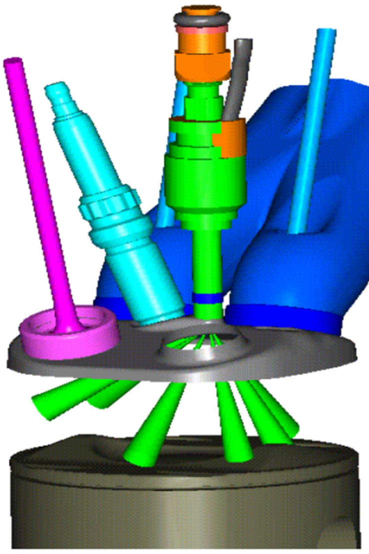

Fig. 2.1 Combustion system layout [56].

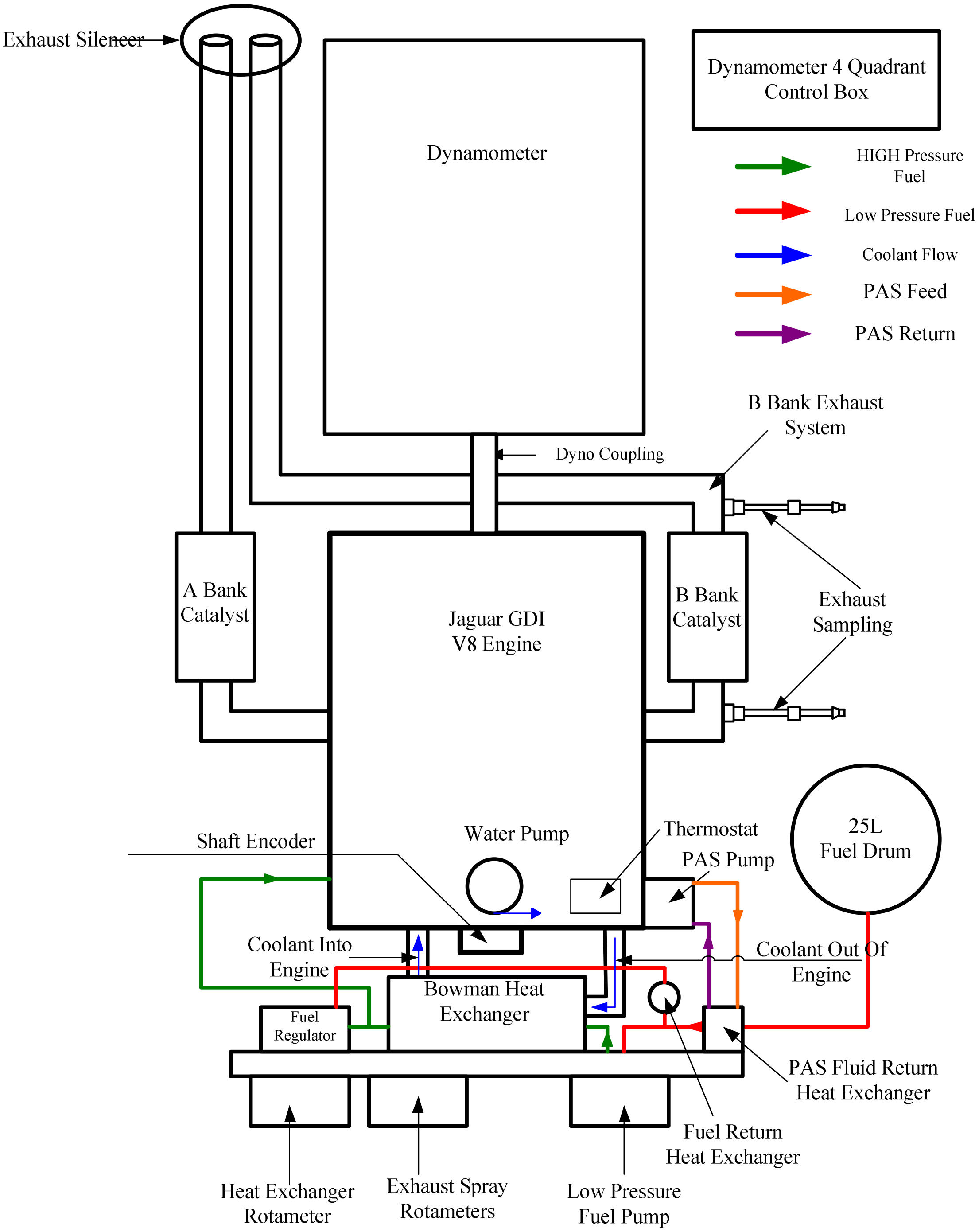

Fig. 2.2 Schematic of the Engine Test Bench

The schematic of the test bench is shown in Fig. 2.2. The exhaust from the two banks of the V8 engine are joined together approximately 3-4 m downstream of the catalysts. This allows a sufficient sample length in order to take exhaust measurements. In the B Bank, two BSP fittings have been welded onto the exhaust pipe upstream and downstream the three-way catalyst (TWC), where the exhaust sample can be taken. A Cambustion DMS500 is used to measure the particle number emissions from the engine, the details of which are described in the next section. A flame ionization detector (FID) is used to measure the Hydrocarbon (HC) emissions, the specifications of which are described below. Slow response pressure transducers are utilized to measure manifold absolute pressure, atmospheric pressure, exhaust pressure, oil pressure, low pressure fuel and coolant pressure. Thermocouples in the engine are used to measure air temperature, exhaust temperature, oil temperature and coolant in and coolant out temperature. These data are then logged into a PC using a LabVIEW DAQ system.

Hydrocarbon Analyser – Model 523

The hydrocarbon analyser detects and measures hydrocarbons using the flame ionization detection (FID) method [57]. The specifications of the analyser are listed in Table 2.2. The signal of the FID is connected to one of the DMS500 analogue inputs and logged together into the DMS data files.

Table 2.2 Analyser Performance

Range Available	0-10/25/100/250//1000/2500/10000 ppm
Measurement Resolution	1 %FS
Repeatability	±1 %FS
Linearity	±1 %FS
Noise at Zero	< 0.25 %FS
Minimum Detectable Concentration	0.1 ppm
Zero Drift	±1 %FS 24 hours
Span Drift	±1 %FS 24 hours
Response Time	90 % to step change at inlet 1.5 s

2.2.2 Data Acquisition System for V8 Engine

Fig. 2.3 illustrates the data acquisition system for the V8 engine. It can be seen that three PCs are used to collect data from the engine test rig. Four National Instruments^{TM} data acquisition cards for acquiring a variety of sensor signals from the V8 engine are installed in one of the PCs. They are operated with different triggering and clock settings. The clock determines the speed at which the data is recorded and the trigger source determines the point when the data acquisition starts.

Two of the DAQ cards are low speed with a sampling rate set to once an engine cycle, which equals to 720 °CA in this 4 stroke engine. These low speed data include engine torque, slow response pressure transducers and thermocouples, such as manifold absolute pressure (MAP), atmospheric pressure, exhaust pressure, oil pressure, low pressure fuel, coolant pressure and various temperatures such as air temperature, exhaust temperature, fuel temperature, coolant and oil temperatures.

Another high speed NI DAQ card is used for logging crank angle resolved data such as in-cylinder pressures for the four B bank cylinders, crank and cam flag. A shaft encoder rotating at the engine speed provides the trigger and clock signals for the high speed DAQ card at the sampling rate of once per degree crank angle, because the shaft encoder can output both once per cycle and once per crank angle TTL pulses simultaneously. A crank flag occurring at a known angle (e.g. compression TDC) must also be logged as this is required for positioning the pressure trace with respect to the crank angle in order to calculate data on the combustion characteristics such as IMEP and the rate of Mass Fraction Burned (MFB). During data processing, the crank flag is checked in the MATALB code to see if it corresponds to the compression or exhaust top dead centre.

One of the PCs is used to acquire data from the DMS500. The signal output from the FID is connected to the analogue input on the DMS. The DMS signal together with the FID signal is logged into the DMS data file. Another PC is connected to the engine ECU via an ETAS data interface to change the operating parameters of the engine and save the ECU parameters into the data file.

The front panel of the LabVIEW software has been created for choosing data logging options (channels, clock and trigger signals) and monitoring key engine parameters as shown in Fig. 2.4.

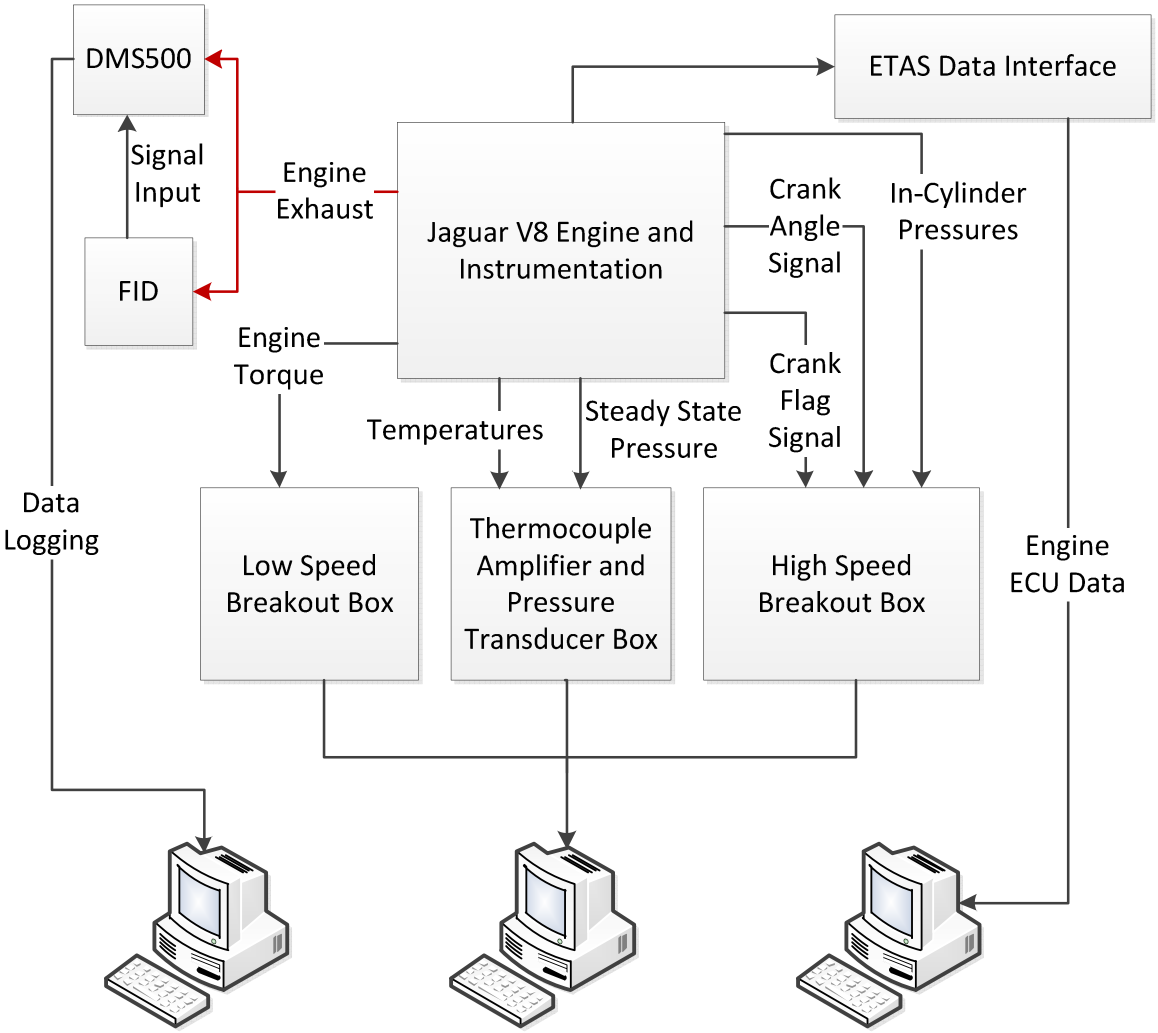

Fig. 2.3 *V8 data acquisition system*

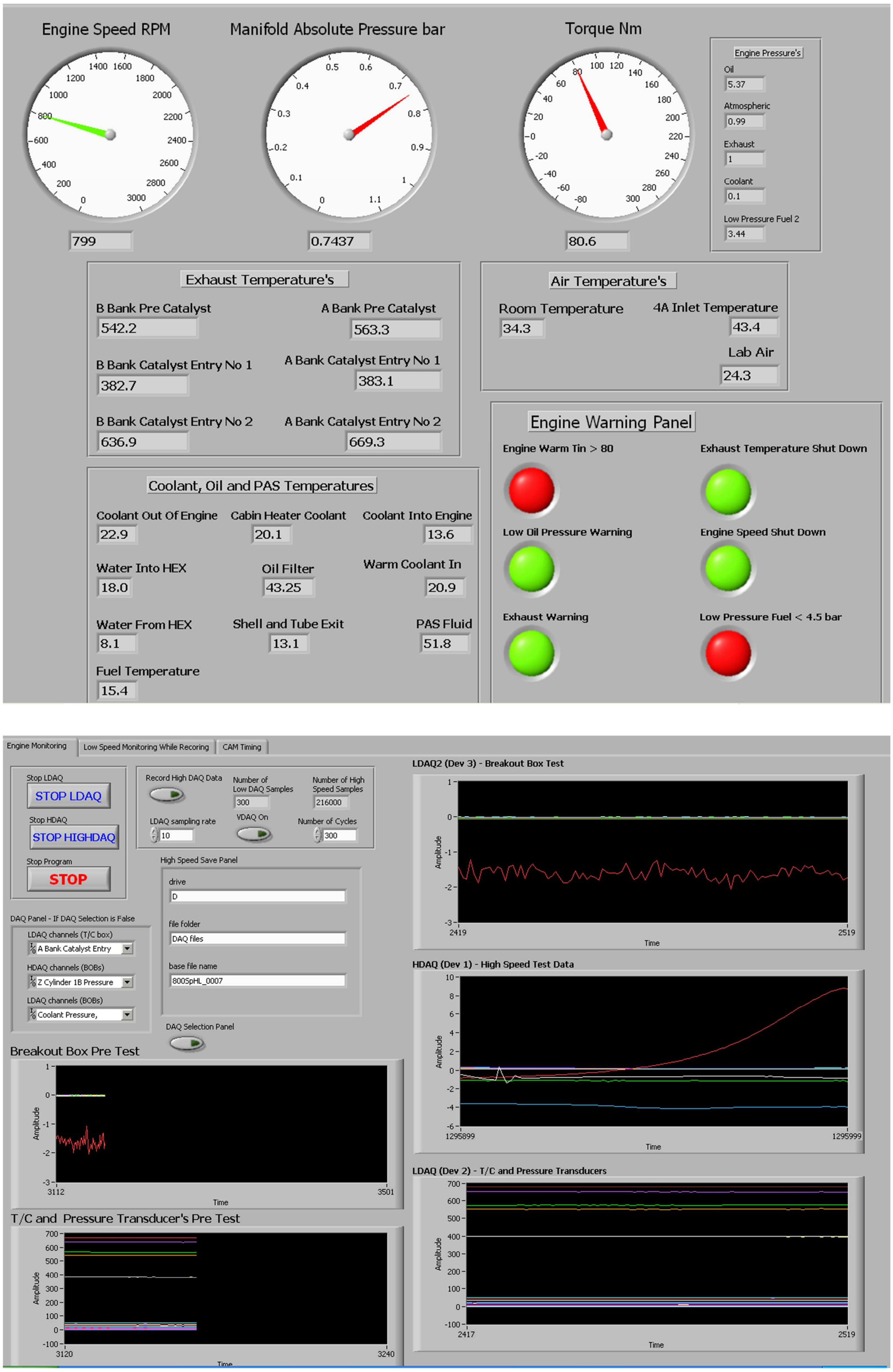

Engine Speed RPM
799

Manifold Absolute Pressure bar
0.7437

Torque Nm
80.6

Engine Pressure's
Oil
5.37
Atmospheric
0.99
Exhaust
1
Coolant
0.1
Low Pressure Fuel 2
3.44

Exhaust Temperature's
B Bank Pre Catalyst
542.2
A Bank Pre Catalyst
563.3
B Bank Catalyst Entry No 1
382.7
A Bank Catalyst Entry No 1
383.1
B Bank Catalyst Entry No 2
636.9
A Bank Catalyst Entry No 2
669.3

Air Temperature's
Room Temperature
34.3
4A Inlet Temperature
43.4
Lab Air
24.3

Coolant, Oil and PAS Temperatures
Coolant Out Of Engine
22.9
Cabin Heater Coolant
20.1
Coolant Into Engine
13.6
Water Into HEX
18.0
Oil Filter
43.25
Warm Coolant In
20.9
Water From HEX
8.1
Shell and Tube Exit
13.1
PAS Fluid
51.8
Fuel Temperature
15.4

Stop LDAQ
Stop HDAQ
Stop Program
Record High DAQ Data
Number of Low DAQ Samples
300
Number of High Speed Samples
216000
LDAQ sampling rate
10
VDAQ On
Number of Cycles
300

High Speed Save Panel
drive
D
file folder
DAQ files
base file name
800SpHL_0007

DAQ Panel - If DAQ Selection is False
LDAQ channels (T/C box)
A Bank Catalyst Entry
HDAQ channels (BOBs)
Z Cylinder 1B Pressure
LDAQ channels (BOBs)
Coolant Pressure,
DAQ Selection Panel

Fig. 2.4 *Front Panel of the V8 DAQ LabVIEW Code*

2.3 Test Data Processing

2.3.1 DMS500 Data Interpretation

This Differential Mobility Spectrometer provides a number / size spectrum for particles between 5 nm and 1000 nm [58]. The instrument uses a classifier column (Fig. 2.5) operating at sub-atmospheric pressure, using a scroll vacuum pump. Sample flow is drawn into the instrument through a conductive rubber sample tube. The sample gas passes through a corona-discharge charger into the classifier column.

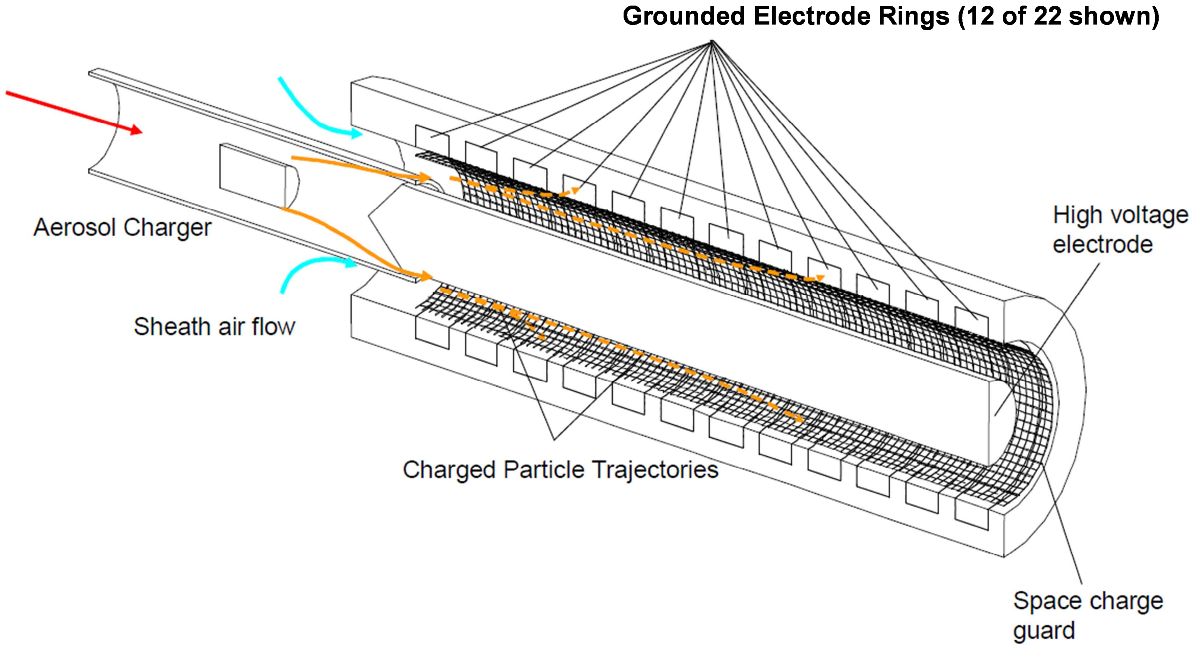

Fig. 2.5 *DMS500 classifier column schematic [59].*

The charged particles flow within a particle-free sheath flow which is a uniform, cylindrical laminar column of air designed to carry the charged particles in a predictable manner. The particles are admitted next to the central electrode, but the positively charged particles are then deflected radially towards the grounded electrometer rings by their repulsion from the central high voltage rod. Their landing position is a function of the ratio of their charge to their aerodynamic drag.

The particles yield their charge to the electrometer amplifiers and the resulting currents are translated by the instrument's user-interface into particle number and size data. Careful design of the sampling system allows a 300 ms response to be achieved using a 5 metre sample line.

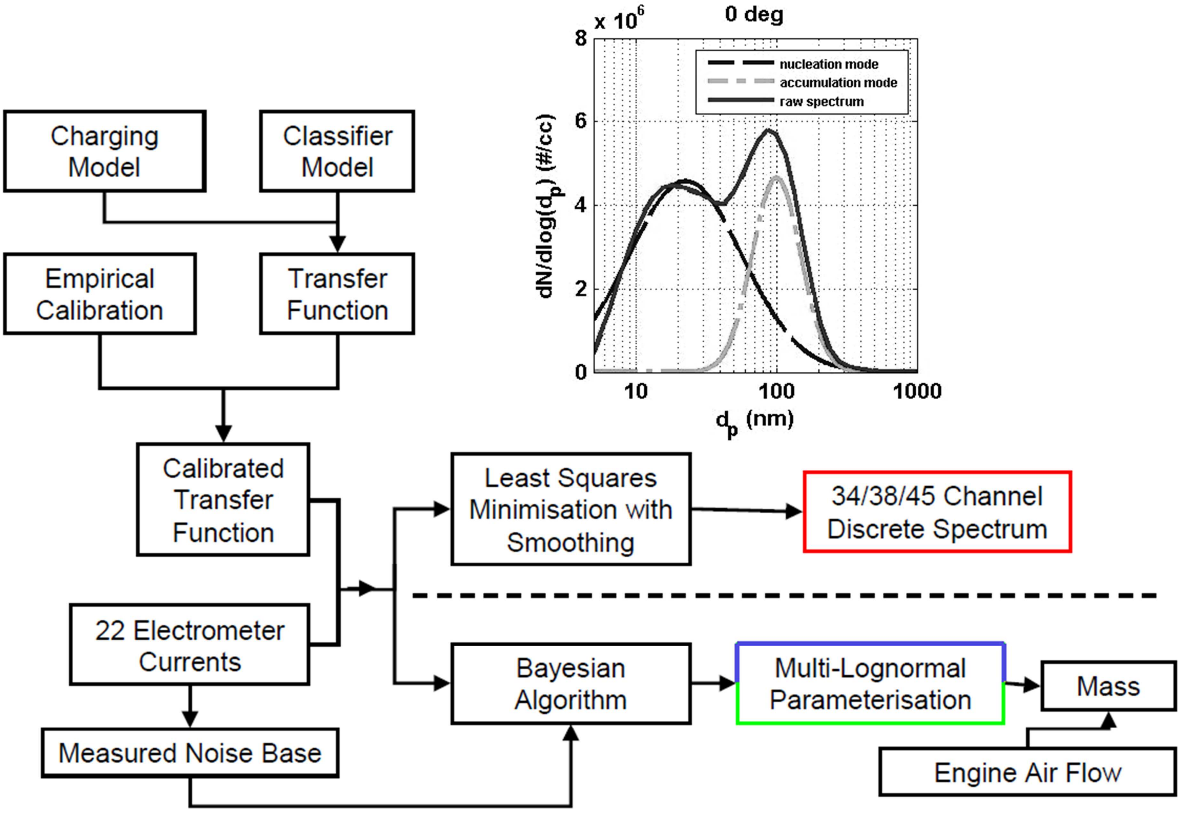

Fig. 2.6 *DMS500 data processing synopsis (adapted from [49])*

A diagram for the DMS500 data processing synopsis is shown in Fig. 2.6. During the experiments, both raw and lognormal spectra were logged into the computer for a number of samples (typically a sampling time of 90 seconds). The lognormal output is generated by a statistical algorithm, which separates the nucleation mode and accumulation mode. The DMS output is a matrix containing number concentration at a given sample number (i.e. time) and particle diameter. The number matrix is then converted to a mass matrix by using an empirical equation. The number matrix and mass matrix are averaged to find a mean concentration plot over particle diameter, which can then be integrated to obtain the total number and total mass of particles emitted by the engine. The formula used to calculate particle mass was obtained previously from back-to-back tests with the DMS500 and a Centrifugal Couette Flow Particle Mass Analyser on the GDI engine being tested here [60].

$$mass_{d\mathrm{p}} = 1.72 \times 10^{-24} \times d_{\mathrm{p}}{}^{2.65} \times n_{d\mathrm{p}} \qquad (2.1)$$

> Where: d_{p} represents the diameter of the particles (nm), $mass_{d\mathrm{p}}$ (kg/cm^3) represents particle mass concentration of diameter d_{p}, $n_{d\mathrm{p}}$ (#/cm^3) represents particle number concentration of diameter d_{p}.

From this equation, it can be seen that the larger particles would contribute much more to the particle mass than smaller particles. The lognormal fitting is particularly useful as it eliminates the noise at both the high and low end of the measured raw spectrum. As a result, it is more appropriate to use lognormal fitting data in calculating particle mass distributions from the particle size distribution.

Legislation requires the particle number emissions measurement equipment to have counting efficiencies at particle sizes of 23 nm (+/-1 nm) and 41 nm (+/-1 nm) electrical mobility diameters of 50 % (+/-12 %) and >90 % respectively [61]. During data post-processing, a digital filter using a Wiebe function was applied to the raw measurement data to simulate this legislation requirement for the counting efficiency. The formula for the filter is as follows.

$$\begin{aligned} f &= 1-\exp\left[-3.54\left(\frac{d_p-14}{40}\right)^{1.09}\right] && \textbf{for} \quad d_p > 14 \\ f &= 0 && \textbf{for} \quad d_p \le 14 \end{aligned} \tag{2.2}$$

where d_p (nm) represents the diameter of the particles.

Applying the Wiebe digital filter to the size distribution output from the DMS500 enables the measurement system to replicate the PMP requirement without any additional dilution systems. A plot of this digital filter is shown in Fig. 2.7, in which the legislative requirements are plotted with cross points. It can be seen that the counting efficiencies represented by the filter fulfil the legislative requirement.

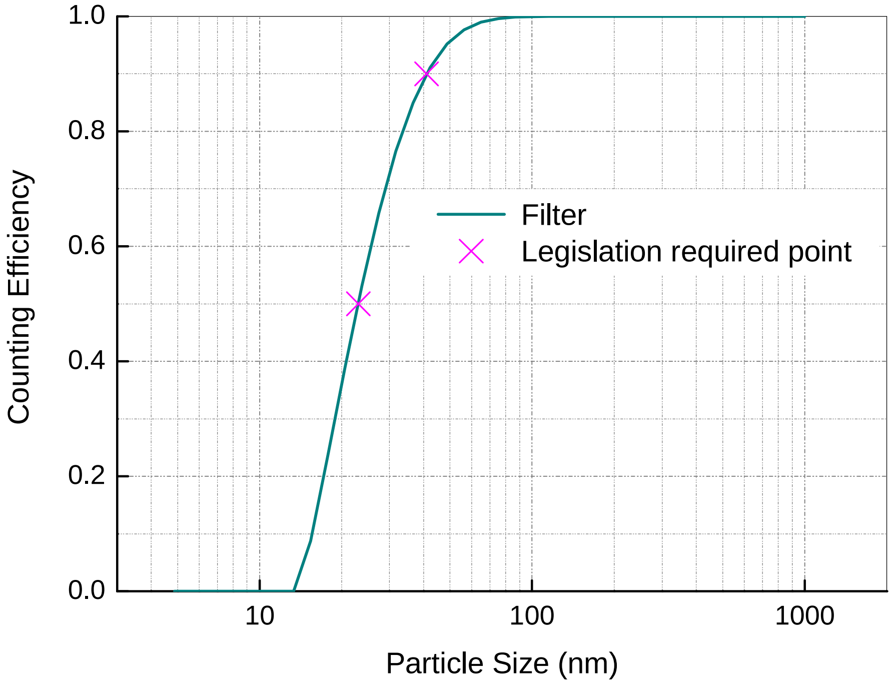

Fig. 2.7 Data Filter to replicate PMP Counting Efficiency.

Comparison of the lognormal fittings using the Cambustion method and MATLAB optimizing method

The DMS500 can output parameters for lognormal fittings in real time. The lognormal parameters such as number concentration, count median diameter (CMD) and geometric standard deviation (GSD) are obtained by minimizing the error term calculated with the measured DMS500 electrometer ring current vector. In the code integrated into the DMS500, this optimisation is conducted by maximising the posterior probability of the lognormal parameters using a Bayesian statistical algorithm [62]. In most cases, it works very well and gives an excellent fit to the raw spectrum as shown in Fig. 2.8(a), where the spectrum of the size distribution is quite broad under the rich operation condition. However, under stoichiometric operating conditions, the particle number concentrations become lower and the size distribution becomes narrower compared to that under rich operation. From Fig. 2.8(b), it can be seen that the peak for the nucleation mode particles and the accumulation mode particles are close to each other and the peak for the accumulation mode particles is moving towards the lower end of the particle size range. In this case, the bi-lognormal size distribution shows a higher discrepancy from the raw size distribution. There are two peaks in the raw spectrum, but this is not shown in the Cambustion computation of the lognormal size distributions. The CMD of the nucleation mode is too large and the concentration of the accumulation mode is too low. As a result, a larger error is shown between the total P_n calculated from the raw data and the sum of the nucleation mode P_n and the accumulation mode P_n calculated using the lognormal fitting parameters output by the DMS. Thus an alternative calculation method is needed to calculate the lognormal fitting parameters under this circumstance.

A MATLAB program has been developed to calculate the lognormal parameters, using a MATLAB function in the optimization toolbox. The function finds the minimum of a constrained nonlinear multi-variable function in order to find the optimized values of the lognormal parameters that give the best fit to the raw size distribution. The calculation procedure for the MATLAB program is described as follows.

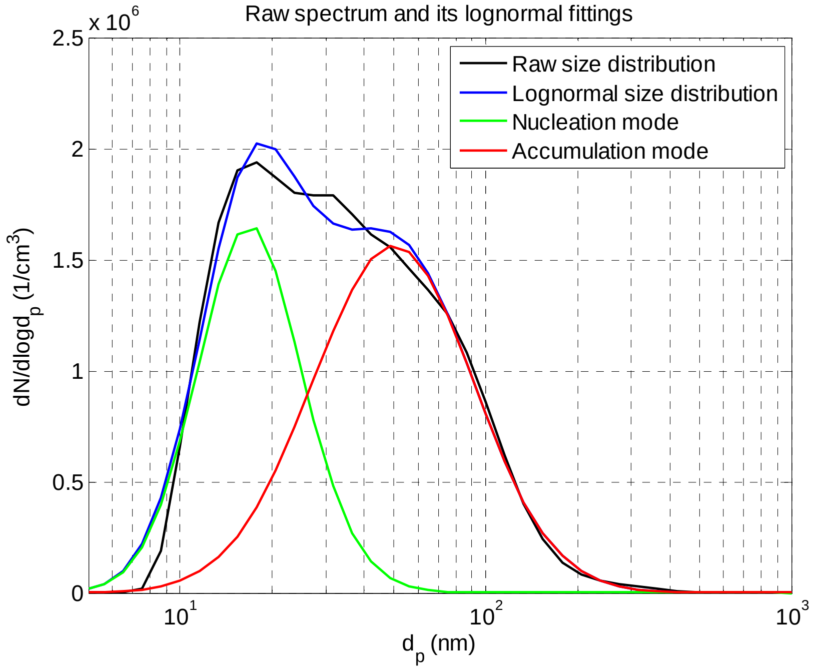

Speed (rpm)	Torque (Nm)	Lambda	Total Pn (#/cm^3)	Nucl Pn fit (#/cm^3)	Acc Pn fit (#/cm^3)
1500	90	0.9	1710084	717010	1035118

(a) Representative size distribution under rich operating condition

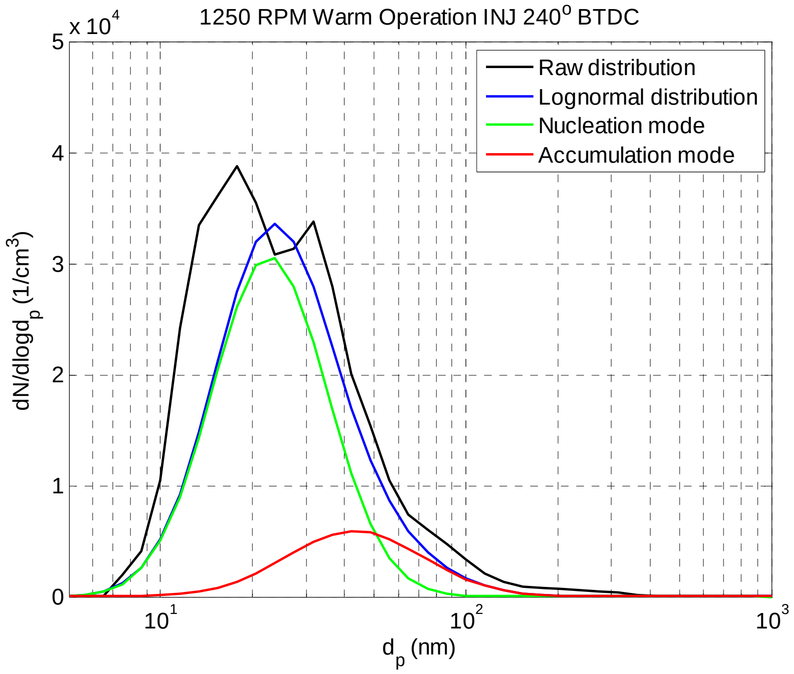

Speed (rpm)	Torque (Nm)	Lambda	Total Pn (#/cm^3)	Nucl Pn fit (#/cm^3)	Acc Pn fit (#/cm^3)
1250	139	1.0	2.40×10^4	1.44×10^4	3.33×10^3

(b) Representative size distribution under stoichiometric operating condition

Fig. 2.8 *Comparision of two number weighted size distributions and their lognormal fits using the Cambustion Bayesian method.*

The least square error between the lognormal spectrum and the raw spectrum was minimized to find the best fit to the raw size distribution. Firstly, the normalized size distribution was calculated by dividing the value of each point in the raw spectrum by the peak value of the spectrum. This gives a normalized spectrum as a curve with a peak value of 1. As the peak value of the raw spectrum could be several orders of magnitudes above 1, using this method reduces the sum of the squared residuals during the calculation, so that the risk of crashing the code is reduced, and the initial concentration can be set more easily. Also, calculating with a normalized spectrum facilitates comparing the results between different optimizing methods or with different initial guesses. In the MATLAB fitting program, the objective function is defined as the sum of the squared residuals (S) between the combined normal probability density function (normpdf) and the normalized raw size distribution. The objective function is expressed below as:

$$S = \sum_{i=1}^{38} \begin{pmatrix} c_1 \times \mathrm{normpdf}\left(\log_{10}\left(d_\mathrm{p}(i)\right), \mu_1, \sigma_1\right) \\ + c_2 \times \mathrm{normpdf}\left(\log_{10}\left(d_\mathrm{p}(i)\right), \mu_2, \sigma_2\right) - s(i) \end{pmatrix}^2 \tag{2.3}$$

Where c_1, μ_1 and σ_1 represent the concentration, CMD and GSD for the nucleation mode (Nucl), respectively, c_2, μ_2 and σ_2 represent the concentration, CMD and GSD for the accumulation mode (Acc), respectively, d_p (nm) represents the diameter of the particles, s represents the raw size distribution.

From Eq. 2.3, it can be seen that i represents the index of the particle sizes. As there are 38 particle size ranges between 5 nm and 1000 nm output by the DMS, i varies from 1 to 38. c_1, μ_1, σ_1, c_2, μ_2, and σ_2 are the variables in the function S which is to be minimized. Certain constraints are applied to all the variables to confine them within a reasonable range. Lower and upper bounds of the optimizing variables are listed in Table 2.3. In the case shown in

Fig. 2.8(b), as the particle sizes are quite small, the bounds for the CMD of the nucleation mode and the accumulation mode are set to 5-30 nm and 35-200 nm, respectively. Depending on the operating conditions, such as stoichiometric or rich combustion, homogeneous or stratified injection, etc., the CMD for accumulation mode particles can vary a lot. However, for a GDI engine, the possibility for the CMD of the accumulation mode particles being lower than 35 nm should be quite small. Then, the MATLAB program is used to minimize the function S and return the corresponding values of the variables between the lower and upper bounds. By multiplying the peak value of the raw spectrum with the calculation results from the fitting procedure, the optimized lognormal fits to the raw spectrum can be acquired.

Table 2.3 The set of Tolerance, lower and upper bounds on the parameters used in the MATLAB lognormal fitting code

	Lower Bound	Upper Bound	Tolerance
Nucl Concentration:	0.1	1	1×10^{-9}
Nucl CMD / nm	5	30	
Nucl GSD / nm	1	10	
Acc Concentration	0.1	1	
Acc CMD / nm	35	200	
Acc GSD / nm	1	10	

Minimizing the function S starts with initial values of the variables. In the nonlinear optimization for this case, the initial value may have some effect on the final results. Generally, with an initial guess close to the final value, it is easier to find the global optimizing point. But, if the deviation between the initial value and final point is too large the global optimizing point may not be found, but a local optimizing value may be shown instead. The optimizing algorithm may even be unable to converge with some initial guesses. However, in this case, with constraints applied to the variables, the algorithm may be less susceptible to divergence as the variables can only vary in a specific range where at least a local optimizing point should be able to be found. So, it is of interest to see if the calculation results would vary with different initial values for the variables. The optimization results calculated with two initial guesses are compared. The initial values and the final optimized values of these two cases are listed in Table 2.4. The concentrations shown in the table are normalized values. It can be seen that with the first initial guess, the difference between the initial CMD of the nucleation mode and the accumulation mode are larger than that with the second initial guess. Both initial values were not chosen to be particularly close to the final optimized values. However, identical results have been obtained with different initial guesses, indicating that the algorithm is quite stable and is not very sensitive to the initial values of the variables. Also, in both cases, the exit flag of the optimization function showed that first-order optimality measure was less than the tolerance on the function value (1×10^{-6}) and all of the constraints were satisfied.

Table 2.4 Initial conditions and calculating results for two initial guesses

Initial Guess:	1	2
Initial Nucl Concentration:	0.5	0.5
Initial Nucl CMD / nm	10	25
Initial Nucl GSD / nm	1.5	1.5
Initial Acc Concentration:	0.5	0.5
Initial Acc CMD / nm	60	45
Initial Acc GSD / nm	1.5	1.5
Optimized Nucl Concentration:	0.348	0.348
Optimized Nucl CMD /nm	15.8	15.8
Optimized Nucl GSD / nm	1.39	1.39
Optimized Acc Concentration:	0.245	0.245
Optimized Acc CMD / nm	35.0	35.0
Optimized Acc GSD / nm	1.41	1.41
Sum of the squared residuals:	0.0624	0.0624

Fig. 2.9 shows the normalized raw spectrum, initial conditions and the lognormal fitting

results. It verifies that the lognormal fits are the same with different initial values and the lognormal distributions calculated are a good approximation to the raw distribution.

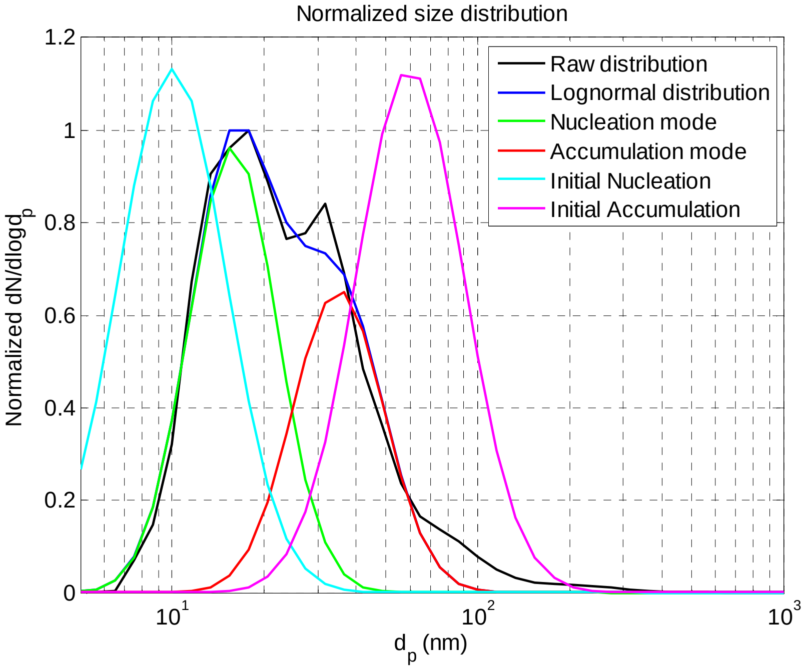

(a) Results with the first initial Guess

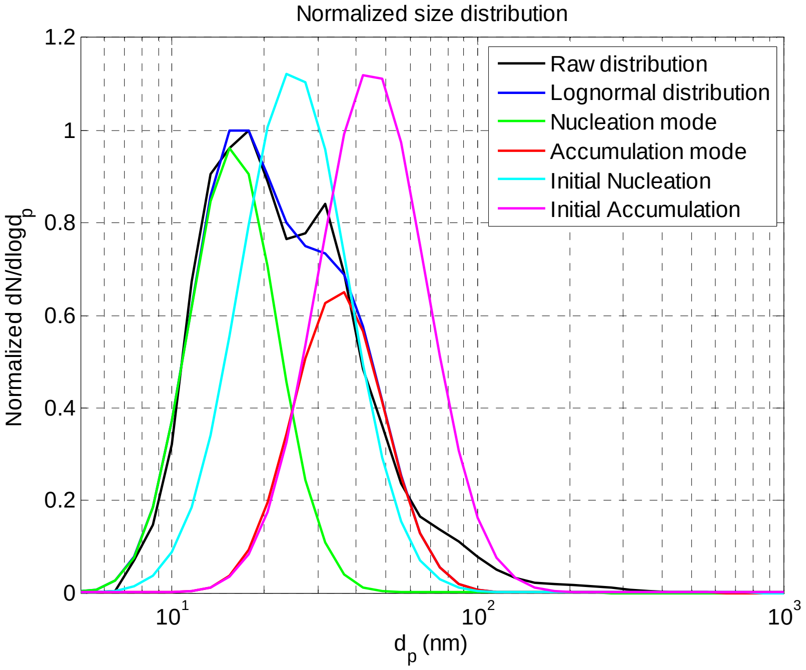

(b) Results with the second initial Guess

Fig. 2.9 *Normalized number weighted size distributions for raw data, initial guess and the calculated lognormal fittings.*

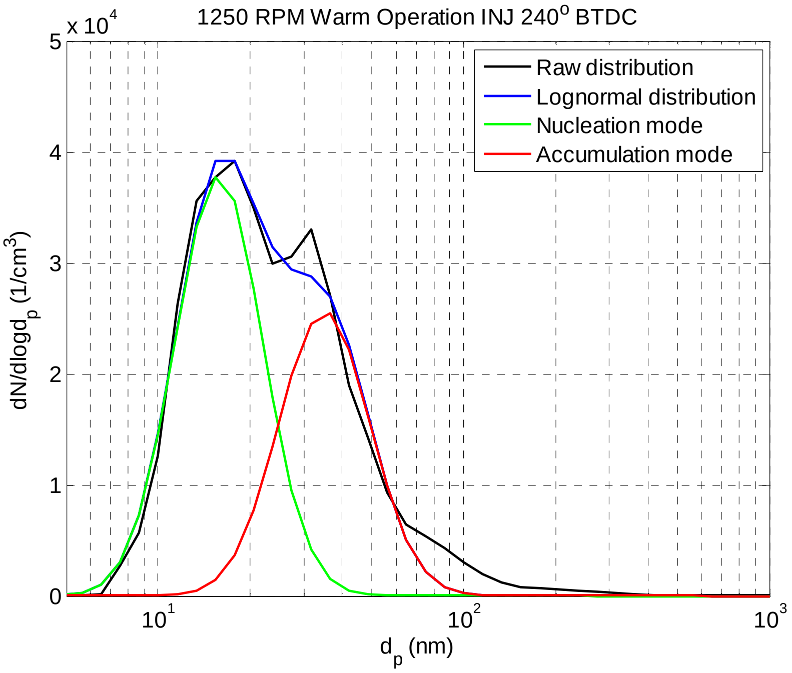

Speed (rpm)	Torque (Nm)	Lambda	Total Pn (#/cm^3)	Nucl Pn fit (#/cm^3)	Acc Pn fit (#/cm^3)
1250	139	1.0	$2.40{\times}10^4$	$1.36{\times}10^4$	$9.60{\times}10^3$

Fig. 2.10 Lognormal fittings using MATLAB optimizing method.

Table 2.5 Comparison of Cambustion Ltd Bayesian method and the MATLAB optimizing method

	DMS500	MATLAB
Total Particle Number / (#/cm^3)	$2.40{\times}10^4$	$2.40{\times}10^4$
Nucl Particle Number / (#/cm^3)	$1.44{\times}10^4$	$1.36{\times}10^4$
Nucl CMD / nm	22.7	15.8
Nucl GSD / nm	1.54	1.39
Acc Particle Number / (#/cm^3)	$3.33{\times}10^3$	$9.60{\times}10^3$
Acc CMD / nm	43.1	35.0
Acc GSD / nm	1.68	1.41
Sum of squared residuals (normalized value):	0.838	0.0624

Fig. 2.10 shows the final results of the lognormal fitting to the raw spectrum. Compared with Fig. 2.8(b), it can be seen that the accumulation mode concentration calculated with MATLAB is much higher than that acquired by the DMS500 and the sum of the nucleation mode P_n and the accumulation mode P_n is much closer to the total P_n distribution of the raw spectrum compared with that calculated using the lognormal parameters output from the DMS. It can be seen that using the MATLAB program, a better fit is obtained compared with using the lognormal fitting parameters output by the DMS500. From Table 2.5, it can be seen that the sum of the squared residuals between the normalized lognormal spectrum to the normalized raw spectrum optimized with MATLAB program is more than an order of magnitude lower than that with the DMS500 lognormal fittings.

2.3.2 Data Processing Program for V8 Engine

In order to facilitate further analysis of the engine data, a data processing program is needed to calculate the data collected from the different sources. Various engine parameters and tests results need to be calculated and written into individual Excel files corresponding to their different sources as well as a summary Excel file for all the tests.

In-cylinder pressure traces are recorded using a high speed data acquisition system and saved into HDAQ text files. Slow response pressures, thermocouples and the engine torque readings are recorded with low speed data acquisition system and saved into the LDAQ text files. The engine ECU parameters monitored with the ETAS engine calibration system are logged using INCA software into ETAS data files. As the measured data from HDAQ, LDAQ, ETAS and DMS are recorded and saved into individual data files, it is useful to integrate all the data together and output the calculated results into separate Excel files and assemble all the results into one summary Excel file. Also, one experiment may consist of various test points with different test parameters, therefore batch processing is required to handle the data files of all the operation points sequentially and group the results of various test points in one Excel File. A diagram illustrating the structure of the V8 data processing program is shown in Fig. 2.11. A MATLAB program has been written to process the engine data in the following 3 stages:

Step 1. The number and the name of all the test points are specified in a graphic user interface so they can be processed sequentially. The program is able to process a batch of test points in a single run, improving the efficiency of data processing and simplifying a comparison of the results from a set of different engine operation points.

Step 2. For each test point, the text files from HDAQ and LDAQ, the Excel file from DMS and the data file from ETAS are read into the MATLAB program and processed separately.

For HDAQ data, the in-cylinder pressure records that were measured using a Kistler pressure transducer for every crank angle degree and are analysed using a MATLAB code in order to calculate the following combustion parameters:

- IMEP, GMEP and PMEP data
- Maximum in-cylinder pressure and its position
- Heat Release
- Combustion duration (0-10, 50 and 90% MFB durations, duration for 0-100 J heat release)

Both cycle by cycle and statistical (mean and standard deviation) results are calculated and the results are sorted into pressure data and burn rate data.

The DMS results are generated from the DMS Excel data file. Particle number (P_n) and mass (P_m) for nucleation mode particles and accumulation mode particles are calculated based on the lognormal parameters output by the DMS, such as number concentration, count median diameter (CMD) and geometric standard deviation (GSD). A digital filter using a Wiebe function (Eq. 2.2) is applied to the number concentration for the accumulation mode particles to simulate the legislative requirement for the counting efficiency. This result is designated as PMP accumulation P_n. Both the transient results (data from each sample point) and the statistical results (mean and standard deviation for all the data points) are calculated.

The relevant conversion equation for converting the CMD to Diameter of Average Mass (DAM) is given by Eq. 2.4, where f is the relevant exponent of d_p from equations correlating the particle mass with the particle diameter, σ_g is the geometric standard deviation.

$$DAM = CMD \times \exp\left(\frac{f}{2}\ln^2\left(\sigma_g\right)\right) \tag{2.4}$$

The DAM is the diameter of a particle whose mass, multiplied by the total PN concentration, gives total particle mass concentration for that particular log-normal distribution. Once the DAM has been calculated, it can then be used with the relevant equation for total particle mass calculation.

Various engine operation and ECU calibration data are recorded into the ETAS data files, which include engine speed, spark timing, intake and exhaust valve timing, fuel injection timing, fuel pressure, engine Lambda, etc. The ETAS data file is firstly imported into the MATLAB code and then the measured parameters are categorized into data sets of 2 ms, 8 ms and 128 ms according to their different sampling periods. This is because some engine parameters, such as engine speed, spark ignition timing, valve timings, injection timing and duration, are recorded with high speed sampling, while some parameters are recorded with low speed sampling. Both the transient readings (data for every sample point) and the statistical results (mean and standard deviation for all the data points) are generated.

The LDAQ data from all the slow response pressure transducers, thermocouples and engine torque are imported from each data file into the MATLAB programme. First, a downsampling of the raw data was used to calculate the average value of each channel every second. Both the transient readings (data from every second) and the statistical results (mean and standard deviation for all the data points) are generated.

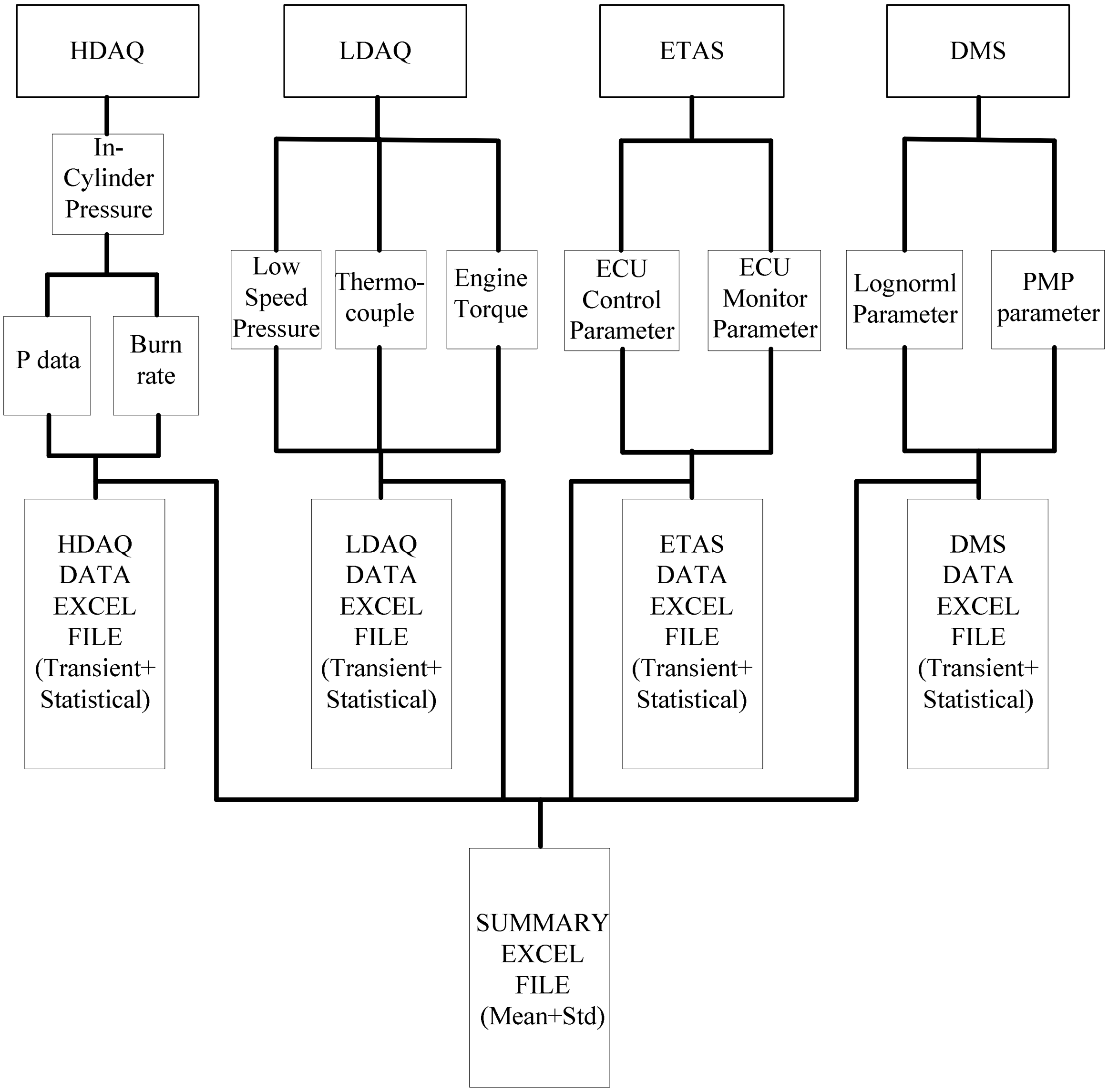

Fig. 2.11 Structure diagram of the V8 data processing Program

Step 3. The results for all the testing points are output into Excel files. The transient results (the calculated results for each cycle or individual sampling points) and the statistical results (the value of mean and standard deviation for the transient data points) for HDAQ, LDAQ, DMS and ETAS are written into individual Excel results files. Also, the entire statistical results from HDAQ, LDAQ, DMS and ETAS for all the testing points are exported into a Single Summary Excel file. A flow chart of the V8 data processing program is shown in Fig. 2.12.

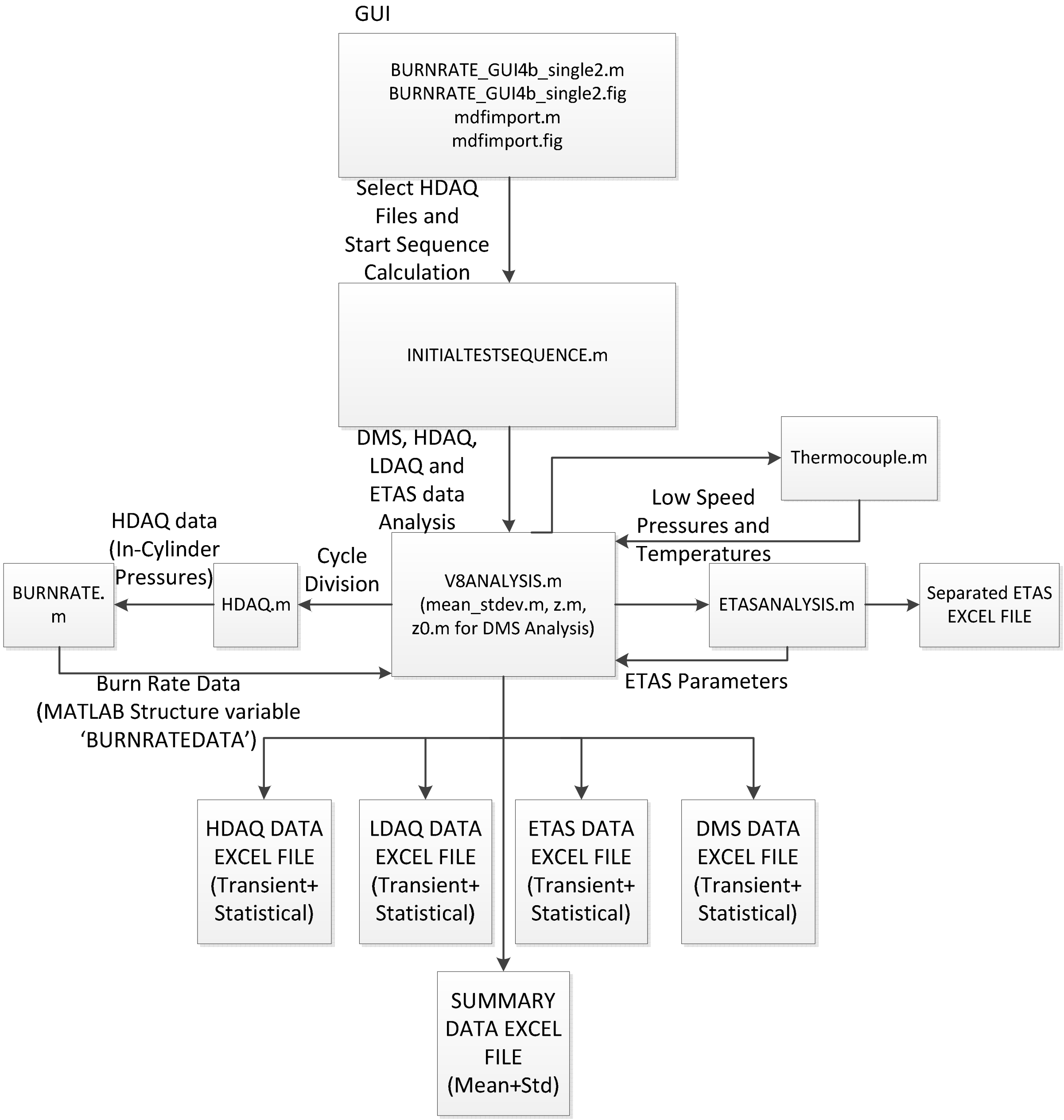

Fig. 2.12 The Flow Chart for the V8 MATLAB Program

Fig. 2.13 shows the graphic user interface of the MATLAB Program, which is used to specify the number of experiments and select the experimental data files for processing.

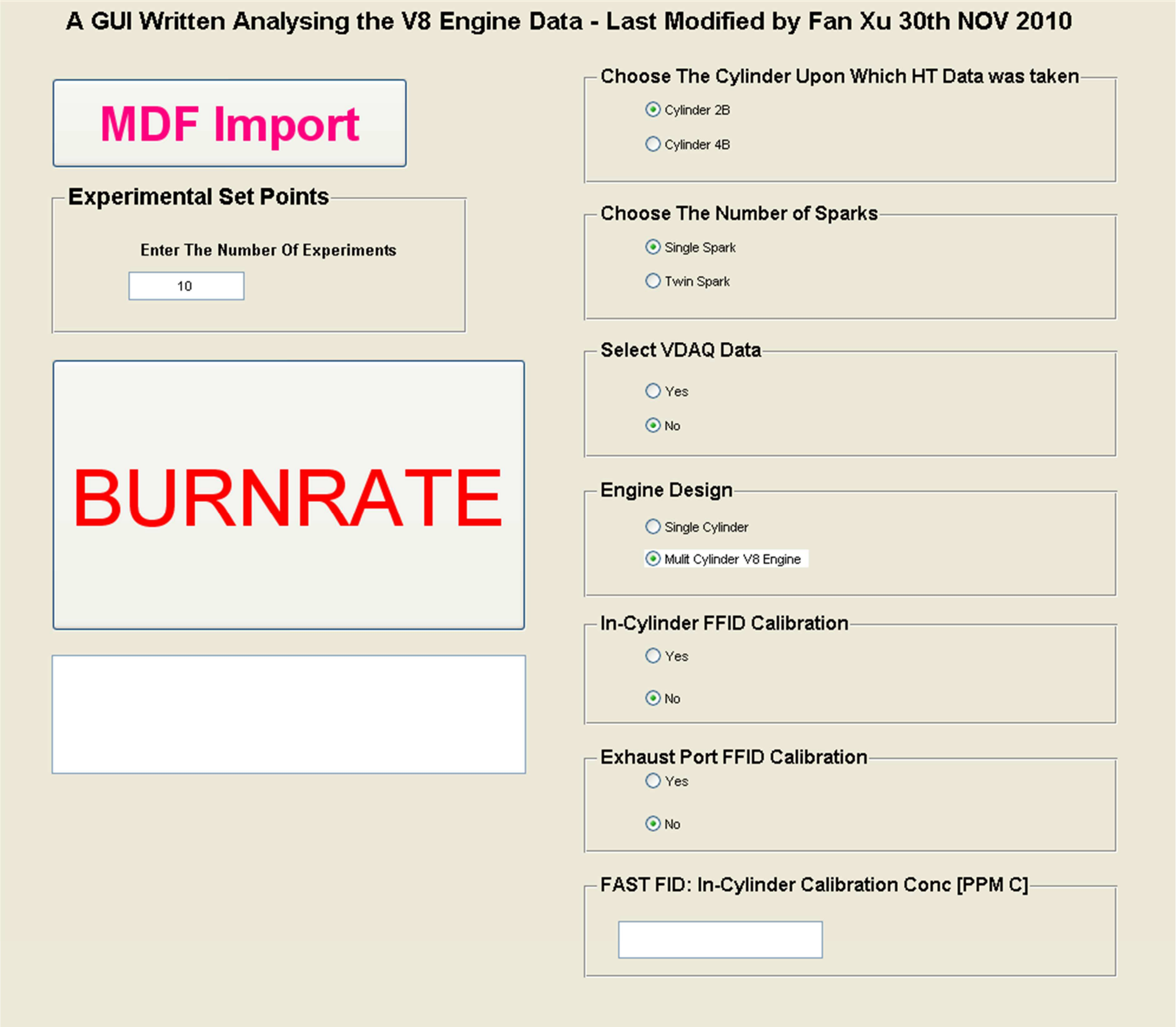

A GUI Written Analysing the V8 Engine Data - Last Modified by Fan Xu 30th NOV 2010

Experimental Set Points
Enter The Number Of Experiments
10

Choose The Cylinder Upon Which HT Data was taken
● Cylinder 2B
○ Cylinder 4B

Choose The Number of Sparks
● Single Spark
○ Twin Spark

Select VDAQ Data
○ Yes
● No

Engine Design
○ Single Cylinder
● Mulit Cylinder V8 Engine

In-Cylinder FFID Calibration
○ Yes
● No

Exhaust Port FFID Calibration
○ Yes
● No

FAST FID: In-Cylinder Calibration Conc [PPM C]

Fig. 2.13 The Graphic User Interface for the V8 MATLAB

2.4 Summary

A Jaguar V8 AJ133 engine has been used in the experiments. Details of the engine specifications, the experimental apparatus in the engine test cell and the data processing methods have been presented.

The LabVIEW programed data acquisition system has been used for recording various engine parameters at low sampling rate (1/cycle) and high sampling rate (1/°CA).

Data interpretation of the DMS500 data has been discussed with a comparison of different algorithms for calculating the bi-lognormal fits to the raw spectrum. A MATLAB code has been developed for optimizing the parameters of the lognormal fits when the lognormal parameters output by the DMS cannot give satisfactory results. This has been shown to be a useful alternative method in calculating the parameters for the nucleation mode and the accumulation mode.

A data integration code has been programed in MATLAB to assemble data from the different acquisition sources. After all of the data has been processed by the code, separated results as well as integrated summary results are output to individual Excel files.

Chapter 3. Filter Sampling Tests and Filtration Efficiency Analysis

3.1 Introduction

Glass fibre filters have been widely used in sampling the particulate emissions from engines and vehicle exhaust. For instance, Thermo-Gravimetric Analysis (TGA) tests can be performed on the filters that have accumulated particles, so as to characterize the particulate emissions from the engine. So, it is of interest to quantify the filtration efficiencies of the filters to see if all of the particles from the sampled gas can be collected.

Firstly, the mechanisms for particulate deposition are analysed based on the classical single-fibre efficiency theory, and the formulas and methods used here for calculating the total filter efficiencies are discussed. Secondly, the experimental apparatus, instrumentation set-up, the method for testing the collection efficiency of the filter and the testing procedures are described. Thirdly, the particle number results from the DMS500 are presented and discussed. The theoretical calculation of the filtration efficiencies were performed to compare with the experimental results.

3.2 Mechanisms for Particulate Deposition

Filtration by fibrous filters is a complicated process and much research has been conducted on characterising the mechanisms for particle deposition on filters. In order to clarify the effect of different parameters on the filtration process, the collection of a particle by an individual fibre has been considered, and the mechanisms by which particles can be collected by the fibre have been analysed.

Four basic mechanisms for particulate deposition are discussed below, which include interception, inertial impaction, diffusion and gravitational settling. These four mechanisms are also called mechanical collection mechanisms [63].

Interception

Collection by interception occurs when a particle follows a gas streamline that happens to come within one particle radius of the surface of a fibre [63], which is shown in Fig. 3.1. The particle hits the fibre and is captured because of its finite size. Thus, for a given size particle, certain streamlines will result in capture of the particle while other streamlines will not. For pure interception, it is assumed that the particles follow the streamlines perfectly; that is, they have negligible inertia, settling, and Brownian motion. Interception is the only mechanism that is not a result of a particle departing from its original gas streamline.

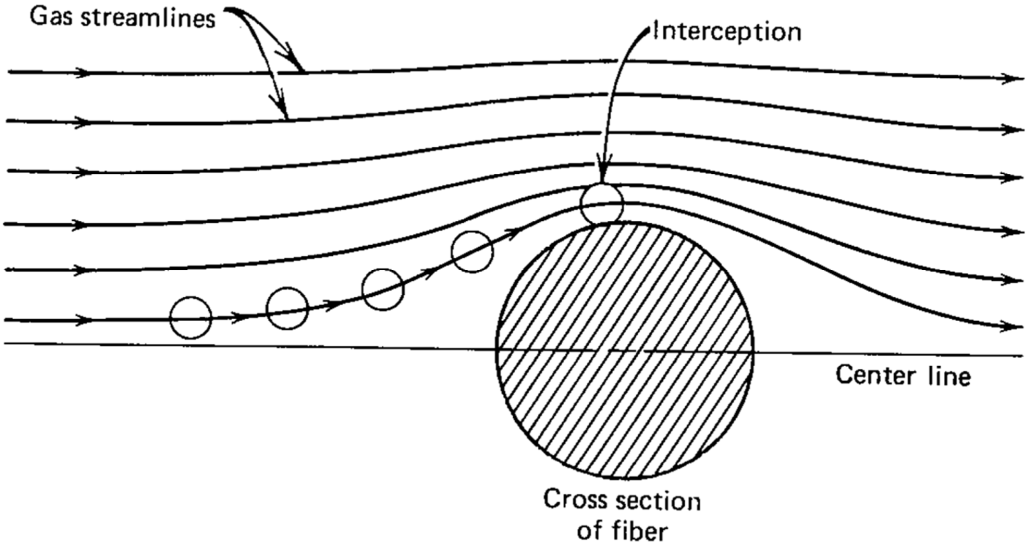

Fig. 3.1 Single-fibre collection by interception [63].

The single-fibre efficiency due to interception depends on the dimensionless parameter R, where

$$R = d_p/d_f \tag{3.1}$$

If the Kuwabara flow [64] is used, the single-fibre efficiency for interception, E_{R} can be written in the following expression [65,66]:

$$E_{\mathrm{R}} = \frac{(1+R)}{2\mathrm{Ku}}\left[2\ln(1+R) - 1 + \alpha + \left(\frac{1}{1+R}\right)^2\left(1-\frac{\alpha}{2}\right) - \frac{\alpha}{2}(1+R)^2\right] \tag{3.2}$$

Where α is the volume fraction of fibres, called the packing density or solidity (1-porosity). For fibrous filters, α is typically between 0.01 and 0.3. Ku is the Kuwabara hydrodynamic factor and has been used in research on filters [64, 66-74]. Ku is a dimensionless factor that compensates for the effect of distortion of the flow field around a fibre because of its proximity to other fibres. Ku depends only on the solidity α.

$$\mathrm{Ku} = -\frac{\ln\alpha}{2} - \frac{3}{4} + \alpha - \frac{\alpha^2}{4} \tag{3.3}$$

E_{R} increases with increasing R, but cannot exceed the maximum theoretical value of $1+R$ based on the definition of single-fibre efficiency. Interception is an important filtration mechanism in the particle size range of minimum filtration efficiency.

Inertial impaction

Inertial impaction of a particle on a fibre occurs when the particle, because of its inertia, is unable to adjust quickly enough to the abruptly changing streamlines near the fibre, so crosses those streamlines to hit the fibre. The parameter that governs this mechanism is the Stokes number [66], defined here as the ratio of particle stopping distance to fibre diameter.

$$\mathrm{Stk} = \frac{\tau U_0}{d_{\mathrm{f}}} = \frac{\rho_{\mathrm{p}} d_{\mathrm{p}}^2 C_{\mathrm{c}} U_0}{18\eta d_{\mathrm{f}}} \tag{3.4}$$

Where ρ_p is the density of the particle, η is the viscosity of the gas; C_c is the Cunningham slip correction factor which is written as [66]

$$C_\mathrm{c} = 1 + 2.492\frac{\lambda}{d_\mathrm{p}} + 0.84\frac{\lambda}{d_\mathrm{p}}\exp\left(-0.435\frac{d_\mathrm{p}}{\lambda}\right) \tag{3.5}$$

Where λ is the mean free path of the gas molecules.

Eq. 3.4 represents the ratio of the 'persistence' of a particle to the size of the target. Single-fibre efficiency for impaction increases with an increasing value of Stokes number, because of a greater particle inertia (greater d_p or ρ_p), a greater particle velocity, or a more abrupt curvature of streamlines, caused by a smaller fibre size. Although it has been indicated that the soot effective density varies with particle size [21], the particle density used in the following calculation of filtration efficiency is assumed to be 1 g/cm^3, as is commonly used in relevant exhaust characterization studies [10,23]. The single-fibre efficiency for impaction E_I is given by Yeh and Liu [67] as,

$$E_\mathrm{I} = \frac{\mathrm{Stk}J}{(2\mathrm{Ku})^2} \tag{3.6}$$

Where

$$J = (29.6 - 28\alpha^{0.62})R^2 - 27.5R^{2.8} \quad \text{for } 0.01 \le R \le 0.4 \text{ and } 0.0035 \le \alpha \le 0.111 \text{ [68]}$$

There is no simple equation for J when $R > 0.4$. For approximate analysis, a value of $J = 2.0$ for $R > 0.4$ can be used. As expected, impaction is the most important mechanism for large particles, but such particles usually have significant collection by interception as well. The sum of E_I and E_R cannot exceed the theoretical maximum of $1 + R$ [63]. Also the simple equation of J is for filters with solidity between 0.0035 and 0.111.

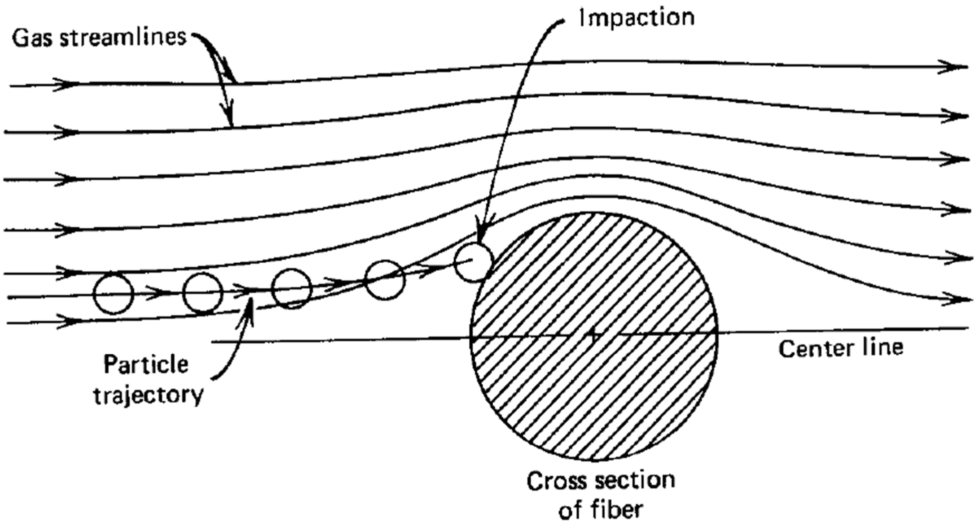

Fig. 3.2 Single-fibre collection by impaction [63].

Diffusion

The Brownian motion of small particles is sufficient to greatly enhance the probability of their hitting a fibre while traveling past it on a non-intercepting streamline. The single-fibre efficiency due to diffusion, E_D, is a function of the dimensionless Peclet number, Pe,

$$\mathrm{Pe} = \frac{d_f U_0}{D} \tag{3.7}$$

Where D is the particle diffusion coefficient. For pure molecular diffusion, D can be written as

$$D = \frac{kTC_c}{3\pi\eta d_p} \tag{3.8}$$

Where k is the Boltzmann constant, T is the absolute temperature, η is the viscosity of the gas and C_c is the Cunningham slip correction factor (Eq. 3.5). The single-fibre efficiency due to diffusion E_D is

$$E_{\mathrm{D}} = 2.6\left(\frac{1-\alpha}{\mathrm{Ku}}\right)^{1/3}\mathrm{Pe}^{-2/3} \tag{3.9}$$

The above equation is given by Lee and Liu [65]. They utilize a multiple-cylinder model that takes into account the flow interference effects of neighbouring fibres. Thus, this model provides a better representation of the actual flow profile in the filter. It can be seen that the single-fibre efficiency for diffusion increases as Pe and particle size decrease. E_{D} is the only deposition mechanism that increases as d_{p} decreases.

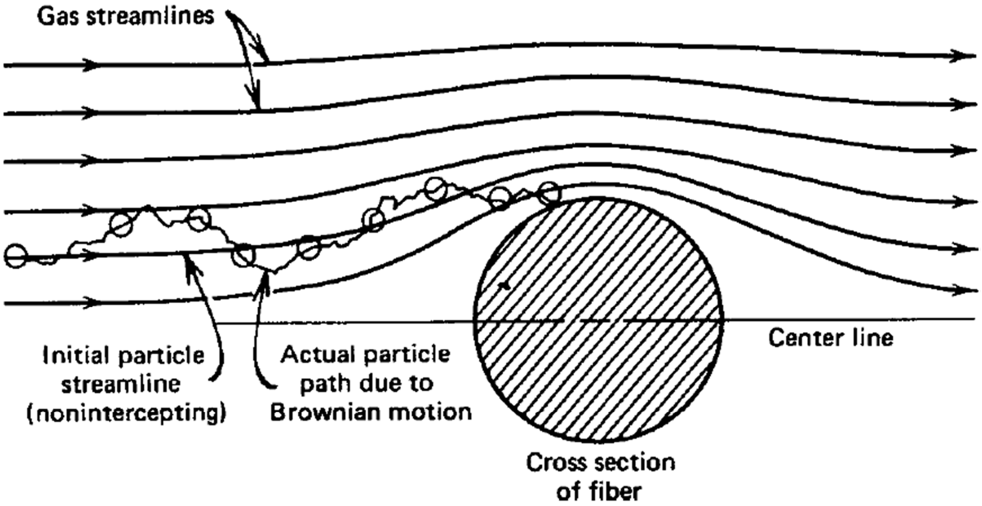

Fig. 3.3 Single-fibre collection by diffusion [63].

In estimating the overall single-fibre collection efficiency near the particle size of minimum efficiency, it is necessary to include an interaction term to account for enhanced collection due to interception of the diffusing particles [63].

$$E_{\mathrm{DR}} = \frac{1.24R^{-2/3}}{(\mathrm{Ku\ Pe})^{1/2}} \tag{3.10}$$

Gravitational Settling

The dimensionless number that controls deposition due to gravitational settling is G [63].

$$G = \frac{V_{\mathrm{TS}}}{U_0} = \frac{\rho_{\mathrm{g}} d_{\mathrm{p}}^2 C_{\mathrm{c}} \mathrm{g}}{18\eta U_0} \tag{3.11}$$

Where V_{TS} is the terminal settling velocity

$$V_{\mathrm{TS}} = \frac{\rho_{\mathrm{g}} d_{\mathrm{p}}^2 C_{\mathrm{c}} g}{18\eta} \qquad \text{for Re} < 1.0 \tag{3.12}$$

When U_0 and V_{TS} are in the same direction, downward airflow, the single-fibre efficiency for settling, E_{G} [63], is

$$E_{\mathrm{G}} \approx G(1+R) \tag{3.13}$$

For gas flow in the direction opposite to V_{TS},

$$E_{\mathrm{G}} \approx -G(1+R) \tag{3.14}$$

And E_{G} decreases overall single-fibre efficiency. When flow is horizontal, E_{G} is much less — of the order of G^2. Generally, E_{G} is small compared with other single-fibre mechanisms, unless the particle size is large and U_0 is low. When U_0 is greater than about 0.1 m/s, impaction is more important than settling. As the face velocity used in this filter sampling test was higher than 0.3 m/s, the effect of gravitational settling was not considered in the calculation of the filtration efficiency.

Assuming the individual mechanisms are independent and additive [66], and that impaction is not important, the single-fibre efficiency E_{Σ} is

$$E_{\Sigma} = E_{\mathrm{R}} + E_{\mathrm{D}} + E_{\mathrm{DR}} \tag{3.15}$$

The overall efficiency or the total efficiency of a filter [66], E, is a function of the single-fibre efficiency, E_Σ.

$$E = 1 - \exp\left[\frac{-4E_\Sigma \alpha L}{\pi d_\mathrm{f}\left(1-\alpha\right)}\right] \tag{3.16}$$

Where L represents the filter depth or thickness. Eq. 3.16 relates the total efficiency of a filter to the microscopic property of the single-fibre efficiency E_Σ. The filter penetration P – the fraction of entering particles that penetrate the filter is

$$P = 1 - E = \exp\left[\frac{-4E_\Sigma \alpha L}{\pi d_\mathrm{f}\left(1-\alpha\right)}\right] \tag{3.17}$$

Eq. 3.16 and Eq. 3.17 have been widely used by various researchers [67,69,71, 73-76] in analysing the total filtration efficiency. It has been reported by various researchers [65, 68-71] that an increase in particle size would cause increased filtration by the interception and inertial impaction mechanisms while a decrease in particle size would enhance collection by Brownian diffusion. So, in between there exists an overlapping region where no mechanisms dominate the filtration process. This is the region where the particle penetration through the filter is a maximum and the collection efficiency of the filter a minimum [69]. For a given fibrous filter, there is a particle size, usually between 0.05 and 0.5 μm, that has the minimum collection efficiency; that is, all particles, larger or smaller than this size, are collected with greater efficiency [63]. Fig. 3.4 shows that the minimum filter efficiency is generally known to occur in the vicinity of 0.3 μm, where is the diffusion and interception regime. It was shown by Stechkina et al. [68] that at moderate flow velocities $U_0 < 1$ m/s, the major role in this region is played by diffusion and interception. By comparing the theory with the experimental data, Lee and Liu [65] indicated that the main filtration mechanisms involved in the region of minimum efficiency are diffusion and interception, with the impaction mechanism playing only a minor role. Another reason for not taking the impaction effect into account is that Eq. 3.6 can only be used when R is smaller than 0.4. For the glass fibre filter tested here, according to Eq. 3.1, that corresponds to d_p smaller than 400nm due to the d_f of the filter being smaller than 1 μm [77], which does not cover the particle size range of 5-1000 nm tested in the experiments. Consequently, only interception (Eq. 3.2), diffusion (Eq. 3.9) and their interaction (Eq. 3.10) will be considered in the following calculation of the filtration mechanisms.

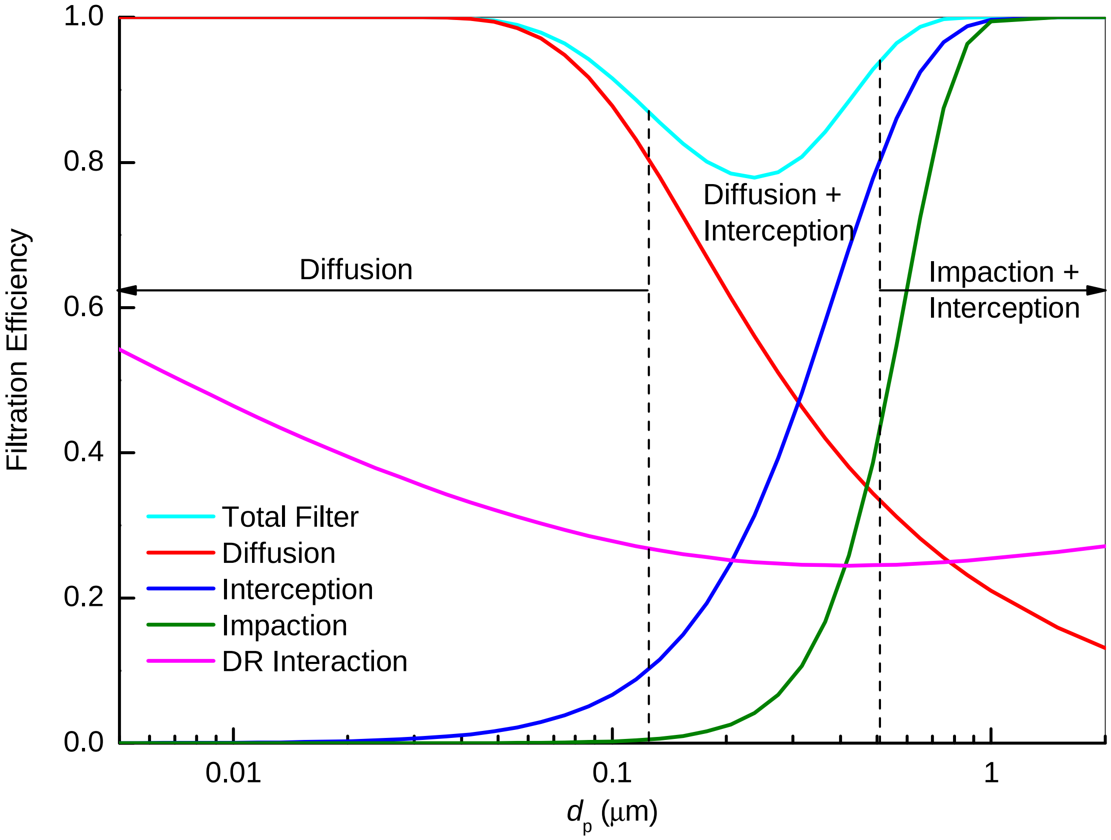

Fig. 3.4 An Example of filter efficiency vs. particle size illustrating the different filtration regimes; L = 750 μm, α = 0.1, d_f = 3 μm, U_0 = 0.1 m/s.

The above analysis is based on the collection of a particle by an individual fibre and only the most elementary parameters are considered. However, the shape of the particles (spherical or non-spherical), the shape of the fibres, the size distribution of the fibres, the particulates accumulated on the filter media *etc.* would have a marked effect on the total particle collection efficiency.

The single-fibre diffusion efficiencies for fibres with elliptical cross-sections were calculated by Regan and Raynor [75]. It is shown that elliptical fibres with the major axis of the cross-section parallel to the incoming flow would have advantages over circular fibres, with both a higher single-fibre diffusion efficiency and less drag than circular fibres. Glass-fibre filters comprising a binary mixture of two fibre sizes have been studied by Brown and Thorpe [78]. It was found that the pressure drop across a mixed-fibre filter is similar to that of a single component filter with the same packing fraction, and the penetration by both diffusion and interception decreases as the mean fibre size is reduced. The deposition of submicron particles on a model filter consisted of ultrafine fibres with a radius in the range of the mean free path of air molecules was studied by Kirsh [79]. It was shown that the radius of the most penetrating particles for these filters was higher than the fibre radius. The effect of heterogeneities in the filter structure on the filter performance was studied by Steffens and Coury [80]. A correction was proposed by defining the filter bed as composed of a number of filters in series, each with the fibre diameter and porosity derived from the fibre size distribution. The results showed a considerable improvement in the prediction of collection efficiency.

Although most filtration studies were carried out with spherical particles, many aerosol particles, e.g. exhaust particles, are agglomerates of small particles, which are non-spherical. A method for characterising non-spherical particles and determination of the interception equivalent diameter has been presented by Lange et al. [81]. The relationship between diffusion equivalent diameter and interception equivalent diameter was compared for both spheres and agglomerates. It was shown that with increasing particle diameter, the effect of interceptional deposition increased and the penetrations of spheres and agglomerates deviate. The interceptional deposition was more important for the agglomerates than for the spheres, which was increasingly the case for larger agglomerate sizes.

Filtration efficiency tests were conducted with silver NP agglomerates by Kim et al. [76]. And agglomerate filtration modelling in terms of diffusion, impaction and interception was investigated. It was found that the larger interception length of agglomerates is responsible for the smaller penetration through a fibrous filter in comparison to spherical particles with the same mobility diameters. The effect of aggregates' parameters, such as fractal dimension, primary particle radius, on the filtration efficiency was investigated theoretically using the modified Brownian dynamics method by Bałazy and Podgórski [73]. There was a noticeable discrepancy between the results determined by the Brownian dynamics approach and the classical single-fibre theory for the most penetrating particles. It was found that Peclet number based on the mobility radius and the interception parameter based on the outer radius were the proper criteria to describe diffusional and the deterministic deposition of aggregates. The morphology and packing density of particle deposits formed by accumulation on steel fibres were studied by Kasper et al. [82] using confocal microscopy. The experiments showed a systematic transition of deposit morphologies with the particle bounce parameter β = Stk/R. Compact, forward facing deposit structures dominated in the case of significant particle bounce (corresponding to higher β), while dendritic structures with pronounced sideways branching were formed at lower β.

By integrating the effect of thermal particle bounce into the classical filter efficiency theory, a model was developed by Wang and Kasper [83] to describe the filter behaviour in the thermal rebound dominated region for the particle size range from 10 nm down to molecules. It was suggested that the thermal impact velocity of a particle would exceed the critical sticking velocity in the size range between 1 and 10 nm, depending sensitively on elastic and surface adhesion parameters. Fibrous filter pressure drop and aerosol collection efficiency were measured in the viscous-inertial transition flow regime by Hubbard et al. [84]. It was shown that existing theories under predicted the measured single-fibre efficiencies. The assumption of uniform flow conditions for each successive layer of fibres was questionable so that the common exponential relationship between single-fibre efficiency and total filter efficiency may not be appropriate in this regime.

In this work, particle number concentrations were measured from both upstream and downstream of a glass fibre filter sampling the diluted exhaust gas from a GDI engine. The objective is to study the characteristic of the particulate emissions from the engine as well as measure the filtration efficiency of the filter. Moderate face velocity ($U_0 < 0.3$ m/s) was used in the filter sampling tests. Single fibre theory (as described above) has been adopted in the calculation of the filtration efficiency to compare with the experimental results.

3.3 Experimental Apparatus

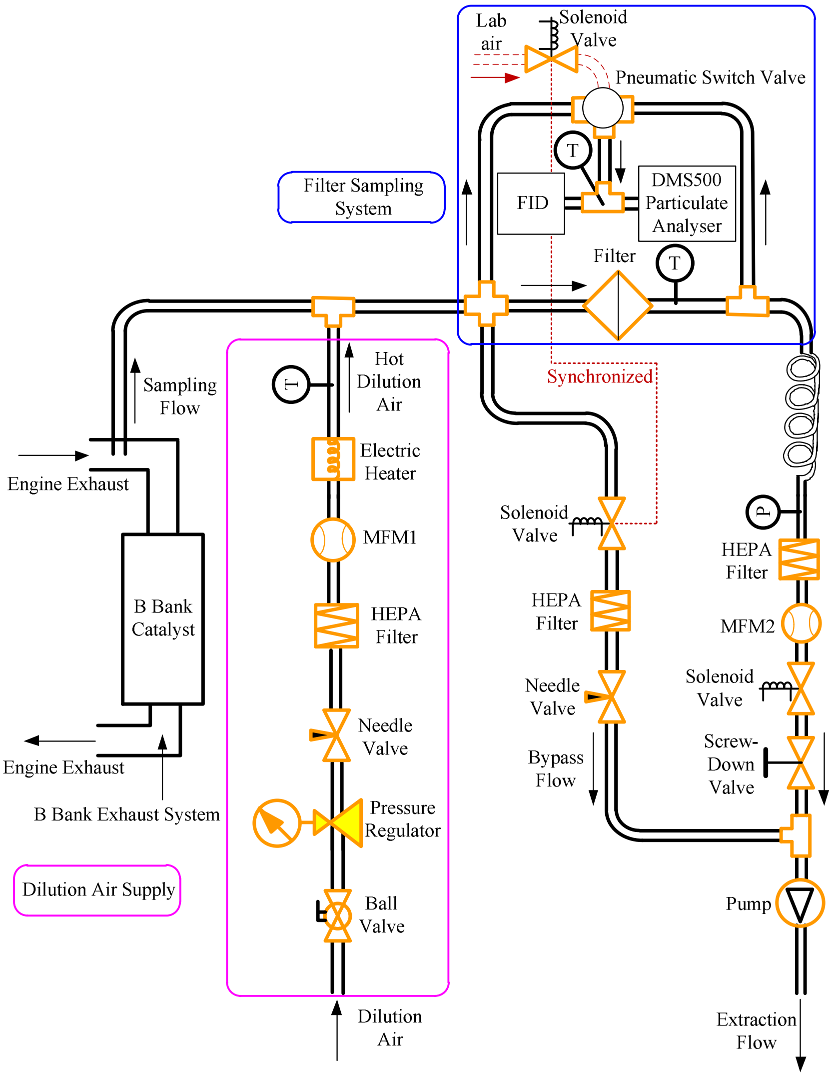

Fig. 3.5 Layout of the Filter Sampling System.

The engine was operated with stratified injection, so that a large portion of accumulation mode particles was generated. This operating point is an adaptation of a cold start operating point (refer to section 4.3) that was known to generate high levels of particulate matter. The engine operation conditions are listed in Table 3.1. Two types of filter (uncoated and fluorocarbon coated) were used in the experiments. The specifications for the filters are listed in Table 3.2. The gas temperature flowing through the glass fibre filter was kept at 47 °C during the particle sampling process by hot air dilution and a closed-loop control system. The particle mass accumulated on the filter was 3.3 mg for the Whatman® GF/A Glass Microfiber filter and 4.4 mg for the Pallflex® Fiberfilm filter. The Pallflex® filter is a borosilicate glass fibre filter with fluorocarbon (TFE) coating. A schematic of the filter sampling system is shown in Fig. 3.5.

The PM emissions pre-filter and post-filter were measured via a Cambustion DMS500 particle sizer, while the HC emissions were sampled by a FID. A pneumatic switching valve was used to select between pre-filter and post-filter. As the mass flow rate through the vacuum pump (MFM_{pump}) was kept constant, it can be seen that when the gas sampling was taken downstream of the filter, the mass flow rate through the filter (MFM_{filter}) would be increased compared to that when the gas sampling was taken upstream of the filter, due to additional gas extraction through the filter by the DMS and FID ($MFM_{DMS+FID}$). As a result, in order to keep the face velocity of the filter constant, a bypass system was added to the sampling system so a quantity of gas flow (corresponding to that taken by the measurement system) would bypass the filter when taking samples post-filter; see Fig. 3.5. A solenoid valve synchronized with the pneumatic switching valve was used to switch on the bypass loop when sampling downstream of the filter. The bypass loop was closed when sampling upstream of the filter. The sampling mass flow rate of the DMS and FID ($MFM_{DMS+FID}$) were measured by a mass flow meter. A needle valve was then fitted in the bypass loop to set the bypass mass flow rate (MFM_{bypass}) equal to that of the $MFM_{DMS+FID}$. Hot air dilution was used to achieve the required dilution ratio and the heater temperature was controlled to keep the filter temperature at 47 °C. The mass flow rate of dilution air (MFM_{air}) was measured with a mass flow meter and was controlled using a needle valve. The formulas used to calculate the mass flow rate through the filter and the dilution ratio (DR) are listed below.

DMS+FID taking sample pre-Filter:

$$MFM_{filter} = MFM_{pump} \tag{3.18}$$

DMS+FID taking sample post-Filter:

$$MFM_{filter} = MFM_{pump} + MFM_{DMS+FID} - MFM_{bypass} \tag{3.19}$$

The formula used to calculate the dilution ratio (DR) is as follows. The averaged dilution ratios were 8.4 and 6.3 for the Whatman® GF/A filter and Pallflex® filter tests, respectively. The results shown in the next section for the particulate and gaseous emissions have been corrected for the dilution ratio.

$$DR = (MFM_{pump} + MFM_{DMS+FID}) / (MFM_{pump} + MFM_{DMS+FID} - MFM_{air}) \tag{3.20}$$

Table 3.1 Engine Operation Conditions for Evaluation of Filters

Engine Speed / rpm	1000
Engine Torque / N·m	30
Ignition Timing	0 ºCA BTDC
Injection Pressure / MPa	4.0
Injection mode:	Split Injection
1st injection timing:	280 ºCA BTDC
2nd injection timing:	0 ºCA BTDC
2nd injection width / ms:	0.35
Relative AFR:	1.0
IVO:	34 ºCA ATDC
IVC:	244 ºCA ATDC
EVO:	244 ºCA BTDC
EVC:	6 ºCA ATDC
Coolant / ºC:	90

The pressure drop between the filter can be as high as 0.5 bar so that the gas pressure downstream of the filter can be lower than 0.5 bar absolute pressure. As a result, the dilution air of the DMS is drawn out of the heated sampling line by the vacuum pump when sampling downstream of the filter. The escaped dilution air is then drawn into the FID, leading to a zero reading for the HC emissions. Thus, during the tests, the dilution ratio of the DMS was set to 1 to avoid this effect, i.e. no dilution air was used by the DMS. Pre-filter sampling of 60 s by the DMS and FID took place at the start and towards the end of each test, individually. A long post-filter sampling took place between the two pre-filter samplings. During the data processing, the post-sampling data points were divided equally into 8 parts. Within each part of the data, the filter sampling parameters, particulate and gaseous emissions were analysed and the averaged results were calculated to show their variation with the sampling time, as shown in the following section.

Table 3.2 Specifications of the Filters

Description	Whatman® GF/A Glass Microfiber Filter	Pallflex® Fiberfilm Filter
Filter Media	Uncoated borosilicate glass fibre filter	borosilicate glass fibre filter with fluorocarbon (TFE) coating
Diameter / mm	47	47
Typical Thickness / µm	260	203
Typical Weight/ (mg)	93	65
Filter Temperature / °C	47	47
Face Velocity / (cm/s)	31.2	31.5

3.4 Measurement of the Filter Transmission Efficiency

Fig. 3.6 shows the averaged number weighted size distributions measured upstream and downstream of the glass fibre filters at the different sampling times. Two types of filters have been tested. The first was an uncoated glass fibre filter from Whatman® (Fig. 3.6(a)) and the second one was a fluorocarbon (TFE) coated glass fibre filter from PALL Life Sciences (Fig. 3.6(b)); the sampling time for the filters was 25 min. During each filter sampling process, the sampling point of the DMS and FID was switched between pre and post the filter. The pre-filter spectra both at the start and at the end of sampling show a large portion of accumulation mode particles and the peak of the spectra are around 200 nm, which is typical for combustion with stratified injection. When the DMS was switched to sampling the gas downstream of the filter, there was a marked reduction in the number concentrations at each particle size. The number concentration for the small size particles diminished to near zero, so nucleation mode particles did not penetrate the filters. However, when sampling post-filter, there was still a peak in the spectrum at around 200 nm.

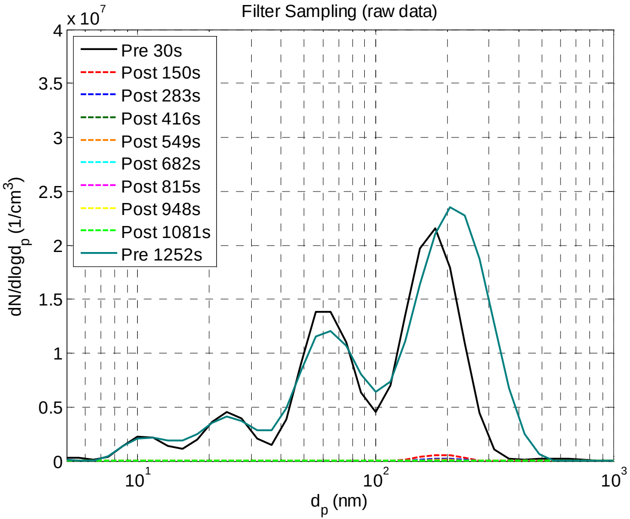

(a) Whatman® GF/A Glass Microfiber Filter

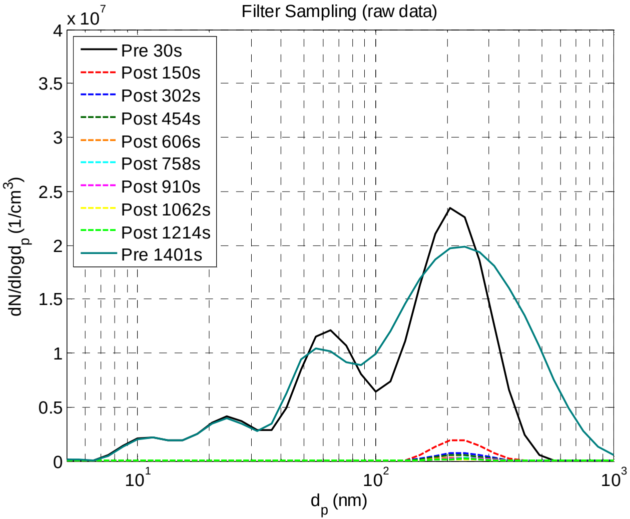

(b) Pallflex® Fiberfilm Filter

Fig. 3.6 PM number weighted size distributions (raw spectra) Pre and Post filter at the different sampling times for an uncoated (a) and a coated (b) filter

Fig. 3.7 shows the log-log plot of the number weighted size distributions, where the post-filter spectra are shown more clearly. It can be seen from the post-filter spectra that the noise at the low end of the particle size range (< 50 nm) for the Whatman® filter (Fig. 3.7(a)) is higher than that of the Pallflex® filter (Fig. 3.7(b)), while the noise at the high end of the particle size range (> 500 nm) for the Whatman® filter is lower than that for the Pallflex® filter. The peak of the post-filter spectrum lowered gradually with the increase in the sampling time. This indicates that the collection efficiencies of filters increased as the sampling gas was filtered for an extended period of time, suggesting that the particulate matter accumulated on the filters had marked effect on their filtration efficiencies. Also, the peaks of the post-filter spectrum for the Pallflex® filter are higher than those for the Whatman® filter.

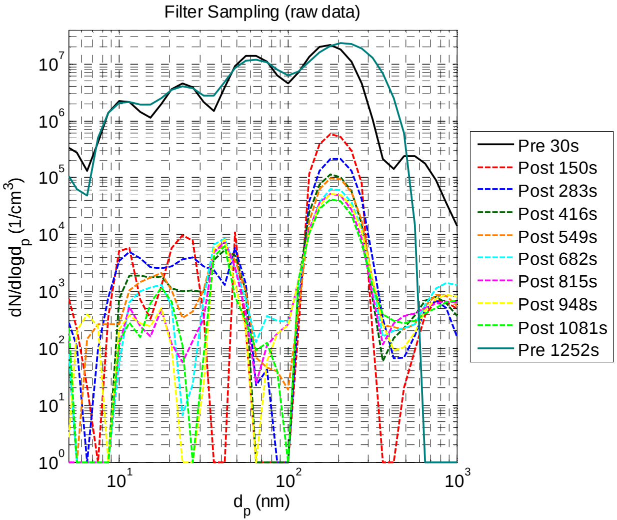

(a) Whatman® GF/A Glass Microfiber Filter

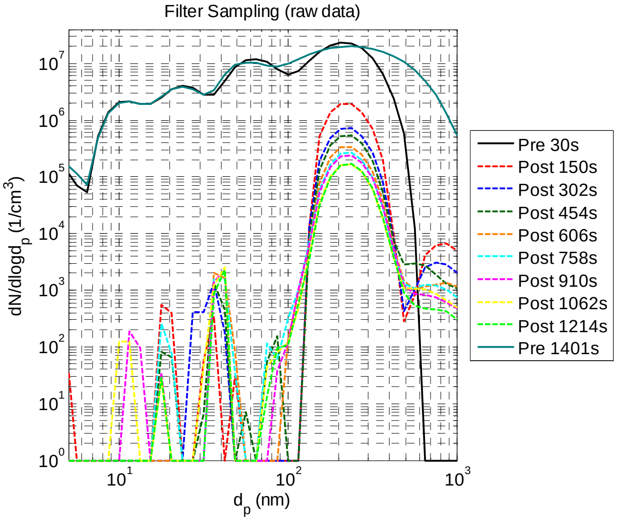

(b) Pallflex® Fiberfilm Filter

Fig. 3.7 PM number weighted size distributions (raw spectra) Pre and Post filter at the different sampling times

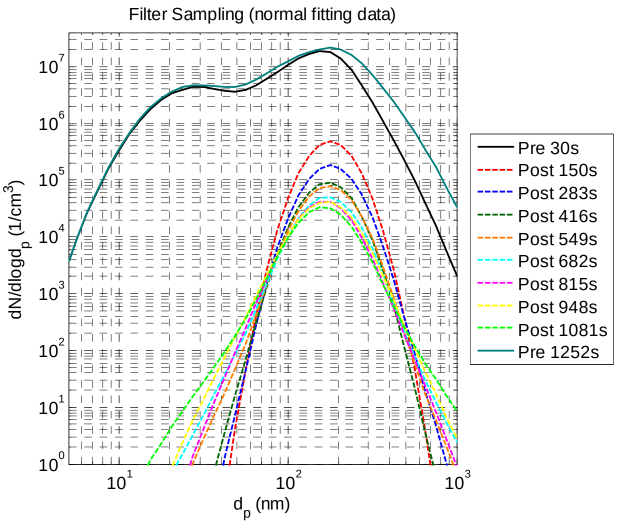

(a) Whatman® GF/A Glass Microfiber Filter

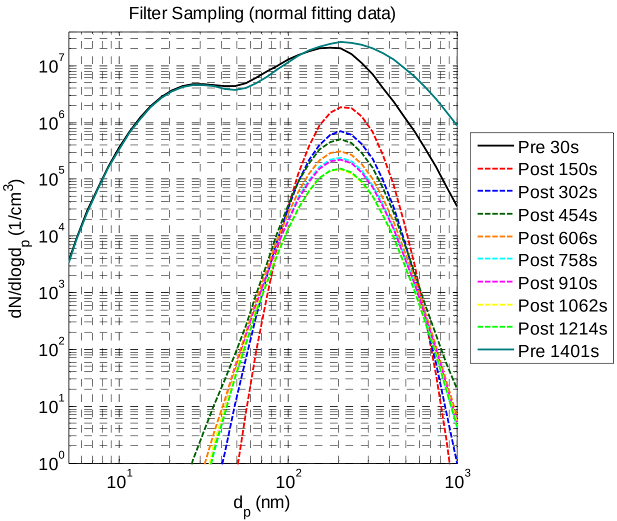

(b) Pallflex® Fiberfilm Filter

Fig. 3.8 PM number weighted size distributions (raw spectra) Pre and Post filter at the different sampling times

Fig. 3.8 shows the number weighted size distributions after applying a bi-lognormal fitting to the raw spectra, which are presented using log-log plots. It can be seen that the lognormal fitting spectra are smoother than the raw spectra, and that the signal noise has been diminished a lot with the lognormal data, while the trends are similar when compared to those of the raw spectra. Also, it can be seen that only accumulation mode particles are presented in the curves of the post-filter spectra, and the nucleation mode particles have been collected by the filter. The particle number concentrations at the high end of the particle size range for the Pallflex® filter are higher than those for the Whatman® filter in the lognormal spectra, which may due to the higher noise level at the large end of the particle size range when sampling with the Pallflex® filter.

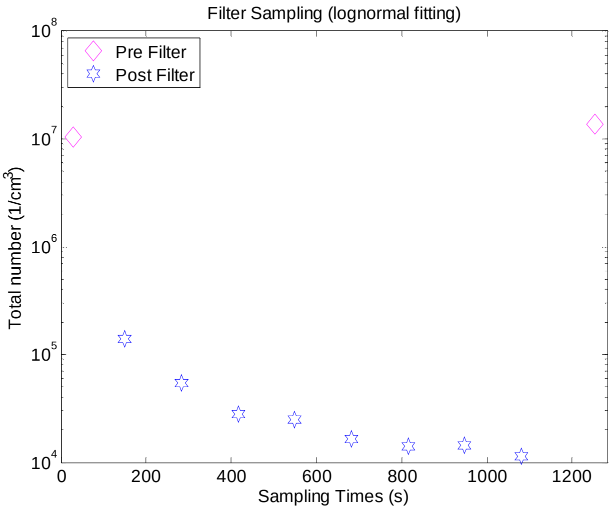

(a) Whatman® GF/A Glass Microfiber Filter

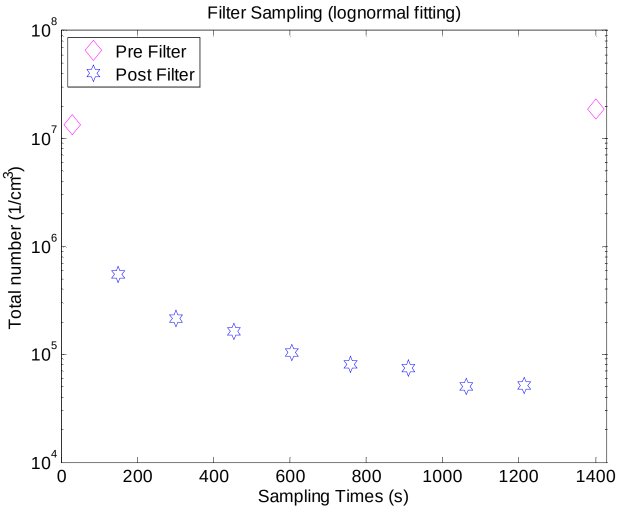

(b) Pallflex® Fiberfilm Filter

Fig. 3.9 Total PM number (applying bi-lognormal fitting to the raw data) Pre and Post filter at the different sampling times

Shown in Fig. 3.9 is the total particle number integrated from the lognormal fitting data for the two filters at the different sampling times. It can be seen that when sampling post-filter, there is a marked reduction in particle number compared to that of pre-filter sampling. Fig. 3.10 shows the total particle mass calculated from the lognormal spectra. It can be seen that the pre-filter total particulate number emissions are similar for both filters; while the pre-filter total particulate mass emissions of the Pallflex® filter is higher than that of the

Whatman® filter. This results from higher particle number concentrations at the large end of the particle size range in the DMS spectrum when the Pallflex® filter was being tested (Fig. 3.7(b)). As large particles contribute much more than small particles to the total particulate mass, so the particulate mass emissions when the Pallflex® filter was being tested were much higher than that when the Whatman® filter was being tested. Both the particle number and particle mass emissions were higher when the Pallflex® filter was being tested.

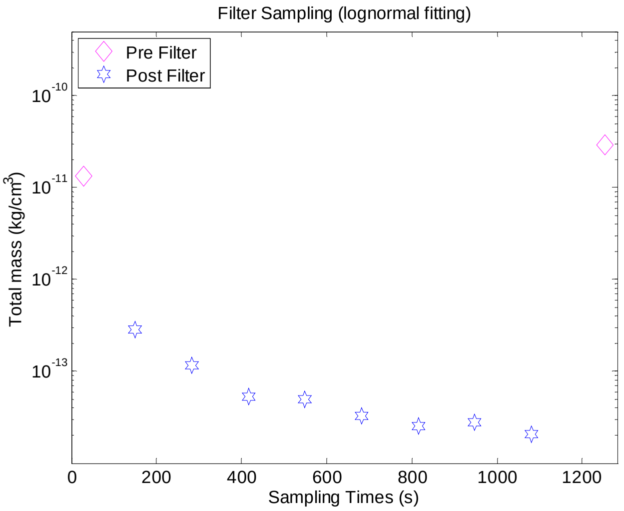

(a) Whatman® GF/A Glass Microfiber Filter

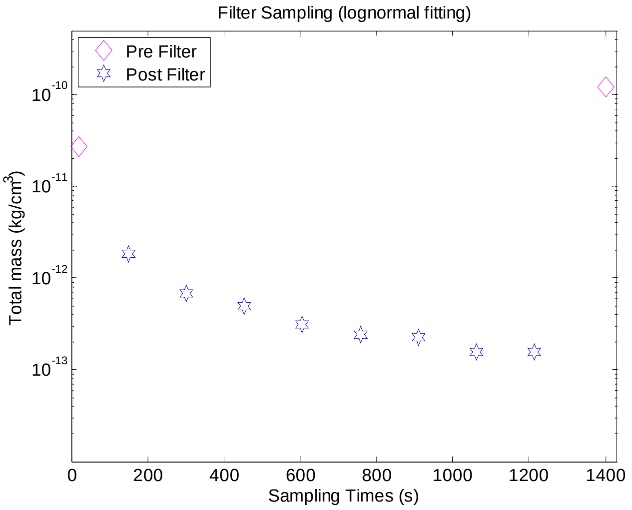

(b) Pallflex® Fiberfilm Filter

Fig. 3.10 Total PM mass (applying bi-lognormal fitting to the raw data) Pre and Post filter at different sampling times

Data after normal fitting for both filters are used in Fig. 3.11, where the total number concentration of nucleation mode and accumulation mode for both pre- and post-filter are plotted separately. From the comparison of particle emissions in the nucleation and accumulation modes, with the sampling gas passing through the filter, the total number in the nucleation mode reduced more significantly than the total number in the accumulation mode. The total number in the accumulation mode on testing the Pallflex® filter is higher than that on testing the Whatman® filter.

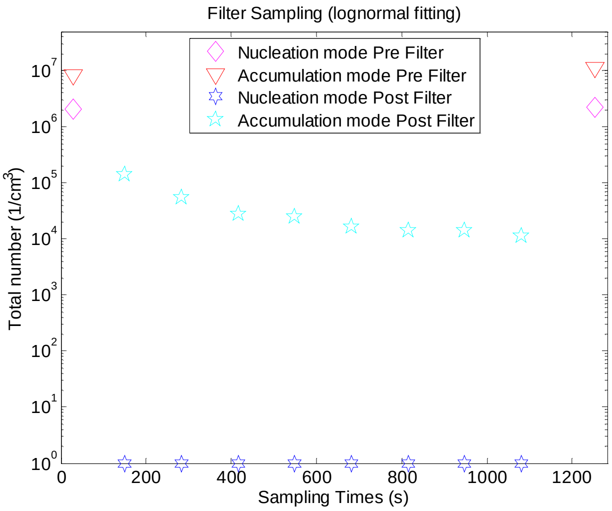

(a) Whatman® GF/A Glass Microfiber Filter

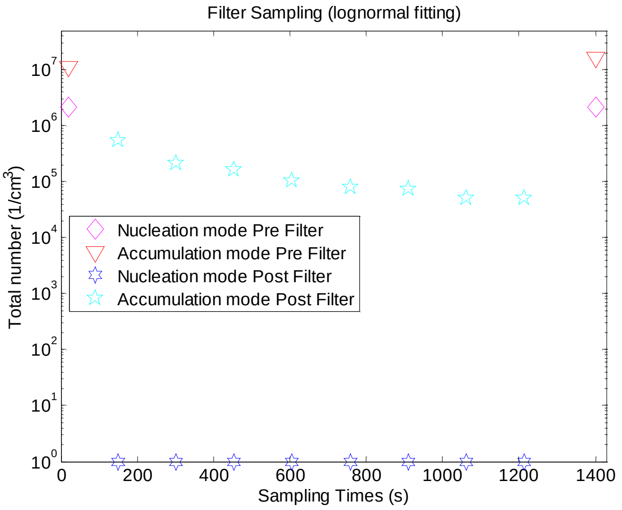

(b) Pallflex® Fiberfilm Filter

Fig. 3.11 Total PM number for different modes Pre and Post filter at the different sampling times

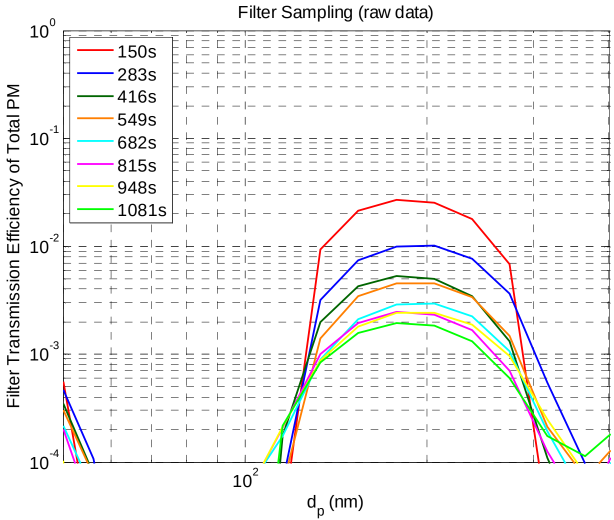

(a) Whatman® GF/A Glass Microfiber Filter

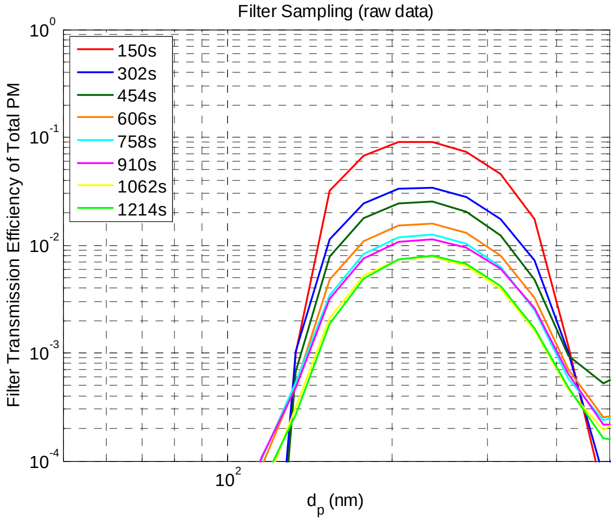

(b) Pallflex® Fiberfilm Filter

Fig. 3.12 Number transmission efficiencies versus d_p *calculated from raw data at the different sampling times.*

The number transmission efficiencies calculated from the raw data for both filters are shown in Fig. 3.12, which is calculated using the post-filter number concentration divided by pre-filter number concentration at particle sizes from 5 nm to 1000 nm. The variation of the number transmission efficiencies with the sampling times are shown in the figures. It can be seen that the transmission efficiencies for particles smaller than 100 nm are close to zero. The peaks of the transmission efficiencies for both of the filters at the different sampling times are located around 200 nm. The diameter corresponding to the maximum transmission efficiency, i.e. the most penetrating particle diameter, is larger for the Pallflex® filter than that for the

Whatman® filter. With the increase of sampling time, the peak values of the transmission efficiencies decrease from 0.03 to 0.002 for the Whatman® filter and from 0.09 to 0.008 for the Pallflex® filter. It can be seen that the Whatman® filter shows a higher collection efficiency than the Pallflex® filter. The number transmission efficiencies calculated with lognormal fitting data for both filters are shown in Fig. 3.13. These curves are smoother compared to those shown in Fig. 3.12 and show similar trends to the results calculated with raw data.

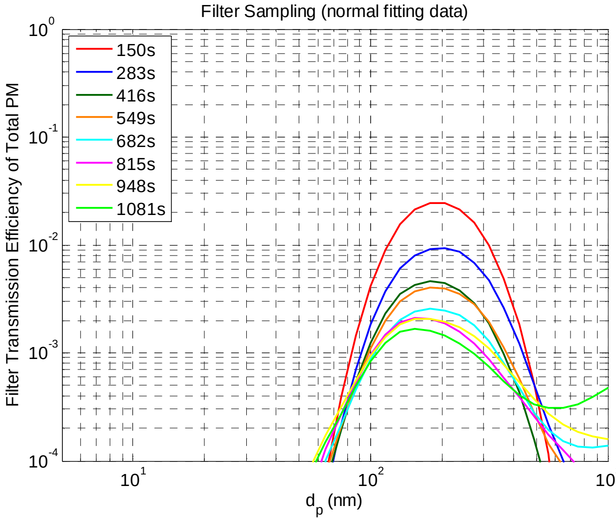

(a) Whatman® GF/A Glass Microfiber Filter

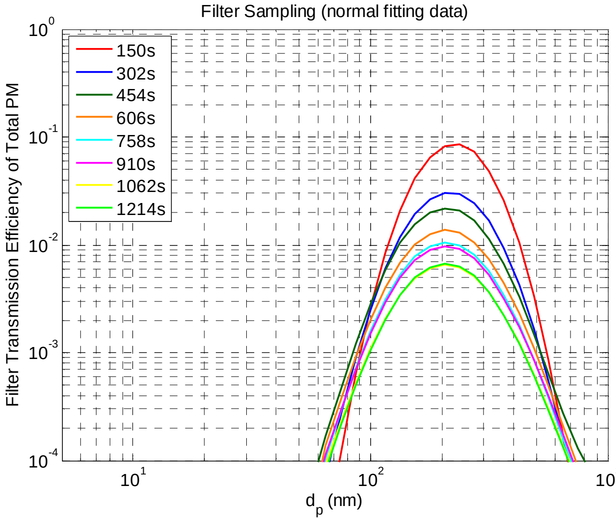

(b) Pallflex® Fiberfilm Filter

Fig. 3.13 Number transmission efficiencies versus d_p *calculated from lognormal fitting data at the different sampling times*

Fig. 3.14 shows the HC emissions pre-filter and post-filter at the different sampling times. It can be seen that the pre-filter HC emissions are nearly unchanged at around 1100 ppm for both filters. Higher fluctuations of the post-filter HC emissions are shown with the Whatman® filter compared to that with the Pallflex® filter. Generally, the post-filter HC emissions were lower than the pre-filter emissions in both of the sampling tests.

The nucleation mode particles can be converted to a mass concentration, and this in turn can be converted to a volume concentration of hydrocarbons (as ppm of CH_2). Fig. 3.15 shows that the conversion of the nucleation mode particle concentration to a hydrocarbon emission leads to negligible equivalent CH_2 emissions (much less than 1 ppm).

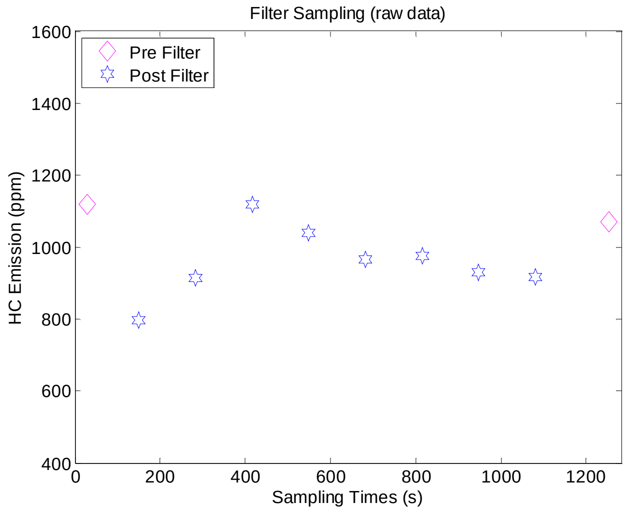

(a) Whatman® GF/A Glass Microfiber Filter

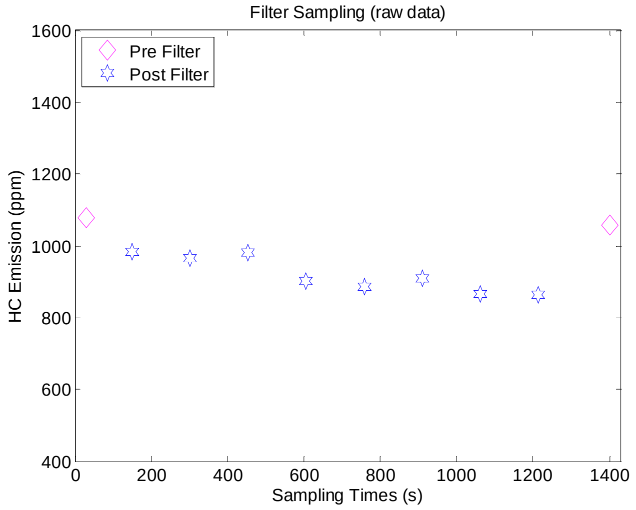

(b) Pallflex® Fiberfilm Filter

Fig. 3.14 HC emissions Pre and Post filter at the different sampling times

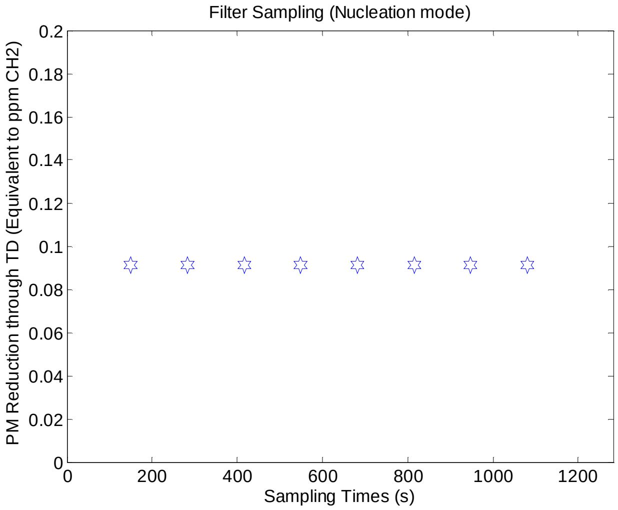

(a) Whatman® GF/A Glass Microfiber Filter

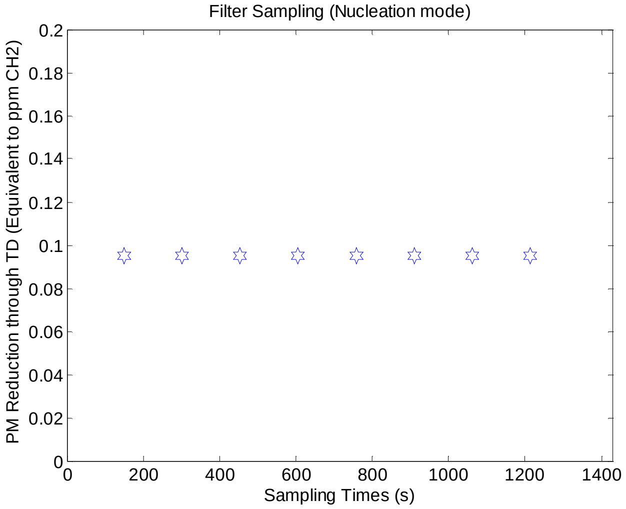

(b) Pallflex® Fiberfilm Filter

Fig. 3.15 Conversion of the nucleation mode particle concentration to an equivalent hydrocarbon concentration (assuming a generic hydrocarbon of C_xH_{2x}) at the different sampling times

The total particle mass (Fig. 3.10) between pre- and post-filter can be used to calculate the rate of mass accumulation on the filters. By averaging the rates at various sampling times, the mean rate of mass accumulation on the filters can be calculated using the mean pre-filter mass concentration minus the mean post-filter mass concentration, which multiplying by the sampling time equals to the particulate mass accumulated on the paper filter. Using this method, the mass of particulate material on each of the filters is 1.6 and 7.4 mg, respectively, which are in broad agreement with the results from the electronic balance (3.3 and 4.4 mg).

The calculated value for the particulate mass of the Pallflex® filter is much larger than that of the Whatman® filter, while the difference between the measured values of the two filters is relatively small. This is also due to the particle number concentrations of large particles from the DMS measurements being larger for the Pallflex® filter test than that of the Whatman® filter test.

Fig. 3.16 shows the gas pressure measured downstream of the filter, as the pressure upstream of the filter was kept close to atmospheric pressure. It can be seen that the pressure decreased steadily as the sampling time increased. This indicates that the particulate material accumulated on the filter would lead to a marked rise in the pressure drop across the filter.

To further understand the existence of the peak in the transmission efficiencies or the filter penetration shown in Fig. 3.12, the calculation of the filter efficiencies was carried out based on the theoretical analysis of the filtration mechanisms in section 3.2. The calculation results can then be qualitatively compared with the experimental results. Table 3.3 shows the main parameters used to calculate the collection efficiency of the Whatman® filter. Fibrous filters normally have high porosity, of which the solidity can be from < 0.01 to 0.3 so that the solidity used in the calculation is set to be 0.1. As the Whatman® GF/C glass fibre filters consist of a thick layer (260 μm) of borosilicate glass fibres of < 1 μm diameter, the fibre diameter is set to 1 μm for a simplification.

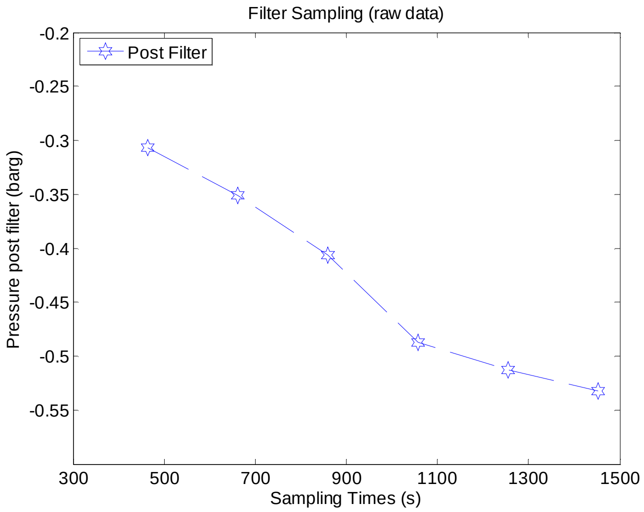

Fig. 3.16 Gas pressure post-filter of at the different sampling times (Whatman® GF/A Glass Microfiber filter).

Table 3.3 Main Parameter for Calculating the Filter Efficiency

Solidity (α)	0.1
Filter Thickness (L) / µm	260
Gas Temperature (T) / °C	47
Face Velocity (U_0) / (cm/s)	31.2
Fibre Diameter (d_f) / µm	1
Particle Diameter (d_p) / nm	5-1000
Particle Density (ρ_p) / (g/cm^3)	1

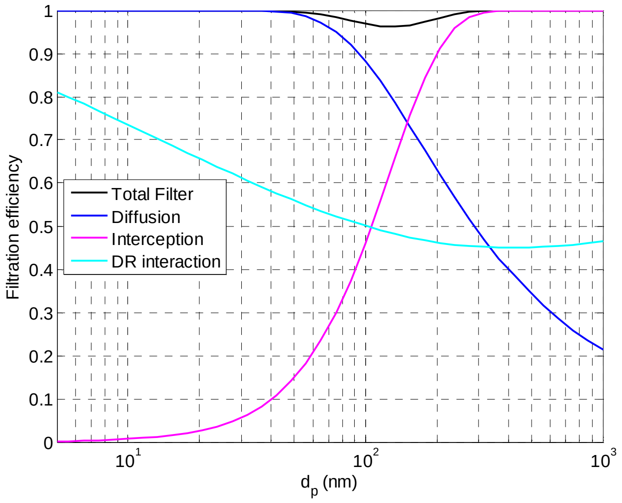

Fig. 3.17 Calculated filter efficiency for individual single-fibre mechanisms and total efficiency (Eq. 3.16), DR interaction: interaction term for enhanced collection due to interception of the diffusing particles (Eq. 3.10).

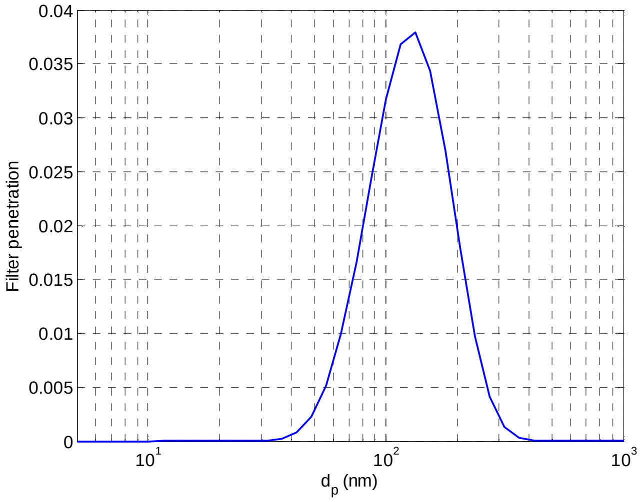

Fig. 3.18 Calculated penetration of the filter (Eq. 3.17).

Fig. 3.17 gives a semi-quantitative calculation of the filter efficiency for interception (Eq. 3.2), diffusion (Eq. 3.9), the interaction term (Eq. 3.10) and the total efficiency (Eq. 3.15 and Eq. 3.16). It can be seen that the diffusion mechanism dominates in the small particle size range and the interception is dominant in the large size range. When the d_p is between 100 and 200 nm, the diffusion efficiency decreases with an increase in the interception efficiency. The minimum efficiency is located in this particle size range, which is the diffusion and interception regime. Fig. 3.18 shows the penetration fraction of the filter (Eq. 3.17) which is equal to 1 minus the filter efficiency. It can be seen that the maximum filter penetration is about 0.038 and the corresponding particle diameter is about 130 nm. The most penetrating particle size of 130 nm is smaller than that measured by the DMS (Fig. 3.12(a)). This is because: firstly, the particulate emissions of the engine are agglomerates and are non-spherical, which was not taken into account in the calculation; secondly, the diameter measured by the DMS is the electrical mobility equivalent diameter [62] which could be different from the diameter of an equivalent spherical particle. However, the calculated results can give a theoretical explanation to the presence of the peak in the experimentally acquired transmission efficiencies of the filter.

3.5 Summary

Particulate emissions from a GDI engine operating with stratified injection were measured with two types of glass fibre filter and their filtration efficiencies were characterized using a DMS500.

(1) High concentrations of particulate emissions in the accumulation mode were observed upstream of the filter, which was typical for this engine operating conditions. The peak of the post-filter particle number concentration is more than an order of magnitude lower than that of the pre-filter particle number concentration. The peak for the greatest penetration of particles was located around 200 nm for both types of filter. Meanwhile, the number concentrations of the nucleation mode particles are close to the noise level of the DMS after the filters.

(2) As the sampling time increased, the transmission efficiency, i.e. the penetration of a filter, decreased gradually for each of the filters, which can be lowered by more than an order of magnitude over the sampling period of 25 minutes. As a result, the particulate number and mass concentrations post-filter decreased with the increase of sampling time. A calculation of the filter efficiency using an individual single-fibre mechanism and the total efficiency has given a theoretical explanation for the penetration of the filter. It has been found that the greatest penetration of the filter was located in the regime where neither diffusion nor interception is dominant in the filtration process.

(3) The particulate material accumulated on the filter led to a rise in the pressure drop across the filter, which increased steadily as the sampling time increased.

(4) The hydrocarbon emissions pre-filter were unchanged when measured at the

beginning and at the end of the sampling process for both of the filters. Moderate fluctuations were observed in the post-filter HC emissions which were generally lower than the pre-filter HC emissions. Conversion of the nucleation mode particle mass concentration to a hydrocarbon emission leads to negligible equivalent CH_2 emission.

Chapter 4. The Effects of Fuel Injection Timing and Valve Timing on PM Emissions from a GDI Engine during Engine Warm-Up Conditions

4.1 Introduction

From recent research, it can be seen that a large portion of particulate emissions from GDI engines are generated during the first 200 seconds in the NEDC cycle [26,27]. Fig. 4.1 shows that the coolant temperature of a GDI engine during 0 to 200 seconds in the NEDC cycle was quite low, lower than 60 °C. In order to further reduce the particulate emissions from a GDI engine, it is of interest to investigate the particle formation during engine warm-up or cold engine operation conditions.

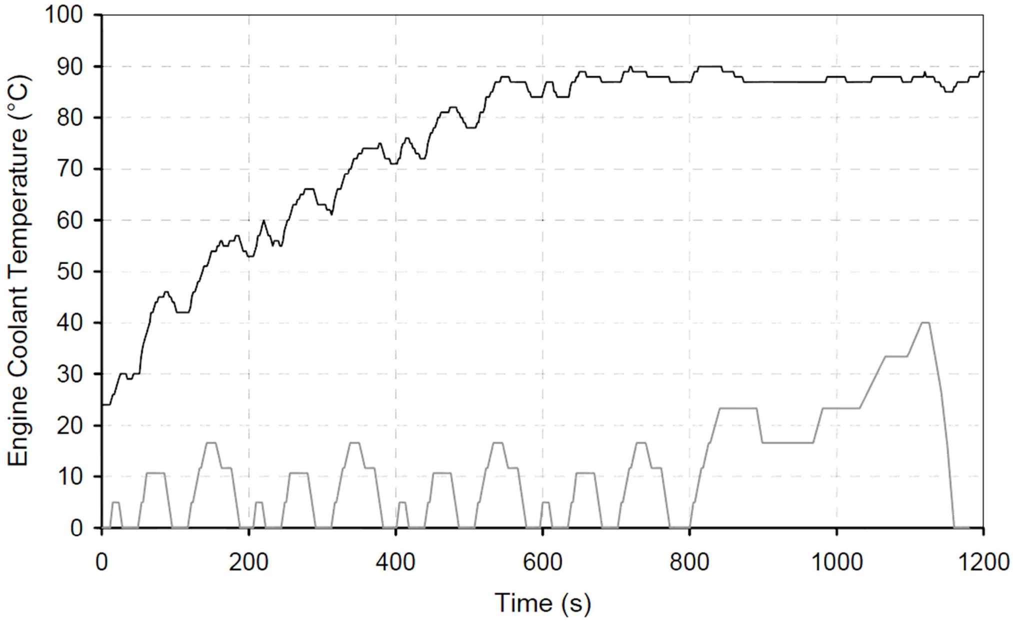

Fig. 4.1 Engine coolant temperature over a NEDC cycle. (adapted from [27])

Catalyst light-off is accelerated by operating the engine with very retarded ignition timing, so that although the engine is essentially idling (no net power output), the inlet manifold pressure can be very high (0.5 bar or higher). The strategy is described in detail by Chen et al. [85], with additional detailed measurements reported by Twiney et al. [86,87]. The engine operating regime is specified in Table 4.1, with Fig. 4.2 showing an example of the pressure traces from an extreme operating point that has been selected to include misfiring cycles.

Table 4.1 An operating regime for the Jaguar AJ133 engine during catalyst light-off [6]

Engine Speed	1350 rpm	Manifold Pressure	0.77 bar
Start of 1st Injection	610 °ABDC	End of 2nd Injection	180-200 °ABDC
Ignition Timing	188 °ABDC	Lambda	1.05
Inlet Valve Opening	574 °ABDC	Inlet Valve Closing	62 °ABDC
Exhaust Valve Opening	340 °ABDC	Exhaust Valve Closing	590 °ABDC

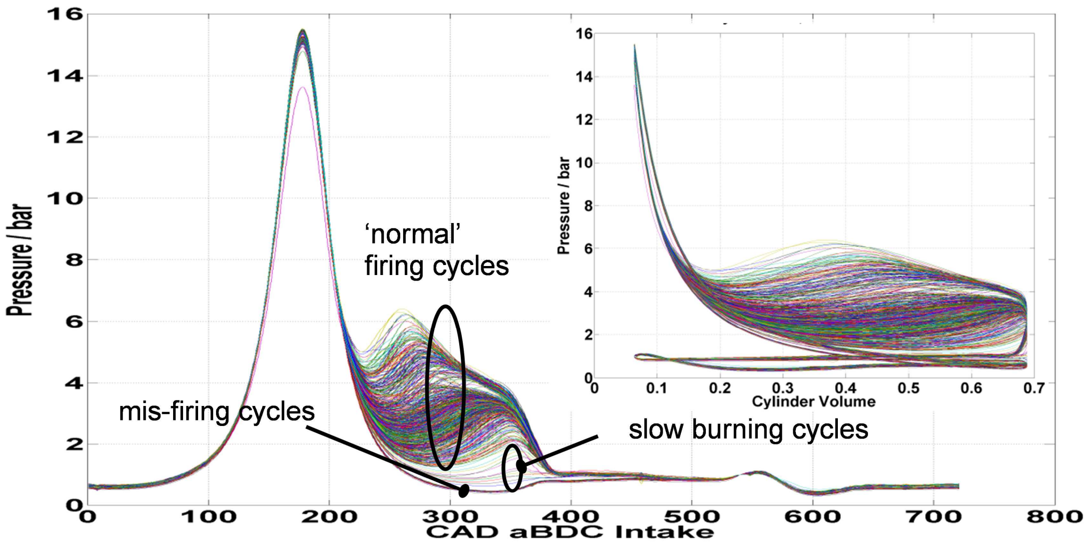

Fig. 4.2 Pressure records for the Jaguar AJ133 engine during catalyst light-off, as specified in Table 4.1. Note that the expansion pressure is lower than the compression pressure until the pressure has fallen to about 6 bar. The end of the second injection was 194 °ABDC, so as to generate misfiring cycles. [6]

The majority of the fuel is injected during the induction stroke so as to provide an overall homogeneous background mixture, and the second injection provides a locally rich mixture in the region of the spark plug at the time of ignition. The overall mixture is weak ($\lambda = 1.05$) so as to reduce CO and HC emissions. With the exhaust valve opening at 340 °ABDC, then Fig. 4.2 clearly shows that combustion is continuing, but by 380 °ABDC the pressure in the exhaust stroke is essentially 1 bar. A single misfiring cycle would lead to unacceptable levels of HC emissions, but the HC emissions from the slow burning cycles are essentially no different from those of the ‘normal’ cycles.

Fig. 4.3 shows the second injection (fuel pressure of 150 bar), with 4 fuel plumes pointing downwards and 2 plumes closer to horizontal that pass either side of the spark plug; the fuel arrives at the spark plug about 1°ca after the end of injection. If injection is too late (relative to the spark), then there is no enrichment, while if the injection is too early, then the mixture at the spark plug can be too rich. The fuel plumes also induce an air flow, and this leads to stretching of the arc and an increase in the arc voltage.

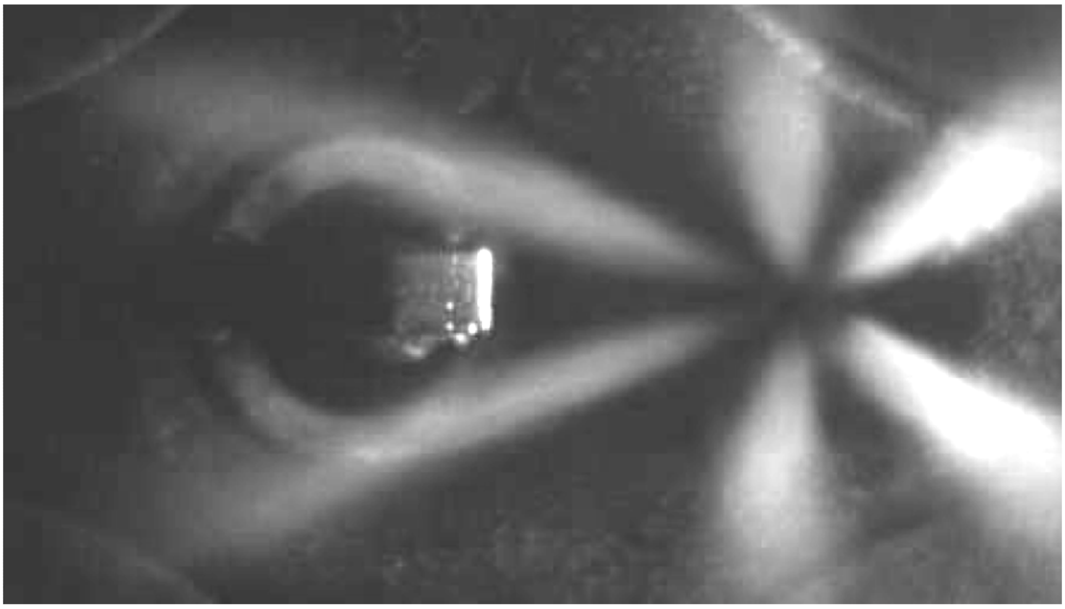

Fig. 4.3 The second injection in the Jaguar AJ133 engine catalyst light-off mode, with the fuel plumes illuminated from the right; note that the central plane of the fuel jets is below the spark plug gap. Combustion can be seen as the ‘bright spots’ immediately adjacent to the earth electrode of the spark plug. [6]

Injection parameters have been shown to have significant impact on particulate matter (PM) emissions. Various valve timings and different injection modes such as double injection with a second injection after compression, single early injection and split early injection were implemented to investigate the PM emissions and combustion characteristics of a GDI engine.

4.2 Experimental Apparatus and Test Method

The tests were performed on the V8 engine, with the DMS500 used to measure particulate emissions and a FID to measure HC emissions. The engine test bench and the instruments have been described in Chapter 2. The engine calibration parameters were recorded for 60 seconds by the INCA software at each operation point. The in-cylinder pressure signal was recorded for 300 cycles, based on which the indicated work and the rate of heat release were calculated.

It has been reported previously that the Three-Way Catalyst (TWC) showed a noticeable reduction effect on volatile particles [49]. Fig. 4.4 shows the ratio between pre- and post-catalyst PM number concentrations plotted using a double-log scale with respect to the particle size. It can be seen that the catalyst exhibited a notable reduction effect on nucleation mode particles (smaller than 50 nm) whilst there was little effect on accumulation mode particles (50 – 200 nm). The trends at large sizes (larger than 200 nm) are unclear, presumably because the absolute PM number concentrations measured by the DMS500 were so low that no clear trends can be found.

In order to separate the effect of the TWC on PM emissions and to investigate the effects of various injection and valve timing parameters on the engine-out particulate emissions, the exhaust Pre-TWC was drawn into the DMS and FID. The DMS sampling line was maintained at 80°C, and internally controlled dilution air was preheated before being mixed with the sample at entry to the sampling line. Before entry to the DMS sampling line, the pipework was maintained at above 80°C.

The tests results are divided into two parts. In the first part, the effects of various fuel injection parameters on particulate emissions are presented. In the second part, the effects of valve timings on particulate emissions are illustrated. During the cold engine operation tests, the engine coolant temperature was kept at an inlet temperature of 20 °C.

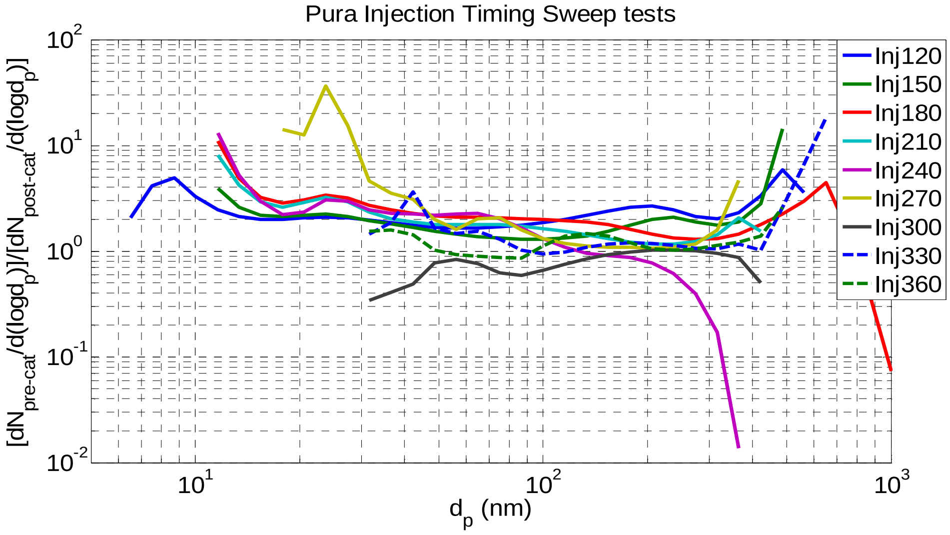

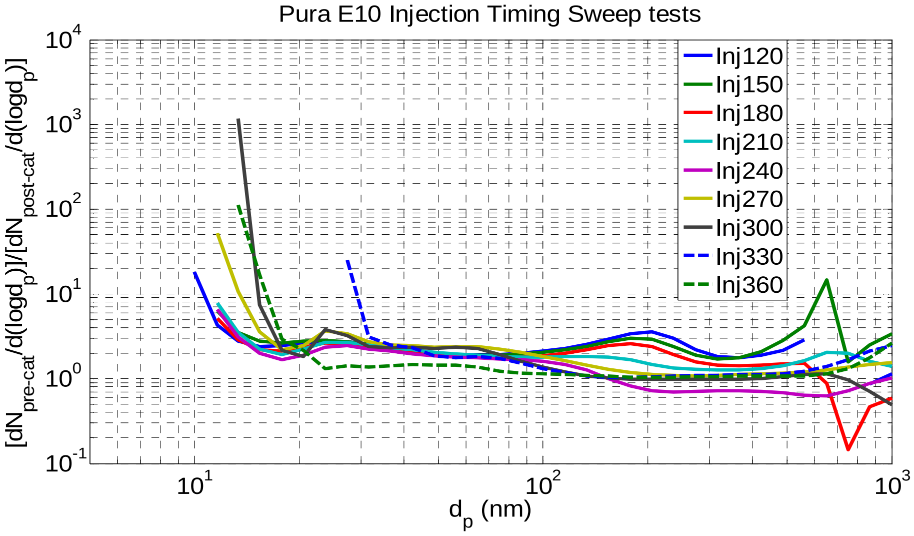

Fig. 4.4 The PM ratios between pre- and post-catalyst samples at different injection timings with PURA (above) and PURA E10 (below). (adapted from [49])

4.3 Results and Discussion

4.3.1 Effects of the Fuel Injection on PM Emissions

Test 1 – Comparison of Double Injection with Compression Injection and Single Intake Injection

Double injection with injection after compression is a common strategy used in GDI engines to facilitate catalyst light-off. Compared with single intake injection, double injection shows lower HC emissions, higher exhaust temperatures and a lower standard deviation of the IMEP. It is of interest to investigate the particle number emissions under these operating conditions. The first test was conducted to compare the particulate emissions under double injection and single injection and the main operation parameters are listed in Table 4.2. During double injection operation, the start of the first injection (main injection) was swept from 100° to 320° BTDC. The second injection was placed around the compression TDC, the injection duration of which was much smaller than that of the first injection. The end of the second injection was set to 7° ATDC. During single injection operation, the injection timing was swept between 220°-320° BTDC.

Fig. 4.5 shows the total P_n, nucleation mode P_n, accumulation mode P_n and accumulation mode P_n after a digital filter (Eq. 2.2) at different first injection timings under double injection and single injection modes. Recent tests [26,27] have shown that the accumulation mode particle number taken from the DMS gives good agreement with the PMP counting system for the particle number measurements. So the accumulation mode particle number calculated from DMS data is of particular interest. It can be seen that, under double injection operations (Fig. 4.5(a)), the lowest value of the accumulation mode P_n is achieved at SOI1 of 280° BTDC. Both retarding and advancing the start of the first injection would lead to an increase in the P_n emissions. At late first injection timings (100° to 140° BTDC), the particulate emissions in the accumulation mode increased significantly compared to that with a SOI1 of 280° BTDC. There is less variation of the P_n in the nucleation mode compared to that in the accumulation mode across the whole injection timing range. Under single injection operation without injection after compression (Fig. 4.5(b)), it can be seen that the particulate number emissions are approximately 2 orders of magnitude lower than those under double injection operation. At the very early injection timing (SOI1 320° BTDC), the particulate number emissions increased significantly. This may be because that advancing the injection towards the intake TDC led to larger amount of injected fuel impinging on the top of the piston, which led to pool fires that increased the tendency to form PM.

Table 4.2 Main tests parameters for Test 1

Injection Mode:	Double	Single
Start of 1st Injection (SOI1):	100°-320° BTDC	220°-320° BTDC
1st Injection Width / ms	Adjusted by the engine management system to maintain stoichiometric operation	
End of 2nd Injection (EOI2):	-7° BTDC	\
2nd Injection Width / ms	0.38	\
Injection Pressure / MPa	15	
Engine Speed / rpm	1200	
Engine Torque / N·m	90	
Spark Timing:	-2° BTDC	
Relative AFR:	1.0	
IVO:	34° ATDC	
IVC:	244° ATDC	
EVO:	224° BTDC	
EVC:	26° ATDC	
Coolant / °C:	20	

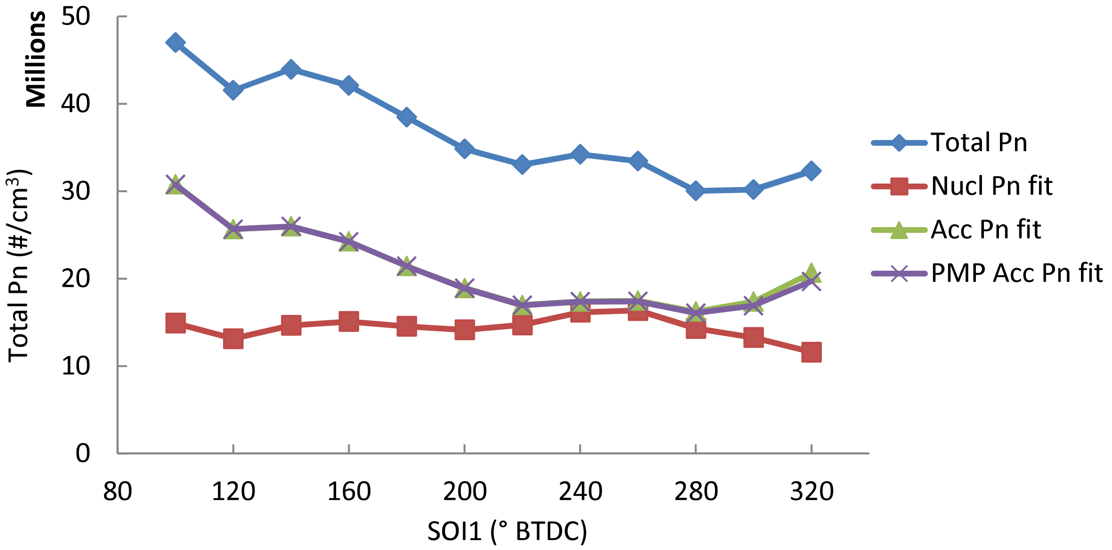

(a) Double injection

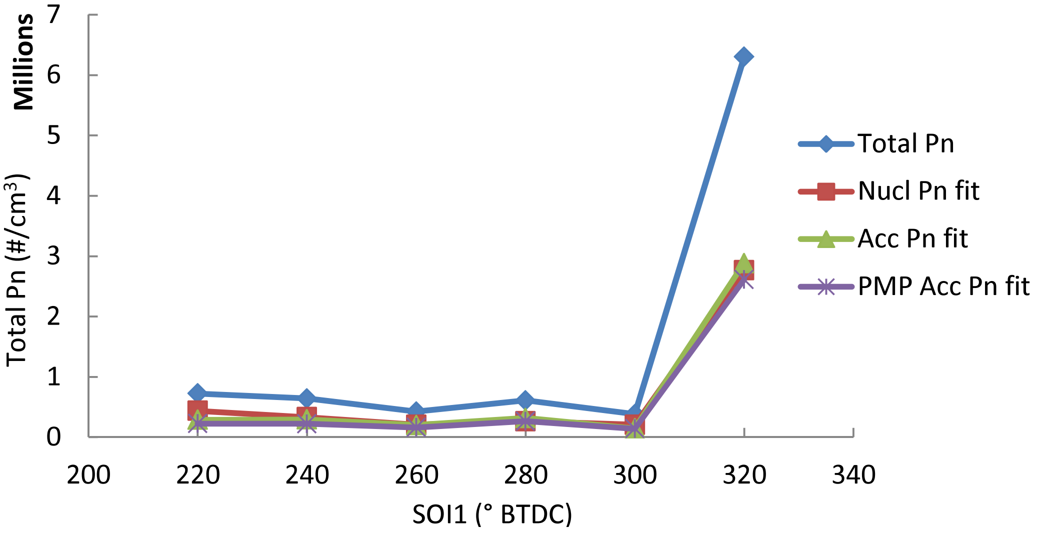

(b) Single injection

Fig. 4.5 Total particle number concentrations at different injection timings with different injection mode (Refer to Table 4.2). SOI1: Start of the first injection, Total Pn: Total particle number, Nucl Pn fit: Particle number in the nucleation mode, Acc Pn fit: Particle number in the accumulation mode, PMP Acc Pn fit: Particle number in the accumulation mode after applying the digital filter (Eq. 2.2).

The particle number ratio (Accumulation mode P_n/Total P_n) for various SOI1 under different injection modes is further analysed in Fig. 4.6. It can be seen that the percentage of the accumulation mode P_n in the total P_n is higher with double injection than that with single injection across the SOI1 sweep. This indicates that under stratified combustion with injection after compression, most of the particles emitted are in the accumulation mode. Shown in Fig. 4.7 is a comparison of the average count median diameter (CMD) in the accumulation mode for the different injection strategies. It can be seen that larger size particles were generated under double injection compared to those under single injection. So most of the particles generated under double injection conditions were in the accumulation mode with the CMD varying between 80-250nm.

Fig. 4.8 shows the HC emissions and the exhaust temperatures during the SOI1 sweep for the different injection modes. Fig. 4.9 shows the standard deviation of IMEPn for all four cylinders in the engine B Bank under the various injection timings and different injection modes. Signals from the first cylinder (B1) pressure transducer had higher noise, which led to the higher standard deviation of IMEPn (Std of IMEPn). The standard deviations of IMEPn from the other 3 cylinders (B2, B3 and B4) are similar. In most cases (SOI1 from 240° BTDC to 320° BTDC), the HC emissions under double injection were much lower than those under single injection, while the exhaust temperatures tend to be higher, suggesting that higher exhaust temperature benefits the oxidation of unburned hydrocarbons. Under single injection operations, as the first injection timing is retarded to 220° BTDC and 240° BTDC, there is a decrease in HC emissions together with an increase in the exhaust temperature. However, Fig. 4.9 shows that the standard deviation of the IMEP increased significantly at these two operation points, indicating that the retarded injection timing led to increasing combustion instability. Also, it can be seen that the standard deviation of the IMEP under double injection is much lower than that under single injection. The standard deviation of the IMEP keeps nearly constant over a wide range of SOI1 under double injection operation. Also, Fig. 4.10 gives that the duration of 0-100J net heat release increased as the first injection timing was retarded to 220° BTDC, under single injection operation. On the other hand, the duration under double injection did not vary much over the whole SOI1 sweeping range.

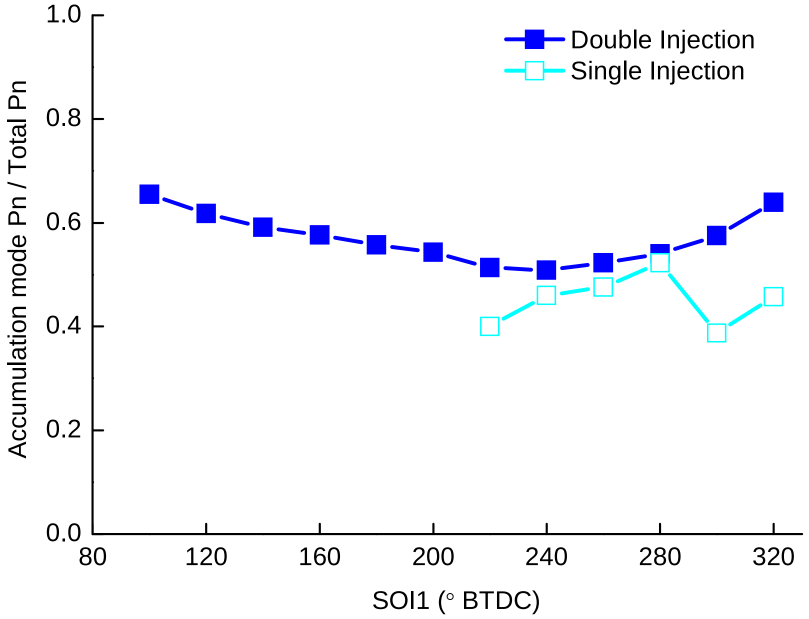

Fig. 4.6 Particle number ratio (Accumulation mode P_n/Total P_n) at different injection timings with two different injection modes (Refer to Table 4.2). SOI1: Start of the first injection.

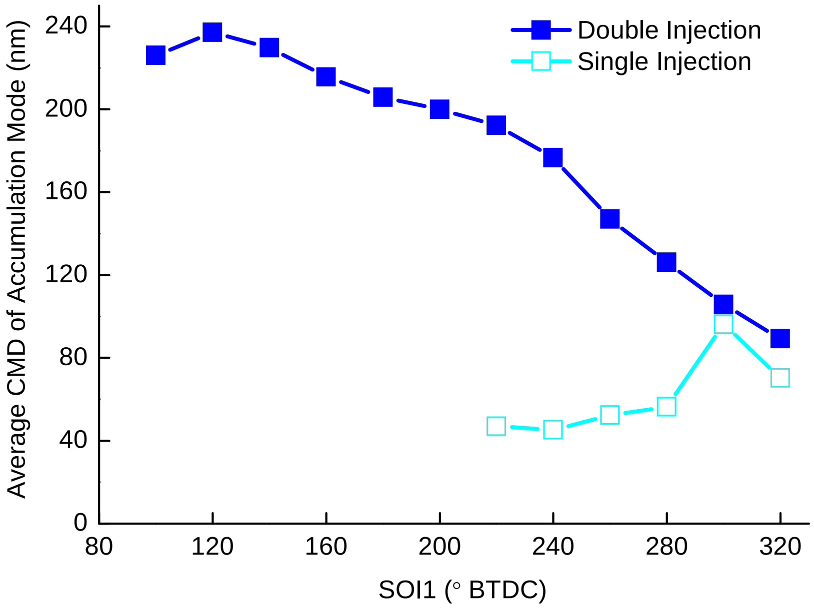

Fig. 4.7 Mean CMD of the accumulation mode at different injection timings with two different injection modes (Refer to Table 4.2). SOI1: Start of the first injection.

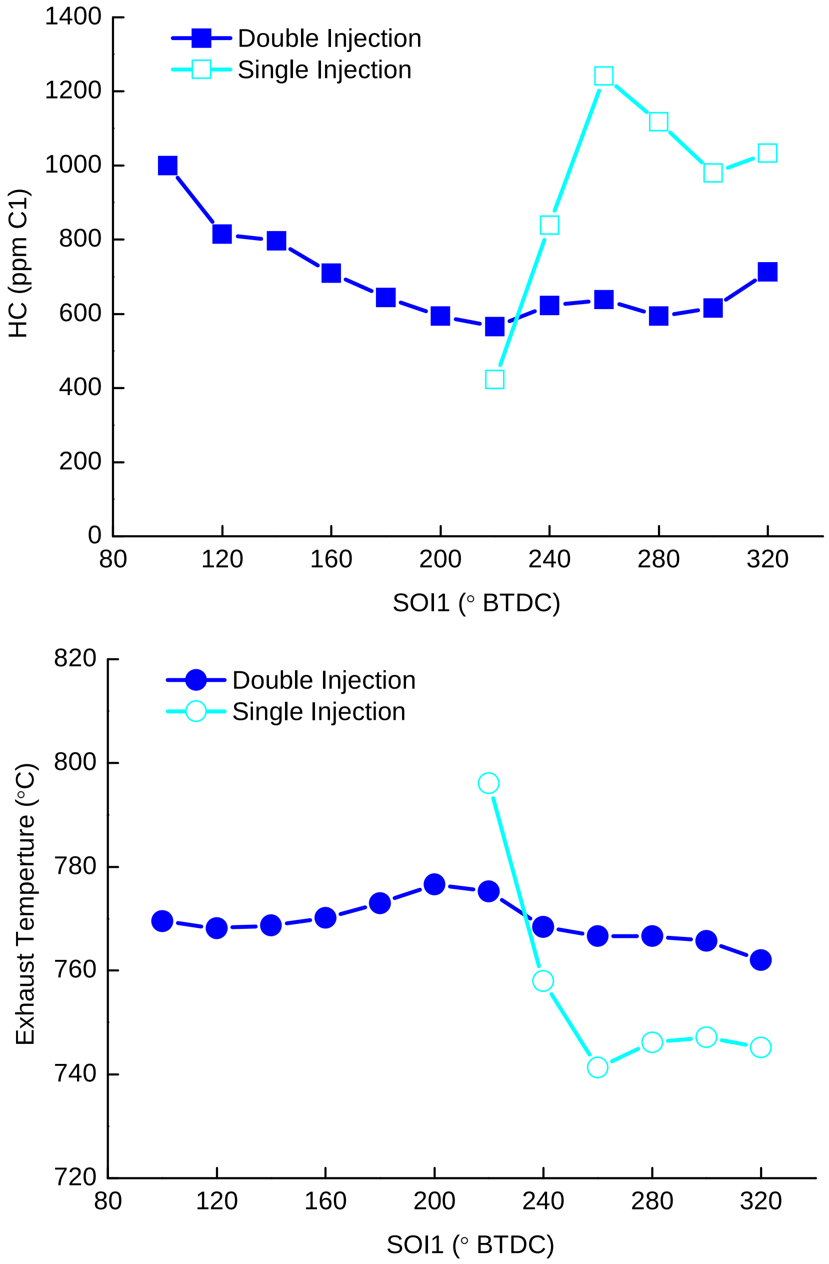

Fig. 4.8 HC emissions and exhaust temperatures at different injection timings with two different injection modes (Refer to Table 4.2). SOI1: Start of the first injection.

In summary, the double injection operation shows higher exhaust temperature, lower HC emissions and lower combustion instability, which would be a benefit for engine warm-up and catalyst light-off. However, the particle number emissions with double injection are much higher than those with single injection during intake. Therefore, optimizing the timing of the double injection operation during engine warm-up would reduce the particulate emissions from GDI engines.

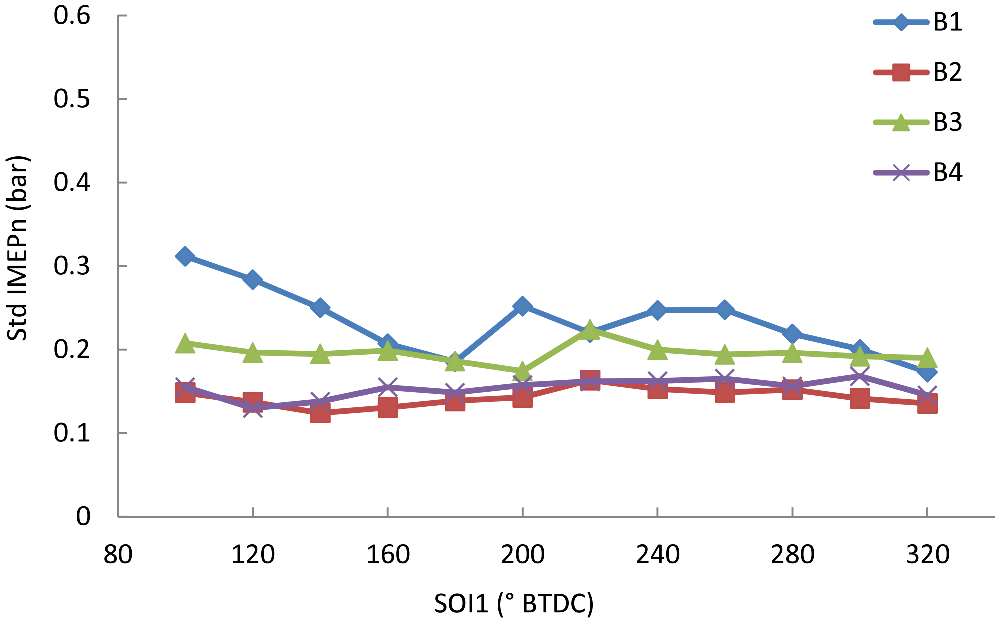

(a) Double Injection

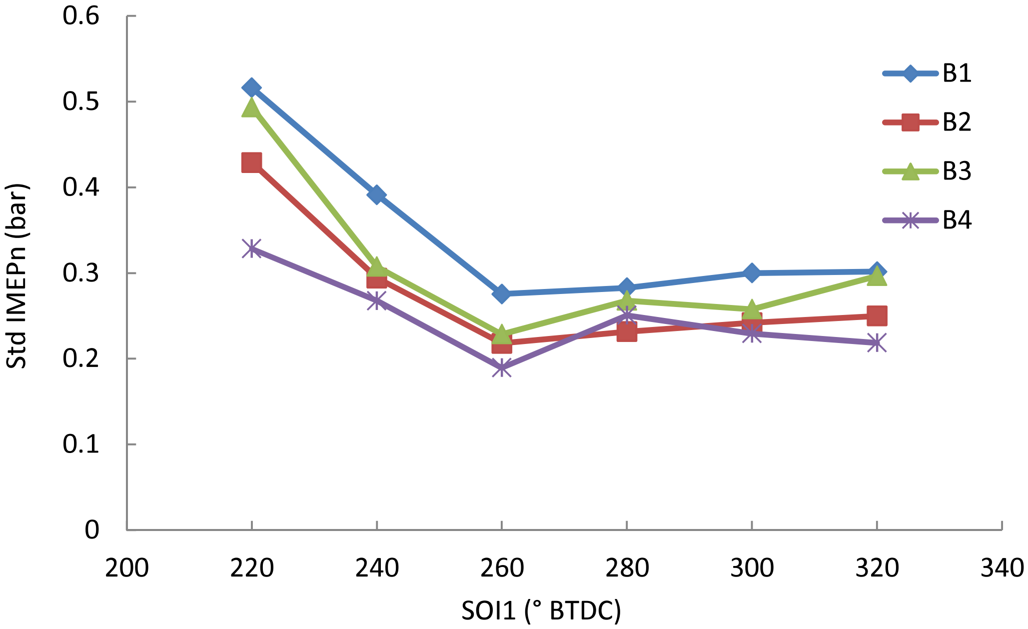

(b) Single Injection

Fig. 4.9 Standard deviation of the net IMEP for 4 cylinders on B bank at different injection timings with different injection modes (Refer to Table 4.2). SOI1: Start of the first injection.

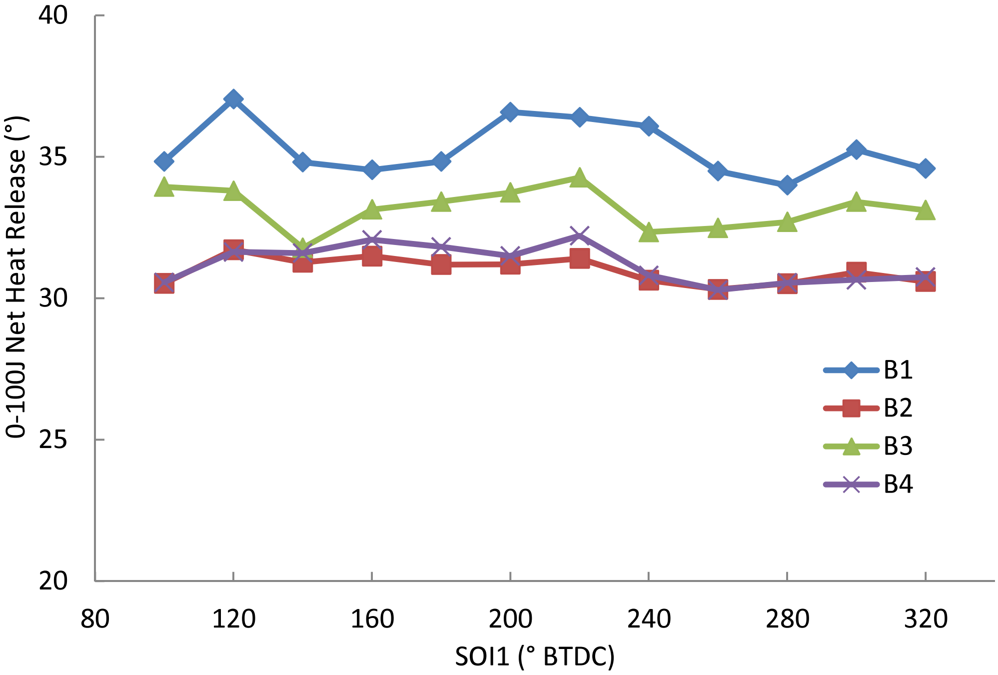

(a) Double Injection

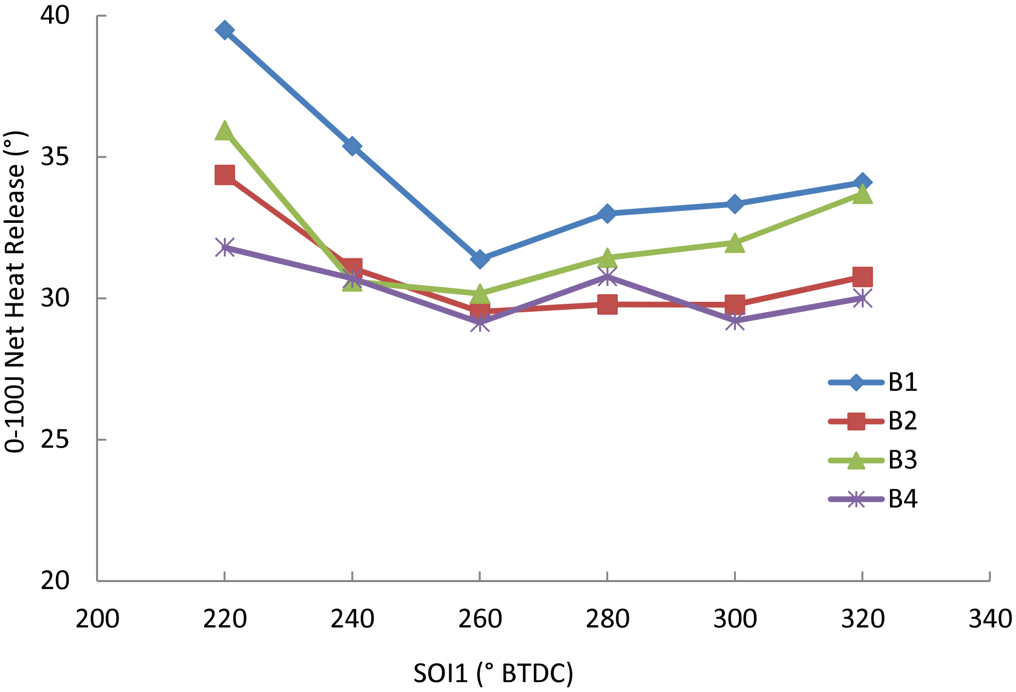

(b) Single Injection

Fig. 4.10 Duration of 0-100J net heat release for 4 cylinders on B Bank at different injection timings with different injection modes (Refer to Table 4.2). SOI1: Start of the first injection.

Test 2 – Comparison of Split Intake Injection and Single Intake Injection

The comparison tests for split intake injection with single intake injection were carried out on the V8 engine during cold operation conditions. With the fuel injection pressure set as high as 15 MPa, especially when the engine is cold, the penetration distance of fuel spray is large so that the fuel spray plumes may hit the cylinder wall or the piston top, which tends to cause wall wetting. Thus, the particulate emissions are likely to be increased under this condition. Split intake injection was investigated to see if the particulate emissions can be reduced by shortening the spray penetration and decreasing the wall wetting tendency. The main operation parameters and test matrix are listed in Table 4.3. During split injection operation, the start of the first injection (SOI1) was swept from 180° to 320° BTDC and the start of the second injection (SOI2) was varied from 30° to 110° after the first injection; the most retarded timing for the second injection was 150° BTDC. The pulse widths for the first and the second injections were the same.

Table 4.3 Main tests parameters and test matrix for Test 2

Injection Mode:	Split								Single
Start of 1st Injection / ° BTDC	180	200	220	240	260	280	290	300	140-310
Start of 2nd Injection / ° BTDC	150	170	190	170, 210	190, 230	170, 210,250	170, 210,250	190, 230,270	\
Injection Pressure / MPa	15								
Engine Speed / rpm	1200								
Engine Torque / N·m	110								
Spark Timing:	10° BTDC								
Relative AFR:	1.0								
IVO:	34° ATDC								
IVC:	244° ATDC								
EVO:	214° BTDC								
EVC:	36° ATDC								
Coolant / °C:	20								

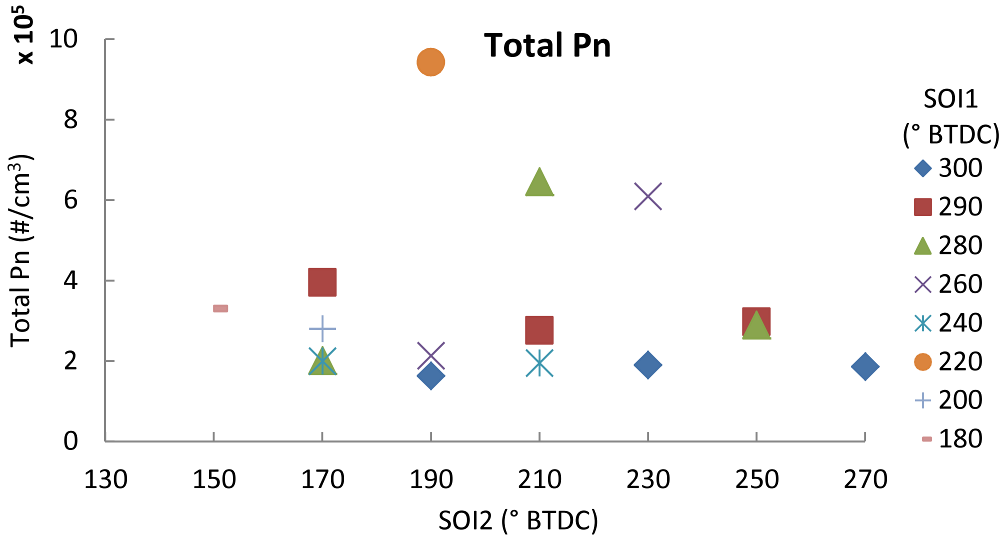

(a) Total particle number

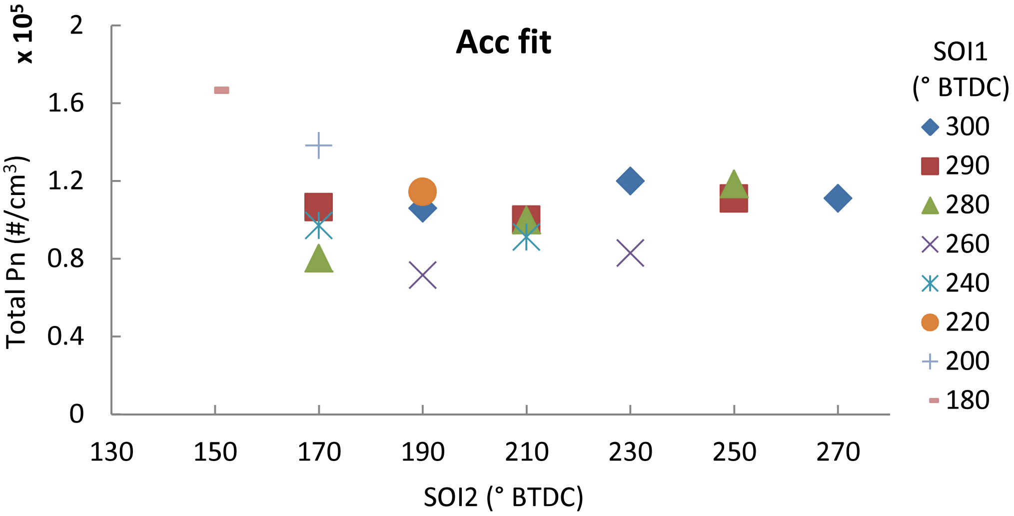

(b) Accumulation mode particle number

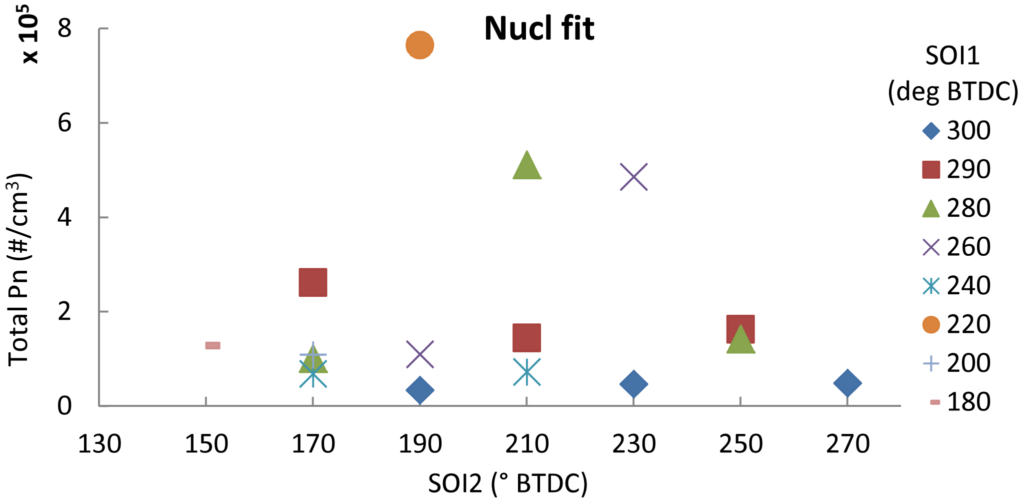

(c) Nucleation mode particle number

Fig. 4.11 Total, accumulation mode and nucleation mode particle number concentrations at different injection timings under split injection operation (Refer to Table 4.3). SOI1: Start of the first injection, SOI2: Start of the Second injection

Fig. 4.11 gives the P_n for total, accumulation mode and nucleation mode particles at different injection timings under split injection operation conditions. It can be seen that at most of the test points, the particulate number emissions are quite low across the test range. The P_n for the accumulation mode particle emissions do not vary much; they are around 1×10^5 #/cm^3. However, the number for the nucleation mode particles is quite unstable, varying from 3×10^4 #/cm^3 to 8×10^5 #/cm^3. Fig. 4.12 shows the total particle number at different injection timings under single injection operation conditions. It can be seen that there is a rise in P_n if the fuel is injected either too late or too early, and the particulate emissions are kept at a low level when the SOI1 is between 290° and 250° BTDC. There is less variation in the number of the accumulation mode particle than that of the nucleation mode particle with different injection timings. Low levels of particulate emissions can also be achieved with single injection under a wide range of injection timings. There is no significant improvement in particle number emissions using split injection, compared with single injection.

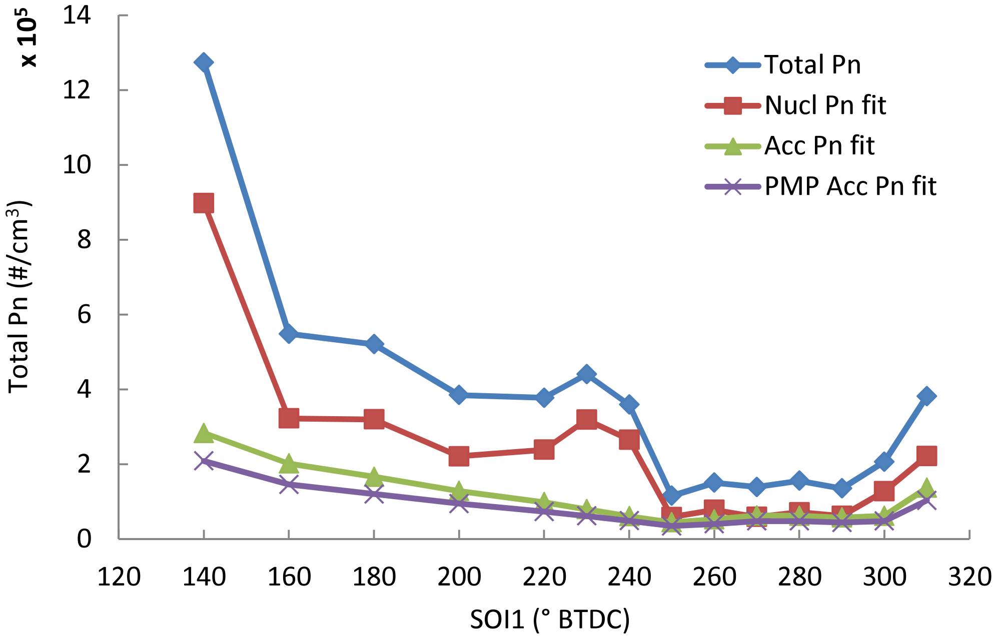

Fig. 4.12 Total particle number concentrations at different injection timings under single injection operation (Refer to Table 4.3). SOI1: Start of the first injection, Total Pn: Total particle number, Nucl Pn fit: Particle number of nucleation mode, Acc Pn fit: Particle number of accumulation mode, PMP Acc Pn fit: Particle number of accumulation mode with a digital filter (Eq. 2.2) applying to it.

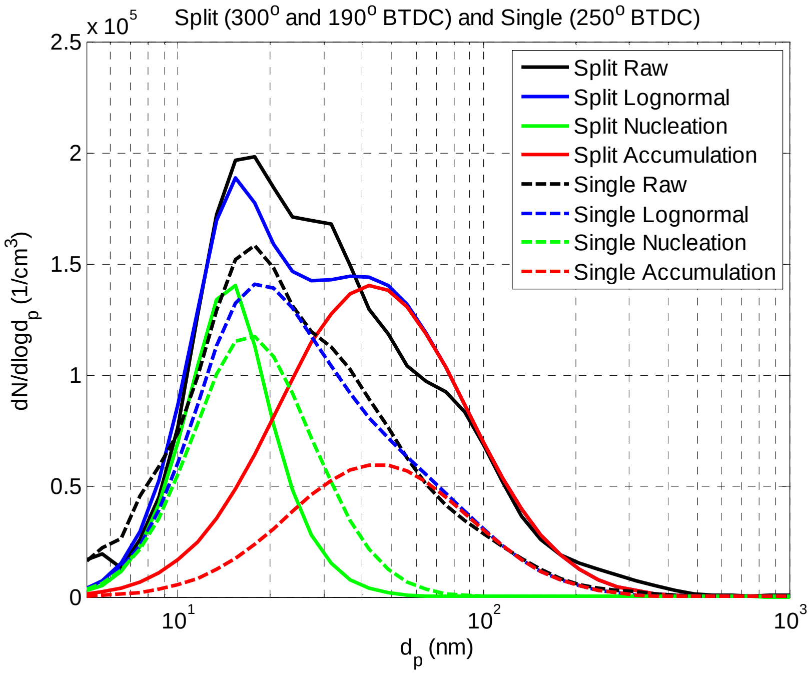

Injection Mode	Total Pn (#/cm^3)	Nucl Pn fit (#/cm^3)	Acc Pn fit (#/cm^3)
Split	186300	48200	111100
Single	115600	58900	44500

Fig. 4.13 Comparison of the number weighted size distributions for a typical split injection operation point (SOI1: 300, SOI2: 270) and a typical single injection operation point (SOI1: 250) showing the raw data and their lognormal fittings.

Fig. 4.13 shows two representative raw size distributions from the DMS data and their lognormal fittings, one for split injection (SOI1: 300, SOI2: 270) and one for single injection (SOI1: 250). The numbers for the total, nucleation mode and accumulation mode particle concentrations are listed below the figure. Both points selected have the lowest total particle number emissions in each case. It can be seen that the particulate emissions with split injection operation do not differ much from those with single injection operation. The number of accumulation mode particles (large particles) under split injection is higher than that under single injection. Even under cold engine operation conditions, low P_n number emissions can be achieved with single injection. The split injection does not show much potential for further reducing the particle number emissions at this engine speed and load.

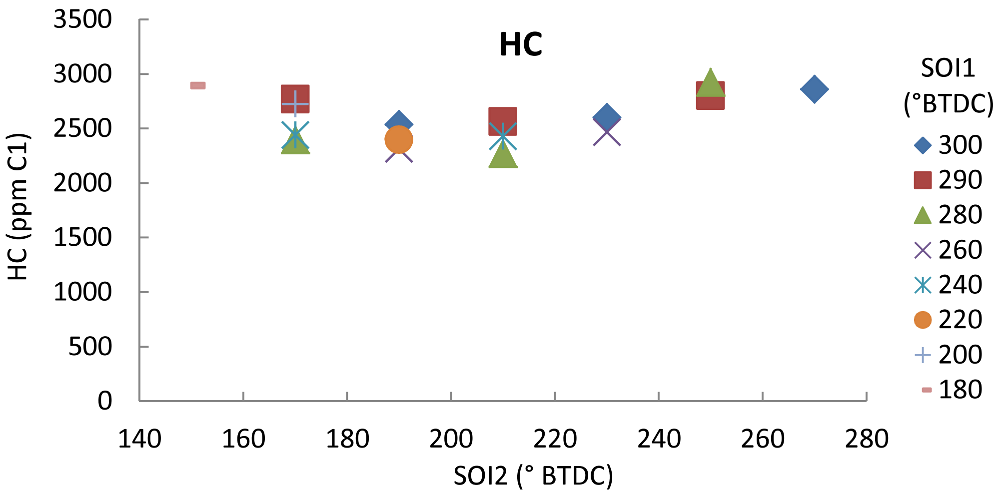

(a) Split Injection

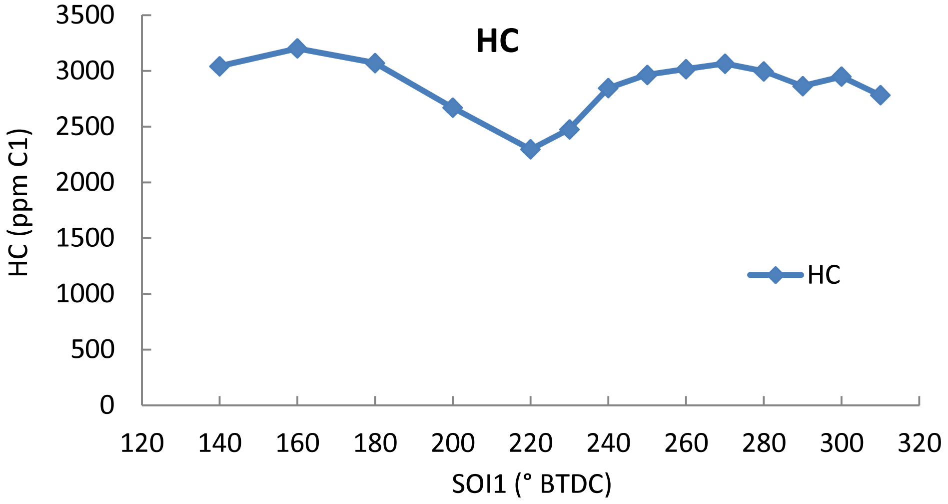

(b) Single Injection

Fig. 4.14 HC emissions at different injection timings with split injection and single injection (Refer to Table 4.3), SOI1: Start of the first injection, SOI2: Start of the Second injection.

Fig. 4.14 shows the HC emissions at different injection timings under split injection and single injection operation. It can be seen that the HC emissions do not change much across the test range, but remain mostly around 2500 ppm. The HC emissions under single injection are similar to those under split injection. Particle size distributions for typical warm and cold operation points are compared in Fig. 4.15, both with early single injection. The coolant temperatures for the cold and warm operation were kept at 20 °C inlet and 90 °C outlet respectively. The lognormal fittings for the warm operation point were calculated using the MATLAB optimizing method described in Chapter 2. It can be seen the peak of the size distribution under cold operation is about 4 times higher than that under warm operation. This suggests that after the engine has been fully warmed-up, then particulate emissions should not be an issue.

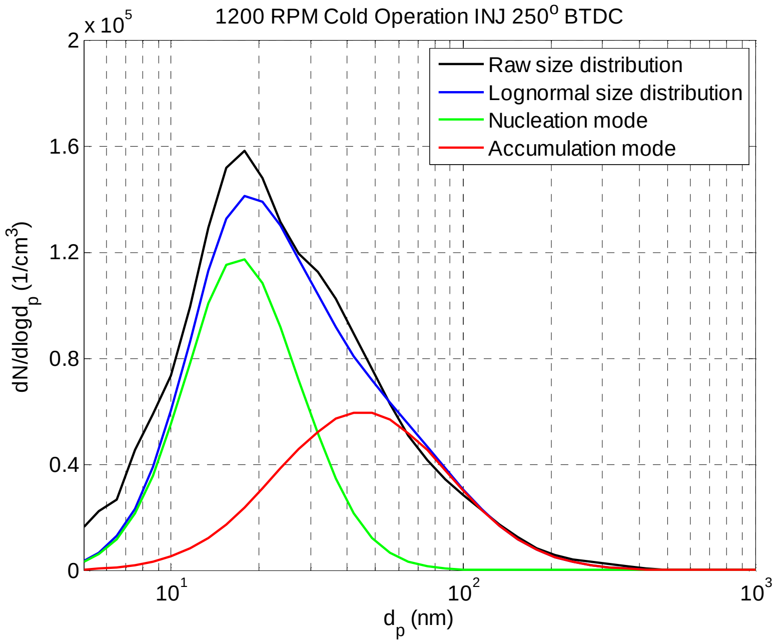

Speed (rpm)	Torque (Nm)	Total Pn (#/cm^3)	Nucl Pn fit (#/cm^3)	Acc Pn fit (#/cm^3)
1200	110	115600	58900	44500

(a) Cold Operation

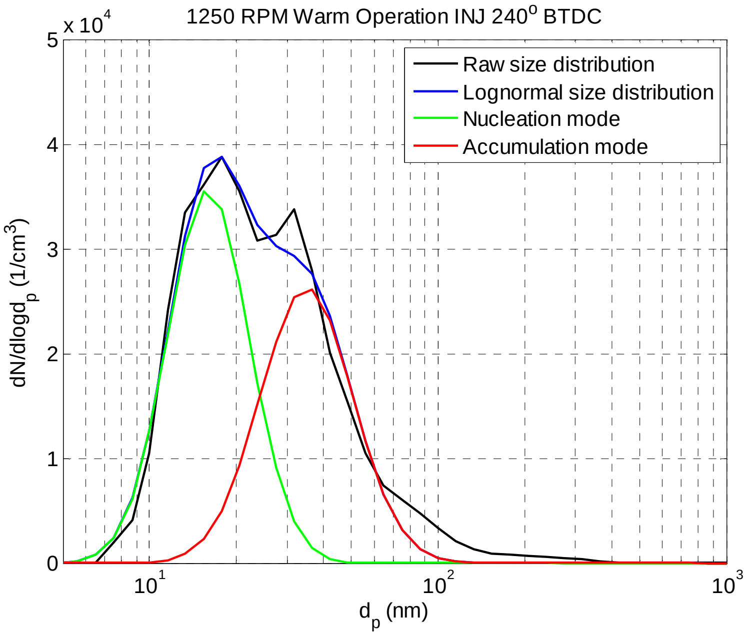

Speed (rpm)	Torque (Nm)	Total Pn (#/cm^3)	Nucl Pn fit (#/cm^3)	Acc Pn fit (#/cm^3)
1250	139	24000	12700	10600

(b) Warm Operation

Fig. 4.15 Comparison of the number weighted size distribution for a typical cold operation point (20 °C coolant inlet) and a typical warm operation point (90 °C coolant outlet) showing the raw data and their lognormal fittings.

Test 3 – Influence of Fuel Injection Pressure on PM Emissions

The tests on the effects of fuel injection pressure on particulate emissions were carried out on the V8 engine during cold operation conditions. Early split injection was utilised to facilitate homogeneous mixture formation and to shorten the spray penetration distance so that the tendency for wall wetting to occur can be reduced. The spark ignition timing during the tests was retarded to imitate the operating conditions during the catalyst light-off phase. The main engine operation parameters are listed in Table 4.4. It can be seen that the fuel pressure was swept from 3.1 MPa to 14.2 MPa.

Table 4.4 Main tests parameters for Test 3

Injection Mode:	Split
Start of 1st Injection (SOI1):	280° BTDC
Start of 2nd Injection (SOI2):	250° BTDC
Injection Pressure / MPa	3.1, 5.9, 8.8, 11.5, 14.2
Engine Speed / rpm	800
Engine Torque / N·m	80
Spark Timing:	-2° BTDC
Relative AFR:	1.0
IVO:	24° ATDC
IVC:	274° ATDC
EVO:	217° BTDC
EVC:	33° ATDC
Coolant / °C:	20

Fig. 4.16 shows the particle number emissions versus fuel pressure. It can be seen that there is a marked reduction in accumulation mode particles as the fuel pressure was increased from 3.1 MPa to 14.2 MPa. The particulate number in the nucleation mode decreased from 4.8×10^5 #/cm^3 to 6.6×10^4 #/cm^3 as the fuel pressure increased from 3.1 MPa to 11.5 MPa. When further increasing the fuel pressure to 14.2 MPa, the P_n in the nucleation mode

increased to 1.2×10^5 #/cm^3. Fig. 4.17 shows the HC emissions at different fuel injection pressures. The HC emissions achieved a minimum value of 1970 ppm at 11.5 MPa fuel injection pressure. The trend of HC emissions varying with fuel pressure is similar to that of nucleation mode particle. This link between HC emissions and the nucleation mode particles can be explained by the nucleation mode being dominated by condensed hydrocarbons. Both the mixture homogeneity and wall impingement would affect the HC and particulate emissions. As the fuel pressure increased, the mixture is more homogeneous so that the HC and PM formation during combustion was reduced. Lower HC emissions resulted in a lower tendency for small particles to be formed from HC nucleating and condensing, so that the number of the nucleation mode particles was reduced. But if the fuel pressure was too high, then fuel impingement would increase, leading to higher HC emissions and increased nucleation mode particle concentrations.

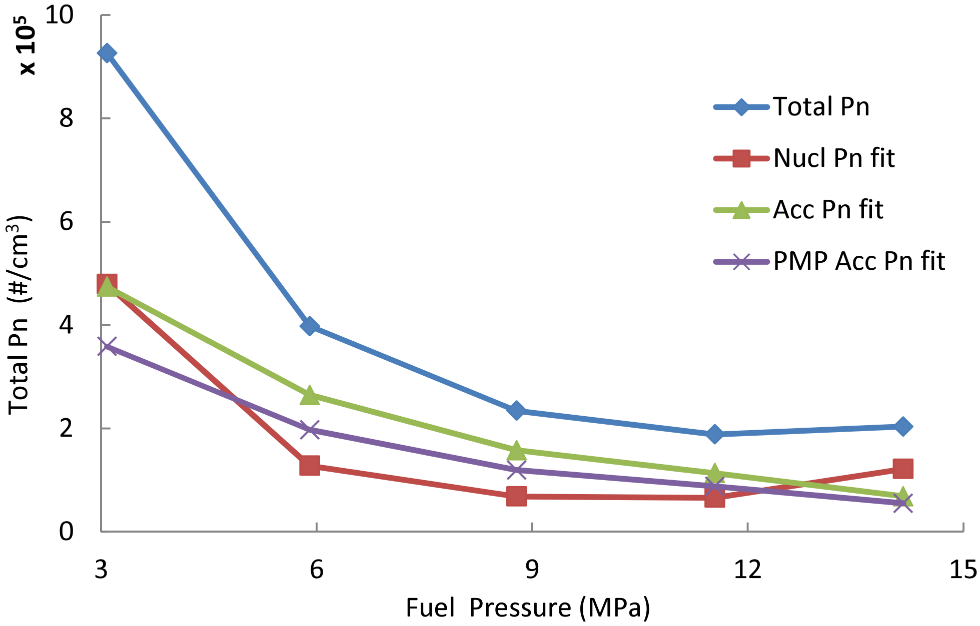

Fig. 4.16 Total particle number at different fuel injection pressure under split injection operation (Refer to Table 4.4). Total Pn: Total particle number, Nucl Pn fit: Particle number of nucleation mode, Acc Pn fit: Particle number of accumulation mode, PMP Acc Pn fit: Particle number of accumulation mode with a digital filter (Eq. 2.2) applied.

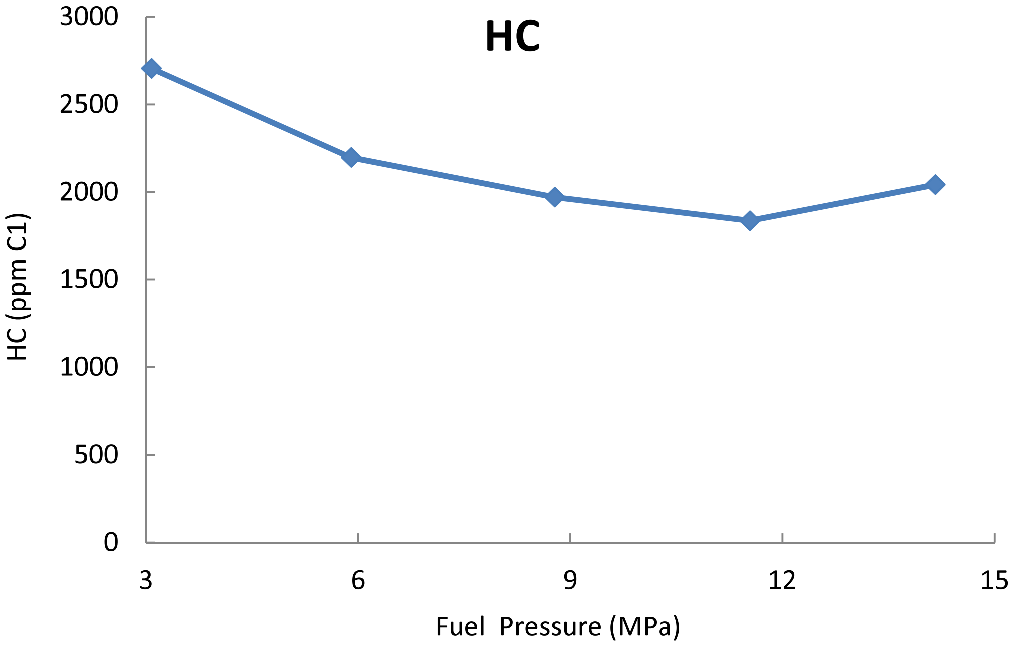

Fig. 4.17 HC emissions at different fuel injection pressure under split injection operation (Refer to Table 4.4).

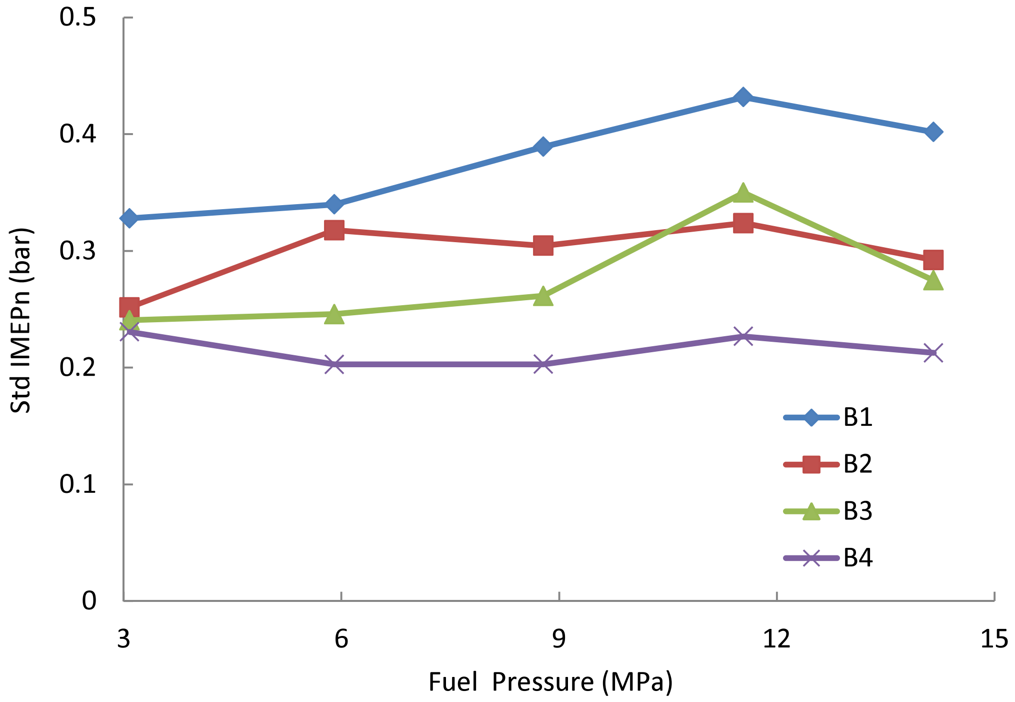

Fig. 4.18 Standard deviation of the net IMEP for 4 cylinders on B Bank at different fuel injection pressure under split injection operation (Refer to Table 4.4).

Fig. 4.18 gives the standard deviation of net IMEP for the cylinders in B bank. It can be seen that the combustion stability did not change much as the fuel pressure varied. Fig. 4.19 shows that the 0-100J net heat release did not vary much for any of the cylinders on B bank as the fuel injection pressure increased.

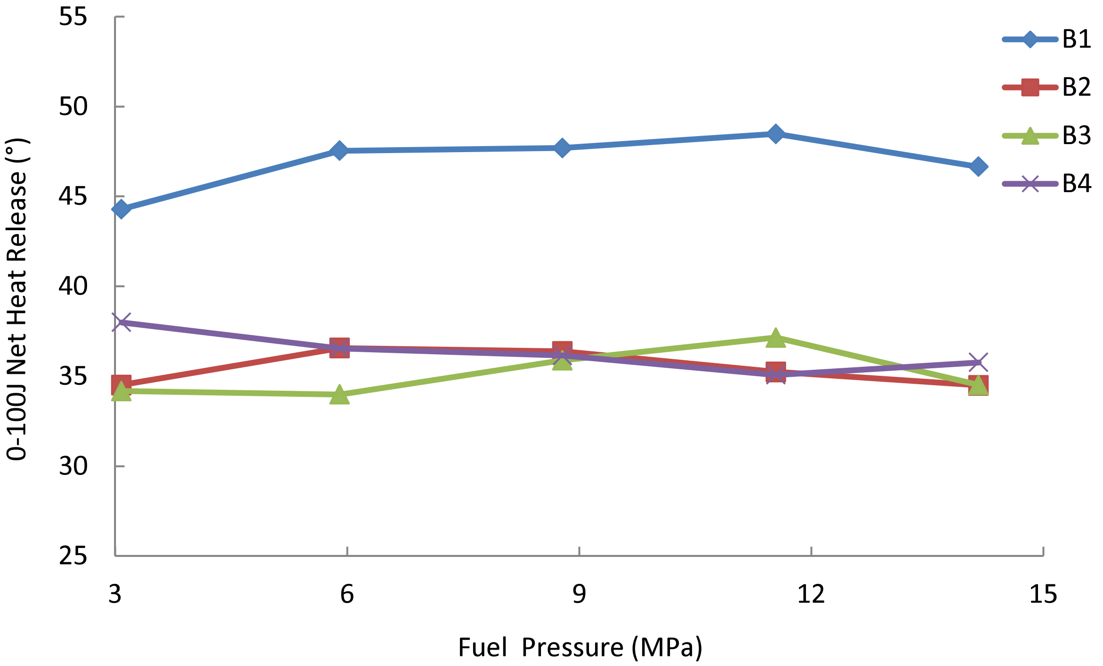

Fig. 4.19 Duration of 0-100J net heat release for 4 cylinders on B Bank at different injection pressure under split injection operation (Refer to Table 4.4).

4.3.2 The Effects of Valve Timing on the PM Emissions

The tests on particulate emissions varying with different valve timings were carried out on the V8 engine during cold operation conditions. Early single injection was utilised to facilitate homogeneous mixture formation and the injection pressure was fixed at 15 MPa. The main engine operation parameters are listed in Table 4.5. There are two operation conditions tested: one is 1200 rpm with 5.5 mm intake valve lift and the other one is 1500 rpm with 10.53 mm intake valve lift. Under each operation conditions, 6 different valve timings were tested, designated as VVTL1-6 and VVTH1-6, respectively. VVTL1 and VVTH1 are the base valve timings for low lift and high lift, where the intake valve timing is in the most retarded point and the exhaust valve timing is in the most advanced point. Details of the valve timings with respect to intake TDC are listed in Table 4.6, where VVI represents the angle for intake valve advancing respect to base timing and VVE represents the angle for exhaust valve retarding respect to base timing. During the valve timing tests, the intake manifold pressure was adjusted to keep the engine torque at 120 N·m under 1200 rpm and 110 N·m under 1500 rpm, respectively.

Table 4.5 Main tests parameters for VVT tests (Valve timings are in Table 4.6)

Engine Speed / rpm	1200	1500
Engine Torque / N·m	120	110
Injection Mode:	Single	Single
Injection Timing:	270° BTDC	280° BTDC
Injection Pressure / MPa	15	15
Spark Timing:	10° BTDC	17° BTDC
Relative AFR:	1.0	1.0
Inlet Valve Lift:	Low 5.5 mm	High 10.53 mm
Valve Timing:	VVTL1-6	VVTH1-6
Coolant / °C:	20	20

Table 4.6 Twelve valve timings with respect to intake TDC

	VVI	VVE	IVO (^{o} ATDC)	IVC (^{o} ATDC)	EVO (^{o} BTDC)	EVC (^{o} ATDC)	Overlap (^{o})
VVTL1	0	0	34	244	244	6	-28
VVTL2	0	15	34	244	229	21	-13
VVTL3	0	30	34	244	214	36	2
VVTL4	15	0	19	229	244	6	-13
VVTL5	15	15	19	229	229	21	2
VVTL6	30	0	4	214	244	6	2
VVTH1	0	0	24	274	244	6	-18
VVTH2	0	15	24	274	229	21	-3
VVTH3	0	30	24	274	214	36	12
VVTH4	15	0	9	259	244	6	-3
VVTH5	15	15	9	259	229	21	12
VVTH6	30	0	-6	244	244	6	12

Fig. 4.20 shows the number concentrations for the total, accumulation mode and nucleation mode particles at the different valve timings. The accumulation mode particles are the main focus here, because their results are more relevant to the emissions legislation. It can be seen that when the exhaust valve timing was retarded from VVE 0 to VVE 30 with the low intake valve lift (Fig. 4.20(a)), the P_n in the accumulation mode reduced steadily from 3.4×10^5 to 1.5×10^5 #/cm^3. This can be explained by an increase in the trapped residuals. However, with the high intake valve lift, the P_n in accumulation mode decreased from 4.0×10^5 to 2.5×10^5 #/cm^3, when the exhaust valve timing was retarded from VVE 0 to VVE 15 and increased to 3.5×10^5 #/cm^3 when the exhaust valve timing was further retarded to VVE 30. Also, the number concentration for the nucleation mode particles is also the highest at VVE 30 with high lift. It can be seen from Table 4.6 that the intake valve opening duration is longer with the high lift than that with the low lift inlet cam. Also, the valve overlap increases with the high lift compared with the low lift, so that the valve overlap at VVE 30 with high lift is higher than that with low lift, which should lead to a higher residual gas content under high valve lift engine operation, especially with the late phasing. It will be seen later that the

higher residuals level led to slower combustion and a higher exhaust temperature, so the combination of more and hotter residuals leads to better evaporation of the fuel and lower particulate matter emissions. The high lift will have a lower inflow velocity so the homogeneity of the residuals will be lower.

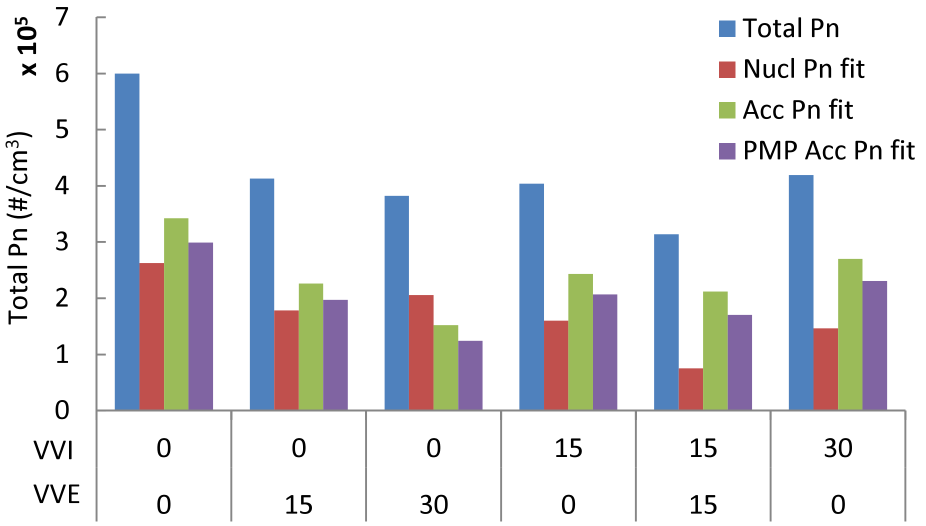

(a) 1200 rpm, 120 N·m, low lift

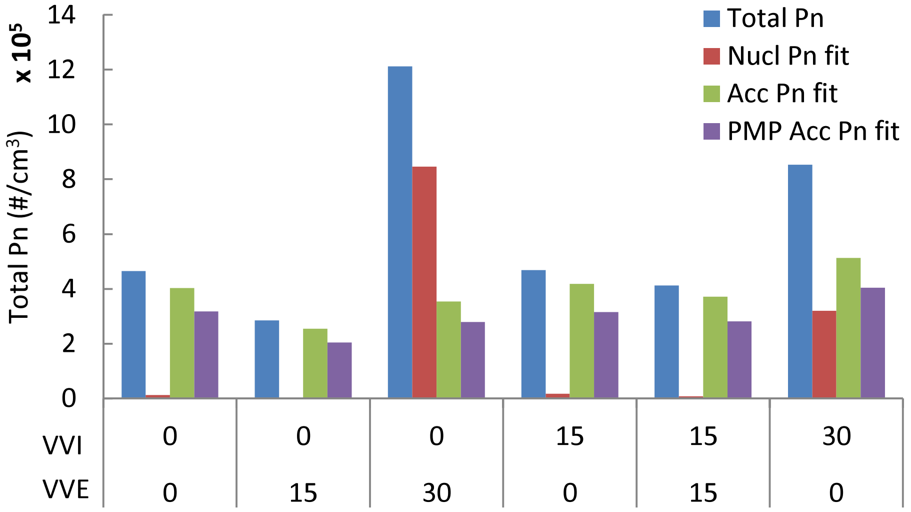

(b) 1500 rpm, 110 N·m, high lift

Fig. 4.20 Total particle number concentrations at various valve timings under different operation conditions (Refer to Table 4.5 and 4.6). VVI: Intake valve advance angle, VVE: Exhaust valve retard angle, Total Pn: Total particle number, Nucl Pn fit: Particle number of nucleation mode, Acc Pn fit: Particle number of accumulation mode, PMP Acc Pn fit: Particle number of accumulation mode with a digital filter (Eq. 2.2) applying to it.

To further analyse the reason for the high PM emissions at VVE 30 with high lift, the combustion characteristics are compared between the operation points of VVE 30 with low valve lift (VVTL3) and high valve lift (VVTH3). From Fig. 4.21, it can be seen that the standard deviation of IMEPn increased as the exhaust valve closing was retarded. And the increase in the standard deviation of IMEPn is much more significant with high intake valve lift than that with low lift. This indicates that with high intake lift and retarded exhaust timing, the combustion became relatively unstable. Also at this point, the valve overlap between intake and exhaust was 12°, higher than that with low lift which was 2°. The combustion stability data also supports the hypothesis that the late valve timings increase the residuals and that there is lower homogeneity with the high lift cam.

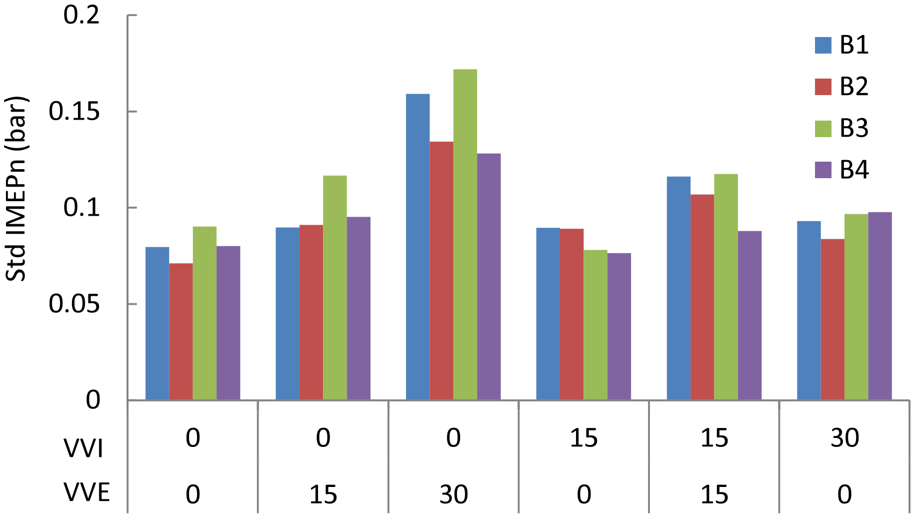

(a) 1200 rpm, 120 N·m, low lift

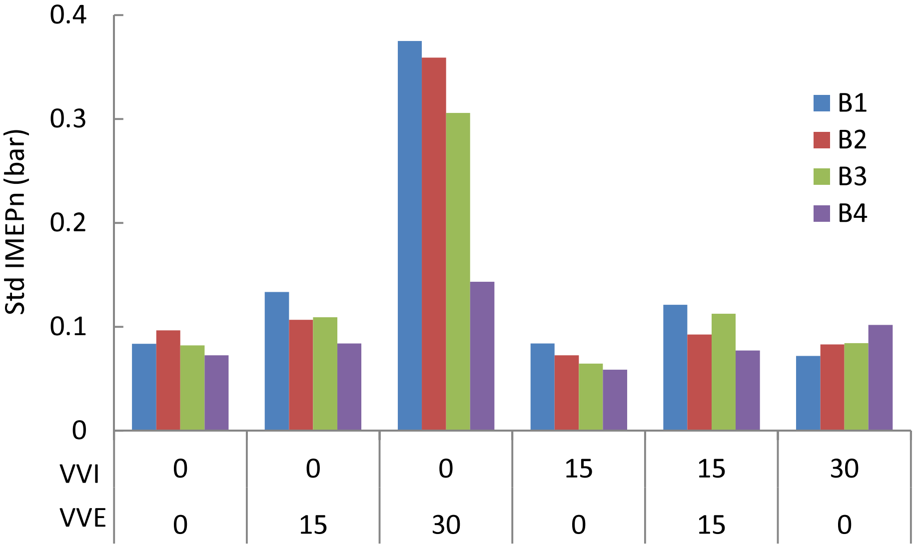

(b) 1500 rpm, 110 N·m, high lift

Fig. 4.21 Standard deviation of net IMEP for the 4 cylinders in B Bank at various valve timings under different operation conditions (Refer to Table 4.5 and 4.6). VVI: Intake valve advance angle, VVE: Exhaust valve retard angle.

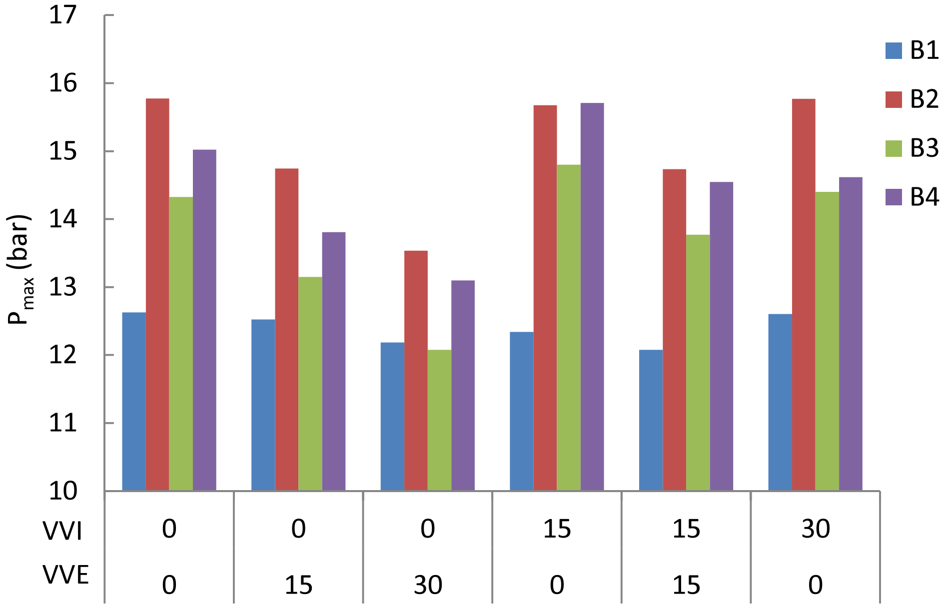

(a) 1200 rpm, 120 N·m, low lift

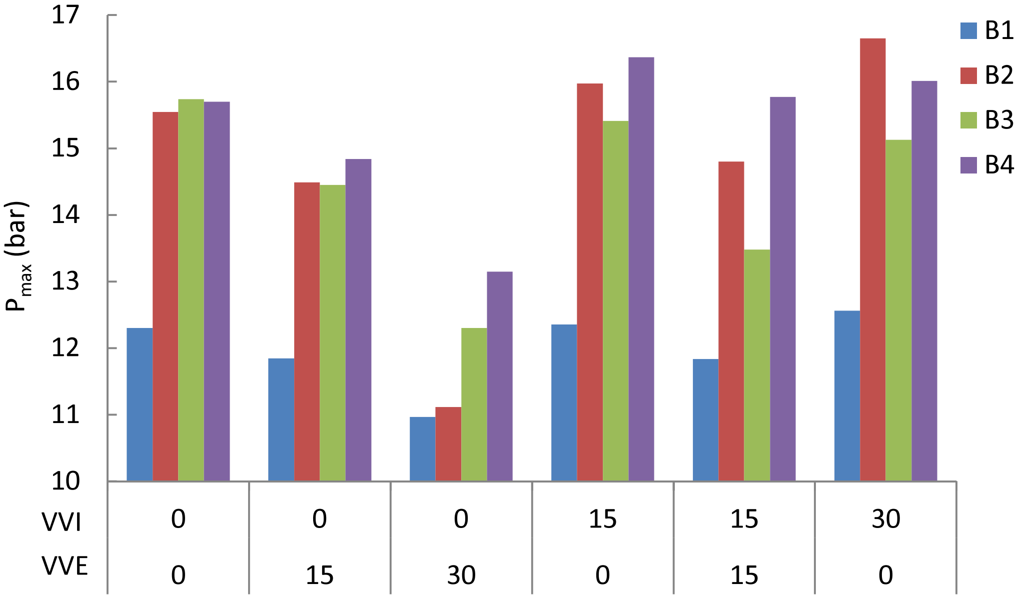

(b) 1500 rpm, 110 N·m, high lift

Fig. 4.22 Mean value of the peak in-cylinder pressure for the 4 cylinders in B Bank at various valve timings under different operation conditions (Refer to Table 4.5 and 4.6). VVI: Intake valve advance angle, VVE: Exhaust valve retard angle.

From Fig. 4.22, it can be seen that the retarded exhaust valve timing also led to a reduced peak in-cylinder pressure for both the low and high valve lift cases. The reduction in the peak in-cylinder pressure with the high lift was larger than that with low lift. On the other hand, the peak in-cylinder pressure was not changing much with the increase in intake valve advance. Similar results are seen in the variation of 0-50% mass fraction burn duration with valve timings (Fig. 4.23). The 0-50% MFB increased markedly with retarding the exhaust valve closure but did not vary much with advancing the intake valve opening. Also, a bigger increase in the 0-50% MFB duration occurs with the high lift compared to that with the low lift, indicating that the combustion duration with high lift increased more significantly as the exhaust valve timing was retarded.

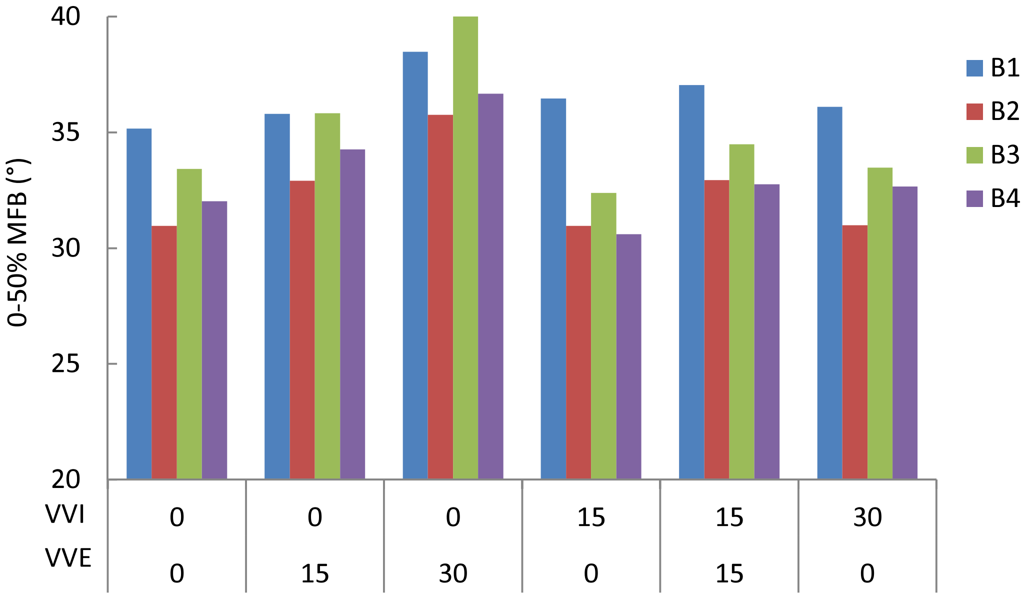

(a) 1200 rpm, 120 N·m, low lift

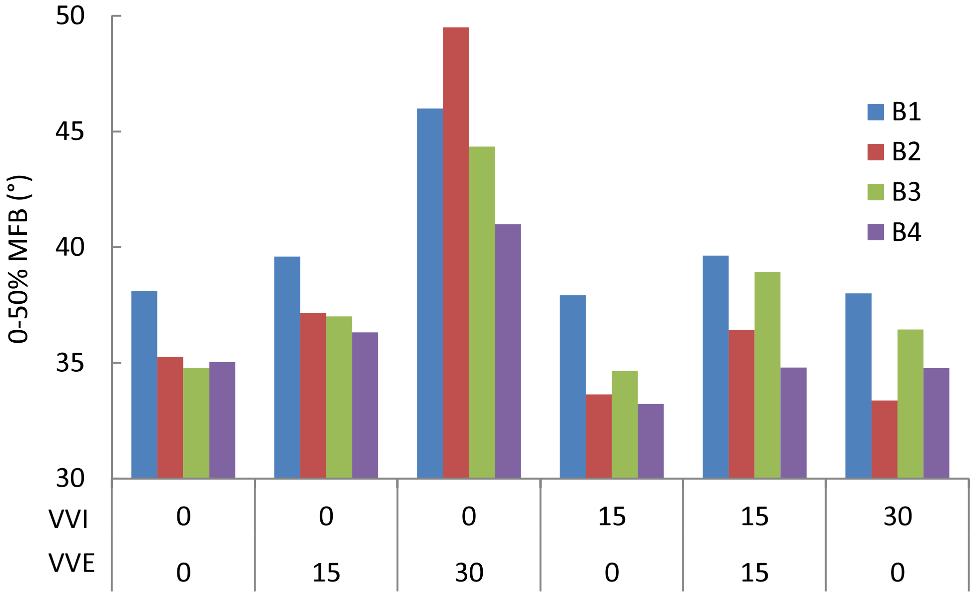

(b) 1500 rpm, 110 N·m, high lift

Fig. 4.23 0-50% mass fraction burnt for the 4 cylinders in B Bank at various valve timings under different operation conditions (Refer to Table 4.5 and 4.6). VVI: Intake valve advance angle, VVE: Exhaust valve retard angle.

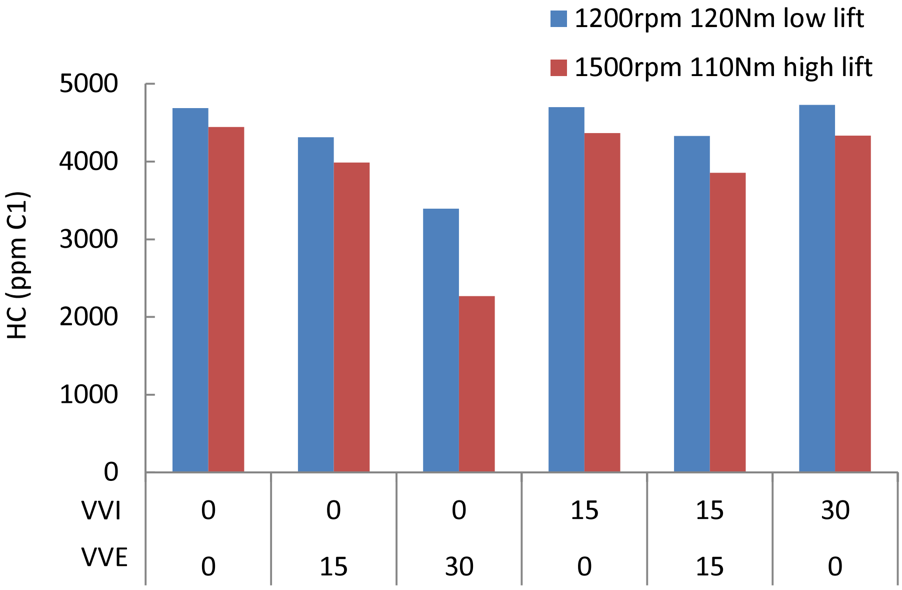

(a) HC emissions

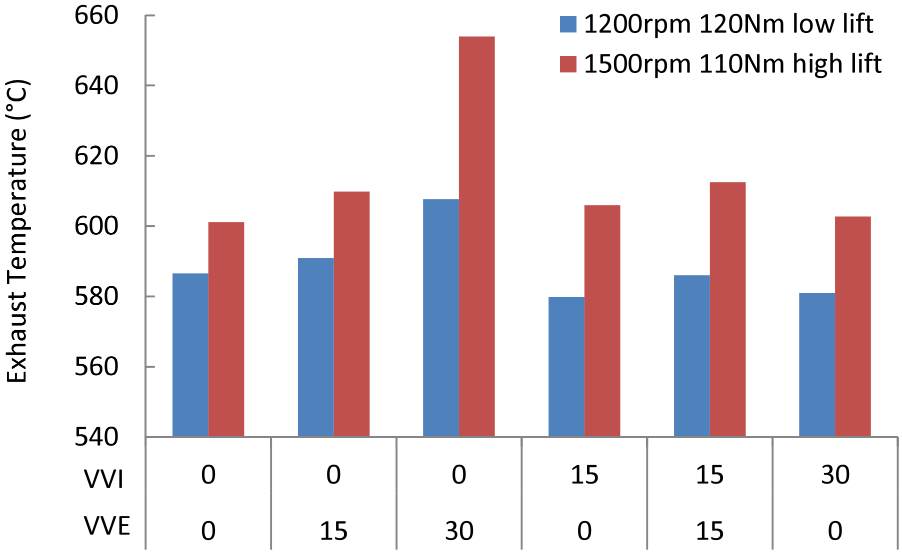

(b) Exhaust Temperatures

Fig. 4.24 HC emissions and exhaust temperatures at various valve timings under different operation conditions (Refer to Table 4.5 and 4.6). VVI: Intake valve advance angle, VVE: Exhaust valve retard angle.

Fig. 4.24 shows the HC emissions and the exhaust temperatures at different valve timings under low lift and high lift operation points. With high valve lift, it can be seen that the HC emissions reduced noticeably as the exhaust valve timing was 30° (VVE 30) retarded from base timing (VVE 0). Correspondingly, the exhaust temperature increased about 50 °C with retarding the exhaust valve closing. In comparison, there were moderate changes in both HC emissions and exhaust temperatures under low intake valve lift conditions. Also, the HC emissions and exhaust temperatures only varied slightly as the intake valve opening was changed from base timing to 30° in advance (VVI 0 to VVI 30). So, the higher residuals level associated with a late exhaust valve opening led to slower combustion and a higher exhaust temperature, so the combination of more and hotter residuals led to better evaporation of the fuel and lower particulate matter emissions.

In summary, the valve timings showed moderate effects on particulate emissions and the exhaust valve timing showed a bigger effect on particulate emissions and combustion characteristics compared to that of intake valve timing. The particulate number concentration in the accumulation mode reduced as the exhaust valve closing was retarded. However, if the exhaust valve closure was further retarded and the valve overlap period between intake and exhaust became longer, the residual content tended to increase, which would affect the combustion stability. If the combustion became unstable, i.e. the standard deviation of the IMEPn was much higher than normal operation, the particulate emissions tended to increase and the combustion duration was prolonged, which was shown in the case of 30° retarded exhaust valve closing with high lift. Meanwhile, advancing the intake valve opening did not show much effect in PM emissions both with low lift and high lift.

4.4 Summary

(1) Particulate emissions from cold engine operation were much higher than those from warm engine operation.

(2) Under cold engine operating conditions, particle number emissions using double injection with injection after compression were more than an order of magnitude higher than those with a single injection during the intake. The main injection timing only had moderate

effects on PM emission.

(3) Under cold engine operation, no reduction effect on PM emissions was shown using split intake injection to further facilitate homogeneous mixture formation compared with single intake injection.

(4) Increasing the fuel injection pressure could form a more homogeneous mixture so that the HC and PM formation during combustion can be reduced. However, if the fuel pressure was too high, spray impingement could increase, leading to higher HC emissions and increased nucleation mode particle concentrations.

(5) Valve timings showed moderate effects on particulate emissions. Properly adjusted timing for exhaust valve closure would lead to reduced particulate emissions and the combustion characteristics would not be adversely affected much. The effect of the intake valve opening on PM emissions was less than that of the exhaust valve closing.

Chapter 5. The Effects of a Catalytic Volatile Particle Remover (VPR) on the PM Emissions from a GDI Engine

5.1 Introduction

Researchers have shown that gasoline engines, especially gasoline direct injection engines, tend to emit large amounts of small size particles compared to diesel engines fitted with Diesel Particulate Filters (DPFs). As a result, the particle number emissions of DISI engines will be restricted by the forthcoming EU6 legislation. The particulate emission level of DISI engines means that they could face some challenges in meeting the EU6 requirement. This paper is an experimental study on the size-resolved particle number emissions from a spray guided DISI engine and the performance of a Catalytic Volatile Particle Remover (VPR), as the EU legislation seeks to exclude volatile particles.

Presented in this chapter is an experimental study on the size-resolved particle number emissions from a spray guided GDI engine and the performance of a Catalytic Volatile Particle Remover (VPR), as the EU legislation seeks to exclude volatile particles. Firstly, the performance of the catalytic VPR was evaluated by varying its temperature and the exhaust residence time. Secondly, the performance of the catalytic VPR being used for post Three Way Catalyst (TWC) oxidation was studied experimentally. Additional air or nitrogen was used to distinguish between chemical and physical effects of the catalytic VPR when there is a reduction in particle numbers.

5.2 Catalytic VPR System and Experimental Set-up

A large portion of the particles emitted by GDI engines are small diameter (< 50 nm), volatile particles. The volatile particles are difficult to measure, because they can experience physical changes in the exhaust and particle sampling system. Fig. 5.1 shows the recommended particulate sampling system of the European Particle Measurement Programme (PMP). It can be deduced from the PMP that a volatile particle remover (VPR) is required upstream of the particle number counter (PNC) [61]. The VPR is heated to vaporize volatile particles in the sample flow.

To investigate the characteristics of particle emissions from engines, a Catalytic Stripper (CS, an oxidation catalyst) has been tested by Kittelson and co-workers [88, 89]. It was reported that complete removal of volatile particles could be achieved but that it also led to the removal of 15-25% of the solid particles. This loss has been attributed to thermophoretic deposition caused by cooling after the catalytic stripper. The particle loss in the catalytic stripper led to the development of a Solid Particle Sampling System (SPSS) [90] that used dilution immediately after an oxidation catalyst. Khalek [90] presents a comprehensive discussion and analysis of the operation of the SPSS, and characterises its performance using salt (NaCl), ammonium sulfate and oil aerosols. The ammonium sulphate decomposed and (as with the oil) led to particle penetration through the SPSS that was always below 10%. In contrast the penetration of the salt aerosol was, within experimental tolerance, 100%. In a subsequent paper Khalek and Bougher [91] compare the performance of the SPSS using a Catalytic Stripper (CS) with an Evaporation Tube (ET) using particles of tetracontane (as specified in the European PMP). They conclude that the Catalytic Stripper outperforms the Evaporation Tube, since the catalytic stripper will oxidise the vaporised hydrocarbons so that there is then no possibility of their re-condensation. So, it is of interest to investigate the performance of the Catalytic Stripper based Volatile Particle Remover System on the PM emissions from a spray guided direct injection engine; previous work has utilised a wall guided direct injection engine

In the work reported here, engine experiments were carried out to study a Catalytic Volatile Particle Remover (VPR), and to find out if it can achieve the transmission efficiencies required by the PMP procedures. Also, experiments with the Catalytic Volatile Particle Remover have used the addition of air or nitrogen to distinguish between chemical and physical mechanisms when there is a reduction in particle numbers.

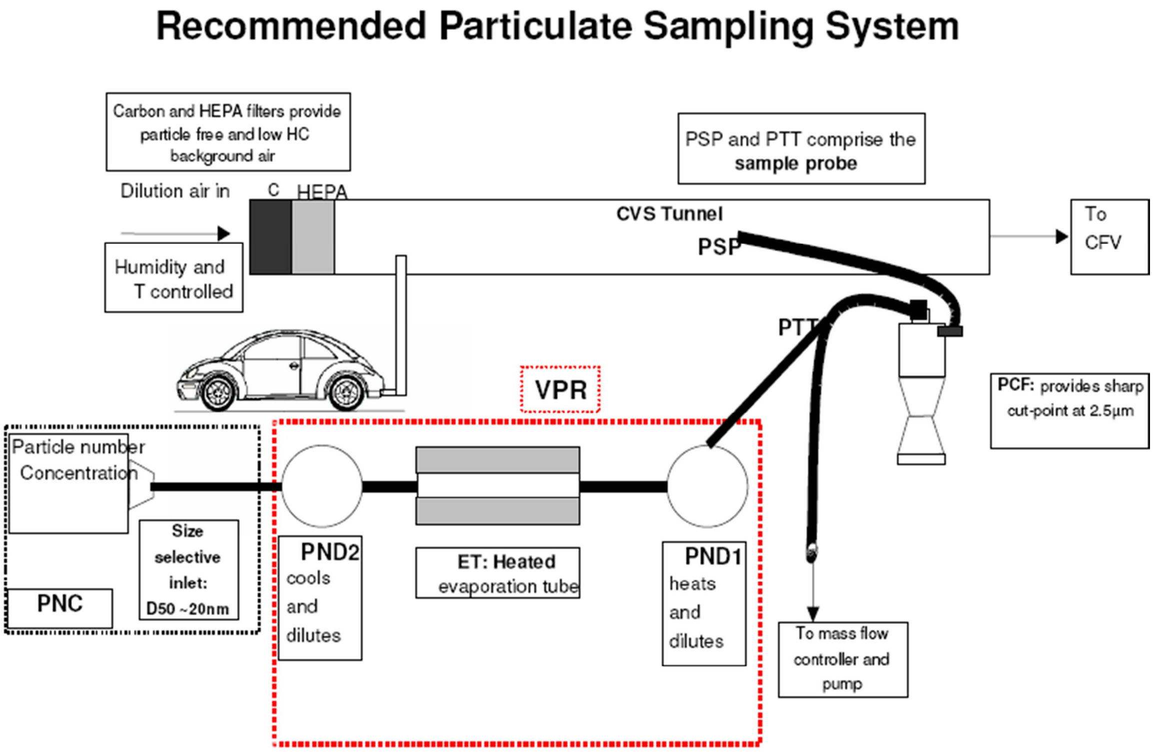

Fig. 5.1 Schematic of the PMP Recommended Particle Sampling System [61].

Table 5.1 Engine Operating Conditions

Engine Speed / rpm	1500
Engine Torque / N·m	90
Injection Pressure / MPa	15
Injection Timing	280° BTDC
Manifold Pressure / (bar absolute)	0.525
Ignition Timing:	30° BTDC
Cam Lift / mm	10.53
IVO/IVC	24° ATDC/274° ATDC
EVO/EVC	244° BTDC/6° ATDC
Coolant Temperature / ºC:	90

The test engine was a Jaguar naturally aspirated, V8 direct injection spark ignition engine [56]. The specifications of the engine and the layout of the combustion system have been described in Chapter 2. The main characteristics of the engine operating conditions are listed in Table 5.1. A representative part load warm operation point was used. During these tests, the engine speed and engine torque were controlled to 1500 rpm and 90 N·m. The spark timing was fixed at 30° before compression TDC. A single injection during the intake stroke was set at 280° before compression TDC and injection pressure of 15 MPa was used. High intake cam lift was selected, with the intake valve phasing set to the most retarded position and the exhaust valve phasing set to the most advanced position.

The catalytic VPR system tested in this work and the dimensions of the catalytic VPR are shown in Fig. 5.2. Its performance as an oxidation catalyst is discussed later in the context of Fig. 5.11. The catalytic VPR system consists of a temperature controlled heated tube with an oxidation catalyst inside. The effects of the VPR temperature and residence time on the catalytic VPR performance were examined

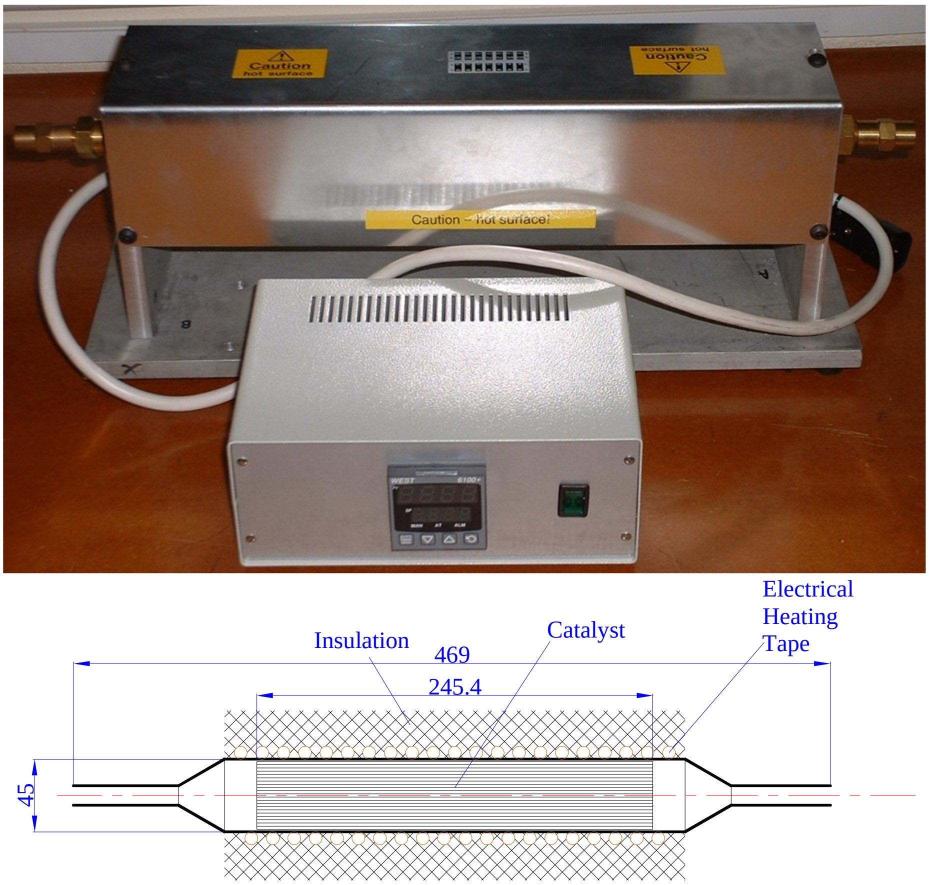

Fig. 5.2 *Catalytic Volatile Particle Remover (VPR) system*

It can be seen from Fig. 5.3 that in test 1, the exhaust pre-TWC was drawn into the catalytic VPR, so that the raw engine exhaust is passed through the VPR. At each test point, the PM emissions pre-VPR and post-VPR were measured using a Cambustion DMS500 particle sizer [58]. The sampling flow rate of the DMS (MFM_{DMS}) was set to 0.02 g/s. A pneumatic switching valve was used to select between pre-VPR and post-VPR. The switching valve was heated by hot air to keep the sampling temperature at around 90 °C, thereby preventing particle formation by condensation. The temperature of the sampling flow pre and post VPR, as well as the flow temperature entering DMS, were measured using thermocouples. Downstream of the catalytic VPR, the exhaust flow then entered a dilution system (shown in the right hand side rectangle in Fig. 5.3), where it mixed with heated dilution air. A needle valve was used to control the flow rate of dilution air (MFM_{air}, the mass flow rate measured by mass flow meter 1). An electric heater was used to control the dilution air temperature to maintain the temperature of the diluted gas (exhaust + dilution air) entering the glass fibre filter at 47 °C. This was achieved by utilizing a LabVIEW PID code to control the output voltage to the electric heater. The heated dilution system was to prevent condensation in the gas flow. Then the diluted gas was extracted out of the dilution system by a pump, of which the flow rate was unchanged. As a result, the flow rate of the vacuum pump ($\mathrm{MFM_{pump}}$, mass flow rate measured from mass flow meter 2) was determined by the pump. The total mass flow rate of exhaust ($\mathrm{MFM_{exhaust}}$) was calculated using the following equation.

$$\mathrm{MFM_{exhaust}} = \mathrm{MFM_{pump}} - \mathrm{MFM_{air}} + \mathrm{MFM_{DMS}} \tag{5.1}$$

The mass flow meters had been calibrated against each other *in situ*, so as to minimise errors in computing the mass flow rate of the exhaust. By varying $\mathrm{MFM_{air}}$, $\mathrm{MFM_{exhaust}}$ would be changed. As a result, the residence time of the exhaust gas in the catalytic VPR was varied, and the effects of exhaust residence time on PM emissions were studied by means of varying the flow rate of the dilution air. Also, in this test, the VPR temperature was changed to investigate its effect on the VPR performance. The test conditions are listed in Table 5.2. The residence time (t_r) is calculated assuming a linear variation in the temperature within the catalytic VPR along its length.

$$\dot{V} = \frac{\dot{m} \times R_s \times (T_1 + T_2)/2}{P} \tag{5.2}$$

$$t_r = V / \dot{V} \tag{5.3}$$

where $\dot{V}$ ($\mathrm{m^3/s}$) represents the volume flow rate through the VPR, $\dot{m}$ (g/s) represents the mass flow rate through VPR, R_s ($\mathrm{J \times g^{-1} \times K^{-1}}$) represents the specific gas constant of exhaust, T_1 (K) represents the pre-VPR temperature, T_2 (K) represents the post-VPR temperature, P (Pa) represents the exhaust pressure, t_r (s) represents the residence time, V (m^3) represents the inner volume of the catalytic VPR.

Table 5.2 Residence times (s) for Test 1

VPR Temperature / °C	$MFM_{exhaust}$ / (g/s)				
	0.02	0.09	0.11	0.14	0.22
150	15.9	3.36	2.68	2.05	1.24
250	14.8	3.01	2.35	1.76	1.08
350	13.8	2.98	2.29	1.71	1.02

In test 2, the exhaust was sampled downstream of the TWC. It can be seen from Fig. 5.4 (in the left hand rectangle) that an additional gas supply route is added to the set-up. To further study the oxidation effect of the catalytic VPR, gaseous emissions were also measured during experiments. A Flame Ionisation Detector (FID) was used to measure hydrocarbon (HC) emissions, and a separate gas analyser was used to measure CO, CO_2, O_2, and NO_x emissions. The FID and gas analyser were sampling at the same point as the DMS500 particle sizer. During the experiments, the engine was operated at both stoichiometric and rich air fuel ratios. To study the oxidation effect of the catalytic VPR on particles, at each air fuel ratio, various amounts of additional gas (Air or N_2) were added upstream of the catalytic VPR. To control the amount of air added, a Lambda sensor was fitted downstream of the catalytic VPR, and when adding N_2, its amount was adjusted to be the same as the air addition using a mass flow meter. Nitrogen was selected as an alternative to air, so as to distinguish between physical and chemical effects when there was a reduction in the number of particles.

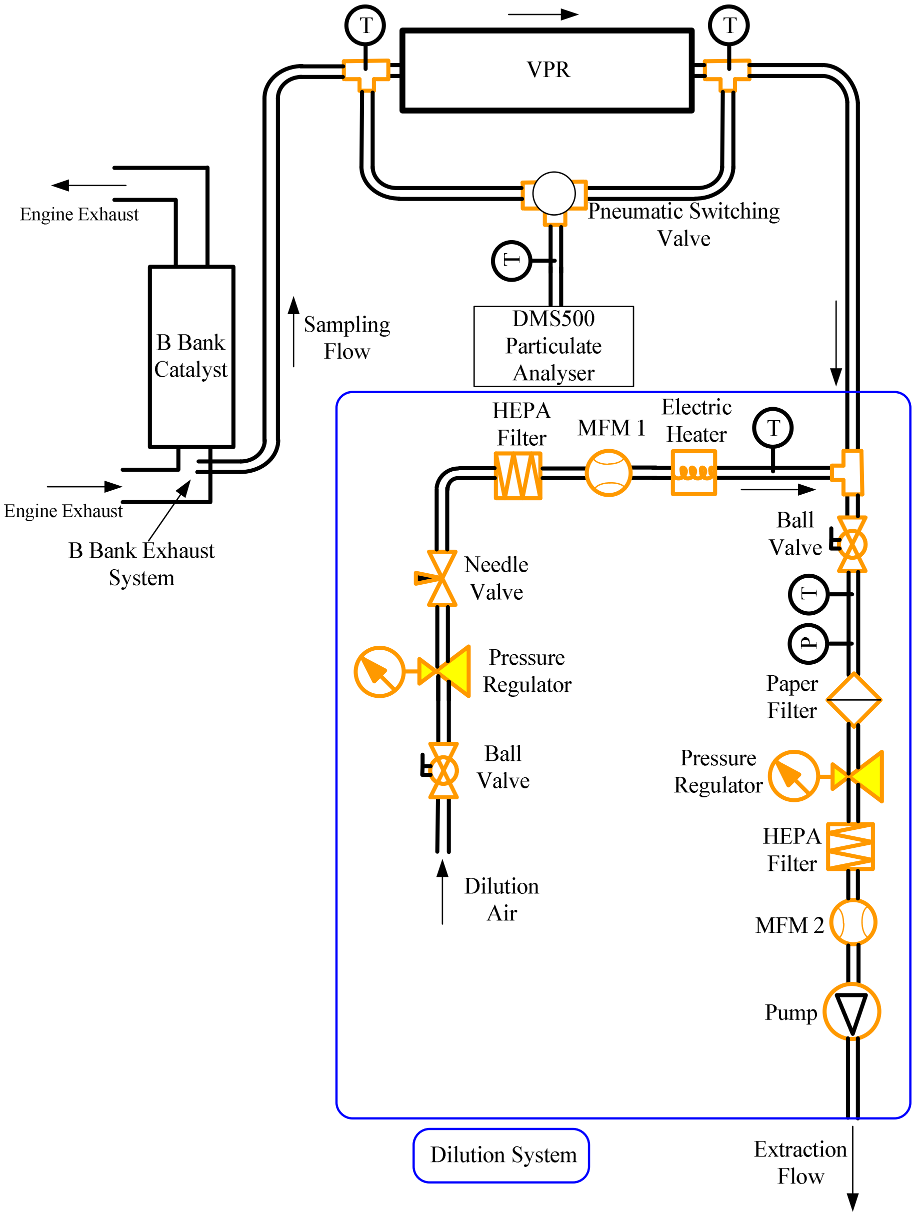

Fig. 5.3 Experimental set-up for Test 1

The test procedure was as follows. At each engine Lambda (actual air to fuel ratio/stoichiometric air to fuel ratio), supplementary air was first used to study the oxidation effect of the catalytic VPR. By adjusting the needle valve in the additional gas supply route, the mass flow rate of the additional air was controlled to give the Lambda meter reading that was 0.1, 0.2 or 0.3 above the Lambda that the engine was operating at. At each Lambda meter reading, the mass flow rate of the additional gas ($MFM_{add\ gas}$) was measured by MFM 3 and was recorded. Then, the air supply was swapped with nitrogen (N_2) to investigate the dilution effects of additional gas on the PM emissions. At each engine operating point, the needle valve was adjusted to let MFM 3 give the same readings as those recorded in the experiments with additional air. By comparing the two sets of results (additional air against N_2), the oxidation effect and dilution effect of the additional gas can be examined separately. The VPR Dilution Factor (VPR-DF) is defined as:

$$\text{VPR-DF} = 1 + (\text{MFM}_{\text{add gas}} / \text{MFM}_{\text{exhaust}}) \tag{5.4}$$

where $\text{MFM}_{\text{exhaust}}$ represents the total mass flow rate of exhaust.

When testing with additional air at stoichiometric conditions, the VPR-DF is the same as the Lambda meter reading downstream of the catalytic VPR. The test point conditions are listed in Table 5.3.

During the experiments, both the raw data and lognormal fits of DMS signal were logged into the computer for a number of samples. The DMS sampling line is maintained at 80 °C, and internally controlled dilution air is preheated before being mixed with the sample at entry to the sampling line. Before entry to the DMS sampling line, the pipework and pneumatic switching valve were maintained at above 80 °C. A typical sample flow into the DMS was 2 LPM so the residence time in the sampling system is very short (~4 s) so diffusion and thermophoretic losses can be ignored. The DMS lognormal output is generated by a Bayesian statistical algorithm [62], which separates the nucleation mode from the accumulation mode particles. The DMS data analysis and the algorithm of the DMS lognormal fitting have already been discussed in Chapter 2. The DMS output is a matrix containing number concentration at a given sample number (i.e. time) and particle diameter. The number matrix is then converted to a mass matrix by using an empirical equation (Eq. 2.1). The number matrix and mass matrix are averaged to find a mean concentration plot over particle diameter, which can then be integrated to obtain the total number and total mass of particles emitted by the engine.

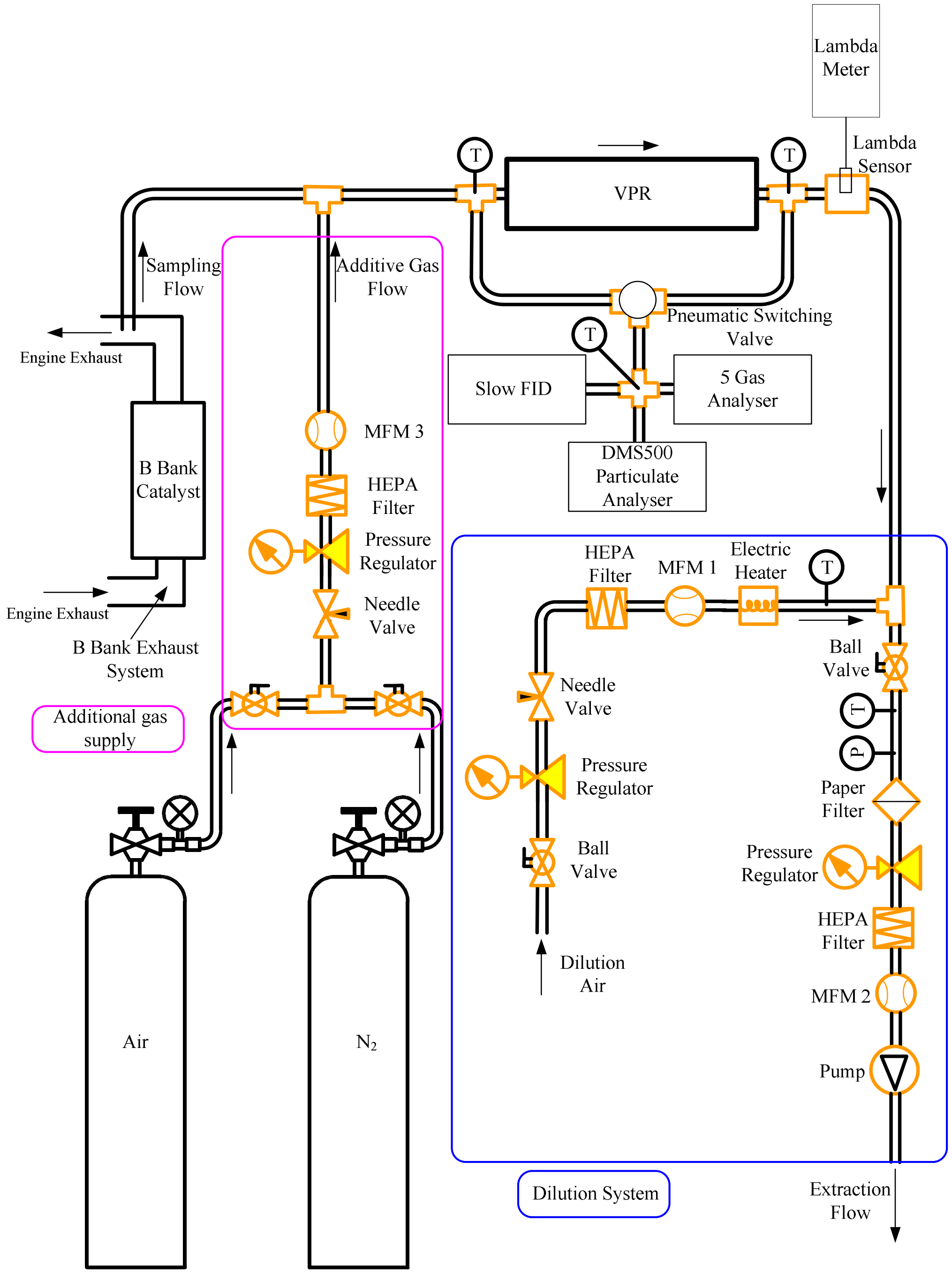

Fig. 5.4 Experimental set-up for Test 2

During the experiments, both the raw data and lognormal fits of the DMS signal were logged for 90 s. The data was logged at 10 Hz and downsampled so that a reading was recorded every second, along with the corresponding bi-lognormal fits. The data were subsequently averaged over the 90 second measurement period.

Table 5.3 Mass flow rate of additional gas (g/s) for Test 2

VPR Temperature / °C	Engine Lambda	Additional Gas	VPR-DF			
			1	1.1	1.2	1.3
250	1	Air	0	0.02	0.04	0.06
		N_2	0	0.02	0.04	0.06
	0.9	Air	0	0.02	0.04	0.06
		N_2	0	0.02	0.04	0.06

5.3 Effects of VPR on Engine Particulate Emissions

The experimental results reported here are divided into two parts corresponding to the tests described above, and are an average of data measured for 90 seconds.

5.3.1 Effects of VPR Temperature and Residence Time on VPR Performance

Fig. 5.5 shows the temperatures of the pre-VPR and post-VPR sample points under different test conditions. It can be seen that the temperatures pre-VPR and post-VPR increase as the mass flow rate of the exhaust becomes higher, showing that the mass flow rate of the exhaust extraction affects the temperature at inlet and outlet of the VPR. This is because as the $MFM_{exhaust}$ increases, the velocity of the exhaust becomes higher, which leads to less cooling per unit mass along the copper pipe connecting the engine exhaust pipe to the catalytic VPR.

Fig. 5.6 shows a representative raw size distribution from the DMS data and its lognormal fitting, which was taken pre-VPR under 250 °C VPR temperature and 0.14 g/s mass flow rate of exhaust. It can be seen that the bi-lognormal result fits the trend of the raw data very well. The peak of the nucleation mode particles is higher than that of the accumulation mode particles, indicating that a large portion of the particles emitted were in the nucleation mode as the exhaust gas was sampled upstream of the three way catalyst. As the lognormal fitting is very useful in eliminating the noise in the raw data at both the high and low end of the particle size range, the lognormal fitting results are used in the following analysis.

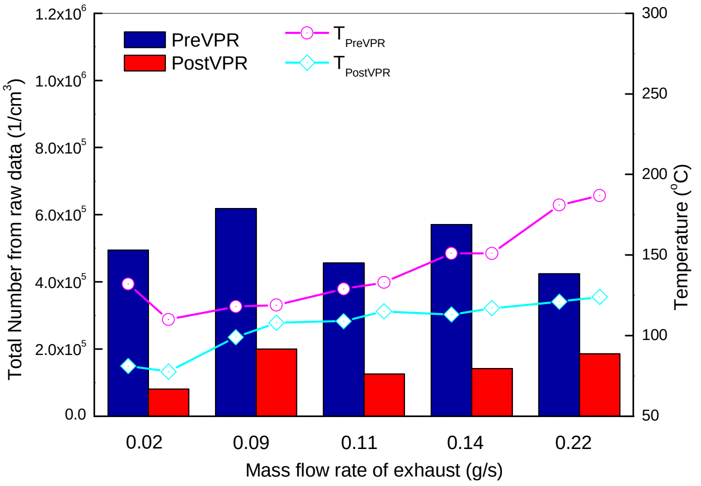

(a) VPR 150 °C

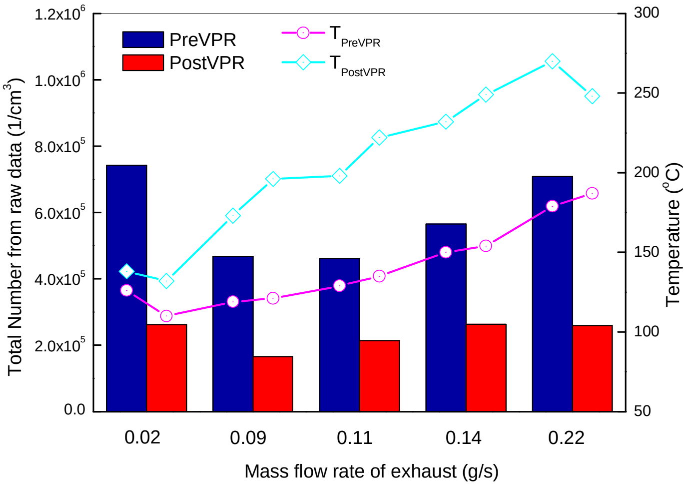

(b) VPR 250 °C

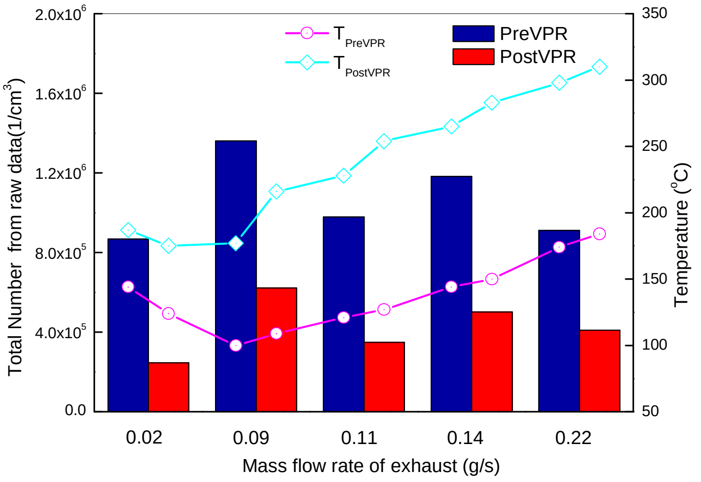

(c) VPR 350 °C

Fig. 5.5 Pre and post VPR temperatures with different mass flow rates of exhaust ($MFM_{exhaust}$) and different VPR temperatures (refer to Table 5.2).

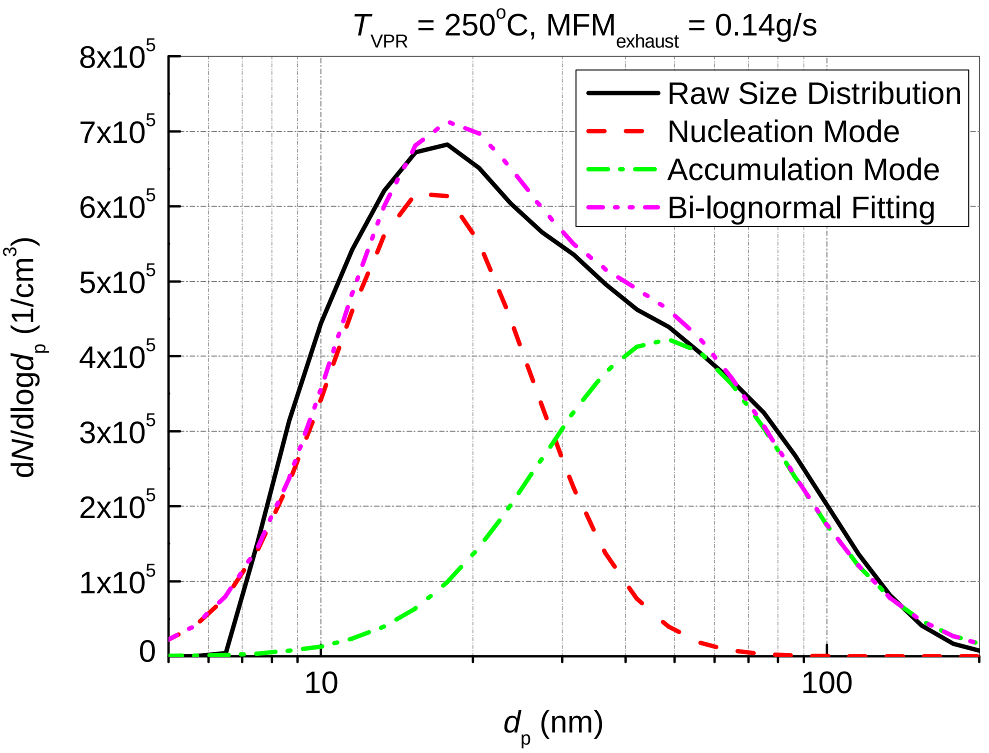

Fig. 5.6 Representative size distribution of raw data and its lognormal fittings (pre-VPR sampling, VPR temperature 250 °C, $MFM_{exhaust}$ = 0.14g/s, refer to Table 5.2).

Further analyzing the total number and mass ratio (Post-VPR/Pre-VPR) of the total PM, nucleation mode and accumulation mode (Fig. 5.7 and Fig. 5.8), it can be seen that at each measurement point, the mass ratio of the Total PM is higher than the number ratio. This indicates that the reduction of PM number in the nucleation mode leads to a more noticeable reduction of total PM number than that of total PM mass. In other words, although the number reduction ratios of the nucleation mode particles are higher than those of the accumulation mode particles, as their sizes are much smaller than those of accumulation mode particles, they contribute more to the reduction of total P_n and less to the reduction of total P_m. The number and mass ratios are in the following order:

nucleation mode < Total PM < accumulation mode.

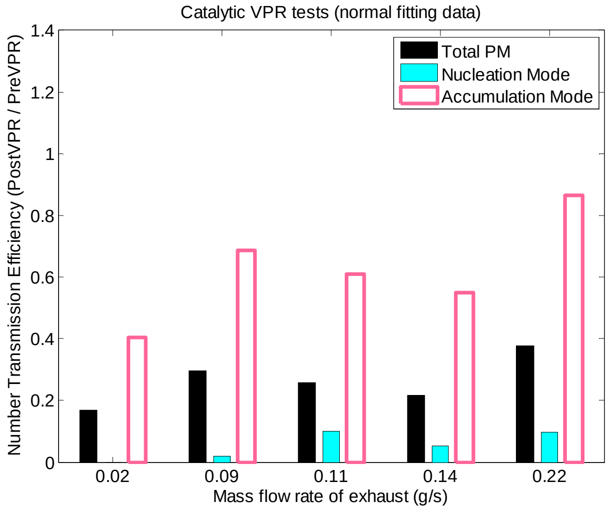

(a) VPR 150 °C, Number ratio

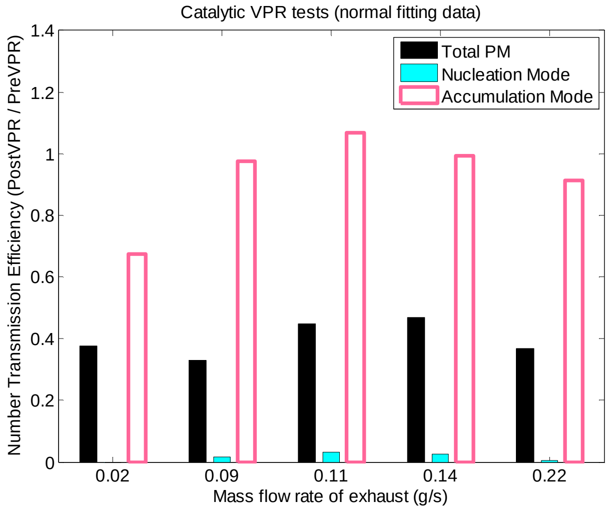

(b) VPR 250 °C, Number ratio

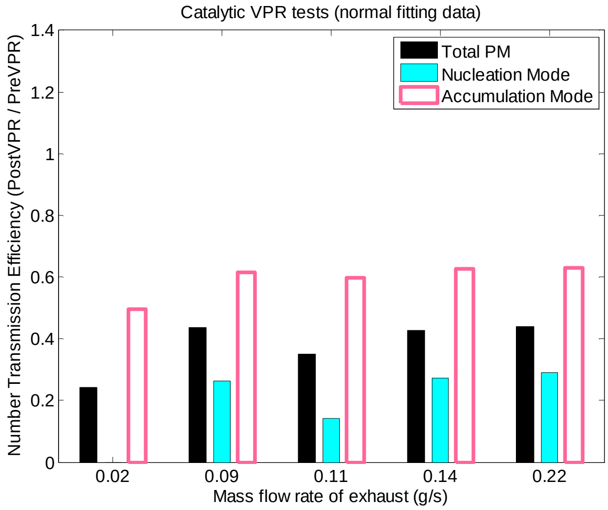

(c) VPR 350 °C, Number ratio

Fig. 5.7 Number transmission efficiencies for different modes (Total, Nucleation and Accumulation) for different sample flow rates ($MFM_{exhaust}$) and different VPR temperatures (refer to Table 5.2).

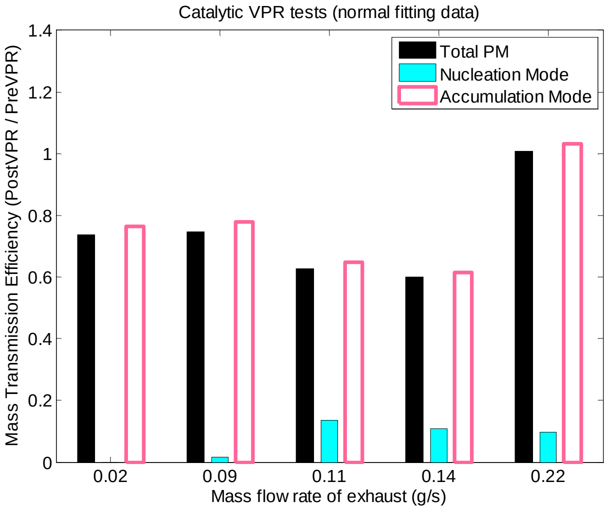

(a) VPR 150 °C, Mass ratio

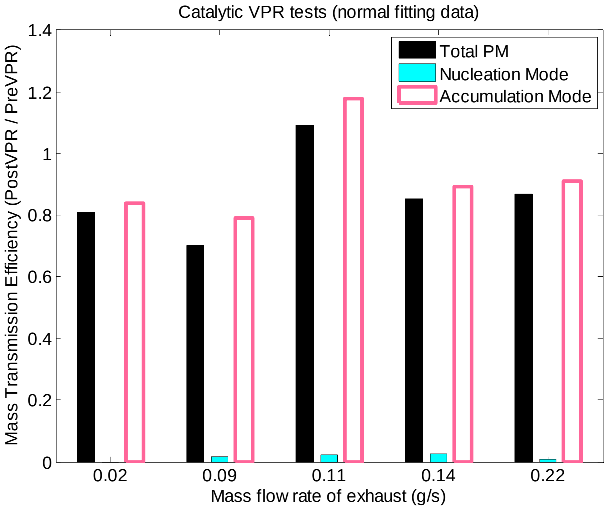

(b) VPR 250 °C, Mass ratio

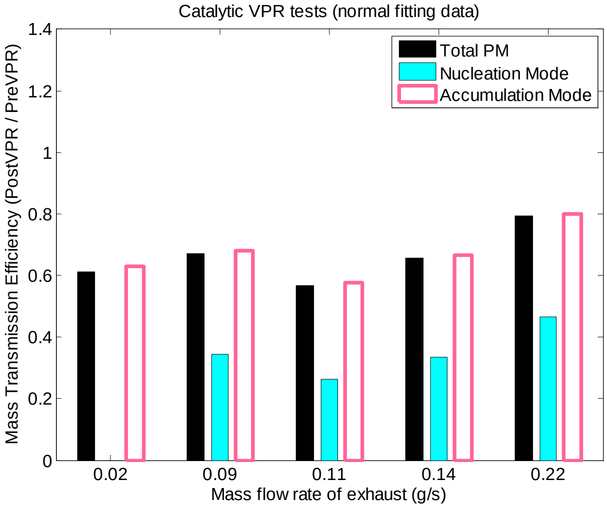

(c) VPR 350 °C, Mass ratio

Fig. 5.8 Mass transmission efficiencies for different modes (Total, Nucleation and Accumulation) for different sample flow rates (MFM$_{exhaust}$) and different VPR temperatures (refer to Table 5.2).

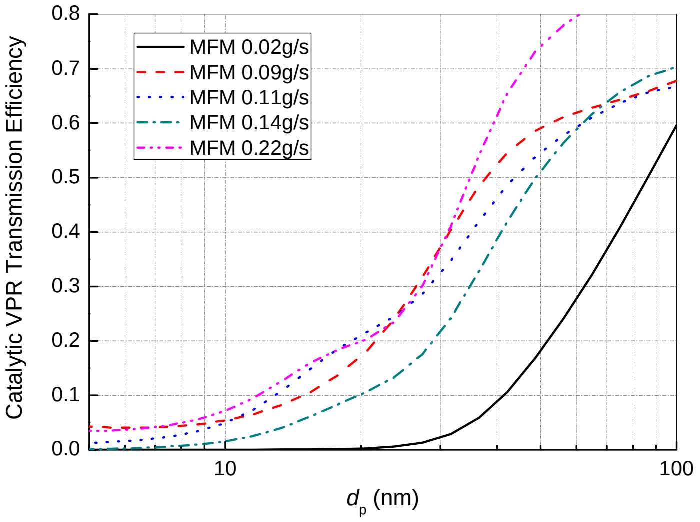

(a) VPR 150 °C

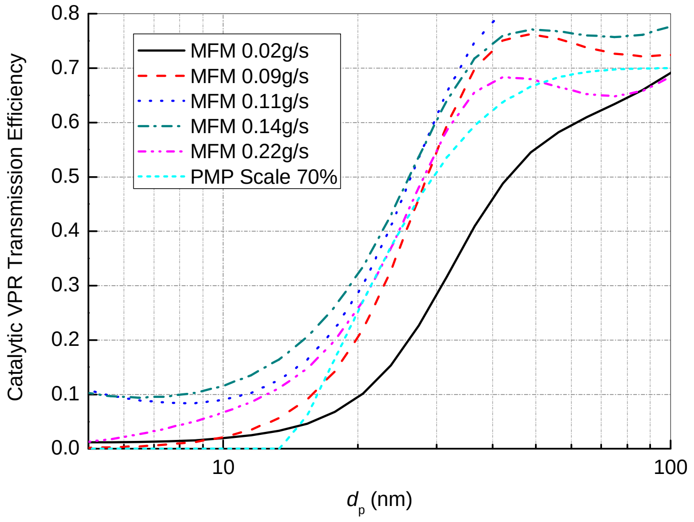

(b) VPR 250 °C

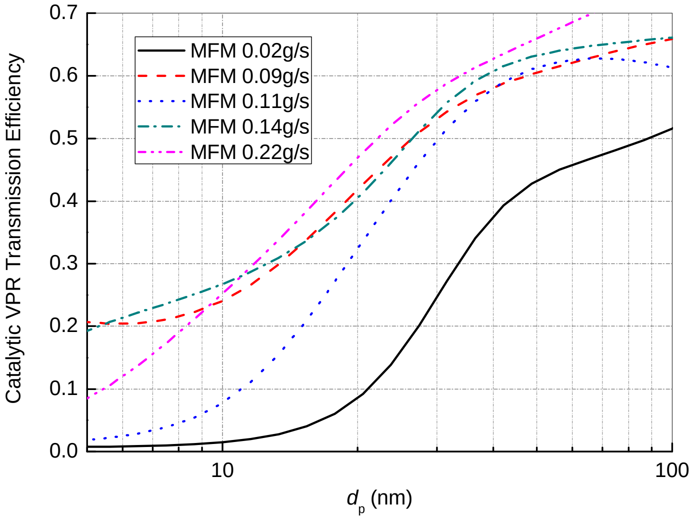

(c) VPR 350 °C

Fig. 5.9 Number transmission efficiencies versus d_p with different sample flow rates taken from the engine exhaust ($MFM_{exhaust}$) and different VPR temperatures (refer to Table 5.2).

The number transmission efficiency across the catalytic VPR is defined as:

$$\eta_{d\mathrm{p}} = n_{d\mathrm{p}}(\mathrm{downstream}) \,/\, n_{d\mathrm{p}}(\mathrm{upstream}) \tag{5.5}$$

where $\eta_{d\mathrm{p}}$ represents the transmission efficiency of the particle with diameter d_p, $n_{d\mathrm{p}}$(downstream) (#/cm^3) represents the number concentration of the particle with diameter d_p downstream of the catalytic VPR, $n_{d\mathrm{p}}$(upstream) (#/cm^3) represents the number concentration of the particle with diameter d_p upstream of the catalytic VPR.

The number transmission efficiencies are shown in Fig. 5.9. The curves are calculated using the DMS lognormal results. It can be seen that the transmission efficiencies increase as the particle size increases. The curves for different VPR temperatures and $\mathrm{MFM_{exhaust}}$ are similar, except that the curves for $\mathrm{MFM_{exhaust}}$ = 0.02 g/s show relatively lower transmission efficiencies at the low end of the particle size range (< 50 nm). Also these results show that the catalytic VPR has more effect on the nucleation mode particles than the accumulation mode particles. In some cases, for example at 250 °C VPR temperature and 0.11 g/s $\mathrm{MFM_{exhaust}}$, a sudden rise of the transmission efficiency can be seen at the high end of the particle size range. This is due to noise in the raw DMS data at the high end of the particle size range. Also, it can be seen for particles with d_p > 40 nm the loss is about 30 % as the exhaust flows through the catalytic VPR (e.g. Fig. 5.9(b)). So as to account for the solid particle loss, the catalytic VPR transmission efficiencies can be compared with the 70 % scaled PMP counting efficiency (Eq. 5.6) as shown in Fig. 5.9(b).

$$f = \left(1 - \exp\left[-3.54\left(\frac{d_\mathrm{p} - 14}{40}\right)^{1.09}\right]\right) \times 0.7 \tag{5.6}$$

where d_p (nm) represents the diameter of the particles.

The PMP specification is for a 50% efficiency at 23 nm, and >90% at 41 nm. Once the $MFM_{exhaust}$ was above 0.09 g/s, the catalytic VPR transmission efficiencies for different size particles showed similar trends with the scaled PMP counting efficiency.

5.3.2 Effects of VPR Temperature and Residence Time on VPR Performance

As explained in section 2, the purpose of these tests is to see if the catalytic VPR could be used as an oxidation catalyst to reduce the particle number concentration. Only lognormal fitting data are used in the following analysis. The tests with nitrogen as a diluent (as opposed to air) enable the physical and chemical effects to be separated, and in order to separate out the dilution effect of the additional gas, a normalized specific PM emission has been calculated. The normalized specific PM emission is defined as the post-VPR PM concentration times the corresponding VPR dilution factor (VPR-DF) then divided by the pre-VPR PM concentration derived from the lognormal fitting data when no dilution gas is added:

$$P_{n,norm} = P_n \times \text{VPR-DF} / P_{n,\text{VPR-DF}=1} \tag{5.7}$$

$$P_{m,norm} = P_m \times \text{VPR-DF} / P_{m,\text{VPR-DF}=1} \tag{5.8}$$

where $P_{n,norm}$ represents normalized specific particle number emission, $P_{m,norm}$ represents normalized specific particle mass emission, P_n represents particle number emission (#/cm^3), P_m represents particle mass emission (kg/cm^3), $P_{n,\text{VPR-DF}=1}$ represents the particle number emission without dilution gas (#/cm^3) and $P_{m,\text{VPR-DF}=1}$ represents the particle mass emission without dilution gas (kg/cm^3).

Fig. 5.10 and Fig. 5.11 respectively show the particle number and particle mass weighted size distributions using the lognormal data, for the various test conditions listed in Table 5.3. In each plot, the lambda value shown in the title represents the engine lambda, while the VPR dilution factor (DF) values shown in the legend represent the sum of the mass flow rate of additional gas and the exhaust gas relative to the mass flow rate of the exhaust gas, under different test conditions. It can be seen that the dN/dlogd_p for a stoichiometric air-fuel ratio is much lower than that with a rich air-fuel ratio. At each combination of additive gas and engine lambda, there is a moderate reduction in dN/dlogd_p of post-VPR compared with that of pre-VPR. However, the dM/dlogd_p of post-VPR does not vary much compared with that of pre-VPR.

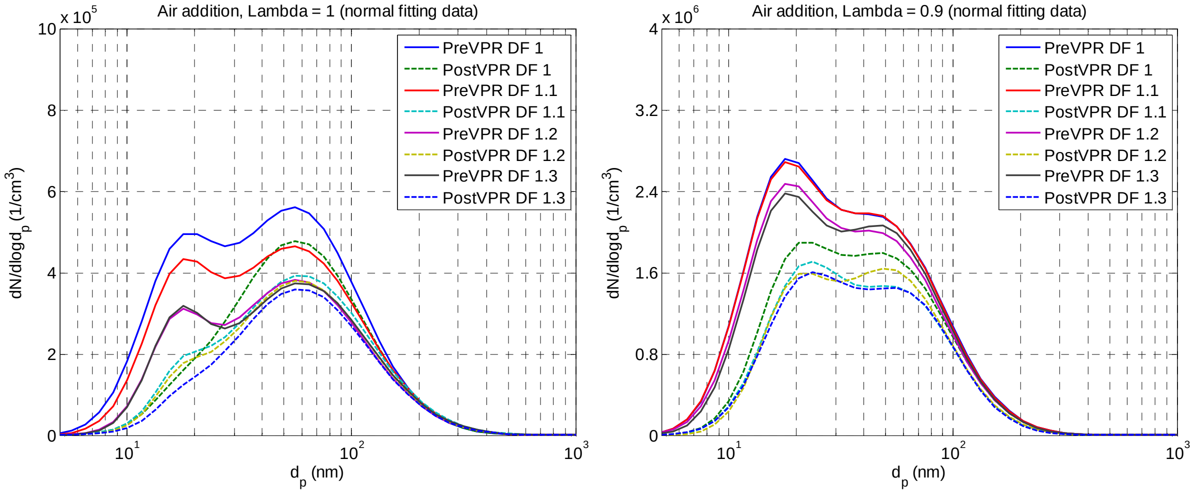

(a) Air addition, Lambda = 1

(c) Air addition, Lambda = 0.9

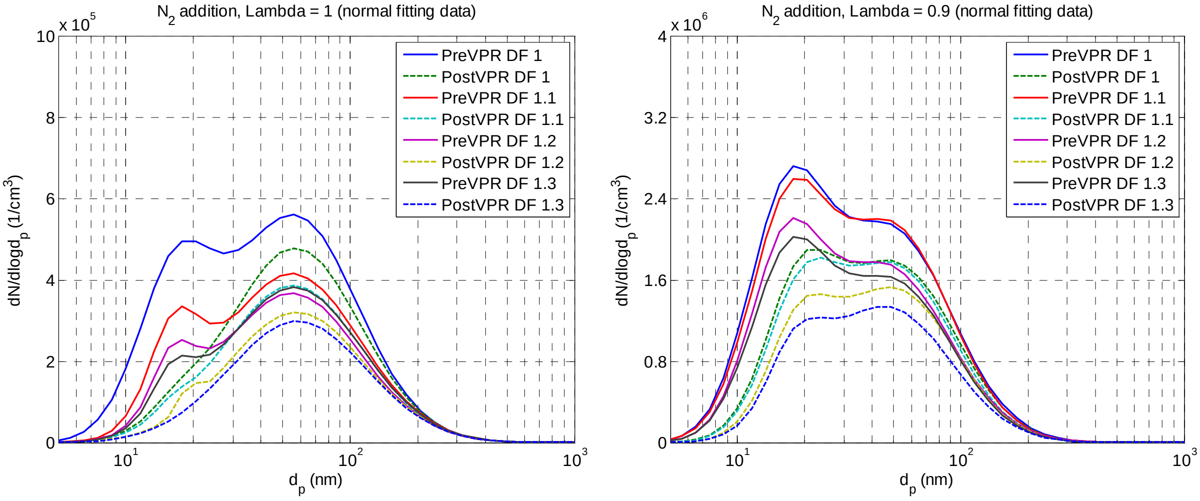

(b) N_2 addition, Lambda = 1

(d) N_2 addition, Lambda = 0.9

Fig. 5.10 PM number weighted size distributions with various gas additions and relative air-fuel ratios (refer to Table 5.3 for the Dilution Factors).

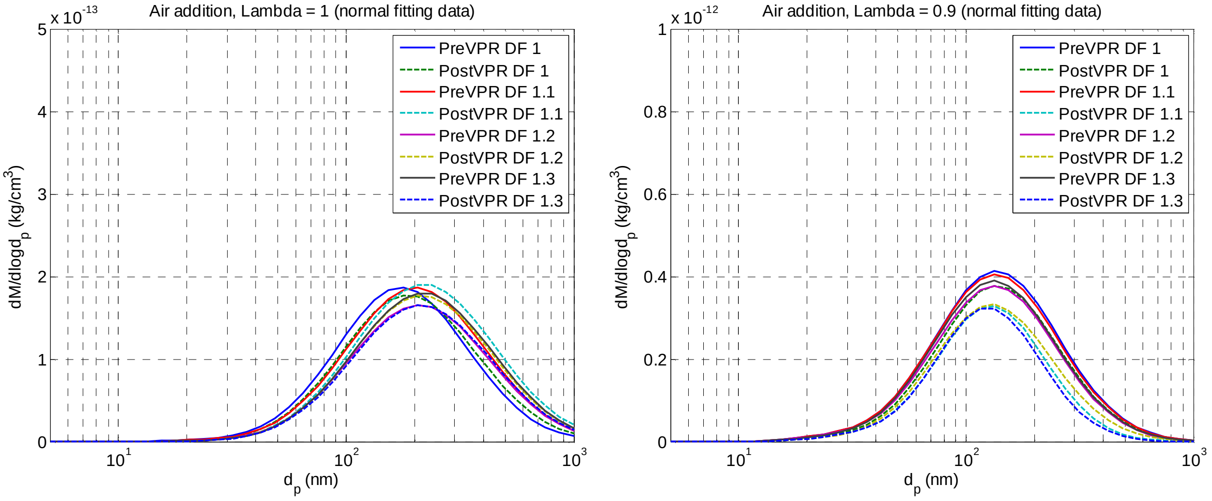

(a) Air addition, Lambda = 1

(c) Air addition, Lambda = 0.9

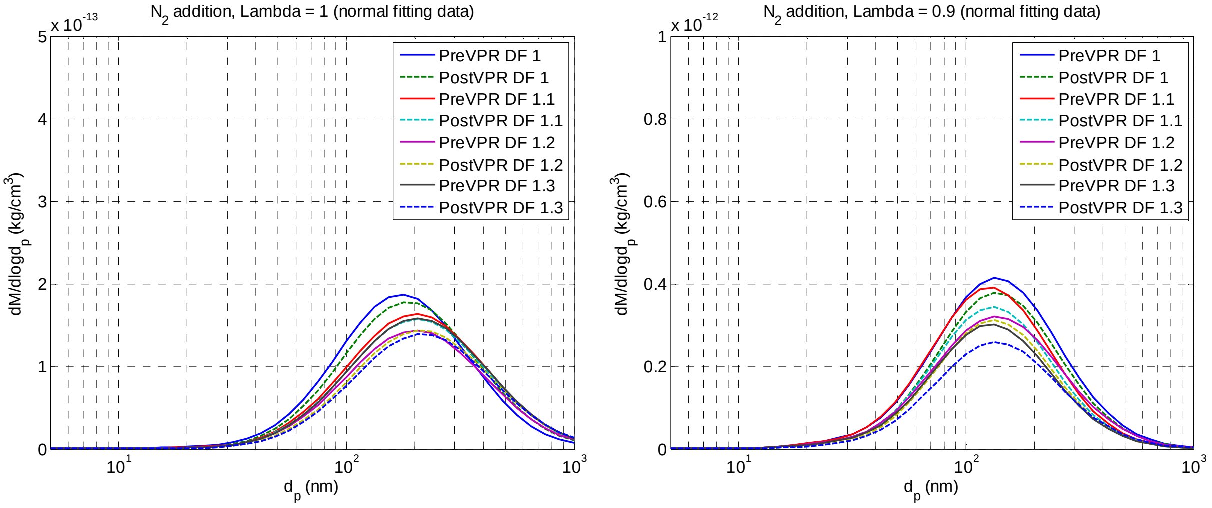

(b) N_2 addition, Lambda = 1

(d) N_2 addition, Lambda = 0.9

Fig. 5.11 PM mass weighted size distributions with various gas additions and relative air-fuel ratios (refer to Table 5.3 for the Dilution Factors).

Fig. 5.12 shows how increasing the Dilution Factor reduces the HC concentration by dilution, and it is for this reason that the PM emissions have been normalized by multiplying with the Dilution Factor. However, when excess air is added it can be seen that hydrocarbon oxidation is very effective, so that any hydrocarbons desorbed from the PM will be oxidised.

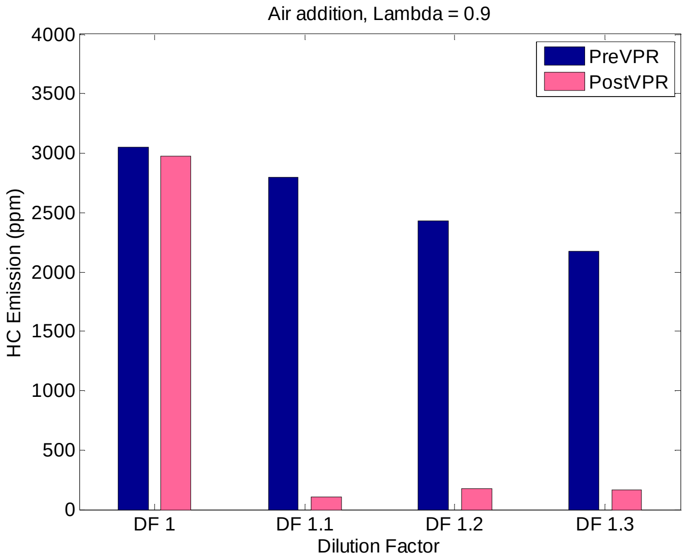

(a) Air addition, Lambda = 0.9

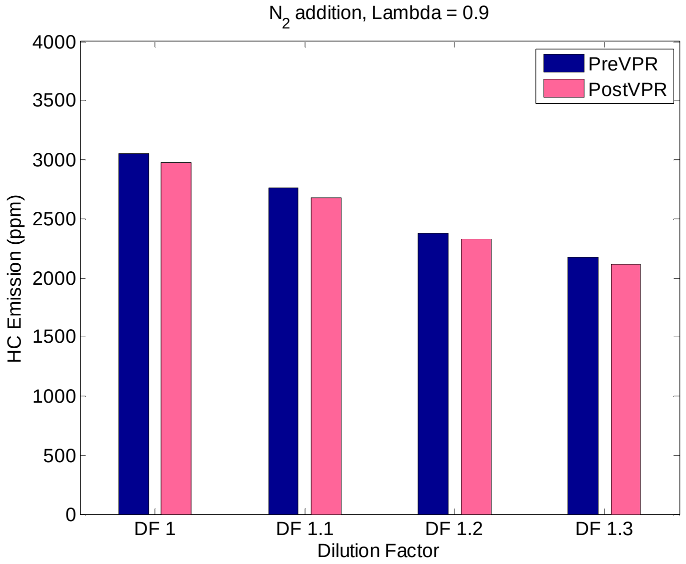

(b) N_2 addition, Lambda = 0.9

Fig. 5.12 HC emissions with either air or nitrogen addition under rich operation (refer to Table 5.3 for the Dilution Factors).

Using Eq. 5.7 and 5.8, Fig. 5.13 and Fig. 5.14 respectively show the normalized specific total particle number and mass concentrations calculated from lognormal fitting to the data under various test conditions. Comparing the post-VPR with the pre-VPR particle emissions, there is a consistent reduction in the total number which is independent of the dilution factor, and this is more clearly seen with the rich mixture (lambda = 0.9). The rich mixture gives a pre-VPR number concentration of typically 2.4×10^6 #/cm^3, and this is about 4 times the concentration at stoichiometric. The trend in the variation of the total mass pre and post VPR is less clear. For stoichiometric mixtures there is no change in mass, while for the rich mixture there is a reduction in mass. Since the reduction in mass occurs with dilution by either air or nitrogen, then this is a physical effect, not a chemical effect. This is further analysed in Fig. 5.15.

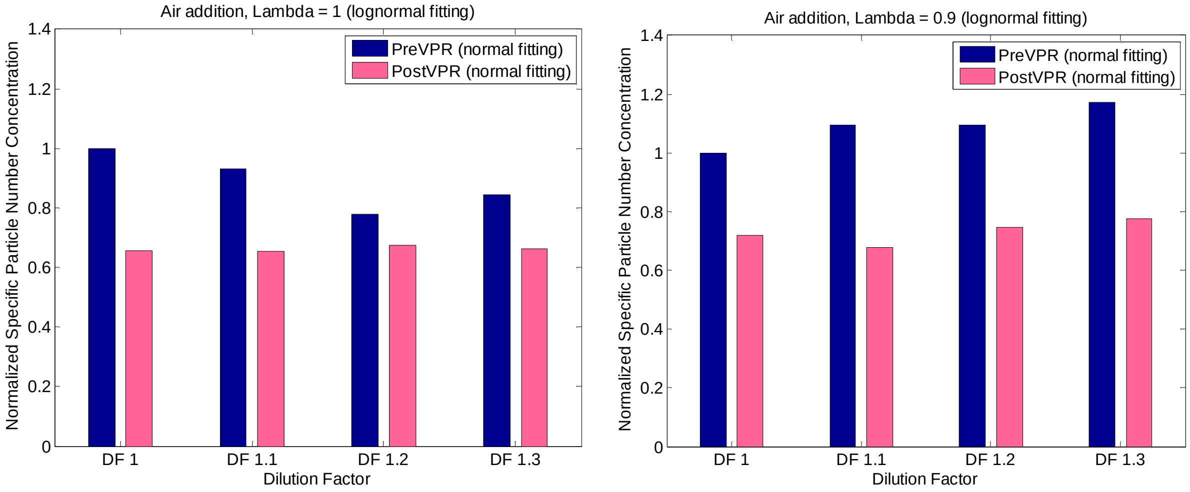

(a) Air addition, Lambda = 1 (c) Air addition, Lambda = 0.9

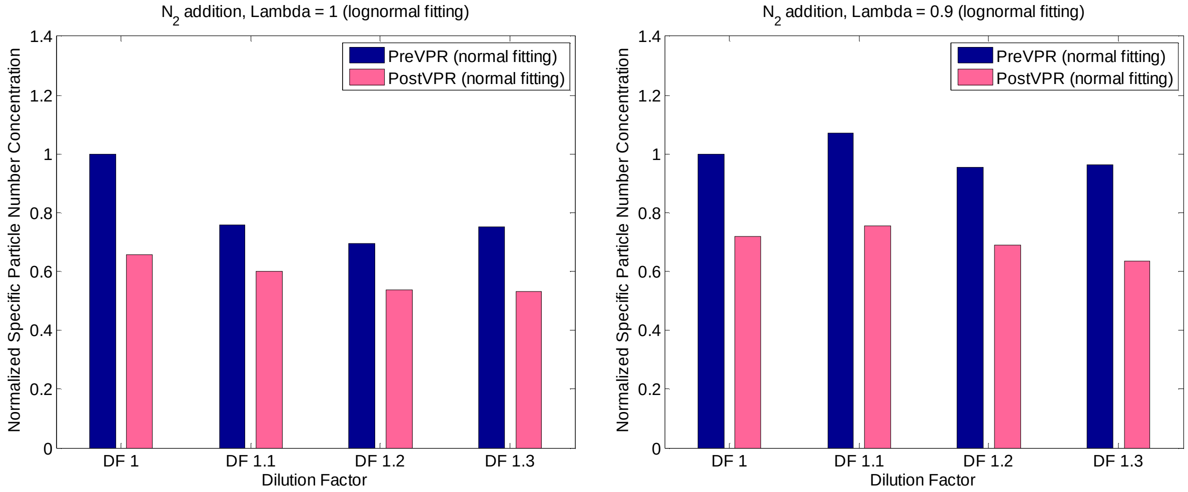

(b) N_2 addition, Lambda = 1 (d) N_2 addition, Lambda = 0.9

Fig. 5.13 Normalized specific particle number concentrations with various gas additions and relative air-fuel ratios (refer to Table 5.3 for the Dilution Factors).

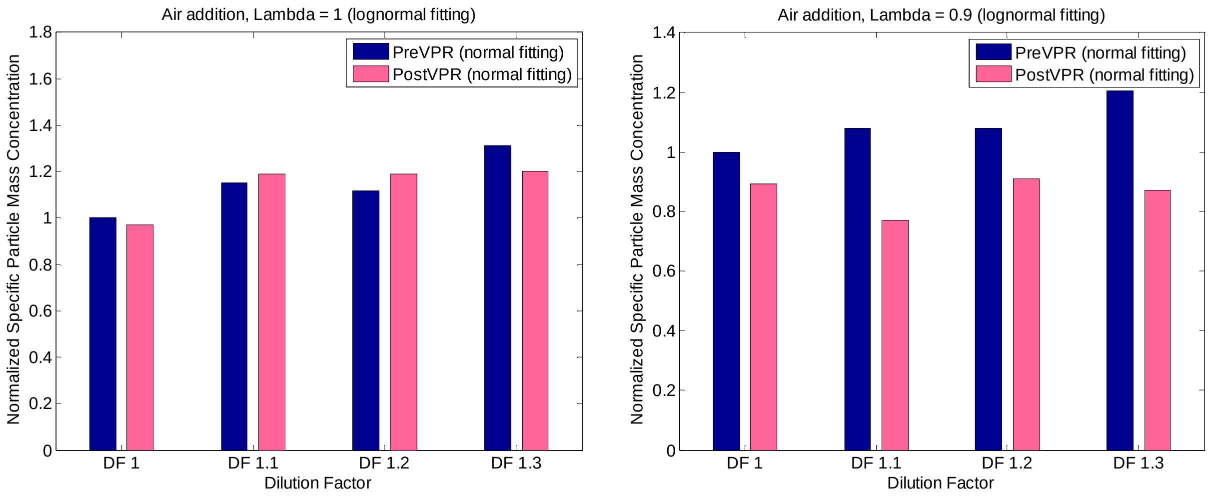

(a) Air addition, Lambda = 1 (c) Air addition, Lambda = 0.9

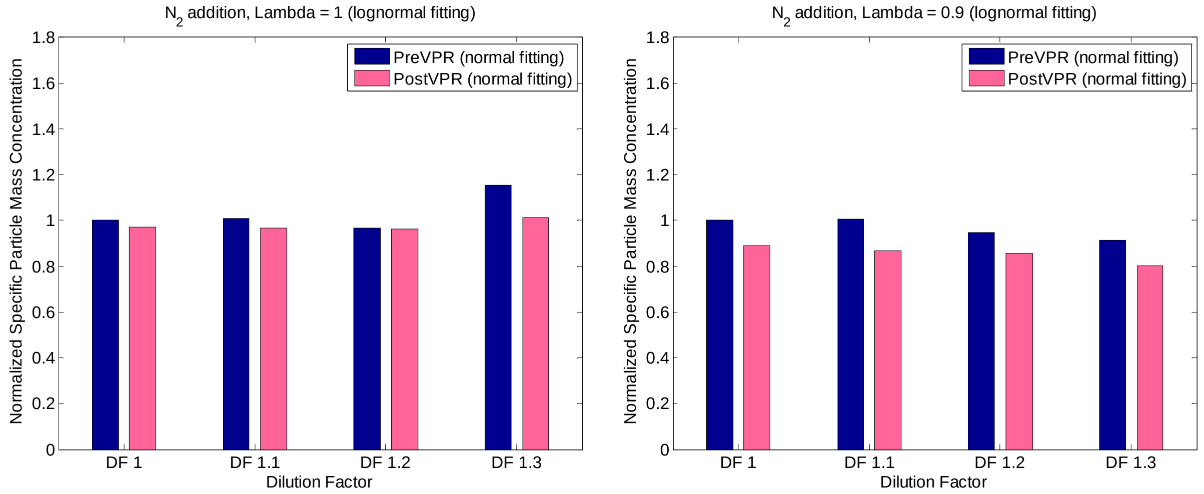

(b) N_2 addition, Lambda = 1 (d) N_2 addition, Lambda = 0.9

Fig. 5.14 Normalized specific particle mass concentrations with various gas additions and relative air-fuel ratios (refer to Table 5.3 for the Dilution Factors).

Data after lognormal fitting are used in Fig. 5.15, where the data from Lambda = 1.0 and 0.9 with a Dilution Factor of 1.2 has been selected as a representative data set. The fitted lognormal data have been used, since this eliminates the effects of noise in the measurements. Since the European legislation prescribes the use of a VPR, this has been achieved numerically by using Eq. 2.2. Digitally processed measurements from the DMS500 have been compared with measurements made in conformance with the European Method for a range of different engine types (including spray guided gasoline), Braisher et al [26], and very good agreement was found. The nucleation mode particle number concentration is lower than the accumulation mode particle number concentration because the exhaust sample is after the TWC. As expected from Eq. 2.2, the reduction in the nucleation mode particle number concentration is greater than for the accumulation mode particles. Also, as would be expected from Fig. 5.13 and Fig. 5.14 there is no difference between air and nitrogen as diluents. The effect of the numerical VPR (Eq. 2.2) is of course greatest for the nucleation mode particles and the difference between pre and post catalytic VPR is small after applying the numerical VPR.

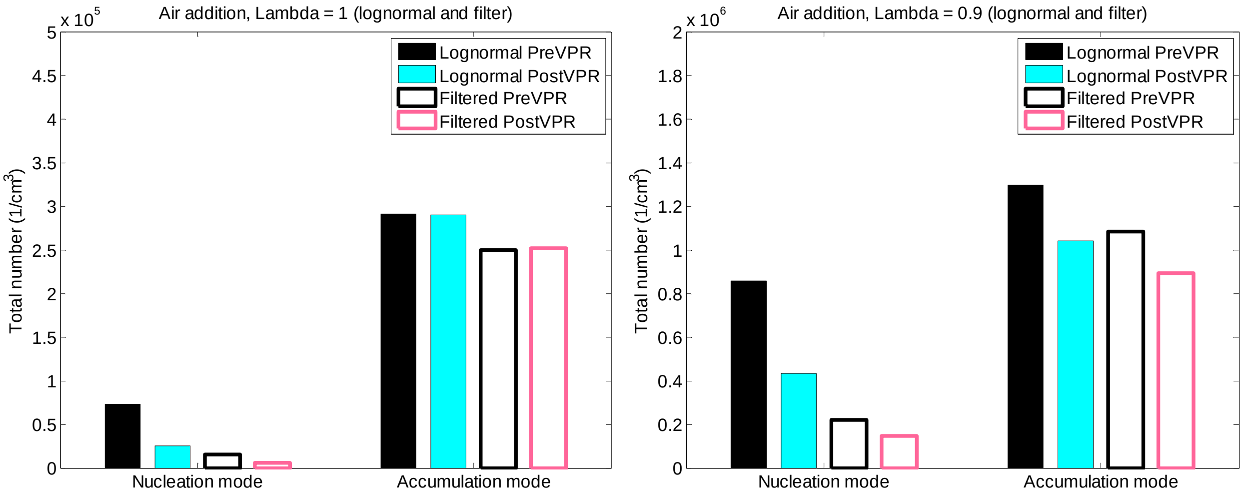

(a) Air addition, Lambda = 1 (c) Air addition, Lambda = 0.9

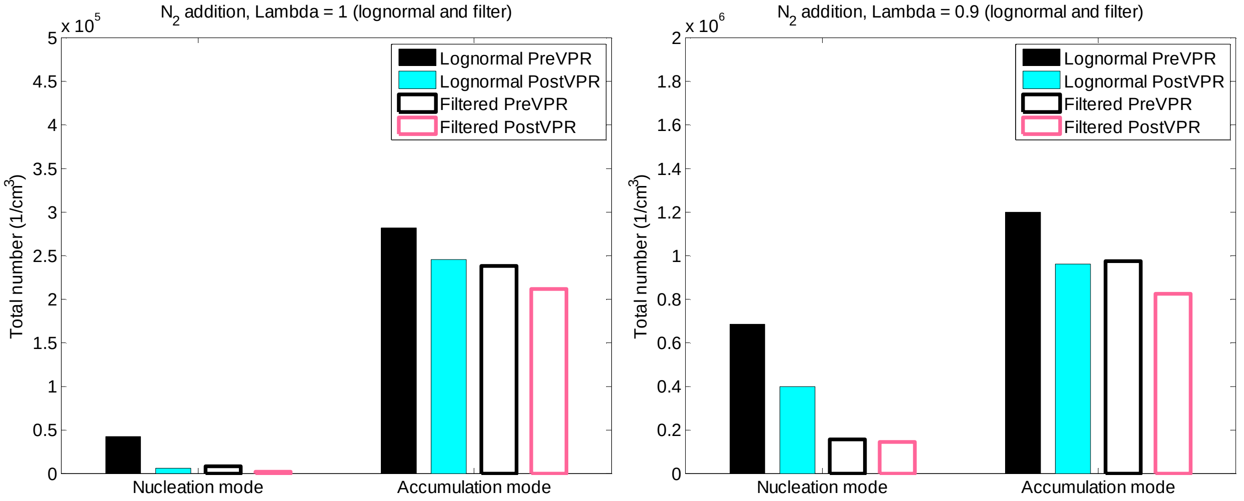

(b) N_2 addition, Lambda = 1 (d) N_2 addition, Lambda = 0.9

Fig. 5.15 Particle numbers in different modes with a Dilution Factor (DF) of 1.2 (refer to Table 5.3) obtained using lognormal fits to the pre and post VPR data and showing the effect of the PMP compliant digital filter.

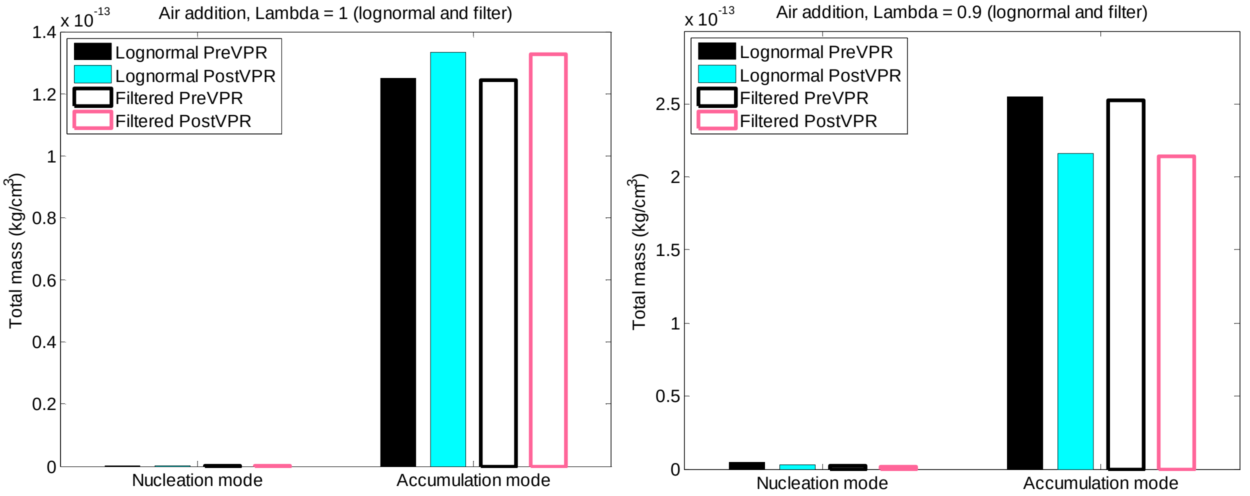

(a) Air addition, Lambda = 1

(c) Air addition, Lambda = 0.9

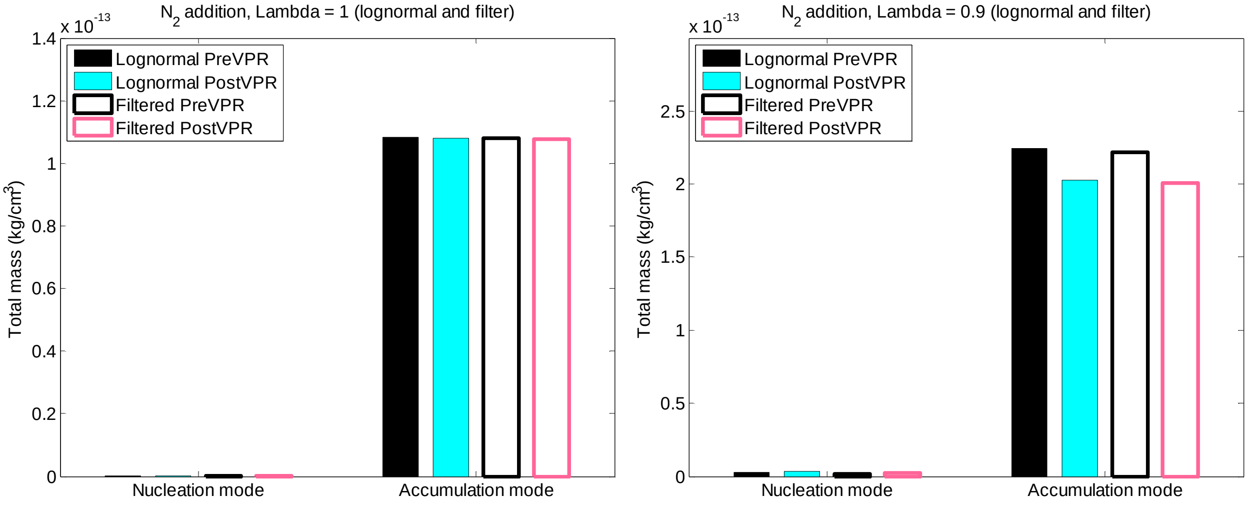

(b) N_2 addition, Lambda = 1

(d) N_2 addition, Lambda = 0.9

Fig. 5.16 Particle mass in different modes with a Dilution Factor (DF) of 1.2 (refer to Table 5.3) obtained using lognormal fits to the pre and post VPR data and showing the effect of the PMP compliant digital filter.

Fig. 5.16 shows the total particle mass concentrations corresponding to the total particle number concentrations shown in Fig. 5.15. It can be seen that the P_m in the accumulation mode is more than an order of magnitude higher than that in the nucleation mode. So the contribution of the nucleation mode particles to the total P_m is negligible. Also, little difference is observed in the total P_m in the accumulation mode with or without applying the numerical VPR and the difference between pre and post catalytic VPR is small. Further analyzing the total number ratio (Post-VPR/Pre-VPR) for the total PM, nucleation mode and accumulation mode (Fig. 5.17), it can be seen that at each measurement point for stoichiometric engine operation, the number ratios are in the following order: nucleation mode < Total PM < accumulation mode; this is not always seen for the rich operation cases. Although the oxidation effect of the catalytic VPR has been verified by the HC results (See Fig. 5.12), it seems that when engine was running rich of stoichiometric, the oxidation effects did not play much role in reducing the particle emissions. Apart from chemical reactions, some physical processes were taking place in the catalytic VPR as well.

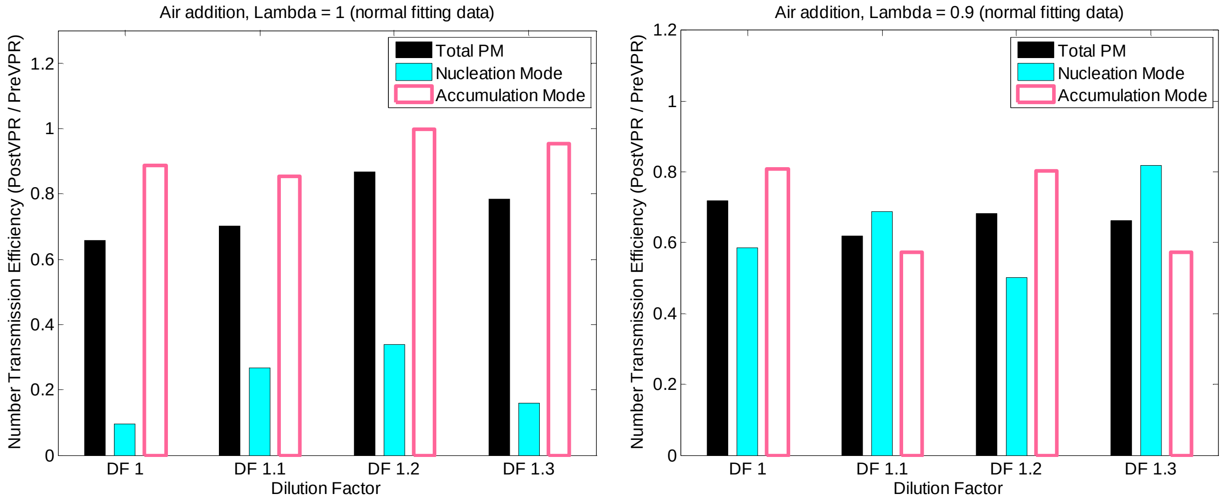

(a) Air addition, Lambda = 1

(c) Air addition, Lambda = 0.9

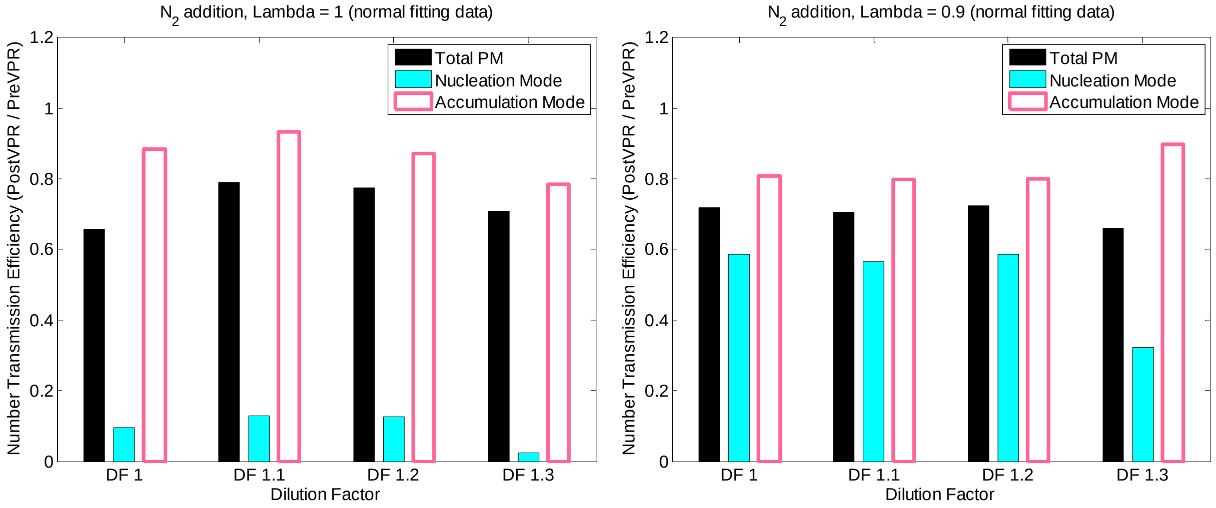

(b) N_2 addition, Lambda = 1

(d) N_2 addition, Lambda = 0.9

Fig. 5.17 Number transmission efficiencies for different modes (Total, Nucleation and Accumulation) with either air or nitrogen addition and Lambdas of 1.0 and 0.9 (refer to Table 5.3 for the Dilution Factors).

The number transmission efficiencies are shown in Fig. 5.18. It can be seen that the transmission efficiencies increase as the particle size increases, and the curves for the different engine lambdas and additional gases are very similar above 10 nm. These results show that the catalytic VPR has a greater reduction effect on the small size particles than the large size particles. The engine IMEP was well controlled and this is shown in the Appendix A (Fig. A1).

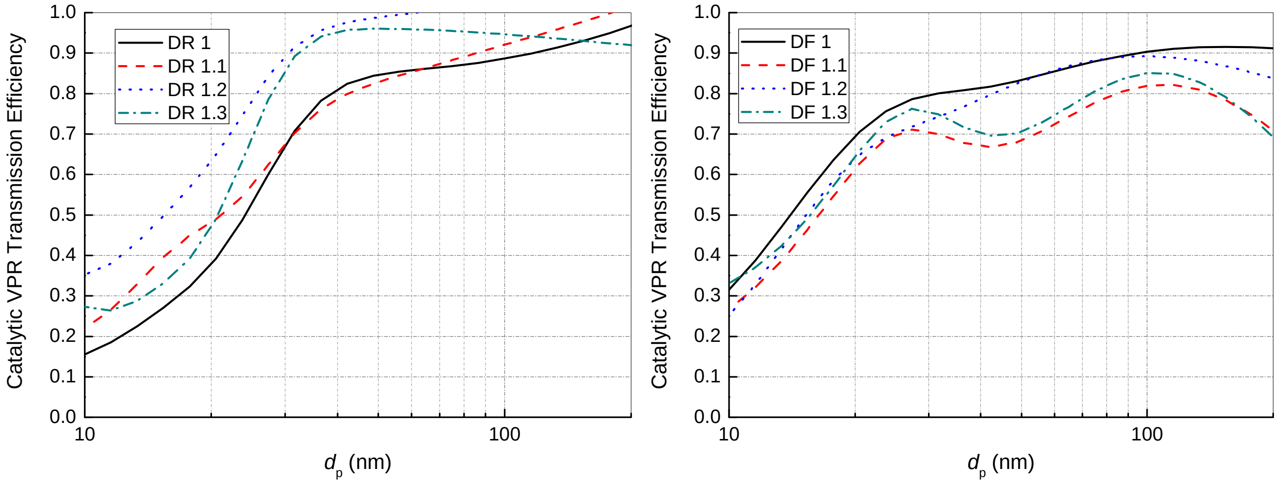

(a) Air addition, Lambda = 1

(c) Air addition, Lambda = 0.9

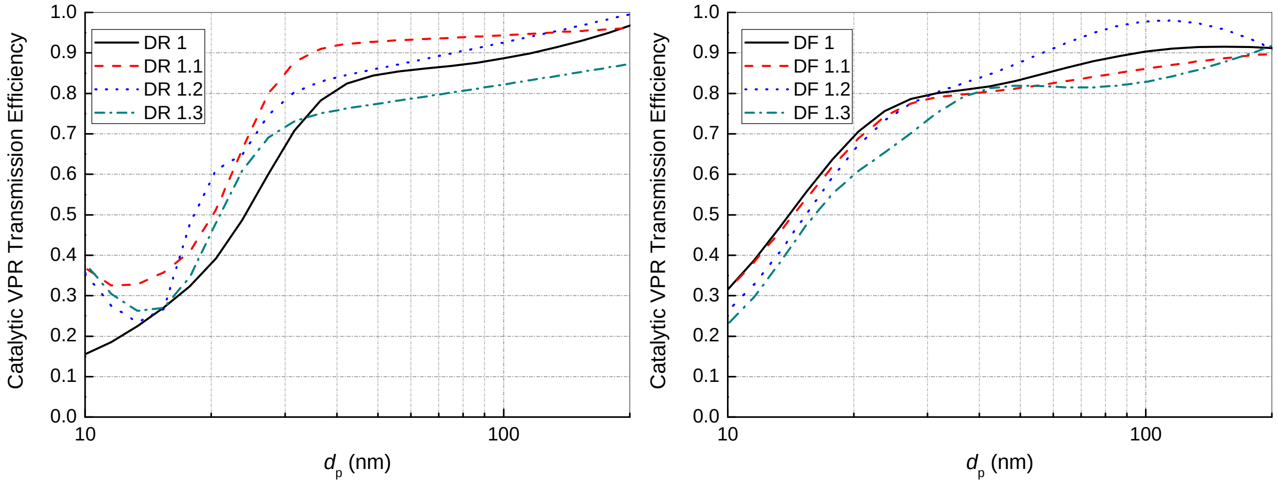

(b) N_2 addition, Lambda = 1

(d) N_2 addition, Lambda = 0.9

Fig. 5.18 *Number transmission efficiencies versus d_p with various gas additions and relative air-fuel ratios (refer to Table 5.3 for the Dilution Factors).*

5.4 Summary

The role of a catalytic VPR as an oxidation catalyst on engine particle emissions has been tested under different operating regimes with a GDI engine. The exhaust pre-TWC was passed through the catalytic VPR in test 1, with varying residence times and VPR temperature. The exhaust post-TWC was passed through the catalytic VPR in test 2, with varying quantities of either air or nitrogen addition, to study the potential of the catalytic VPR to further eliminate particle emissions. The results can be summarized as follows.

(1) With the pre-TWC engine exhaust, nucleation mode particles constitute a large portion of the total particle number but only constitute a small portion of the total particle mass. The catalytic VPR led to a significant reduction in the particle number, especially the smaller size (nucleation mode) particles.

(2) The VPR temperature and exhaust residence time ($MFM_{exhaust}$) did not have much influence on the catalytic VPR performance once the $MFM_{exhaust}$ was above 0.09 g/s. The catalytic VPR transmission efficiencies for different size particles showed similar trends for the various VPR temperatures and $MFM_{exhaust}$ tested. Generally, the transmission efficiencies of the VPR follow the trends of the scaled PMP counting efficiency.

(3) When post-TWC exhaust was introduced to the catalytic VPR, it showed a moderate reduction effect on the number of particles. With a stoichiometric air-fuel ratio, the performance of the catalytic VPR was not affected by the use of additional air. Even with rich mixture combustion, there was still not a noticeable effect with increasing additional air on the catalytic VPR performance. However, the oxidation effect of the catalytic VPR on HC emissions was significant. The HC emissions were reduced from 2800 ppm pre-VPR to 105 ppm post-VPR with the dilution factor of 1.1 (Fig. 5.12(a)).

(4) For each air-fuel ratio, the transmission efficiency of the catalytic VPR did not change much with different types and varying amounts of additional gas. A comparison between adding air or nitrogen as a diluent showed that the reduction in particle number through the catalytic VPR is more likely to be due to physical than chemical processes.

Chapter 6. The Effects of Hot Air Dilution and an Evaporation Tube (ET) on the PM Emissions from a GDI Engine

6.1 Introduction

The emission of nanoparticles from combustion engines has been shown to have a poorly understood impact on the atmospheric environment and human health, and legislation tends to err on the side of caution. Researchers have shown that Gasoline Direct Injection (GDI) engines tend to emit large amounts of small sized particles compared to diesel engines fitted with Diesel Particulate Filters (DPFs). This chapter presents size-resolved particle number emissions measurements from a spray guided GDI engine and evaluates the performance of an Evaporation Tube (ET). Unlike a thermo-denuder there was no active charcoal for removing vaporised hydrocarbons. The performance of an Evaporation Tube and hot air dilution system with a 7:1 dilution ratio has been studied, as the EU legislation uses these to exclude volatile particles. A low value of dilution ratio was used as the particle number emissions were quite low and a higher dilution ratio would have compromised the signal to noise ratio of the DMS500.

The Evaporation Tube was tested over a range of engine operating conditions with a Spray Guided Direct Injection engine with or without hot air dilution. The test conditions included single early injection with stoichiometric or rich mixture and double injection with a second injection after compression.

6.2 Evaporation Tube and Experimental Set-up

In recent years, the Particle Measurement Programme (PMP) has been set-up as a working group of the UN-ECE GRPE [17, 25], focusing on the development of new particle counting techniques to complement or replace the existing particulate mass measurement technique, with special consideration to measuring particle emissions at very low levels. The particle counting measurement system (reference system (RS)) consists of a cyclone, a volatile particle remover (VPR) and particle number counters (PNCs). Figure 5.1 shows how the VPR comprises a primary hot diluter (PND1), an Evaporation Tube (ET) and a secondary cold diluter (PND2) [61]. The aim of the system is to revaporise condensed material and then to dilute the sample so that the partial pressure of the volatile material is reduced so that even when the sample is cooled, the nucleation and condensation of the semi-volatile material is prevented.

The thermodynamics of nucleation and evaporation are discussed very clearly by Kasper [92], who shows how hot dilution followed by cooling can avoid nucleation, that would occur if there was just dilution and cooling to the same temperature and concentration – this is due to the ‘hysteresis’ caused by super-saturation. Kasper [92] also shows how heating of a sample in which nucleation has occurred, followed by heated dilution and cooling, can remove and inhibit nucleation.

The tests reported here examined separately the performance of an Evaporation Tube and hot air dilution as a means of eliminating the nucleation mode particles from a Spray Guided Direct Injection engine. Particle number distributions were measured with a Cambustion DMS500 which provided sample dilution after the Evaporation Tube and hot air dilution. The Evaporation Tube is essentially a thermo-denuder but without active charcoal for removing vaporised hydrocarbons.

Thermo-denuders (TDs) have already been widely utilized in studying atmospheric aerosols, as a means of achieving separate measurements of the volatile and non-volatile fractions of aerosols [93-101]. The TD normally consists of a heating section (like the Evaporation Tube) for heating the aerosol to a pre-set temperature followed by a cooling section filled with active carbon for adsorbing the evaporated gas-phase compounds. A model for aerosol volatility measurements has also been studied by Cappa et al. [102], who report that their model can be used to provide quantitative understanding of aerosol volatility measurements of single and multi-component aerosols using thermo-denuders. A TD was also used in roadside nanoparticle measurements to examine the influence of the volatile components in the nanoparticle size range [103]. A thermo-denuder can also be used in the integrated volume method for estimating saturation pressure and enthalpy of vaporization of a whole aerosol distribution [104, 105].

TDs have been used for characterizing diesel exhaust aerosols both on-road and in the laboratory [106]. It is suggested that the nucleation mode particles form by nucleation of low volatility species, followed by growth driven by the condensation of lighter hydrocarbons. A TD was also used in the research into the emissions from different alternative diesel fuels by Yehliu et al. [107]. They reported that when the temperature of the thermal denuder was reduced from 400°C to 30°C, the increase in total particle concentration with pure soyabean methyl ester was much higher than that with ultra low sulfur diesel fuel, and the increase in particle mean diameter with pure soybean methyl ester was much higher than that with ultra low sulfur diesel fuel, indicating that the organic fraction emissions of biodiesel were much higher than those from conventional diesel.

Kasper [92] also reports comparative tests with a hot diluter, thermo-desorber after a hot diluter, a thermo-diluter and post-dilution thermo-conditioning. The exhaust sample came from a two-stroke engine with a very high particle concentration (10^9 /cm^3) so dilution of order 10^4 was needed. Even so, the thermo-desorber was not able to eliminate the nucleation mode. Kasper also tested a themo-conditioner (dilution followed by heating) with a tetracontane aerosol, and showed that it was completely able to evaporate particles with a number concentration of 5×10^5 /cm^3 with a mean diameter of 95 nm.

A Catalytic Stripper and a thermal denuder used to separate the solid and volatile particles were compared by Swanson et al. [108]. They showed that the TD method introduced semi-volatile particle artefacts due to nucleation or condensation of vapours, while measurements using the Catalytic Stripper did not show such artefacts.

Due to the presence of volatile components (that can condense or evaporate depending on the prevailing conditions of temperature and pressure), the behaviour of nanoparticles is unstable when measurements are made of vehicle exhaust emissions, so an Evaporation Tube is a useful tool in removing the volatile fractions. In the work reported here, engine experiments were carried out to study the performance of an Evaporation Tube with and without hot air dilution using the exhaust from a Spray Guided GDI engine.

The test engine was a Jaguar naturally aspirated, V8 Spray Guided Direct Injection spark ignition engine [56]. The specifications of the engine have been described in Chapter 2. The main characteristics of the engine operating point are listed in Table 6.1, and the Evaporation Tube temperature was maintained at 450 °C using a closed-loop controller.

A schematic of the particulate emissions measurement system and the dimensions of the Evaporation Tube used in this work are shown in Fig. 6.1. The Evaporation Tube system consists of a temperature controlled heated tube, with flow in an annular gap. The performance of the Evaporation Tube on the particulate emissions from the GDI engine was examined under different engine operating conditions.

It can be seen from Fig. 6.1 that during the tests, the exhaust pre-Three-Way Catalyst (TWC) was drawn into the Evaporation Tube. At each test point, the PM emissions pre-Evaporation Tube and post-Evaporation Tube were measured using a Cambustion DMS500 particle sizer [59]. The sampling flow rate of the DMS (MFM_{DMS}) was set to 0.02 g/s (1 LPM), and the residence time of the Evaporation Tube was longer than 2 seconds. A pneumatic switching valve was used to select between pre-Evaporation Tube and post-Evaporation Tube. The switching valve was heated so as to keep the sampling temperature at around 90 °C, thereby preventing particle formation by condensation. The temperature of the sampling flow pre and post the Evaporation Tube, as well as the flow temperature entering DMS, were measured using thermocouples.

The hot air dilution system (using a 7:1 dilution ratio) used a pressure regulator and thermal mass flow controller to regulate the flow. Temperature regulation was by a closed loop controller and the exhaust sample and dilution air were mixed in a concentric flow arrangement. The system operation was logged by a LabVIEW based system that also provided real time displays.

Table 6.1 Parameters of the Engine and the Evaporation Tube

Engine Speed / rpm	800
Engine Torque / N·m	80
Injection Pressure / MPa	15
Manifold Pressure / (bar absolute)	0.55
Cam Lift / mm	5.5
Ignition Timing:	-2° BTDC
Evaporation Tube Temperature / °C	450

The engine operating points were chosen to represent conditions during engine warm-up and TWC light-off as this is associated with high levels of particulate emissions, so the coolant inlet temperature of the engine was controlled at 20 °C. Early single injection with different injection timings and relative air-fuel ratios and split injection were tested, as listed in Table 6.2. The split injection was used as it generates more accumulation mode particles and is a combustion strategy that can be used during catalyst light-off.

During the experiments, both the raw data and lognormal fits of the DMS signal were logged for 90 s. The data was logged at 10 Hz and downsampled so that a reading was recorded every second, along with the corresponding bi-lognormal fits. Averaged spectra and particle number data were subsequently calculated over the 90 second period. The DMS data post processing and the algorithms for the bi-lognormal calculations have been described in Chapter 2.

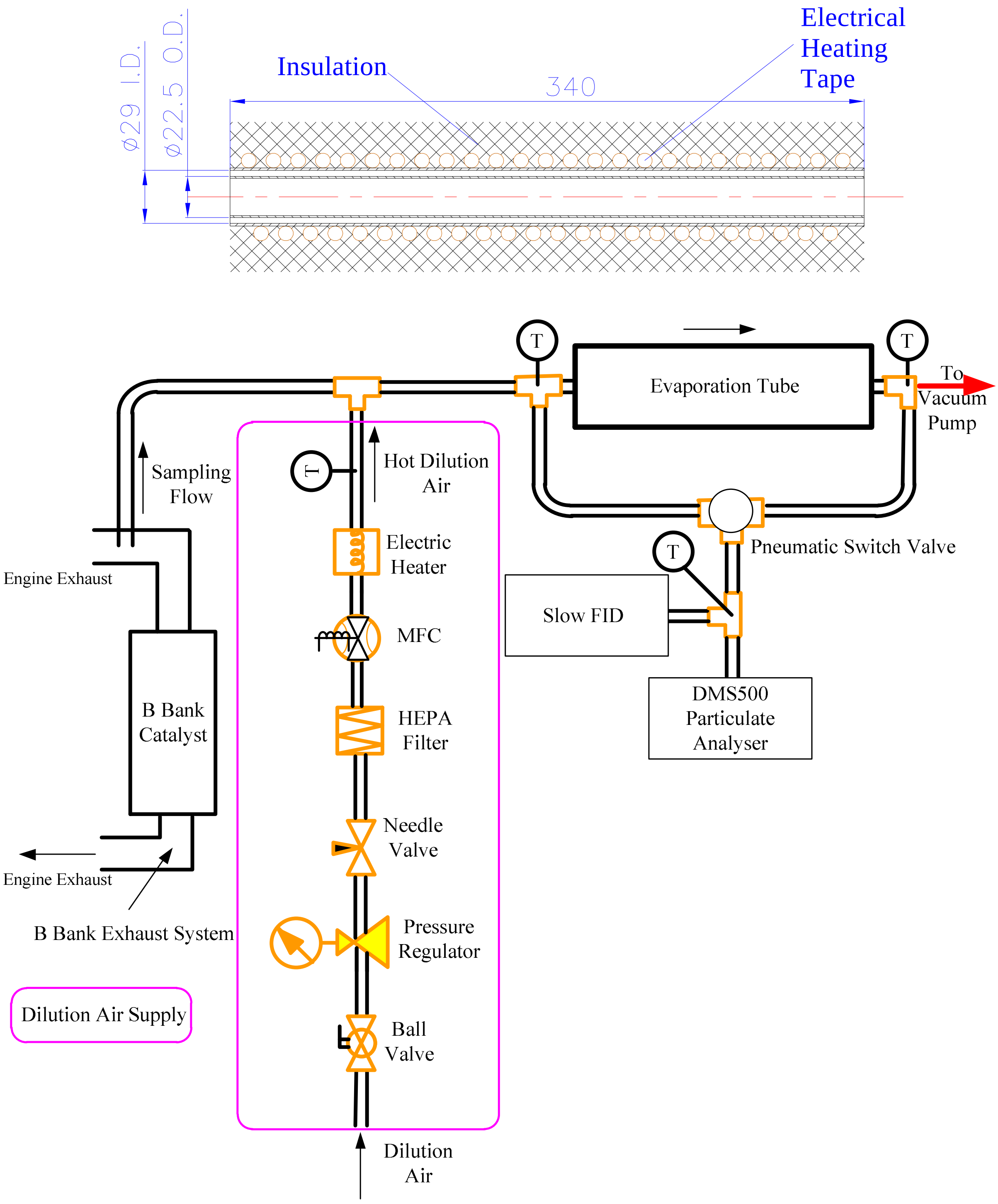

Fig. 6.1 Experimental set-up, and geometric details of the Evaporation Tube.

Table 6.2 Evaporation Tube Tests Conditions

	SIN1 320 1.0	SIN1 320 0.8	SIN1 310 0.8	SP1 320 1.0
Injection mode:	Single	Single	Single	Split
1st injection timing:	320° BTDC	320° BTDC	310° BTDC	320° BTDC
2nd injection timing:				-2° BTDC
2nd injection width / ms:				0.25
Relative AFR:	1.0	0.8	0.8	1.0
IVO:	24° ATDC			
IVC:	244° ATDC			
EVO:	224° BTDC			
EVC:	26° ATDC			
Coolant / °C:	20			

6.3 Effects of Hot Air Dilution and Evaporation Tube on Engine Particulate Emissions

Fig. 6.2 shows the particle number weighted size distribution at various engine operating points pre and post-Evaporation Tube (ET), which are plotted as raw spectra. The spectra shown in Fig. 6.2(b) have been corrected for the hot air dilution ratio of 7 (DR7). It can be seen that at each particle size, there is a marked reduction of $\mathrm{d}N/\mathrm{dlog}d_\mathrm{p}$ for post-Evaporation Tube compared with that of pre-ET, and the reduction is more significant for the smaller particle sizes. It can be seen that using hot air dilution (Fig. 6.2(b)) reduces the pre-Evaporation Tube number concentration of small size particles significantly, and this reduction is also present post-ET.

The measurements in Fig. 6.2(b) show that hot dilution alone reduces the concentration of the nucleation mode particles, and this provides evidence that the nucleation mode is semi-volatile material. Even if the gasoline contained 10 ppm sulfur and combustion was rich of stoichiometric, then there will only be about 1 ppm sulfuric acid in the exhaust and (even with no dilution) this would have to be cooled to below about 50 °C for sulphuric acid to nucleate, so it seems reasonable to assume that the semi-volatile material is hydrocarbons. Fig. 6.3 compares the data from a single operating point (single injection 320°BTDC with lambda = 0.8), and this shows a significant reduction in nucleation mode particles with hot air dilution before the Evaporation Tube.

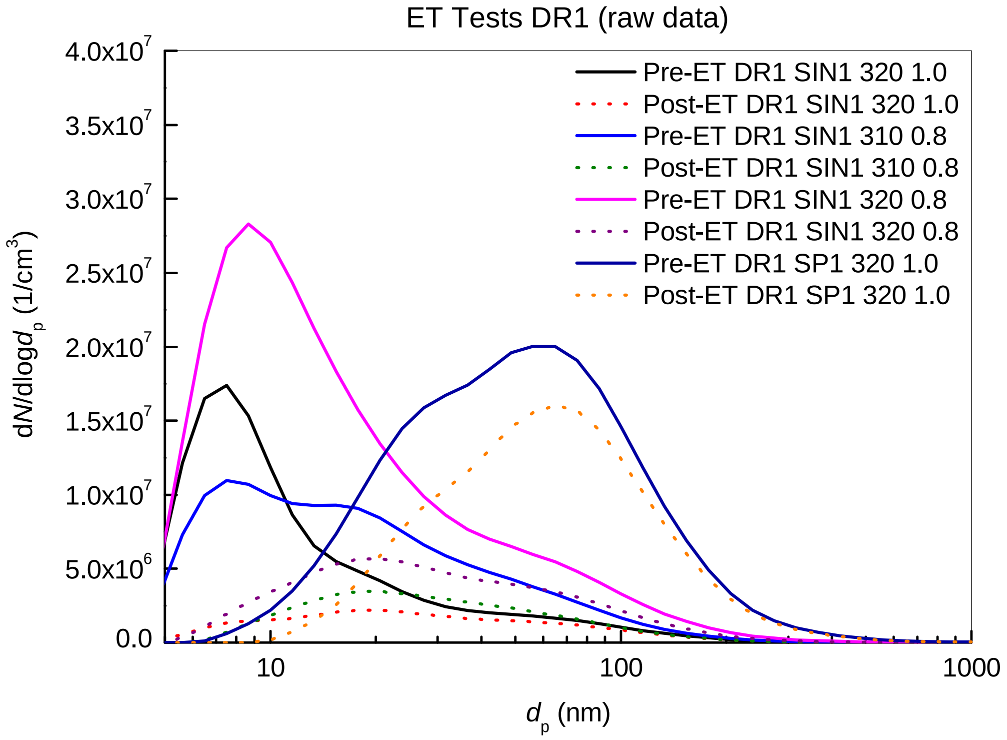

(a) Without hot air dilution (DR1)

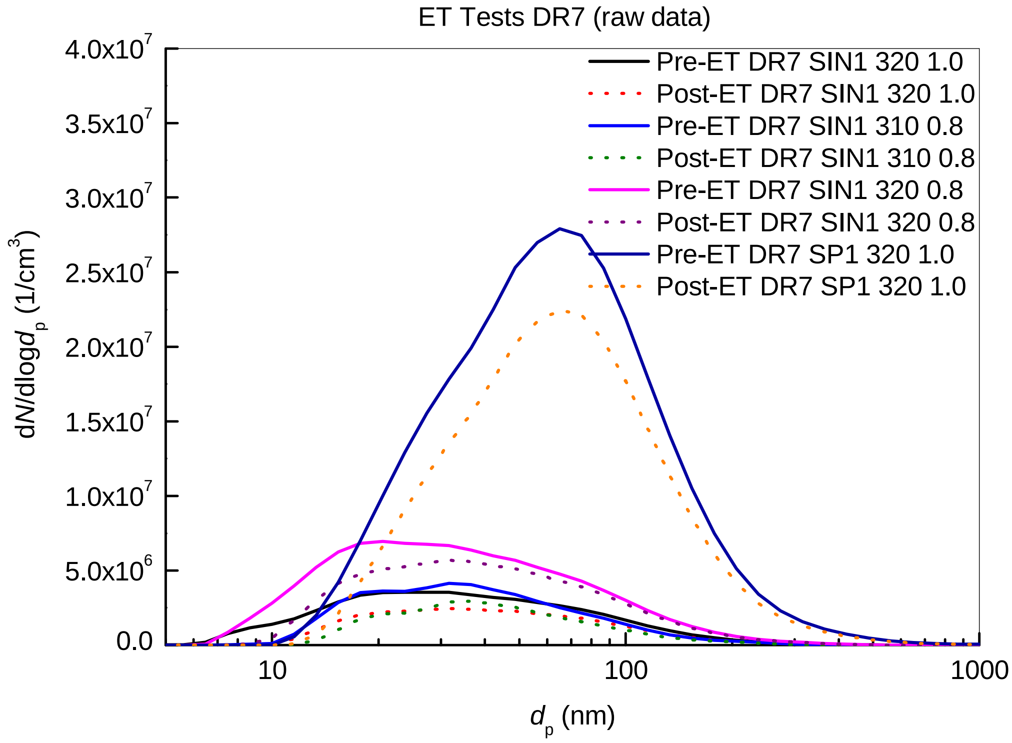

(b) With hot air dilution (Dilution Ratio of 7; the data points have been corrected for the dilution ratio)

Fig. 6.2 Particle number size distribution before and after the Evaporation Tube, (Test conditions as defined in Table 6.2).

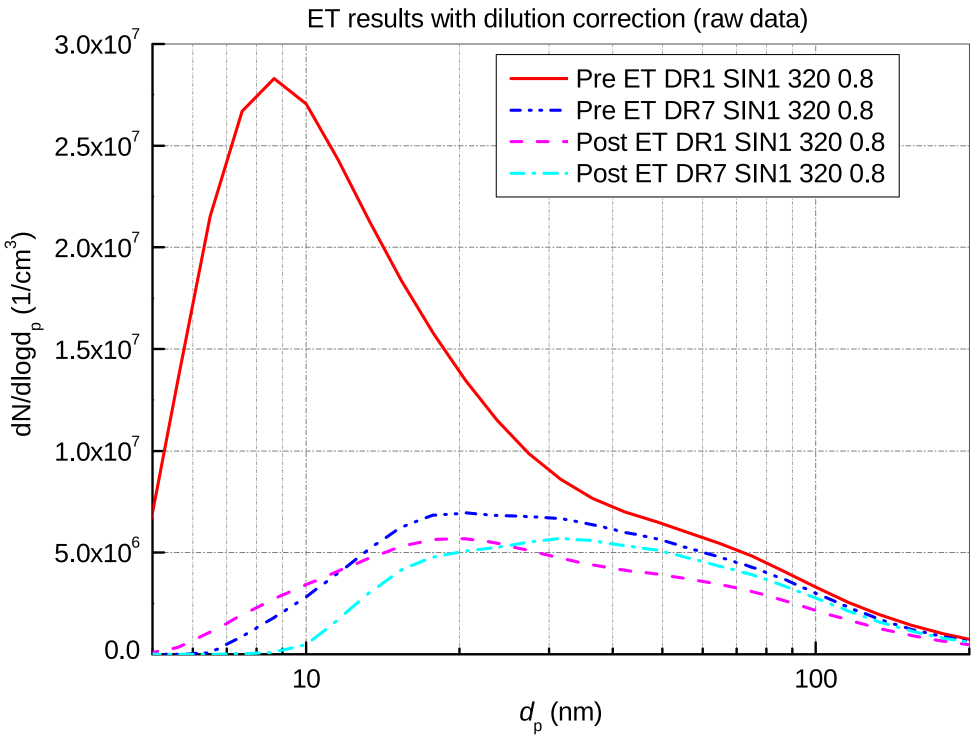

Fig. 6.3 Particle number size distributions at a single engine operating point with (DR7) and without (DR1) hot air dilution (SIN1 320 0.8, as defined in Table 6.2).

The effect of hot air dilution is comparable to an undiluted sample flowing through the Evaporation Tube. With hot air dilution there was a further slight reduction in the nucleation mode as the sample gas flowed through the Evaporation Tube, and a lower loss in the accumulation mode particles after the Evaporation Tube. The results for this and the other single injection data are summarised in Fig. 6.4, that has used the Cambustion bi-lognormal fitting algorithm to divide the flow into the nucleation (N) and accumulation (A) modes.

Fig. 6.4 shows the effect of the Evaporation Tube (ET) and hot air dilution on particle number concentrations for the different engine operating conditions. Adding hot air dilution did not have any significant effect on the accumulation mode particles. Fig. 6.4 shows that the particulate material in the raw engine exhaust included a large portion of nucleation mode particles, but that these were not always entirely removed by hot air dilution. However, the total number of particles post-Evaporation Tube (all of which are in the accumulation mode) is in essence the same as the number of accumulation mode particles pre-Evaporation Tube. For reference, the results of the bi-lognormal fitting are shown in Table 6.3.

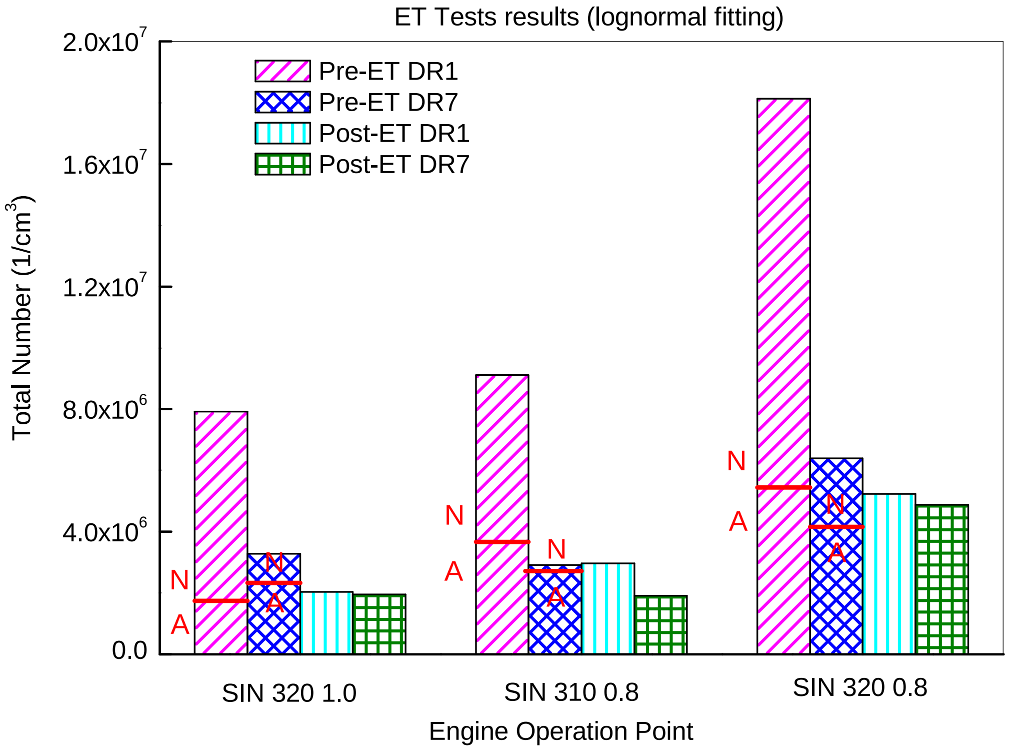

Fig. 6.4 Particle number concentrations at different engine operating conditions (as defined in Table 6.2) with (DR7) and without (DR1) hot air dilution; the horizontal lines divide the nucleation (N) and accumulation (A) modes.

Fig. 6.5 shows the effect of applying the PMP transmission function (as a digital filter, Eq. 2.2) to the whole of the data after the lognormal fitting. The bold horizontal lines in each bar show if the PMP filter has caused a reduction in the particle count. As would be expected, the PMP filter has the greatest effect on the pre-Evaporation Tube measurements when there is no dilution. For post-Evaporation Tube, the PMP numerical filter (Eq. 2.2) has a negligible effect whether or not there has been dilution. The effect of the PMP filter is, in broad terms, the same as the Evaporation Tube if the variation in the test data is allowed for.

Comparison between Fig. 6.4 and Fig. 6.5 shows that using the number of particles that are in the accumulation mode (as defined by the DMS500) is comparable with the number of particles measured after the Evaporation Tube, which is also comparable with the number of particles pre-Evaporation Tube from undiluted measurements with the PMP filter. Comparisons of the Evaporation Tube transmission efficiency with the PMP filter can also be made as function of particle size.

Table 6.3 Bi-lognormal fitting to the pre-Evaporation Tube measurements with (DR7) and without (DR1) heated dilution air; CMD – Count Mean Diameter, GSD – Geometric Standard Deviation. The operating points are defined in Table 6.2

Operating Points		Pre-ET DR1 SIN1 320 1.0	Pre-ET DR7 SIN1 320 1.0	Pre-ET DR1 SIN1 310 0.8	Pre-ET DR7 SIN1 310 0.8	Pre-ET DR1 SIN1 320 0.8	Pre-ET DR7 SIN1 320 0.8
Nucleation Mode:	CMD (nm)	7.76	17.15	9.61	17.41	9.49	17.22
	GSD (nm)	1.45	1.49	1.58	1.21	1.59	1.49
	Concentration (#/cm3)	6.9×10^{6}	1.3×10^{5}	5.9×10^{6}	2.7×10^{4}	1.4×10^{7}	3.1×10^{5}
Accumulation Mode:	CMD (nm)	40.99	46.58	37.65	39.55	42.63	46.99
	GSD (nm)	2.01	2.01	1.98	1.95	2.01	2.01
	Concentration (#/cm3)	1.8×10^{6}	3.2×10^{5}	3.7×10^{6}	3.7×10^{5}	5.5×10^{6}	5.6×10^{5}
Operating Points		Post-ET DR1 SIN1 320 1.0	Post-ET DR7 SIN1 320 1.0	Post-ET DR1 SIN1 310 0.8	Post-ET DR7 SIN1 310 0.8	Post-ET DR1 SIN1 320 0.8	Post-ET DR7 SIN1 320 0.8
Nucleation Mode:	CMD (nm)	15.40	18.55	15.87	27.34	16.00	18.26
	GSD (nm)	1.60	1.33	1.56	1.58	1.59	1.37
	Concentration (#/cm3)	9.7×10^{5}	9.1×10^{3}	1.3×10^{6}	0	2.5×10^{6}	1.3×10^{5}
Accumulation Mode:	CMD (nm)	50.19	43.89	43.52	40.75	50.20	46.19
	GSD (nm)	2.01	2.01	1.99	1.93	2.00	2.01
	Concentration (#/cm3)	1.1×10^{6}	2.6×10^{5}	1.7×10^{6}	2.6×10^{5}	2.7×10^{6}	5.3×10^{5}

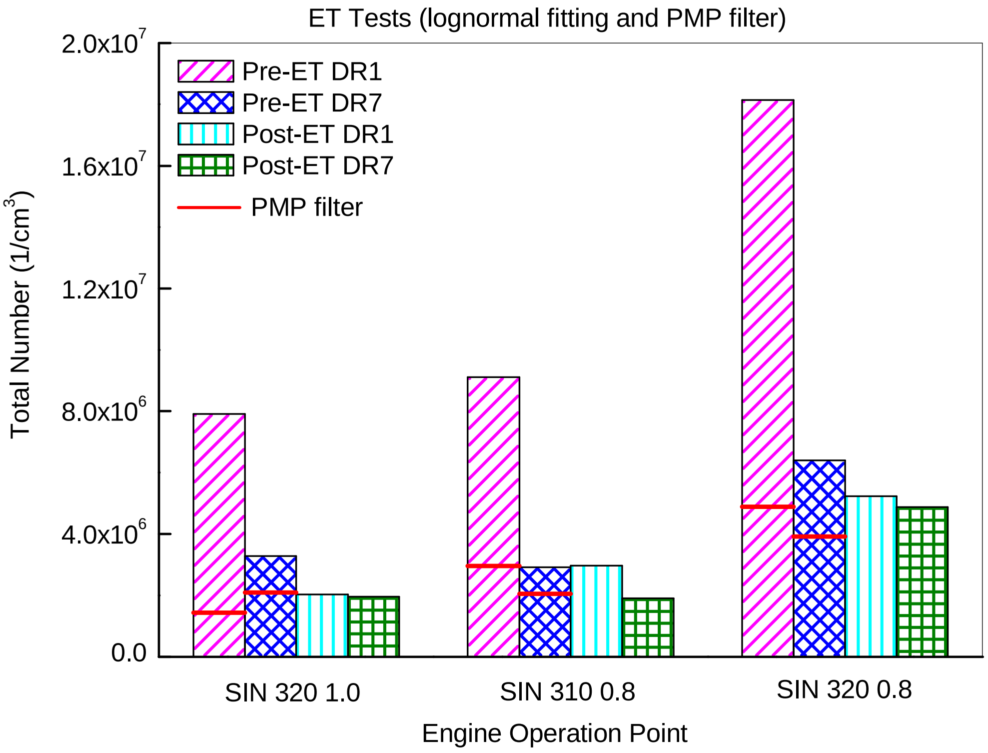

Fig. 6.5 Effect of applying the PMP transmission function (as a digital filter, Eq.2.2) at different engine operating conditions (as defined in Table 6.2) with (DR7) and without (DR1) hot air dilution; the horizontal lines show the reduction that would be caused by the PMP filter (Eq. 2.2).

The number transmission efficiencies for the Evaporation Tube, with and without hot air dilution, are shown in Fig. 6.6 alongside the PMP filter specification (for which an error bar shows the tolerance on the PMP transmission efficiency). As expected, the transmission efficiencies increase as the particle size increases, and the trends for the different operating points are similar. The transmission efficiency of the Evaporation Tube at the lower end of the particle size range is higher than the PMP filter, while it is lower than the PMP filter at the higher end of the particle size range.

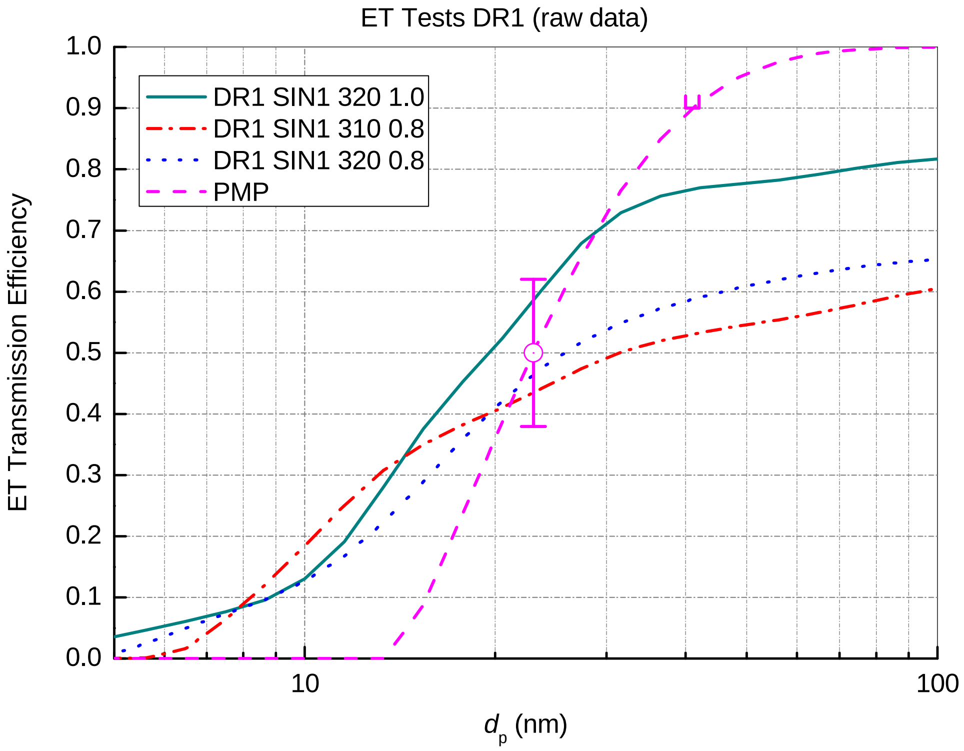

(a) Without dilution

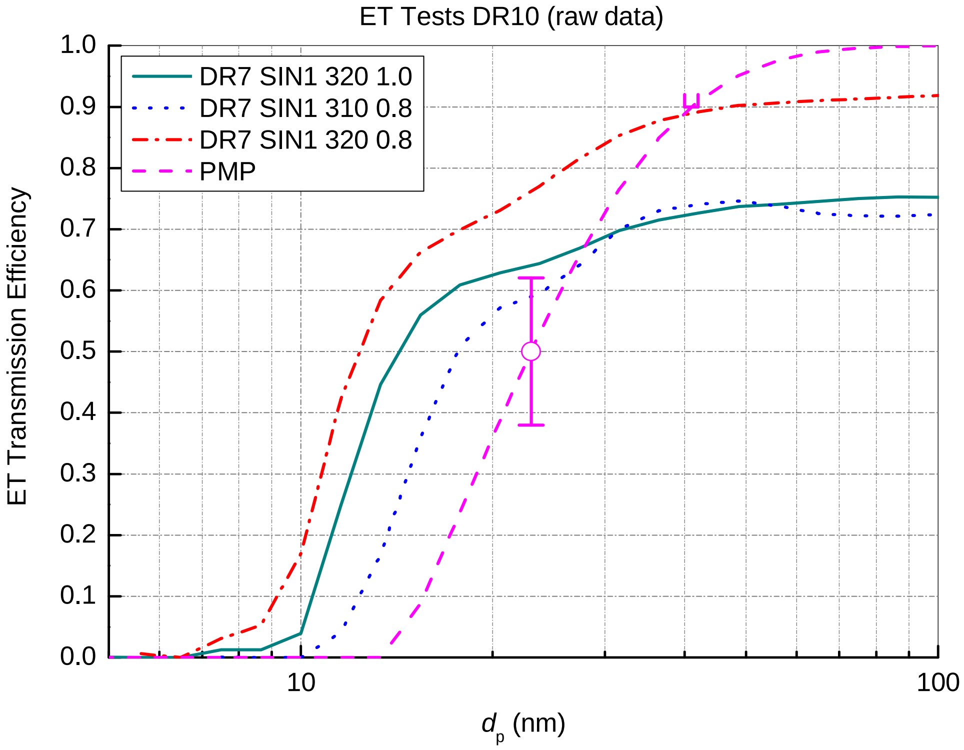

(b) With hot air dilution

Fig. 6.6 Number transmission efficiency of Evaporation Tube versus d_p at different engine operating conditions (as defined in Table 6.2) compared with the PMP requirement (Eq. 2.2).

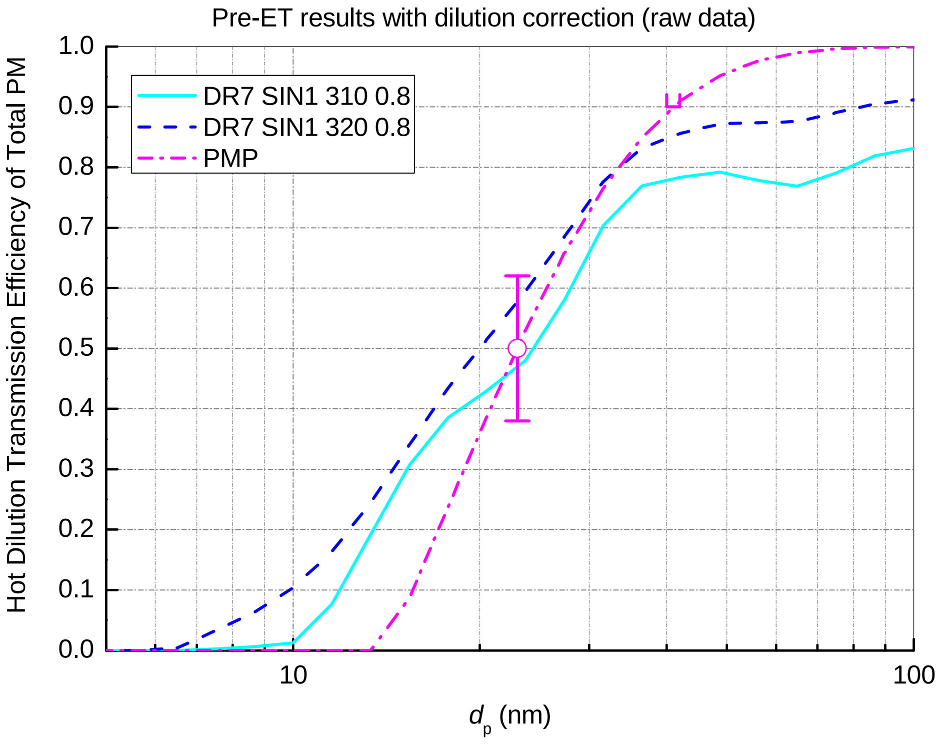

Fig. 6.7 Number 'transmission efficiency' of hot air dilution (7:1 Dilution Ratio) versus d_p *(operating points as defined in Table 6.2) compared with the PMP requirement (Eq. 2.2).*

Fig. 6.7 shows the 'transmission efficiencies' of the hot air dilution under rich operation conditions with early single injection, and again the PMP filter is plotted as a reference. The rich operation points have been selected because they have higher particle number concentrations and give a better signal to noise ratio compared to the stoichiometric single injection point. It can be seen that the trends for the 'transmission efficiency' with hot air dilution are comparable to the PMP filter. At 23nm, the transmission efficiencies are within the error range of the PMP specification, while at 41nm the transmission efficiencies are lower than that required by the PMP specification.

The particle loss seen in Fig. 6.6 and Fig. 6.7 are primarily due to diffusion and thermophoresis, and these mechanisms are well described in books such as Hinds [63] or Baron and Willeke [66]. It might be argued that, rather than trying to remove particles of a certain size, it is better to measure the size distribution of everything (with as little hardware as possible between the sample and instrument), and then to post-process the results, such as the approach advocated by Cambustion in the use of the accumulation mode fit.

The nucleation mode particles can be converted to a mass concentration, and this in turn can be converted to a volume concentration of hydrocarbons (as ppm of CH_2). Fig. 6.8 shows that the conversion of the nucleation mode particle concentration to a hydrocarbon emission leads to negligible equivalent CH_2 emissions (much less than 1 ppm).

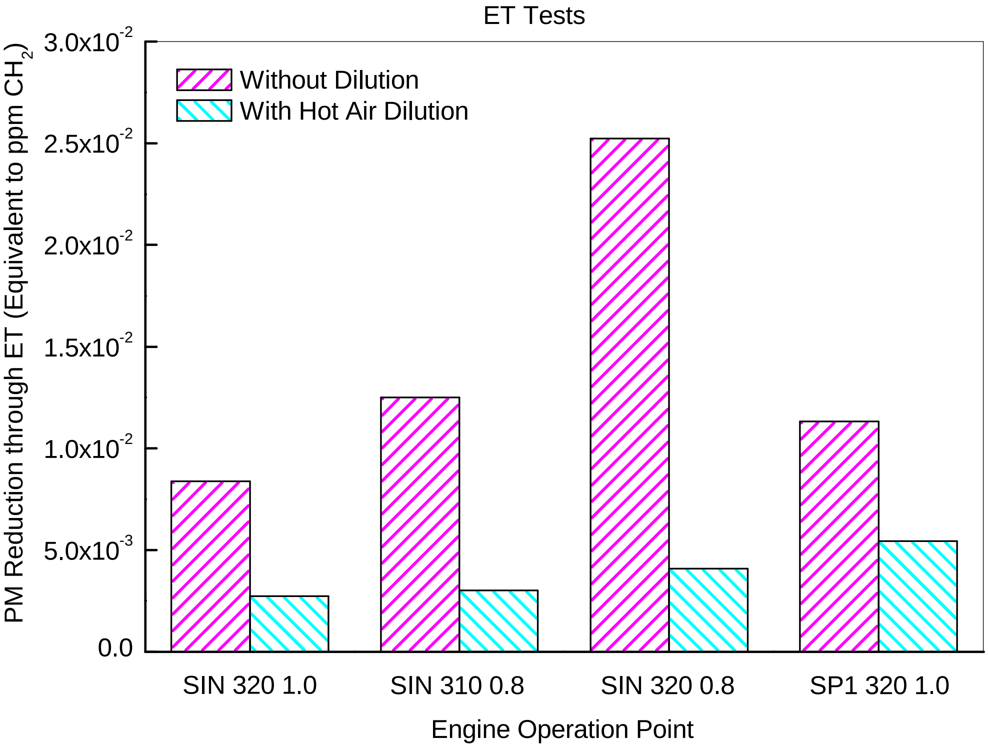

Fig. 6.8 Conversion of the nucleation mode particle concentration to an equivalent hydrocarbon concentration (assuming a generic hydrocarbon of C_xH_{2x}).

Fig. 6.9 compares the transmission efficiencies between the Evaporation Tube and the catalytic VPR which has been described in Chapter 5. The curve for the catalytic VPR was chosen from a typical testing point with a VPR temperature of 250 °C and mass flow rate of 0.09 g/s. The efficiency curves for the Evaporation Tube with and without hot dilution are shown in the figure. It can be seen that the particle transmission efficiencies for the ET and VPR at the high end (> 40 nm) of the particle size range are quite similar, while the transmission efficiencies of the ET with and without dilution for the particle sizes of less than 30 nm are higher than that of the VPR. Both systems have some particle loss mainly due to the physical effects of diffusion and thermophoresis.

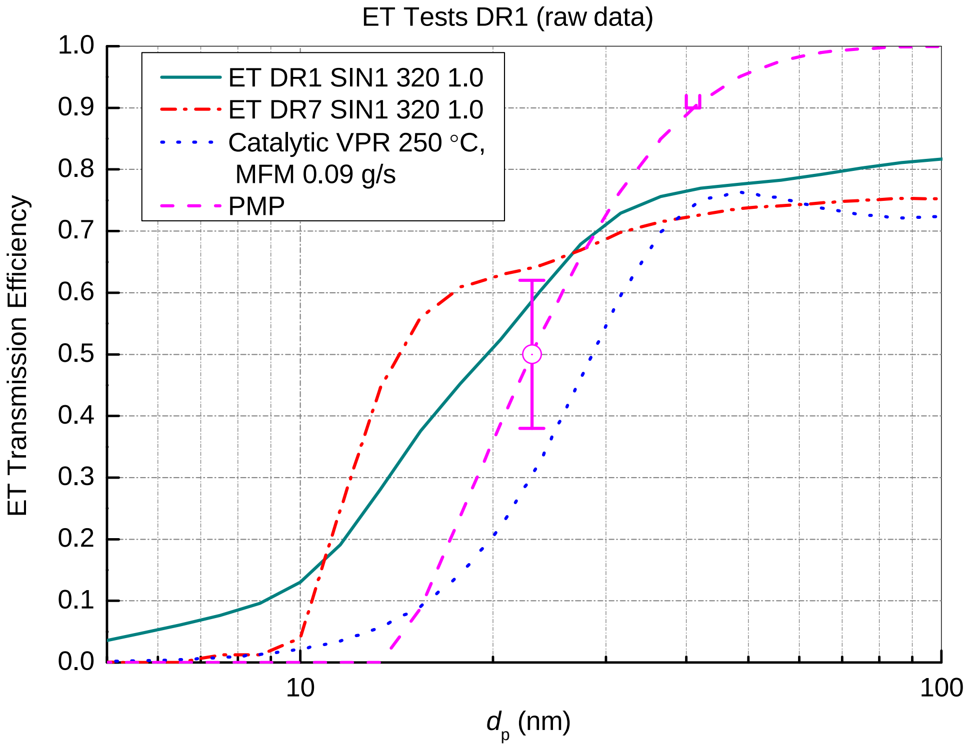

Fig. 6.9 Comparison of the transmission efficiencies between the Evaporation Tube (refer to Table 6.2), the catalytic VPR (refer to Table 5.2) and the PMP requirement (Eq. 2.2).

6.4 Calculation of the Particle Loss in the Evaporation Tube System

It can be seen from the above test results that there were some solid particle losses within the Evaporation Tube. Brownian diffusion and thermophoresis are considered to be the main mechanisms for transporting the particles to the wall. A theoretical analysis is performed to calculate the particle penetration efficiencies with those mechanisms.

Brownian diffusion

Brownian motion is the irregular 'wiggling' motion of an aerosol particle in still air that is caused by random collisions of gas molecules against the particle. Diffusion is the net transport of these particles in a concentration gradient. The direction of this transport is always from a region of higher concentration to a region of lower concentration. Both processes are characterized by the particle diffusion coefficient *D* (Eq. 3.8). The larger the value of *D*, the more vigorous the Brownian motion and the more rapid the particle transfer in a concentration gradient [63].

As the aerosol flows axially through the annular space between the two concentric tubes of the ET system used in this test, the penetration of diffusion (P_{diff}) can be estimated using the following equations [63].

$$P_{\text{diff}} = \frac{n_{\text{out}}}{n_{\text{in}}} = 1 - 5.50\mu^{2/3} + 3.77\mu \quad \text{for } \mu < 0.009$$

$$P_{\text{diff}} = 0.819\exp(-11.5\mu) + 0.0975\exp(-70.1\mu) \quad \text{for } \mu \geq 0.009 \tag{6.1}$$

Where μ is the dimensionless deposition parameter. For laminar flow with $d_2 - d_1 << d_1$, μ can be expressed as

$$\mu = \frac{\pi DL(d_1 + d_2)}{Q(d_2 - d_1)} \tag{6.2}$$

Where *D* is the particle diffusion coefficient, *L* is the length of the Evaporation Tube, *Q* is the volume flow rate through the Evaporation Tube, d_1 and d_2 are the inner and outer diameters of the annular flow path, respectively.

Thermophoresis

When a temperature gradient exists in a gas, particles in the gas experience a force in the direction of decreasing temperature. The motion of the particle arising from this force is called thermophoresis. The magnitude of the thermal force depends on the gas and particle properties, as well as the temperature gradient [63].

According to Walker et al. [109], the particle penetration of thermophoresis (P_{th}) as gas flowing through a tube can be expressed as

$$P_{\mathrm{th}} = \frac{n_{\mathrm{out}}}{n_{\mathrm{in}}} = 1 - \frac{\mathrm{Pr}\, K}{1+\theta^{*}} \tag{6.3}$$

Where Pr is the Prandtl number, K is the thermophoretic coefficient and θ^{*} can be expressed as

$$\theta^{*} = \frac{T_{\mathrm{min}}}{T_{\mathrm{max}} - T_{\mathrm{min}}} \tag{6.4}$$

Where T_{min} is a constant minimum tube wall temperature and T_{max} is the temperature of the gas entering the deposition zone. The expression for the thermophoretic coefficient K is given by Talbot et al. [110] as

$$K = 2C_{\mathrm{s}} \frac{\dfrac{k_{\mathrm{g}}}{k_{\mathrm{p}}} + C_t \dfrac{\lambda}{a}\left[1 + \dfrac{\lambda}{a}\left(1.2 + 0.41\exp\left(-0.88\dfrac{a}{\lambda}\right)\right)\right]}{\left(1 + 3C_{\mathrm{m}}\dfrac{\lambda}{a}\right)\left(1 + 2\dfrac{k_{\mathrm{g}}}{k_{\mathrm{p}}} + 2C_{\mathrm{t}}\dfrac{\lambda}{a}\right)} \tag{6.5}$$

Where λ is the mean free path of the gas molecules, a is the radius of the particle, $C_{\mathrm{s}} = 1.147$ is the thermal creep coefficient, $C_{\mathrm{t}} = 2.2$ is the temperature jump coefficient, and $C_{\mathrm{m}} = 1.146$ is the velocity jump coefficient, k_{g} and k_{p} are the thermal conductivities of the gas and particles, respectively.

As the characteristics of the particles emitted by the engine can vary a lot under different operating conditions, the exact value of $k_{\mathrm{g}}/k_{\mathrm{p}}$ is difficult to determine. So, it is of interest to investigate the effect of k_g/k_p on the calculation of the thermophoretic penetration. Fig. 6.10 shows the thermophoretic penetration efficiencies at different particle diameters with k_g/k_p as a parameter. It can be seen that in the particle size range of 5 to 1000 nm, the thermophoretic penetration does not vary much with the increase of particle size. Also, the curves for different k_g/k_p are very similar, indicating that the thermophoretic penetration is not sensitive to k_g/k_p in the particle size range tested here. Batchelor et al. [111] also reported that the thermophoretic coefficient K did not change much with the Knudsen number λ/a or k_g/k_p when λ/a was higher than 1. So, in the following calculation, the value for k_g/k_p is set to 0.2.

Assuming the diffusion and thermophoresis mechanisms act independently, the total penetration equals to the diffusion penetration times the thermophoresis penetration. Fig. 6.11 gives the calculated diffusion, thermophoresis and total penetration fractions for the sampling gas flowing through the Evaporation Tube. It can be seen that the diffusion penetration increases significantly as the particle size increases, while the thermophoresis penetration fraction increases slightly from 0.812 at 5 nm to 0.839 at 1000 nm. So the calculated particle losses due to thermophoresis are about 16-19% and the thermophoretic losses took place in the copper sampling pipe downstream of the Evaporation Tube as the gas temperature was reduced from 450 °C to 90 °C. This calculation gives a theoretical explanation to the particle number losses measured in the Evaporation Tube.

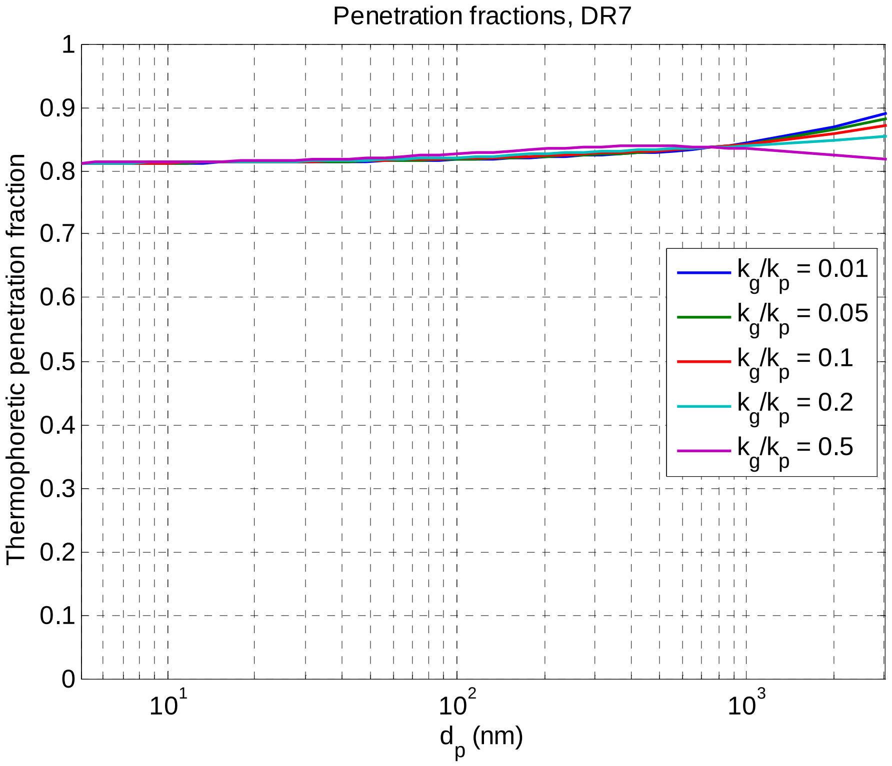

Fig. 6.10 Calculated particle penetration through the Evaporation Tube for thermophoresis with different k_g/k_p, where k_g and k_p are the thermal conductivities of the gas and particles, respectively.

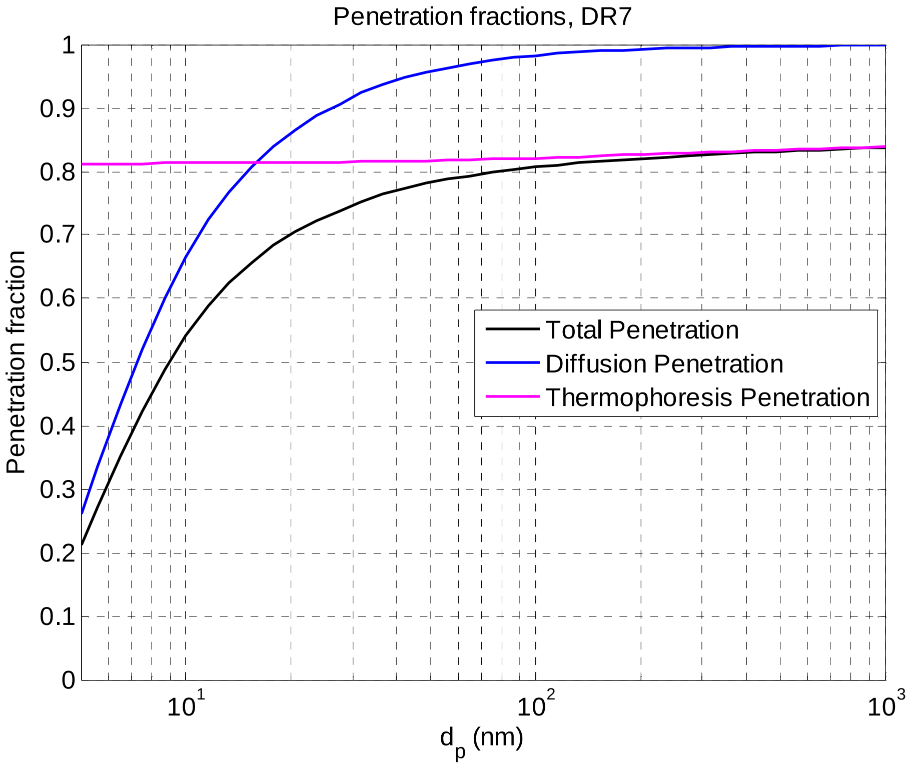

Fig. 6.11 Calculated particle penetration through the Evaporation Tube for the diffusion and thermophoresis mechanisms and the total efficiency (using Eq. 6.1 to 6.5, at conditions defined in Table 6.1, the dimensions of the Evaporation Tube are defined in Fig. 6.1).

6.5 Summary

(1) The use of hot air dilution has confirmed that the nucleation mode particles in undiluted exhaust are primarily condensed semi-volatile material, but the mass is negligible in terms of the equivalent ppm of unburned hydrocarbons (well below 1 ppm).

(2) Hot air dilution has been shown to have a broadly similar effect to an Evaporation Tube operating at 450 °C

(3) At a temperature of 450 °C, the Evaporation Tube has shown a more significant reduction effect on nucleation mode than accumulation mode particles, and that the overall response is close to the PMP requirement.

(4) Measurements taken by the DMS500 of undiluted exhaust can be analysed by using a digital filter to replicate transmission efficiency of the PMP filter or by using the accumulation mode (obtained from a bi-lognormal fit), in order to estimate a particle number concentration that would be consistent with PMP protocol. This facilitates measurements from engines (as opposed to vehicles or engines with their exhaust connected to dilution tunnels), so that measurements can be obtained from transients without ‘smearing’ of the data.

Chapter 7. Conclusions and Suggestions for Future Work

7.1 Conclusions

Gasoline Direct Injection Engines have been intensively developed by automotive manufacturers in the past decade because of their potential for reducing fuel consumption. Combined with forced induction, gasoline direction injection is a key enabler to facilitate engine downsizing. However, GDI engines tend to emit one order of magnitude more particulate matter number emissions than conventional PFI engines. Particle number and particle mass emissions from gasoline engines will be limited in the upcoming European legislation on vehicle exhaust emissions. So it is essential to characterize the PM emissions from GDI engines to see if their further deployment would be restricted by the legislation.

In this chapter, conclusions are made from the results of various engine experiments described in Chapters 3, 4, 5 and 6. The majority of the findings are divided into three categories. Firstly, the filtration efficiencies of glass fibre filters were measured using a testing system that extracted diluted exhaust gas from a GDI engine through the filters. The filtration efficiency was theoretically calculated, taking different mechanisms into account. Secondly, the effects of engine operating parameters on PM emissions during engine warm-up operating conditions were studied, i.e. the effects of injection timings, injection pattern, injection pressure and valve timings on PM emissions. Thirdly, the characteristics of the PM emissions from a GDI engine were studied using a catalytic Volatile Particle Remover (VPR) and an Evaporation Tube (ET) with hot air dilution, separately. The main conclusions are summarized as follows.

7.1.1 Filtration Efficiency Analysis for the Filter Sampling Tests

Two types of glass fibre filter were tested, a Whatman ® GF/A Glass Microfiber filter (which is an uncoated filter) and a Pallflex® Fiberfilm filter (which has a fluorocarbon (TFE) coating). Coated filters are favoured for air monitoring applications because they are inert to catalysing chemical transformations and less moisture sensitive [66]. However, only uncoated filters are suitable when Thermo-Gravimetric Analysis is to be used.

- Particulate emissions from a GDI engine operating with stratified injection were measured with both types of glass fibre filter and their filtration efficiencies were characterized using a DMS500.

- High concentrations of particulate emissions in the accumulation mode were observed upstream of the filter, which was typical under the engine operating condition with stratified injection. The peak of the post-filter particle number concentration is more than an order of magnitude lower than that of the pre-filter particle number concentration. The peak for the greatest penetration of particles was located around 200 nm for both types of filter. Meanwhile, the number concentrations of the nucleation mode particles are close to the noise level of the DMS after the filters.

- As the sampling time increased, the transmission efficiency, i.e. the penetration of a filter, decreased gradually for each of the filters - the penetration of a filter can be lowered by more than an order of magnitude over the sampling period. As a result, the particulate number and mass concentrations post-filter decreased as the sampling time increased. A calculation of the filter efficiency using an individual single-fibre mechanism and the total efficiency gave a theoretical explanation for the penetration of the filter. It was found that the greatest penetration of the filter (at 200 nm) was located in the regime where neither diffusion nor interception is dominant in the filtration process.

- The particulate material accumulated on the filter led to a rise in the pressure drop across the filter, which increased steadily as the sampling time increased.

- The hydrocarbon emissions pre-filter were unchanged when measured at the beginning and at the end of the sampling process for both of the filters. Moderate fluctuations were observed in the post-filter HC emissions which were generally lower than the pre-filter HC emissions. Conversion of the nucleation mode particle mass concentration to a hydrocarbon emission would lead to a negligible (below 1 ppm) equivalent CH_2 emission.

7.1.2 The Effects of Engine Operating parameters on PM Emissions during Engine Warm-Up Conditions

- Particulate emissions from cold engine operation were much higher than those from warm engine operation.

- Under cold engine operating conditions, particle number emissions using double injection (with the second injection after compression) were much higher than those with single injection during the intake. (But this injection strategy is important for improving combustion stability.) The main injection timing only had moderate effects on PM emission.

- Under cold engine operation, no reduction effect on PM emissions was shown using split intake injection to further facilitate homogeneous mixture formation compared with single intake injection.

- Increasing the fuel injection pressure could form a more homogeneous mixture so that the HC and PM formation during combustion were reduced. However, if the fuel pressure was too high, spray impingement could increase, leading to higher HC emissions and increased nucleation mode particle concentrations.

- Valve timings showed moderate effects on particulate emissions. Properly adjusted timing for exhaust valve closure led to reduced particulate emissions and the combustion characteristics were not adversely affected much. The effect of the intake valve opening on PM emissions was less than that of the exhaust valve closing.

7.1.3 The Effects of a Catalytic Volatile Particle Remover (VPR), Hot Air Dilution and an Evaporation Tube (ET) on the PM Emissions from a GDI Engine

The role of a catalytic VPR, hot air dilution and an Evaporation Tube on engine particle emissions were tested under different operating regimes with a GDI engine. The performance of the catalytic VPR was evaluated by varying its temperature and the exhaust residence time. The performance of a catalytic Volatile Particle Remover (VPR) when used for post Three Way Catalyst (TWC) oxidation was studied subsequently. Also, the performance of an Evaporation Tube and hot air dilution system with a 7:1 dilution ratio was studied, as the EU legislation uses these to exclude volatile particles.

- With the pre-TWC engine exhaust, nucleation mode particles constituted a large portion of the total particle number but only constituted a small portion of the total particle mass. The catalytic VPR led to a significant reduction in the particle number, especially the smaller size (nucleation mode) particles.

- The VPR temperature and exhaust residence time ($MFM_{exhaust}$) did not show much effect on the catalytic VPR performance once the $MFM_{exhaust}$ was above 0.09 g/s. The catalytic VPR transmission efficiencies for different size particles showed similar trends at the various VPR temperatures and $MFM_{exhaust}$ tested. Generally, the transmission efficiencies of the VPR follow the trends of the scaled PMP counting efficiency specification.

- When post-TWC exhaust was introduced to the catalytic VPR, it showed a moderate reduction effect on the number of particles. With a stoichiometric air-fuel ratio, the performance of the catalytic VPR was not affected by the use of additional air. Even with rich mixture combustion, there was still not a noticeable effect with increasing additional air on the catalytic VPR performance. However, the oxidation effect of the catalytic VPR on HC emissions was significant.

- For each air-fuel ratio, the transmission efficiency of the catalytic VPR did not change much with different types and varying amounts of additional gas. A comparison between adding air or nitrogen as a diluent showed that the reduction in particle number through the catalytic VPR is more likely to be due to physical than chemical processes.

- The use of hot air dilution has confirmed that the nucleation mode particles in undiluted exhaust are primarily condensed semi-volatile material, but their mass is negligible in terms of the equivalent ppm of unburned hydrocarbons (well below 1 ppm).

- Hot air dilution has been shown to have a broadly similar effect to an Evaporation Tube operating at 450 °C

- At a temperature of 450 °C, the Evaporation Tube showed a more significant reduction effect on nucleation mode than accumulation mode particles, and the overall response was close to the PMP requirement.

- Measurements taken by the DMS500 of undiluted exhaust can be analysed, either using a digital filter to replicate the transmission efficiency of the PMP ‘filter’, or by using the accumulation mode data (obtained from a bi-lognormal fit), in order to estimate a particle number concentration that would be consistent with the PMP protocol. This facilitates measurements from engines (as opposed to vehicles or engines with their exhaust connected to dilution tunnels), so that measurements can be obtained from transients without ‘smearing’ of the data.

- Comparison of the typical transmission efficiencies between the Evaporation Tube (ET) and the catalytic VPR shows that particle transmission efficiencies for the ET and VPR at the high end (> 40 nm) of the particle size range are quite similar, while the transmission efficiencies of the ET with and without dilution for the particle size less than 30 nm are higher than that of the VPR. Both systems have some particle loss mainly due to the physical effects of diffusion and thermophoresis.

7.2 Suggestions for Future Work

A large portion of particulate emissions from GDI engines are generated during the first 200 seconds in the NEDC cycle. In order to reduce the PM emissions from a GDI engine, the engine control strategy during engine start and cold operating conditions should be further investigated. Compromises will need to be made based on catalyst light-off, CO and HC emissions and PM emissions to achieve an overall optimized result. The fuel injection, combustion and emissions during the firing cycles at the beginning of the engine start is of particular interest, as the fuel pressure is just being established and the temperature in the combustion chamber is very low.

Future engines are likely to have both direct injection (DI) and port fuel injection (PFI), so there is scope for optimising the injection split between the two modes. If the majority of the fuel during catalyst light-off was injected by PFI, then a more homogeneous background mixture would be formed, and the only locally rich regions would be near the spark plug as a consequence of the very delayed direct injection.

More research is needed into the impact of oxygenated fuels. The use of ethanol in unleaded gasoline is now well established, but there are different reports as to whether this increases or decreases the particulate matter emissions. There is no doubt that for rich mixtures, then fuels with ethanol reduce the particulate matter emissions, but there are contradictory reports for stoichiometric operation. This might be because a nominally stoichiometric mixture has had rich mixture excursions, or it might be dependent on the fuel components that are present in the base gasoline – experiments could be conducted with model fuels, or with fuels of known composition into which specific components are added. Other oxygenates such as methanol and the various isomers of butanol are also being considered for addition to gasoline, so their impact on particulate emissions also needs to be assessed

As gasoline engines tend to emit a large number of nucleation mode particles, further research can be made to investigate the composition of nucleation particles under different engine operating conditions. Thermo-Gravimetric Analysis combined with Gas Chromatography-Mass Spectrometry (TGA-GCMS) would be a useful method to determine the volatile component accumulated on a filter.

Other techniques that can be considered are the use of a Differential Mobility Analyser, so that a particular size range of particles is collected on a filter and subject to TGA-GCS. The particle surface area could also be measured by the BET isotherm for different sized particles, and more information on the structure of the soot can be obtained from X-ray Photoelectron Spectroscopy (XPS) and Raman Spectroscopy (RS), as have been used by several research groups to investigate diesel exhaust particulates.

The PM emissions during engine transient operating conditions, such as acceleration and changing load, should be examined on a chassis dynamometer or an engine transient dynamometer to optimize the ECU calibration so that the PM emissions can be reduced. This will be a particular challenge for vehicles that have a stop-start strategy. The stop-start strategy leads to catalysts that are cooler and full of air, and the strategy used to reduce gaseous emissions (initial operation slightly rich of stoichiometric) will increase the particulate matter emissions.

References

[1] Schwarz, Ch., Schünemann, E., Durst, B., Fischer, J., and Witt, A., Potential of the Spray-Guided BMW DI Combustion System. SAE paper, No.2006-01-1265.

[2] Bickerstaffe, S., By the Numbers-Ford 1.0 Ecoboost. Automotive Engineering. 2012, vol.37(1): 18-19.

[3] Bickerstaffe, S., Raising the Bar-Renault Energy TCe 115. Automotive Engineering. 2012, vol.37(2): 16-17.

[4] Kirwan, J.E., Shost, M., Roth, G., and Zizelman, J., 3-Cylinder Turbocharged Gasoline Direct Injection: A High Value Solution for Low CO_2 and NO_x Emissions. SAE paper, No.2010-01-0590.

[5] UNECE. Euro 5 & 6: 715/CE/2007 et 692/2008/CE

[6] Stone, R., Introduction to Internal Combustion Engines (Fourth Edition). 2012, Palgrave Macmillan.

[7] Eastwood, P., Particulate Emissions from Motor Vehicles. 2008, Wiley.

[8] Raj, A., Celnik, M., Shirley, R., Sander, M., Patterson, R., West, R., and Kraft, M., A Statistical Approach to Develop a Detailed Soot Growth Model Using PAH Characteristics. Combustion and Flame. 2009, vol.156: 896-913.

[9] Kittelson, D.B., Engines and Nanoparticles: A Review. Journal of Aerosol Science. 1998, vol.29(5/6): 575-588.

[10] Maricq, M.M., Posdiadlik, D.H., and Chase, R.E., Gasoline Vehicle Particle Size Distribution: Comparison of Steady State, FTP and US06 Measurements. Environmental Science & Technology. 1999, vol.33: 2007-2015.

[11] Geller M.D., Ntziachristos, L., Mamakos, A., Samaras, Z., Schmitz, D.A., Froines, J.R., and Sioutas, C., Physicochemical and redox characteristics of particulate matter (PM) emitted from gasoline and diesel passenger cars. Atmospheric Environment. 2006, vol.40: 6988-7004.

[12] Kasper, A., Burtscher, H., Johnson, J.P., Kittelson, D.B., Watts, W.F., Baltensperger, U., and Weingartner, E., Particle Emissions from SI-Engines During Steady State and

Transient Operation Conditions. SAE paper, No.2005-01-3136.

[13] Kittelson, D.B., Watts, W.F., Johnson, J.P., Schauer, J.J., and Lawson, D.R., On-Road and laboratory evaluation of combustion aerosols--Part 2: Summary of spark ignition engine results. Journal of Aerosol Science. 2006, vol.37: 931-949.

[14] Zervas, E., Dorlhène, P., Forti, L., Perrin, C., Mornique, J.C., Monier, R., Ing, H., and Lopez, B., Interlaboratory Study of the Exhaust Gas Particle Number Measurement Using the Condensation Particle Counter (CPC). Energy & Fuels. 2006, vol.20: 2426-2431.

[15] Lee, H., Kim, J., Myung, C.L., and Park, S., Experimental Investigation of Nanoparticle Formation Characteristics from Advanced Gasoline and Diesel Fueled Light Duty Vehicles under Different Certification Driving Modes. Journal of Mechanical Science and Technology. 2009, vol.23: 1591-1601.

[16] BOSCH (2007). Automotive Handbook 6th Edition. Robert Bosch Gmbh.

[17] Andersson, J., Giechaskiel, B., Muñoz-Bueno, R., Sandbach, E., and Dilara, P., Particle Measurement Programme (PMP) Light-duty Inter-laboratory Correlation Exercise (ILCE_LD) Final Report. 54th GRPE, 4-8 June 2007, agenda item 3. GRPE-54-08-Rev.1.

[18] Graskow, B.R., Kittelson, D.B., Ahmadi, M.R., and Morris, J.E., Exhaust Particulate Emissions from a Direct Injection Spark Ignition Engine. SAE paper, No.1999-01-1145.

[19] Smallwood, G.J., Snelling, D.R., Gülder, Ö.L., Clavel, D., Gareau, D., Sawchuk, R.A., and Graham, L., Transient Particulate Matter Measurements from the Exhaust of a Direct Injection Spark Ignition Automobile. SAE paper, No.2001-01-3581.

[20] Harris, S.J. and Maricq, M.M., Signature size distributions for diesel and gasoline engine exhaust particulate matter. Jounal of Aerosol Science. 2001, vol.32: 749-764.

[21] Maricq, M.M. and Xu, N., The effective density and fractal dimension of soot particles from premixed flames and motor vehicle exhaust. Jounal of Aerosol Science. 2004, vol.35: 1251: 1274.

[22] Mathis, U., Mohr, M., and Forss, A.M., Comprehensive particle characterization of modern gasoline and diesel passenger cars at low ambient temperatures. Atmospheric Environment. 2005, vol.39: 107-117.

[23] Ntziachristos, L., Mamakos, A., Samaras, Z., Mathis, U., Mohr, M., Thompson, N., Stradling, R., Forti, L., and Serves, C., Overview of the European "Particulates" Project on the Characterization of Exhaust Particulate Emissions From Road Vehicles: Results for Light-Duty Vehicles. SAE paper, No.2004-01-1985.

[24] Ericsson, P., Holmström, M., Amberntsson-Carlsson, A., Ohlson, C., Skoglundh, M., Andersson, B., and Carlsson P.A., Characterization of Particulate Emissions and Methodology for Oxidation of Particulates from Non-Diesel Combustion Systems. SAE paper, No. 2008-01-1746.

[25] Giechaskiel, B., Dilara, P., Sandbach, E., and Andersson, J., Particle measurement programme (PMP) light-duty inter-laboratory exercise: comparison of different particle number measurement systems. Measurement Science & Technology. 2008, vol.19: 095401(16pp).

[26] Braisher, M., Stone, R., and Price, P., Particle Number Emissions from a Range of European Vehicles. SAE paper No.2010-01-0786.

[27] Peckham, M., Campbell, B., and Finch, A., Study of transient particulate and gaseous emissions from a modern GDI engine. IMeche Conference, Internal Combustion Engines: Improving Performancem, Fuel Economy and Emissions. 29-30 November 2011.

[28] CONCAWE (2009) Comparison of particle emissions from advanced vehicles using DG TREN and PMP measurement protocols. Report No. 2/09. Brussels: CONCAWE.

[29] Kayes, D. and Hochgreb, S., Mechanisims of Particulate Matter Formation in Spark-Ignition Engines. 1. Effect of Engine Operating Conditions. Environ. Sci. Technol. 1999, vol.33(22): 3957-3967.

[30] Kayes, D. and Hochgreb, S., Mechanisms of Particulate Matter Formation in Spark-Ignition Engines. 2. Effect of Fuel, Oil, and Catalyst Parameters. Environ. Sci. Technol. 1999, vol.33(22): 3968-3977.

[31] Kayes, D. and Hochgreb, S., Mechanisms of Particulate Matter Formation in Spark-Ignition Engines. 3. Model of PM Formation. Environ. Sci. Technol. 1999, vol.33(22): 3978-3992.

[32] Sandquist, H., Lindgren, R., and Denbratt, I., Sources of Hydrocarbon Emissions

from a Direct Injection Stratified Charge Spark Ignition Engine. SAE paper, No.2000-01-1906.

[33] Wyszynski, L., Aboagye, R., Stone, R., and Kalghatgi, G., Combustion Imaging and Analysis in a Gasoline Direct Injection Engine. SAE paper, No.2004-01-0045.

[34] Price, P., Stone, R., Collier, T., and Davies, M., Particulate Matter and Hydrocarbon Emissions Measurements: Comparing First and Second Generation DISI with PFI in Single Cylinder Optical Engines. SAE paper, No. 2006-01-1263.

[35] Drake, M.C., Fansler, T.D., Solomon, A.S., and Szekely, G.A. Jr, Piston Fuel Films as a Source of Smoke and Hydrocarbon Emissions from a Wall-Controlled Spark-Ignited Direct-Injection Engine. SAE paper No.2003-01-0547.

[36] Stojkovic, B.D., Fansler, T.D., Drake, M.C., and Sick, V., High-speed imaging of OH* and soot temperature and concentration in a stratified -charge direct-injection gasoline engine. Proceedings of the Combustion Institute. 2005, vol.30: 2657-2665.

[37] Drake, M.C. and Haworth, D.C., Advanced gasoline engine development using optical diagnostics and numerical modeling. Proceedings of the Combustion Institute. 2007, vol.31: 99-124.

[38] Siewert, R.M., A phenomenological Engine Model for Direct Injection of Liquid Fuels, Spray Penetration, Vaporization, Ignition Delay and Combustion. SAE paper, No.2007-01-0673.

[39] Mosbach, S., Celnik, M.S., Raj, A., Kraft, M., Zhang, H.R., Kubo, S., and Kim, K.O., Towards a detailed soot model for internal combustion engines. Combustion and Flame. 2009, vol.156: 1156-1165.

[40] Abdul-Khalek, I.S., Kittelson, D.B., Graskow, B.R., Wei, Q., and Brear, F., Diesel Exhaust Particle Size: Measurement Issues and Trends. SAE paper, No.980525.

[41] Graskow, B.R., Ahmadi, M.R., Morris, J.E., and Kittelson, D.B., Influence of Fuel additives and Dilution Conditions on the Formation and Emissions of Exhaust Particulate Matter from a Direct Injection Spark Ignition Engine. SAE paper, No.2000-01-2018.

[42] Giechaskiel, B., Dilara, P., and Andersson, J., Particle measurement Programme (PMP) Light-Duty Inter-Laboratory Exercise: Repeatability and Reproducibility of the Particle Number Method. Aerosol Science and Technology. 2008, vol.42: 528-

543.

[43] Campbell, B., Peckham, M., Symonds, J., Parkinson, J., and Finch, A., Transient Gaseous and Particulate Emissions Measurements on a Diesel Passenger Car including a DPF Regeneration Event. SAE paper No.2006-01-1079.

[44] Riddle, S.G., Jakober, C.A., Robert, M.A., Cahill, T.M., Charles, M.J., and Kleeman, M.J., Large PAHs detected in fine particulate matter emitted from light-duty gasoline vehicles. Atmospheric Environment. 2007, 41: 8658-8668.

[45] Bergvall, C. and Westerholm, R., Dertermination of highly carcinogenic dibenzopyrene isomers in particulate emissions from two diesel- and two gasoline-fuelled light-duty vehicles. Atmospheric Environment. 2009, 43: 3883-3890.

[46] CONCAWE (2005) Fuel effects on the characteristics of particle emissions from advanced engines and vehicles. Report No. 1/05. Brussels: CONCAWE.

[47] Price, P., Twiney, B., Stone, R., Kar, K., and Walmsley, H., Particulate and Hydrocarbon Emissions from a Spray Guided Direct Injection Spark Ignition Engine with Oxygenate Fuel Blends. SAE paper, No.2007-01-0472.

[48] Myung, C.L., Lee, H., Chio, K., Lee, Y.J., and Park, S., Effects of Gasoline, Diesel, LPG, and Low-carbon Fuels and Various Certification Modes on Nanoparticle Emission Charcteristics in Light-duty Vehicles. International Journal of Automotive Technology. 2009, vol.10(5): 537-544.

[49] Chen, L., Measurement of Particulate Emissions from Gasoline Direct Injection Combustion Engines, in Engineering Science. 2010, University of Oxford.

[50] Khalek, I.A., Bougher, T., and Jetter, J.J., Particle Emissions from a 2009 Gasoline Direct Injection Engine Using Different Commercially Available Fuels. SAE paper No.2010-01-2117.

[51] Aikawa, K., Sakurai, T., and Jetter, J.J., Development of a Predictive Model for Gasoline Vehicle Particulate Matter Emissions. SAE paper No.2010-01-2115.

[52] Gidney, J.T., Twigg, M.V., and Kittelson, D.B., Effect of Organometallic Fuel Additives on Nanoparticle Emissions from a Gasoline Passenger Car. Cambridge Particle Meeting 2009.

[53] Wei, J., Wassermann, K., and Li, Y.J., Gasoline Engine Emissions Treatment

Systems Having Particulate Traps. United States Patent Application Publication. Pub. No.: US 2009/0193796 A1.

[54] Andersson, J., Keenan, M., and Åkerman, K., GDI Particles - Legislation, Current Levels and Control. Ricardo, RD. 09/99801.1.

[55] Rubino, L., Crane, R.I., Shrimpton, J.S., and Arcoumanis, C., An electrostatic trap for control of ultrafine particle emissions from gasoline-engined vehicles. Proc. IMechE. Vol.219 Part D: J. Automobile Engineering. pp535-546.

[56] Sandford, M., Page, G., and Crawford, P., The All New AJV8. SAE paper, No.2009-01-1060.

[57] High Temperature Hydrocarbon Analyser Model 523. Instruction Manual. Rotork Analysis Limited.

[58] DMS500 Fast Particulate Spectrometer Unit M16. User Mannual v2.3. Cambustion Limited 2007.

[59] Reavell, K., Hands, T., and Collings, N., A Fast Response Particulate Spectrometer for Combustion Aerosols. SAE paper, No. 2002-01-2714.

[60] Symonds, J., Price, P., Williams, P., and Stone, R., Density of particles emitted from a gasoline direct injection engine. 12th ETH-Conference on Combustion Generated Nanoparticles, June 2008.

[61] ECE/TRANS/WP.29/GRPE/2008/page 62 Appendix 5. Particle Number Emissions Measurement Equipment. http://www.unece.org.

[62] Symonds, J., Reavell, K., Olfert, J., Campbell B., and Swift, S., Diesel soot mass calculation in real-time with a differential mobility spectrometer. Aerosol Science. 2007, vol.38: 52-68.

[63] Hinds, W.C., Aerosol Technology: properties, behaviour, and measurement of airborne particles (Second Edition). 1999, New York: Wiley.

[64] Kuwabara, S., The forces experienced by randomly distributed parallel circular cylinders or spheres in viscous flow at small Reynolds numbers. Journal of the Physical Society of Japan. 1959, vol.14: 527-532.

[65] Lee, K.W. and Liu, Y.H., Theoretical Study of Aerosol Filtration by Fibrous Filters. Aerosol Science and Technology. 1982, vol.1: 147-161.

[66] Baron, P.A. and Willeke, K., Aerosol Measurement: Principles, Techniques, and Applications (Second Edition). 2001, New York: Wiley.

[67] Yeh, H.C. and Liu, B.Y.H., Aerosol Filtration by Fibrous Filters-I. Theoretical. Journal of Aerosol Science. 1974, vol.5: 191-204.

[68] Stechkina, I.B., Kirsch, A.A., and Fuchs, N.A., Studies on Fibrous Aerosol Filters-IV Calculation of Aerosol Deposition in Model Filters in the Range of Maximum Penetration. Annals of Occupational Hygiene. 1969, vol.12: 1-8.

[69] Lee, K.W. and Liu, B.Y., On the Minimum Efficiency and the Most Penetrating Particle Size for Fibrous Filters. Air Pollution Control Association. 1980, vol.4: 377-381.

[70] Ramarao, B.V., Tien, C., and Mohan, S., Calculation of single Fiber Efficiencies for Interception and Impaction with Superposed Brownian Motion. Journal of Aerosol Science. 1993, vol.25: 295-313.

[71] Gougeon, R., Boulaud, D., and Renoux, A., Comparison of Data from Model Fiber Filters with Diffusion, Interception and Inertial Deposition Models. Chemical Engineering Communications. 1996, vol.151: 19-39.

[72] Liu, Z.G. and Wang, P.K., Pressure Drop and Interception Efficiency of Multifiber Filters. Aerosol Science and Technology. 1997, vol.26: 313-325.

[73] Bałazy, A. and Podgórski, A., Deposition Efficiency of Fractal-like Aggregates in Fibrous Filters Calculated Using Brownian Dynamics Method. Journal of Colloid and Interface Science. 2007, vol.311: 323-337.

[74] Steffens, J. and Coury, J.R., Collection Efficiency of Fiber Filters Operating on the Removal of Nano-sized Aerosol Particles: I-Homogeneous Fibers. Separation and Purification Technology. 2007, vol.58: 99-105.

[75] Regan, B.D. and Raynor, P.C., Single-Fiber Diffusion Efficiency for Eliptical Fibers. Aerosol Science and Technology. 2009, vol.43: 533-543.

[76] Kim, S.C., Wang, J., Emery, M.S., Shin, W.G., Mulholland, G.W., and Pui, D.Y.H., Structural Property Effect of Nanoparticle Agglomerates on Particle Penetration through Fibrous Filter. Aerosol Science and Technology. 2009, vol.43: 344-355.

[77] Hickel, W., Seston retention by Whatman GF/C glass-fiber filters. Marine Ecology –

Progress Series. 1984, vol.16: 185-191.

[78] Brown, R.C. and Thorpe, A., Glass-Fibre Filters with Bimodal Fibre Size Distributions. Powder Technology. 2001, vol.118: 3-9.

[79] Kirsh, V.A., The Deposition of Aerosol Submicron Particles on Ultrafine Fiber Filters. Colloid Journal. 2004, vol.66: 311-315.

[80] Steffens, J. and Coury, J.R., Collection Efficiency of Fiber Filters Operating on the Removal of Nano-Sized Aerosol Particles II. Heterogeneous fibers. Separation and Purification Technology. 2007, vol.58: 106-112.

[81] Lange, R., Fissan, H., and Schmidt-Ott, A., A New Method for Determination of the Interception Equivalent Diameter. Journal of Aerosol Science. 2000, vol.31: 221-231.

[82] Kasper, G., Schollmeier, S., and Meyer, J., Structure and Density of Deposits Formed on Filter Fibers by Inertial Particle Deposition and Bounce. Journal of Aerosol Science. 2010, vol.41:1167-1182.

[83] Wang, H.C. and Kasper, G., Filtration Efficiency of Nanometer-Size Aerosol Particles. Journal of Aerosol Science. 1991, vol.22: 31-41.

[84] Hubbard, J.A., Brockmann, J.E., Dellinger, J., Lucero, D.A., Sanchez, A.L., and Servantes, B.L., Fibrous Filter Efficiency and Pressure Drop in the Viscous-Inertial Transition Flow Regime. Aerosol Science and Technology. 2012, vol.46: 138-147.

[85] Chen, X., Fu, H., Smith, S., and Sandford, M., Investigation of Combustion Robustness in Catalyst Heating Operation on a Spray Guided DISI Engine. SAE paper, No. 2009-01-1489.

[86] Twiney, B., Stone, R., Chen, X., and Edmunds, G., Investigation of Combustion Robustness in Catalyst Heating Operation on a Spray Guided DISI Engine, Part 1 - Measurements of Spark Parameters and Combustion. SAE paper, No. 2010-01-0593.

[87] Twiney, B., Stone, R., Chen, X., and Edmunds, G., Investigation of Combustion Robustness in Catalyst Heating Operation on a Spray Guided DISI Engine, Part II - Measurements of Spray Development, Combustion Imaging and Emissions. SAE paper, No. 2010-01-0603.

[88] Abdul-Khalek, I.S. and Kittelson, D.B., Real Time Measurement of Volatile and Solid Exhaust Particles Using a Catalytic Stripper. SAE paper, No.950236.

[89] Kittelson, D.B., Watts, W.F., Savstrom, J.C., and Johnson, J.P., Influence of a catalytic stripper on the response of real time aerosol instruments to diesel exhaust aerosol. Jounal of Aerosol Science. 2005, vol.36: 1089-1107.

[90] Khalek, I., Sampling System for Solid and Volatile Exhaust Particle Size, Number, and Mass Emissions. SAE paper, No.2007-01-0307.

[91] Khalek, I. and Bougher, T., Development of a Solid Exhaust Particle Number Measurement System Using a Catalytic Stripper Technology. SAE paper, No. 2011-01-0635.

[92] Kasper., M., The Number Concentration of Non-Volatile Particles – Design Study for an Instrument According to the PMP Recommendations. SAE paper, No. 2004-01-0960.

[93] Slanina, J., Lamoen-doornenbal, L.V., Lingerak, W.A., Meilof, W., Klockow, D., and Nießner, R., Application of a Thermo-Denuder Analyser to the Determination of H_2SO_4, HNO_3 and NH_3 in Air. International Journal of Environmental Analytical Chemistry. 1981, vol.9: 59-70.

[94] Turpin, B.J., Saxena, P., and Andrews, E., Measuring and Simulating Particulate Organics in the Atmosphere: Problems and Prospects. Atmospheric Environment. 2000, vol.34: 2983-3013.

[95] Huffman, J.A., Ziemann, P.J., Jayne, J.T., Worsnop, D.R., and Jimenez, J.L., Development and Characterization of a Fast-Stepping/Scanning Thermodenuder for Chemically-Resolved Aerosol Volatility Measurements. Aerosol Science and Technology. 2008, vol.42: 395-407.

[96] Riipinen, I., Pierce, J.R., Donahue, N.M., and Pandis, S.N., Equilibration Time Scales Of Organic Aerosol Inside Thermodenuder: Evaporation Kinetics Versus Thermodynamics. Atmospheric Environment. 2010, vol.44: 597-607.

[97] Verma, V., Pakbin, P., Cheung, K.L., Cho, A.K., Schauer, J.J., Shafer, M.M., Kleinman, M.T., and Sioutas, C., Physicochemical and Oxidative Characteristics of Semi-Volatile Components of Quasi-Ultrafine Particles in an Urban Atmosphere. Atmospheric Environment. 2011, vol.45: 1025-1033.

[98] Burtscher, H., Baltensperger, U., Bukowiecki, N., Cohn, P., Hüglin, C., Mohr, M., Matter, U., Nyeki, S., Schmatloch, V., Streit, N., and Weingartner, E., Separation of

Volatile and Non-Volatile Aerosol Fraction by Thermodesorption: Instrumental Development and Applications. Aerosol Science. 2001, vol.32: 427-442.

[99] Park, D., Kim, S., Choi, N.K., and Hwang, J., Development and Performance Test of a Thermo-Denuder for Separation of Volatile Matter from Submicron Aerosol Particles. Journal of Aerosol Science. 2008, vol.39: 1099-1108.

[100] Wehner, B., Philippin, S., and Wiedensohler, A., Design and Calibration of a Thermodenuder with an Improved Heating Unit to Measure the Size-Dependent Volatile Fraction of Aerosol Particles. Journal of Aerosol Science. 2002, vol.33: 1087-1093.

[101] Kawai, T., Lee, J., Goto, Y., and Odaka, M., Influence of Thermo-Denuder Dimensions on Nano-particle Measurement. SAE paper, No. 2003-01-2018.

[102] Cappa, C.D., A Model of Aerosol Evaporation Kinetics in a Thermodenuder. Atmospheric Measurement Techniques. 2010, vol.3: 579-592.

[103] Minoura, H., Takekawa, H., and Terada, S., Roadside Nanoparticles Corresponding to Vehicle Emissions During One Signal Cycle. Atmospheric Environment. 2009, vol.43: 546-556.

[104] Saleh, R., Walker, J., and Khlystov, A., Determination of Saturation Pressure and Enthalpy of Vaporization of Semi-Volatile Aerosols: The Integrated Volume Method. Journal of Aerosol Science. 2008, vol.32: 876-887.

[105] Saleh, R., Shihadeh, A., and Khlystov, A., Determination of Evaporation Coefficients of Semi-Volatile Organic Aerosols Using an Integrated Volme-Tendem Differential Mobility Analysis (IV-TDMA) Method. Journal of Aerosol Science. 2009, vol.40: 1019-1029.

[106] Kittelson, D.B., Watts, W.F., and Johnson, J.P., On-Road and Laboratory Evaluation of Combustion Aerosols-Part 1: Summary of Diesel Engine Results. Journal of Aerosol Science. 2006, vol.37: 913-930.

[107] Yehliu, K., Boehman, A.L., and Armas, O., Emissions from Different Alternative Diesel Fuels Operating with Single and Split Fuel Injection. Fuel. 2010, vol.89: 423-437.

[108] Swanson, J. and Kittelson, D.B., Evaluation of Thermal Denuder and Catalytic Stripper Methods for Solid Particle Measurements. Journal of Aerosol Science. 2010,

vol.41: 1113-1122.

[109] Walker, K.L., Homsy, G.M., and Geyling, F.T., Thermophoretic Deposition of Small Particles in Laminar Tube Flow. Journal of Colloid and Interface Science. 1979, vol.69: 138-147.

[110] Talbot, L., Cheng, R.K., Schefer, R.W., and Willis, D.R., Thermophoresis of particles in a heated boundary layer. Journal of Fluid Mechanics. 1980, vol.101: 737-758.

[111] Batchelor, G.K. and Shen, C., Thermophoretic Deposition of Particles in Gas Flowing over Cold Surfaces. Journal of Colloid and Interface Science. 1985, vol.107: 21-37.

Appendix A

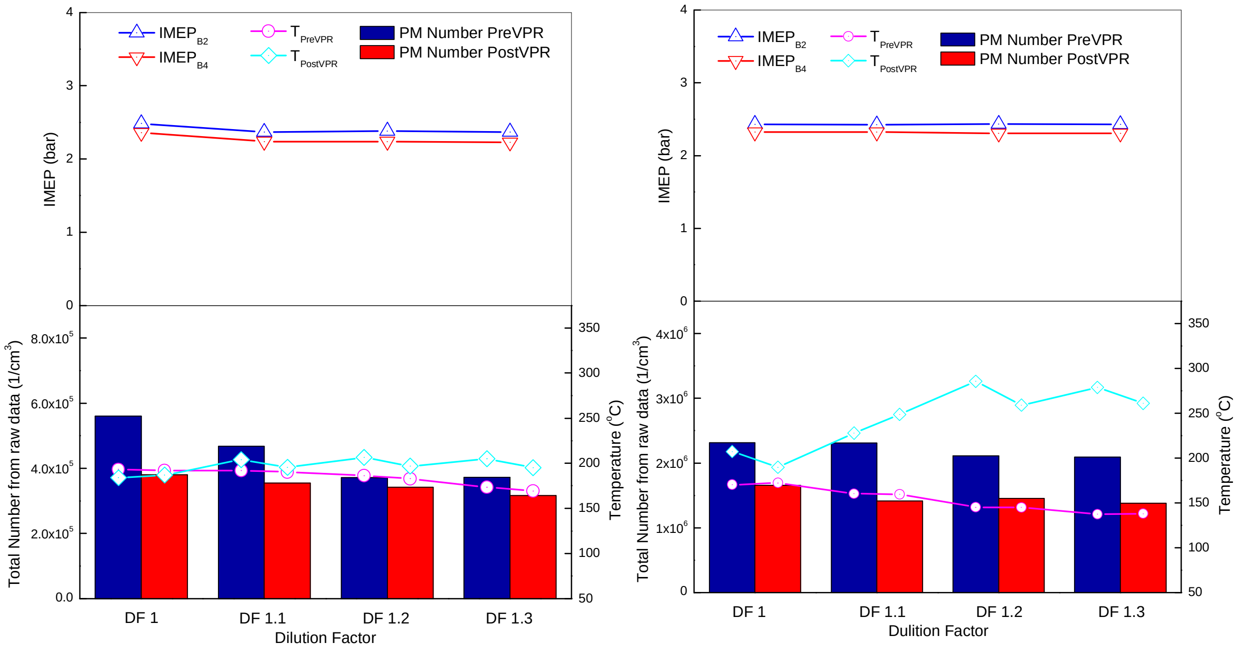

(a) Air addition, Lambda = 1 (c) Air addition, Lambda = 0.9

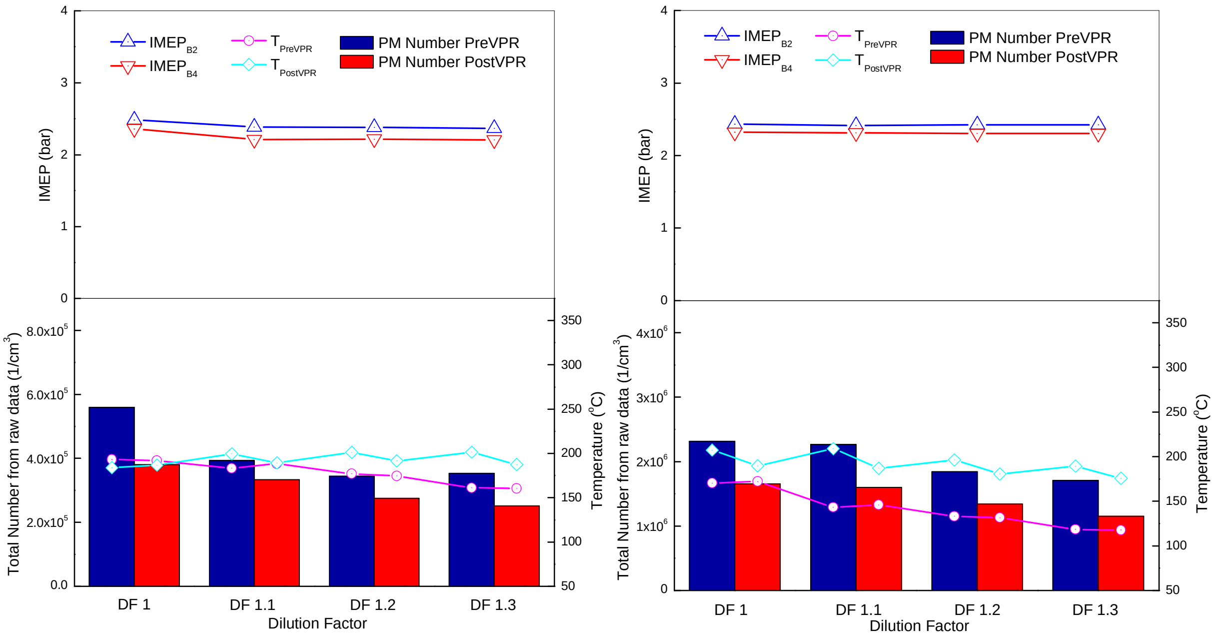

(b) N_2 addition, Lambda = 1 (d) N_2 addition, Lambda = 0.9

Fig. A1 IMEP, pre and post VPR temperatures with various gas additions and relative air-fuel ratios (refer to Table 5.3).

Fig. A1 shows the temperatures of pre-VPR and post-VPR, and IMEP (average of 100 engine cycles) under different test conditions. It can be seen that IMEP is stable during the tests.

When lambda is rich, with additional air, the temperature of post-VPR rises significantly. This is due to the oxidation reaction of air and exhaust in the VPR.

Publications

1. **Fan Xu**, Richard Stone. The Effects of Hot Air Dilution and a Thermo-Denuder (TD) on the Particulate Matter Emissions from a Direct Injection Spark Ignition Engine. SAE 2012 World Congress, Paper NO. 2012-01-0436.
2. **Fan Xu**, Longfei Chen, Richard Stone. The Effects of a Catalytic Volatile Particle Remover on the Particulate Matter Emissions from a Direct Injection Spark Ignition Engine. Environmental Science & Technology. 2011, 45(20):9036-9043. (Publication Date (Web): September 08, 2011, DOI: 10.1021/es2008209)
3. **Fan Xu**, Richard Stone. Testing of a Volatile Particle Remover (VPR) and a Thermo-denuder (TD) Using a GDI Engine. 15th ETH-Conference on Combustion Generated Nanoparticles. June 26th – 29th 2011, ETH Zurich.
4. L Chen, **F Xu**, R Stone, D Richardson. Spray Imaging, Mixture Preparation and Particulate Matter Emissions Using a GDI Engine Fuelled with Stoichiometric Gasoline/Ethanol Blends. IMeche Conference on Internal Combustion Engines: Improving Performance, Fuel Economy and Emissions. 29-30 November 2011, London.
5. L Chen, N Hinton, F Leach, R Stone, **F Xu**. GDI Engine Operation with Ethanol/Gasoline Blends and Aqueous Ethanol. Journal of Automotive Safety and Energy. (Accepted for publication)